Yann Kevin Petit, MSc

Singlet oxygen in metal-air batteries: origins, consequences, and mitigation

DOCTORAL THESIS

to achieve the university degree of

Doktor der technischen Wissenschaften

submitted to

Graz University of Technology

Supervisor

Priv.-Doz. Dipl.-Ing. Dr.sc.ETH Stefan Freunberger

Institut für Chemische Technologie von Materialen

Graz, January 2020

AFFIDAVIT

I declare that I have authored this thesis independently, that I have not used other than the declared sources/resources, and that I have explicitly indicated all material which has been quoted either literally or by content from the sources used. The text document uploaded to TUGRAZonline is identical to the present doctoral thesis.

Date

Signature

There's more to the picture
than meets the eye.

Neil Young

Table of contents

List of Figures

Acknowledgements

The bird a nest, the spider a web, man friendship.
William Blake

One can never emphasise enough that a Ph.D. thesis is first and foremost a common effort that could not be achieved without the insights, help and support of a number of people. These three years have been rich not only scientifically but also humanly.

My thesis was performed at the ICTM of TU Graz, Austria. For welcoming me to this institute, I would like to thank the head of the institute Prof. Martin Wilkening. I am deeply indebted to the European Research Council (ERC) for my thesis financial support through the OMICON project obtained by Dr. Freunberger. I am grateful to the technical chemistry, chemical and process engineering, biotechnology doctoral school and Prof. Klaus Reichmann for their help concerning the organization of this thesis.

My first thanks go, naturally, to Prof. Philipp Adelhelm and Prof. Torsten Mayr for doing me the honour of examining my thesis and being part of my jury. Furthermore, I want to particularly acknowledge my supervisor Dr. Stefan Freunberger who has instilled the necessary motivation and provided me with the chance to perform my Ph.D. study in his group. I would also like to thank Prof. Christian Slugovc for his benevolence through the course of these three years.

I thank all the hard-working technical and administrative staff at TU Graz, in particularly Ms. Brigit Ehmann, Ms. Christina Albering, Mr. Johann Schlegl and Mr. Lukas Troi. They have provided me tremendous help with technical support. I would also thank Prof. Robert Saf from the ICTM of TU Graz, for his advice on mass spectrometry; Prof. Sergey Borisov from the ACFC of TU Graz, for his technical and theoretical support on the analytical methods performed throughout these three years; and Dr. Gernot Strohmeier from ACIB GmbH, for his formation on high-performance liquid chromatography. I want, moreover, to address acknowledgements to Dr. Sergio Brutti from the chemistry department of Sapienza University and Prof. Egbert Zojer from the IF of TU Graz who collaborated with my supervisor for the DFT calculations present in this thesis.

I also want to address special thanks to all my coworkers at TU Graz and particularly my working groups for their warm welcome and the pleasant working atmosphere. I particularly want to acknowledge Aleksej Samojlov, your cheerfulness and kindness has been of great help during my stay in Austria. I especially appreciated the express Serbian course and the scientific discussions I had with Daniel Mijailovic for which I want to thank you. Last but not least, I express my gratitude to Dr. Éléonore Mourad for your unconditional support and scientific advice during my Ph.D. thesis.

My final thanks go to my family and friends for continuous support in life and through these stressful times. I wish to dedicate my thesis to my grandmother who sadly passed away during my Ph.D.

Abstract

This thesis is concerned with the presence of singlet oxygen in non-aqueous batteries and more particularly metal-air batteries. Despite promising capacities, non-aqueous metal-air technology development has been stalled by crippling parasitic chemistry preventing long term cyclability. Pinpointing a culprit is rather complex due to the new "beyond-intercalation" approach of such batteries. The aggressive singlet oxygen, the first oxygen excited state, was recently shown to be a source of side reactivity in metal-air batteries on which this study is centred.

After developing adapted in/ex-situ analysis methods, singlet oxygen presence was found to be correlated with parasitic chemistry presence in metal batteries. We identified three different formation pathways which are namely the oxidation of alkali oxides at high overpotentials, the oxidation of side products common to all lithium based batteries, and superoxide disproportionation. Superoxide-like species are formed as an intermediate species at all stages of cycling and only the superoxide disproportionation can explain the presence of singlet oxygen during discharge and charge at low overpotentials.

Our mechanistic study of this reaction revealed the propensity for superoxide disproportionation to its peroxide in presence of hard Lewis acidic cations such as Li^+ and Na^+ whereas softer Lewis acids such as K^+ are stable in superoxide form. Strikingly, additional soft Lewis acid presence favours singlet oxygen production via disproportionation, which results in increased parasitic products on both discharge and charge. This has serious consequences for metal-air technology, notably for the discharge products or the electrolyte as situations bound for superoxide disproportionation and soft Lewis acid should be avoided.

Disproportionation appears inevitable currently and $^1O_2$ mitigation means are essential to improve the stability of Li- and Na-O_2 batteries. $^1O_2$ physical quenchers, which deactivate singlet oxygen to its ground state without additive consumption, are well indicated to reduce the parasitic product accumulation. The design and use of an adapted quencher resulted in a clear improvement of desired reaction yields during charge and discharge. Beside the introduction of a new type of additives, this thesis confirms the role of singlet oxygen as a major side reaction source in metal-air batteries.

Oxidation mediators are a promising type of mediators to bypass electron conduction in the resistive alkali oxides and allow for high reaction rates at low overpotentials during charge. To design efficient mediators and potentially reduce the production of singlet oxygen, the reaction mechanisms need to be understood. We showed that the mediated reaction proceed similarly to a non-mediated charge via superoxide as an intermediate product. To reduce the disproportionation importance, oxidation mediators must show maximized reaction kinetics towards superoxide.

The mediated reaction kinetics were determined to follow the Marcus theory and shows a maximum as a function of the mediator redox potential, which should be targeted for future mediators. The reaction is dominated by the reorganisation energy of the solid phase and, hence, the rate does not depend strongly on the chemical class of the mediators. The mediator chemical nature, however, dictates the stability of the mediators to singlet oxygen exposure and its ability to quench $^1O_2$ is associated with higher reaction yields and thus preferable. We could also demonstrate that mediator chemical stability must be ensured before further characterisations.

Singlet oxygen in non-aqueous metal-air batteries is spotlighted by this thesis as a major source of parasitic chemistry. Here, we provide our insights on its formation mechanisms, consequences of its presence, and possible mitigation strategies. Awareness of singlet oxygen gives a rationale for future researches towards achieving highly reversible cell operation.

Abbreviations

AFM	Atomic force microscopy
CV	Cyclic voltammetry
DEMS	Differential electrochemical mass spectrometry
DFT	Density functional theory
DSC	Differential scanning calorimetry
EPR	Electron paramagnetic resonance
HPLC	High-performance liquid chromatography
IR	Infrared radiation
MS	Mass spectrometry
NMR	Nuclear magnetic resonance
OEMS	Online electrochemical mass spectrometry
RRDE	Rotating ring disk electrode
SECM	Scanning electrochemical microscopy
SEM	Scanning electron microscopy
TEM	Transmission electron microscopy
TLC	Thin layer chromatography
UV-vis	Ultra-violet and visible
XANES	X-ray absorption near edge structure
XPS	X-ray photoelectron spectroscopy
XRD	X-ray diffraction
AN	Acceptor number
CT	Charge transfer
DN	Donor number
e^-	electron
isc	Intersystem crossing
SEI	Solid-electrolyte interphase
BP	N-N bridged pyrrolidines and piperidines
BP55	1-1'-bipyrrolidine
BP56	1-(pyrrolidin-1yl)piperidine
BP66	1-1'-bipiperidine
DABCO	1,4-diazabicyclo[2.2.2]octane
DCM	Dichloromethane
DMA	9,10-dimethylanthracene
DME	Dimethoxyethane
DMPZ	5,10-dihydro-5,10-dimethylphenazine
DMSO	Dimethyl sulfoxide
DPA	9,10-Diphenylanthracene
EtOAc	Ethyl acetate
Fc	Ferrocene
Im^+	Imidazolium
LFP	Lithium iron phosphate
MBT_2	2-2'-dithiobis(benzothiazole)
MeCN	Acetonitrile
Me-Im	1-methylimidazole
NASICON	Na super ionic conductor
$^3O_2$	Ground state dioxygen ($^3\Sigma_g^-$)
$^1O_2$	First singlet state dioxygen ($^1\Delta_g$)
PC	Propylene carbonate
Pd4F	Palladium (II) meso-tetra(4-fluorophenyl)-9-tetrabenzoporphyrin
PeDTFSI	1-pentyl-1,4-diazacyclo[2,2,2]octan-1-ium TFSI
TBA^+	Tetrabutylammonium
TDPA	tris[4-(diethylamino)phenyl]amine
TEGDME	Tetraethylene glycol dimethyl ether
TEMPO	(2,2,6,6-Tetramethylpiperidin-1-yl)oxyl
$TFSI^-$	Bis(trifluoromethanesulfonyl)imide
THF	Tetrahydrofuran
TMPD	N,N,N',N'-tetramehyl-p-phenyldiamine
TTF	Tetrathiafulvalene
18-crown-6	1,4,7,10,13,16-hexaoxacyclooctadecane

Motivation and structure

The present thesis is part of the overall effort to enhance energy stockage capacity and answer the coming societal demands, a major current research subject. With the popularisation of lithium-ions batteries, portable electronic devices have seen a multiplication of their uses and challenged the current technologies. The required higher storage capacity can only be achieved through a new technological paradigm shift. Among the proposed novel chemistries, non-aqueous metal-air batteries present a high theoretical capacity and improved sustainability. This potential has triggered high interest, unfortunately dampened by the difficulties encountered by these technologies. The main hurdles to metal-air batteries are side reactivity and oxide low conductivity that prevent high rate, low overpotential and long term cyclability. Singlet oxygen, an excited state of molecular O_2, was recently identified in metal-air batteries. Considering the high reactivity of singlet oxygen towards organic molecules, it was hypothesized to be a main source of parasitic chemistry and of prime importance to unlock metal-air battery potential. Here, I will present the work performed during my Ph.D. thesis to assess the singlet oxygen significance by deciphering its formation mechanisms during cycling and their consequences in terms of cell design. We notably propose mitigation means to actively reduce the side product formation and improve the metal-air battery yields.

Before presenting the consequences of singlet oxygen presence, the current state of the art in metal-air batteries needs to be understood and their mechanisms will be given in ch. 1. We will start by presenting the peculiar chemistry of metal-air batteries reposing on alkali oxide for charge storage rather than intercalation as commonly used in alkali based batteries. This introductory chapter will focus on lithium-air chemistry based on Li_2O_2, the most promising of these technologies, though also the most complex one since other metal-air batteries commonly stop at the superoxide step. The reaction mechanism and the presence of aggressive species, such as superoxide, impose specific properties for the cell components. Nevertheless, the rise of adapted cells does not prevent setbacks concerning the achievable rechargeability. Using physical and electrochemical metrics, we will show that reduced oxygen species is not sufficient to provide an explanation for the damaging parasitic reactions which must arise from other sources.

In ch. 2, we suggest singlet oxygen ($^1O_2$) as a source of unwanted reactivity. Singlet oxygen presents a different reactivity than the ground state oxygen. Its dienophile and electrophile characters are particularly threatening for organic molecules which usually compose the metal-air working electrode and electrolyte. The cell decomposition results in the accumulation of side products and we designed suitable in-situ and ex-situ analytic methods to determine the parasitic reactivity and the singlet oxygen presence. Singlet oxygen could, hence, be observed during both discharge and charge, arising through three possible pathways. First, alkali oxide oxidation above a potential threshold fixed by the reaction thermodynamics can directly produce $^1O_2$. Second, this species can arise similarly from carbonate oxidation, a common side product in alkali based batteries and has implications beyond the sole metal-air battery technologies. Finally, we could show that superoxide disproportionation can produce singlet oxygen. Disproportionation is a favoured process for LiO_2 and NaO_2 which, aside from explaining the higher stability of K-O_2 cells, provides the only production pathway during discharge and at low overpotential during charge.

Disproportionation holds the key for the cyclability of metal-air batteries and is further deciphered in ch. 3. We could show that disproportionation is highly dependent on the cations present. As expected from thermodynamics and the Pearson acid-base concept, superoxide is stabilized by softer Lewis acids whereas stronger Lewis acids, such as Li^+ or Na^+, promote the formation of peroxide through superoxide disproportionation. On the contrary, the $^1O_2$ production by disproportionation is enhanced by the presence of soft Lewis acids, for example organic cations used in ionic liquids. DFT calculation, done in collaboration with the Sapienza University, demonstrated a destabilisation of alkali superoxide dimers by soft Lewis acids, resulting in an easier pathway to singlet oxygen. The inclusion of soft Lewis acids in lithium-air electrolytes give rise to lower reaction yields and increase parasitic products during cycling, imposing disproportionation as a reaction corner stone. The disproportionation importance has drastic influence on the metal-air development paths and mechanisms, notably on the electrolyte and reaction products.

Disproportionation currently appears as an inevitable process and so is the $^1O_2$ formation in metal-air batteries. The noxious consequences of $^1O_2$ should hence be mitigated. Physical $^1O_2$ quenchers are well indicated in battery operations, avoiding the accumulation of decomposition products. In ch. 4, we present a $^1O_2$ quencher stable and efficient in metal-air chemistries. The utilization of $^1O_2$ quencher as electrolyte additive provides an extensive amelioration of the reaction yield both in discharge and charge. The heavy impact of $^1O_2$ quencher on parasitic chemistry confirms the role of $^1O_2$ as a stability hurdle in metal-air batteries. Physical quencher emerges, hence, as a new and primordial class of additives in the metal-air technology to provide long term cycling.

Oxidation mediators are another type of additives often proposed in the lithium-air chemistry. Oxidation mediators allow bypassing charge transport through the poorly conductive alkali oxide and reach disconnected particles that can form while cycling. These additives were shown to reduce charge overpotential and to increase the reaction rate, which was hypothesized to reduce parasitic chemistry. In ch. 5, we unravel the mediated charge mechanism. The presence of mediators in the electrolyte does not prevent the formation of superoxide and subsequent $^1O_2$ release either via alkali oxide oxidation or disproportionation. The presence of $^1O_2$ imposes additional requirements to efficient oxidation mediators, usually organic molecules, which were mostly studied based on their potentials. They should ideally possess a high reaction rate to diminish the occurrence of disproportionation, a high stability towards $^1O_2$ provided by their chemical natures, and be chemically stable against oxygen, peroxide and superoxide.

Based on these criteria, in ch. 6, we introduce design rules for oxidation mediators to suppress $^1O_2$ presence thanks to a new class of mediators, organic hydrazines. The main conclusion of our study is the applicability of the Marcus theory to the mediated oxidation kinetic. Consequently, the reaction rate mainly depends on the oxidation mediator potential and presents a maximum that should be aimed at. We could also confirm the desirability of quenching moeties to reduce $^1O_2$ reactivity and to increase the mediator stability. We propose, therefore, to design mediators with a potential corresponding to the maximum predicted by the Marcus theory, chemically stable against oxygenated species, and with an efficient $^1O_2$ quenching chemical class.

Singlet oxygen presence in metal air batteries has tremendous consequences even in small produced quantities that could be overlooked. Advance in understanding its formation mechanisms is fundamental to rationalize parasitic reactions in metal-air chemistry and to achieve true long term cycling. Through this manuscript, we present the achieved understanding and insights on $^1O_2$ formation and mitigation in the course of this thesis to progress further towards high capacity batteries.

Oxygen chemistry, a pathway to next generation batteries

What a gift we have been given to be born in an atmosphere with oxygen.
Marina Keegan

Contents

Figures

Chapter based on Petit et al.[1]

Introduction

The ever rising importance of energy storage in modern society imposes massive and quick technological changes. Lithium-ion battery technology is currently the solution of choice for many applications; new technologies based on sustainable lightweight active and inactive elements with increased electrons exchanged per redox centre are nevertheless indispensable for future electric vehicles[2–5]. A proposed famiIly of batteries to reach these objectives are "beyond-intercalation chemistries", notably metal-air, abandoning the intercalation paradigm[2,4–6]. Among them, organic Li-air technology has received a particular enthusiasm, sometimes for misaddressed reasons, because of the high theroretical capacity of Li_2O_2 (1168 $mA{\cdot}h{\cdot}g^{-1}$[7]) and will be the focus of this introductory chapter.

Li-air batteries are based on a lithium metal anode and a porous electron conducting matrix filled with electrolyte as cathode where oxygen will react to form lithium peroxide during discharge followed by the inverse process on charge as illustrated in Fig. 1.1. The exact reaction mechanisms are, however, complex and still not fully clarified. The consensus tends to a two step reaction during both discharge and charge; the reaction is divided between the formation of superoxide through a one-electron exchange and a subsequent one-electron process or superoxide disproportionation[8–12]. The mentioned steps are influenced by numerous parameters such as the electrolyte, the species present, or the applied potential[13–15]. The reaction product itself is a wide band gap insulator and consequently the exact reaction interface is still unknown. We will present the current understanding of the different implications of this convoluted reaction mechanism which are the stepping stones for this thesis results.

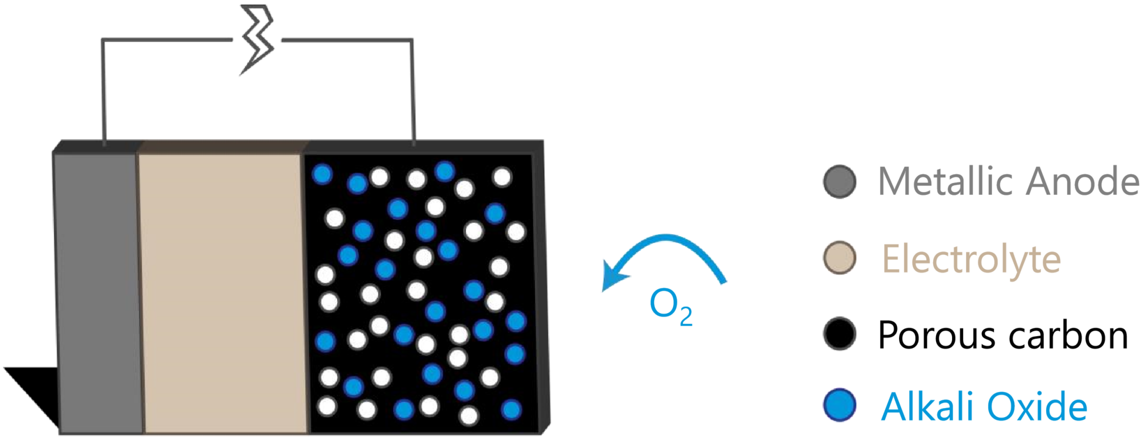

Figure 1.1: **Scheme of the metal-air battery principle on discharge.**

The Li-air battery cathode is based on a porous matrix that needs to sustain the Li_2O_2 formation and provide electrical contact rather than to directly store the charge. The material of choice is carbon due to its lightweight, adaptable and inexpensive nature. We will discuss the stability of carbon electrodes in metal-air chemistry which can be problematic and the proposed replacement materials. Concerning the lithium metal anode, its poor coulombic efficiency is fairly known, especially under metal-air conditions, and we will explore solutions offered by contemporary researches. The Li-air electrolyte is also subject to constraining limitations due to the presence of aggressive oxygen species and their roles in the reaction mechanism. Hence, we will review here the advantages and disadvantages of organic solvents, ionic liquids and solid-state electrolytes in Li-air batteries. The main distinction of metal-air from intercalation batteries is the formation and disappearance of new products while cycling. The consequences on the capacity calculation imposed by "beyond-intercalation" chemistries will be introduce to realistically compare the different technologies.

Severe parasitic reactions are the major hurdle to efficient Li-air batteries[11,16]. These reactions are known to degrade both the electrolyte and electrodes which in turn provoke high charge voltage, poor reversibly and short cell lifetime. Due to the novelty of this chemistry, specific performance metrics and analytical methods have been developed, taking in consideration the gaseous species involved. From the analytical methods, side reactivity has often solely been attributed to reduced oxygen species owing to their reactivity with common lithium-ion electrolytes. We will, however, show that the crippling parasitic chemistry cannot be substantially attributed to the potential reactivity of superoxide or peroxide species with the development of adapted cell components. It can rather be partly associated to the formation of singlet oxygen. Its formation mechanisms, consequences, and options to mitigate it are thus the subject of this thesis.

1.1 Metal-air batteries: principles and advantages

1.1.1 Beyond-intercalation batteries

The technological breakthrough of lithium-ion batteries in the early 1990s has led to a paradigm shift in our habits with the spur of portable electronics, electric vehicles, or integration to the electrical grid[17,18]. With multiplied needs and applications of energy storage, the use of lithium technology has seen a tremendous increase in the past decades. Hence, energy storage came to the forefront of societal changes and research[2,17]. Lithium-ion battery technology approaches its theoretical limits and imposes new technologies, especially due to the expected expansion of the electrical vehicle market[2–5].

Lithium-ion battery capacities are notably plagued by the substantial fraction of electrochemically inactive materials. This technology rests on transition metal oxides at the cathode and carbon at the anode which act as host materials[3]. Lighter redox active elements, increased number of electrons exchanged and lightweight cells are necessary to achieve the high capacity needed for future technologies. Li-rich transition metal oxide cathodes, featuring higher voltage and capacity, are one possible pathway towards next generation batteries but still depend on insertion chemistries[5]. Together with the sustainability demands rising, this motivates "beyond-intercalation chemistry" technologies[2,4–6]. Charge storage in these promising chemistries involves distinctively different processes compared to the well-known intercalation reactions.

Strategies to overcome these problems concern both the anode and the cathode. Alloying materials such as Si or direct use of alkali metal anodes are for example proposed to reduce inactive materials at the anode[17,19,20]. Concerning the cathode, the principal hinder towards high capacity batteries, the main direction is to avoid transition metal redox chemistry; the charges are then stored through the formation of new products by reacting alkali ions with either O_2 or S.[17] [21–25].

1.1.2 Metal-air batteries

Among the proposed technologies, the non-aqueous metal-air technology receive a significant interest due to its high theoretical capacity albeit its lower voltage (theoretically 1168 $mA{\cdot}h{\cdot}g^{-1}$ for Li-O_2[7]). As every battery, metal-air cells are comprised of two electrodes separated by an electrolyte. Yet, as part of "beyond-intercalation" technologies, the graphite anode is replaced by alkali metal and the transition metal compound by an oxygen cathode. The cathode is composed of a porous electron conductive matrix, usually carbon, filled with non-aqueous alkali cation electrolyte. Oxygen will diffuse to the cathode surface where its redox chemistry will act as charge storage. On discharge, oxygen is reduced to form superoxide or peroxide which is oxidized back to the alkali cation and O_2 on charge.

Despite its lower coulombic efficiency and higher overpotentials compared to state of the art Na or K cells[23,26], Li-O_2 chemistry is interesting due to its higher energy density; it is the more lightweight alkali metal and leads to the two-electron oxygen reduction product Li_2O_2[27]. The chemistry of the O_2/MO_2 (M = Li_2, Na, K) redox couple in aprotic media is a rather recent research subject and the still incomplete mechanistic understanding is a barrier for practical realization. By virtue of the similarities between the different metal-air technologies, emphasis will be put on Li-O_2 battery given its higher specific capacity. Li-O_2 cells, furthermore, involve the more complicated reactivity and the mechanisms encountered in lithium chemistry encompass the other alkali cases which usually favour the formation of alkali superoxide[26,28–30].

1.2 The state of the art of the lithium-air technology

1.2.1 Reaction mechanisms

1.2.1.1 Discharge

The discharge reaction in Li-O_2 batteries is the O_2 reduction in presence of lithium ions to form Li_2O_2 according to an overall 2 e^- reaction (Eq. 1.1). Li_2O_2 formation in aprotic media is complicated and the exact mechanism still not entirely understood. It is commonly accepted that the reaction is divided in two steps. Discharge commences with a 1 e^- O_2 reduction to superoxide (O_2^-) which may combine with Li^+ to form LiO_2 (Eq. 1.2)[8,31,32]. This step is followed by either a second 1 e^- reduction (Eq. 1.3) or disproportionation of the superoxide to form its peroxide (Eq. 1.4)[8–11]. The second step pathways are governed by the equilibrium between solvated and adsorbed superoxides (Eq. 1.5)[13]. Adsorbed superoxide can undergo a second reduction at the electrode surface or disproportionate. A solvated LiO_2 is disconnected from the electrode and can only undergoes disproportionation followed by subsequent precipitation. Both lead to an overall two-electron reduction of oxygen, as schematically shown in Fig. 1.2.

$$O_2 + 2\,e^- + 2\,Li^+ \longrightarrow Li_2O_2 \tag{1.1}$$

$$O_2 + e^- + Li^+ \longrightarrow LiO_2 \tag{1.2}$$

$$LiO_2 + e^- + Li^+ \longrightarrow Li_2O_2 \tag{1.3}$$

$$2\,LiO_2 \longrightarrow Li_2O_2 + O_2 \tag{1.4}$$

$$LiO_2 \rightleftharpoons Li^+_{(sol)} + O^-_{2\,(sol)} + \text{ion pairs} + \text{higher aggregates} \tag{1.5}$$

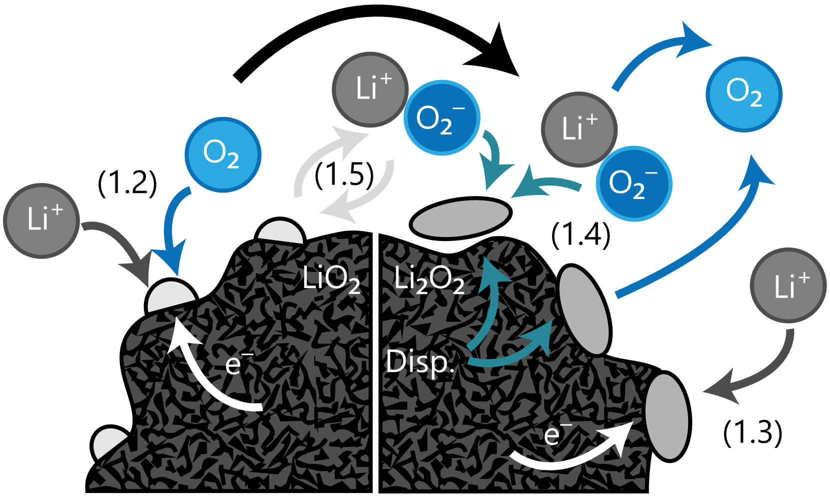

Figure 1.2: **Scheme of the discharge reaction and the equations corresponding to each step.**

Given the prominent role of the LiO_2 solvation equilibrium (Eq. 1.5), all factors influencing it have been recognized as strongly influencing the discharge mechanism. The cation solvation depends on the coordination strength with the solvent characterised by its Lewis basicity, measured with the Guttman donor number (DN)[9,13,33,34]; superoxide solvation correlates reciprocally with the solvent Lewis acidity characterised by the acceptor number

(AN), even though its influence is lower[33]. Common organic solvents cover an extensive range of DN. Among them are the nitriles and sulfones (DN = 14-16), glymes (DN = 20-24), amides (DN ≈ 26), and sulfoxide (DN ≈ 30)[13,34]. A high DN solvent leads then to a higher solvation of the lithium superoxide and disproportionation proportion. Solvation free energies of LiO_2 in a number of solvents as a function of AN and DN are given in Fig. 1.3. An alternative explanation concerning the reaction pathway control by the electrolyte is the solvent effective polarity[35]. Addition of additives tuning the solvent polarity changed the second reduction activation barrier, an effect which is not explainable by the previous theory.

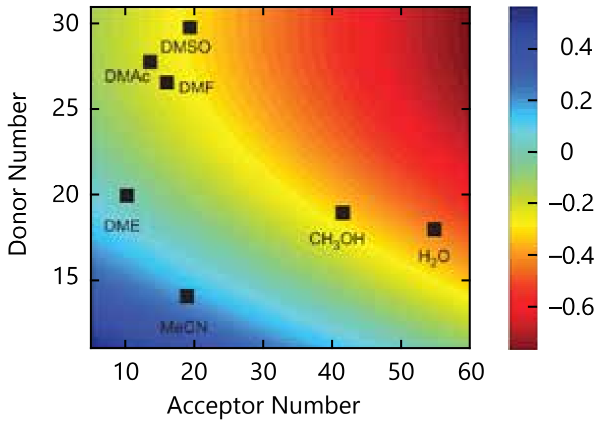

Figure 1.3: **Free energy of LiO_2 dissolution in different solvents in function of the solvent Acceptor Number and Donor Number, adapted from[36].** The energy value are relative to dimetoxyethane.

Solvating properties of the electrolytes are further influenced by additives. Strongly Li^+ coordinating salt anions like NO_3^-, associated with poor dissociation, increase solubilized superoxide but at the expanse of electrolyte conductivity[14,37–39]. Other examples are Lewis or Brønsted acids used to improve the superoxide solvation as water, alcohols, onium cations, or other alkali ions despite the noted potential to increase side reactivities[36,40,41,41–43]. Favouring solution growth through additives has grown more important since highly Lewis basic solvents are also more susceptible to nucleophilic attack by O_2^-[44].

Given the O_2/Li_2O_2 and O_2/O_2^- standard potentials, 2.96 and ~2.6 V_{Li/Li^+} respectively, the higher stability of peroxide versus superoxide in presence of Li^+ drives disproportionation[45]. The second reduction from superoxide to peroxide has also a strong driving force at all discharge potentials, the standard potential of O_2^-/Li_2O_2 being ~3.3 V_{Li/Li^+}[13]. The disproportionation reaction appears, however, to be the most favoured reaction at low overpotentials[13,15,46,47]. Higher overpotentials increase the second reduction rate to the detriment of disproportionation and favour surface growth.

The prevailing pathway of Li_2O_2 growth has a major importance for the discharge capacity. Electrolytes such as acetonitrile and dimethoxyethane (DME) solvate LiO_2 poorly and lead to an apparent conformal coating of the electrode by peroxide, as illustrated in Fig. 1.4(a). The potential curves are characterised by a very quick decay associated with the passivation of the electrode. The reaction would in this case occur at the Li_2O_2/electrolyte interface, the reaction being more facile on the peroxide than at the electrode interface[11,48–50]. Beyond a layer thickness of only 5 to 10 nm, charge transport resistance increases drastically due to the poor conductivity of peroxide; Discharge ceases when electrons cannot be transported through the layer, corresponding to low capacities[46,49,51,52]. A higher current density is associated, moreover, with a higher nucleation rate, further favouring the surface deposition and a quicker death of the electrode[46].

A solution mechanism delays the appearance of a dense Li_2O_2 layer and allows for higher capacity. Fig. 1.4(c) shows that higher capacities are obtained with higher donor number electrolytes. Due to the lower nucleation driving force, particles grow as large micrometre-sized toroidal particles composed of lamellaes[13,36], as illustrated in Fig. 1.4(b). Superoxide like species have been found on the surface of such structures[53]. The local overpotential increases with the covering of the matrix by the toroidal structure favouring a surface growth as the charge proceeds. This leads to the formation of smaller and flatter particles as the discharge progresses[54]. Surface blocking finally leads to the end of discharge. Impedance spectroscopy showed a similar surface blocking for either pathway, resulting in increased charge transfer resistance[52].

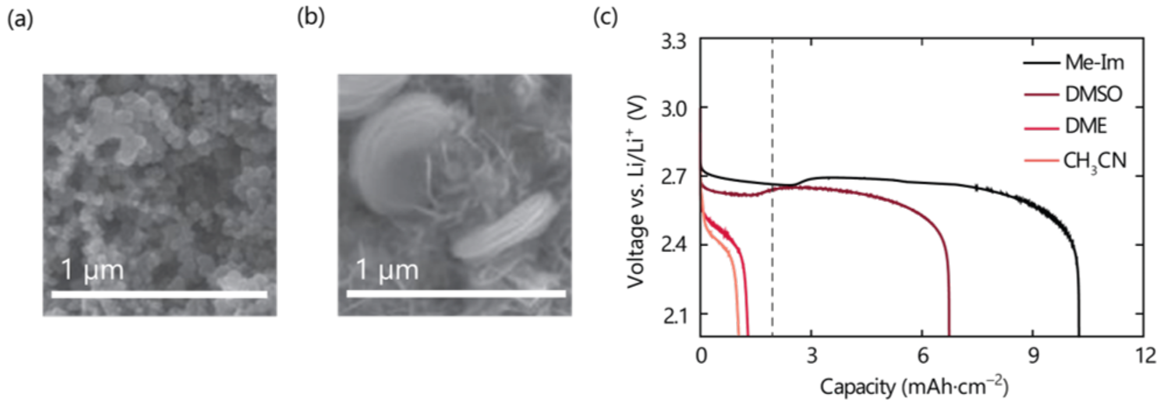

Figure 1.4: **The influence of the reaction pathway on the discharge.** (a) SEM image of Li_2O_2 obtained in low DN solvent via surface mechanism, adapted form[36], (b) SEM image of Li_2O_2 toroids obtained via the solution mechanism, adapted from[36]. (c) Dependence of galvanostatic discharge with the solvent donor numbers (0.1 M $LiClO_4$), adapted from[13]. The dashed line represent a 7 nm Li_2O_2 thickness, the limit of the hypothesized achievable capacity by a pure surface mechanism.

1.2.1.2 Charge

The Li_2O_2 oxidation mechanism is less understood than the discharge mechanism. Several points have still been determined. First, the oxidation proceeds incipiently at low overpotentials with oxygen evolution at potentials as low as 3 V_{Li/Li^+}; the thermodynamic potential being 2.96 V_{Li/Li^+}[11,55,56]. Second, the voltage rise correlates with side product formation from the charge onset. The side products are harder to oxidize than Li_2O_2 which further accelerates the potential rise[11,57,58]. Third, overpotentials arise to a lesser extent by increasingly difficult electron transfer as Li_2O_2 recedes[59].

With these considerations in mind, three different mechanistic models were discussed, each backed by experiments and calculations. First, a direct two-electron oxidation, due to the absence of LiO_2 in acetonitrile, as shown by in-situ surface-enhanced Raman spectroscopy[8]. Second, a topotactic delithiation forming a metastable $Li_{2-x}O_2$ comprising Li_2O_2 and LiO_2 domains, based on DFT calculations and X-ray diffraction experiments[45,60]. Third, the formation of a LiO_2 surface layer at low overpotentials and a direct two-electrons oxidation at high overpotentials, based on electrochemical experiments[61]. LiO_2 formation and consequent disproportionation was supported by TEM analysis[62]. DFT calculations have shown possible lithium extraction at low overpotentials with progressive delithiation of the

Li_2O_2, while O_2 evolution is responsible for the high overpotentials and is the more difficult step.[45,63,64].

A unified charge model governed by the solvent DN, in a similar fashion to discharge, was recently proposed[12]. Using thin-film RRDE experiments, dissolved LiO_2 was detected during charge at the ring in a high DN solvent (DMSO) while it was absent in a lower DN solvent (TEGDME), as shown in Fig. 1.5. Similarly, XANES experiments showed the formation of LiO_2 at the surface upon charging only in high DN solvent.

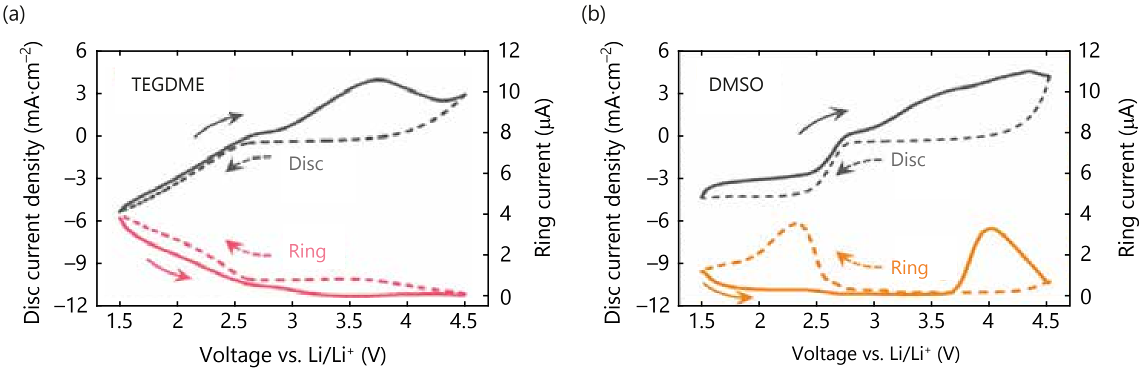

Figure 1.5: **Thin-film RRDE cyclic voltammetry in presence of oxygen in different electrolyte (0.2 M LiTFSI) at 50 mV.s^{-1} and a rotating speed of 900 rpm, adapted from[12].** The Au ring potential was 4.0 V_{Li/Li^+}, sufficient for superoxide oxidation. (a) in TEGDME, (b) in DMSO.

As for discharge, the solvent influences the Li_2O_2 decomposition pathway, either via solvated superoxide or topotactic surface delithiation. A higher kinetic applied by a higher overpotential favours the surface route as for discharge. Hence, the overall 2 e^- oxidation comprises a two step charge transfer mechanism (Eq. 1.6); it commences with a first delithiation forming superoxide-like species. The second step, as for discharge, is either a second oxidation (Eq. 1.7) or disproportionation (Eq. 1.8). In high DN solvents, $Li_{2-x}O_2$ is partly dissolved to $LiO_{2(sol)}$ that can disproportionate. Dependence on the solvation strength of the solvent might explain the absence of a LiO_2 detection in acetonitrile[8]. The reaction scheme is summarized in Fig. 1.6.

$$Li_2O_2 \longrightarrow Li_{2-x}O_2 + x\,Li^+ + x\,e^- \tag{1.6}$$

$$Li_{2-x}O_2 \longrightarrow O_2 + (2-x)\,Li^+ + (2-x)\,e^- \tag{1.7}$$

$$2\,LiO_{2\,(sol)} \longrightarrow Li_2O_2 + O_2 \tag{1.8}$$

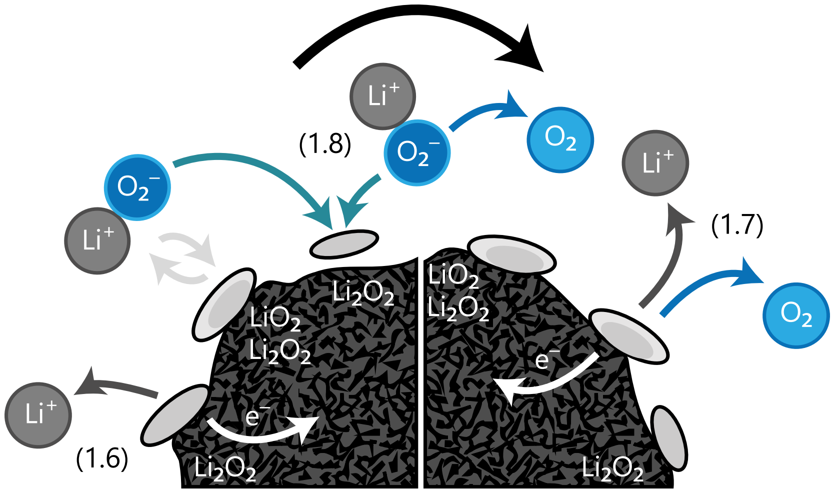

Figure 1.6: **Scheme of the charge reaction (simplified to x = 1) and the equations corresponding to each steps.**

It remains elusive if the adsorbed LiO_2 after initial delithiation will undergo disproportionation or only direct oxidation. Evidences seem to indicate disproportionation of absorbed LiO_2 during charge[62,65]. In any case, the disproportionation in charge is beyond doubt in high DN solvent. This is supported by the conversion of chemically synthesized Li_2O_2 into lamellar morphologies due to disproportionation after being partly oxidized, as illustrated by Fig. 1.7. This phenomenon is accompanied by the formation of nanocrystalline Li_2O_2 as detected by XANES[12].

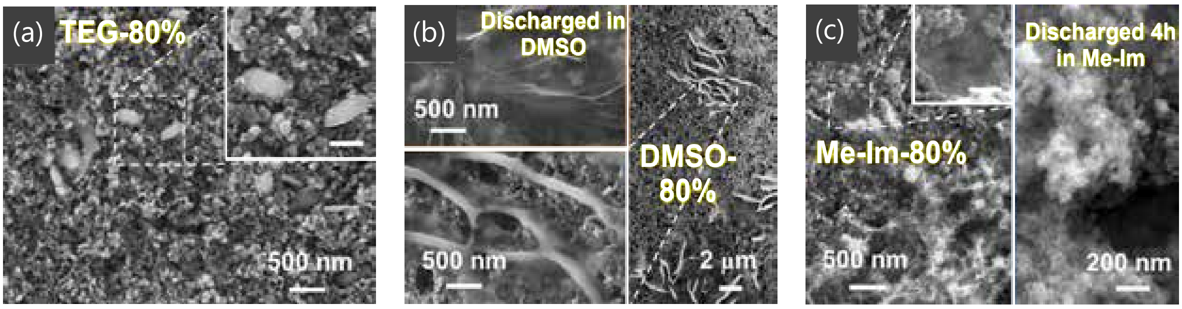

Figure 1.7: **SEM of Li_2O_2 at 80% of the charge in different electrolytes, adapted form[12].** The electrolytes are 1 M LiTSFI (a) in TEGDME, (b) in DMSO, and (c) in Me-Im. The insert mentioning discharge are here for comparison with solution mechanism during discharge. If not mentioned, the scale bars represent 200 nm.

1.2.1.3 Discharge product

$Li-O_2$ batteries, being a "beyond-intercalation" technology, heavily rely on the properties of the discharge product and notably mass/charge transport in Li_2O_2. Crystallinity, defects and applied voltage govern the charge transport properties of the peroxide. The deposition mechanism may impose two distinct morphologies as described in part 1.2.1.1. The formation of a well-contacted amorphous Li_2O_2 layer, through the surface pathway, results in lower oxidation potential[12,60,66,67]. The reaction is facilitated by defect-rich peroxide; large amounts of defects in nanocrystalline peroxide result in two orders of magnitude lower transport resistance compared to larger crystallites formed by disproportionation as illustated by Fig. 1.8[66,68,69]. Li_2O_2 toroidal morphologies, despite allowing higher discharge capacities, lead to higher overpotentials on charge and hence more side products.

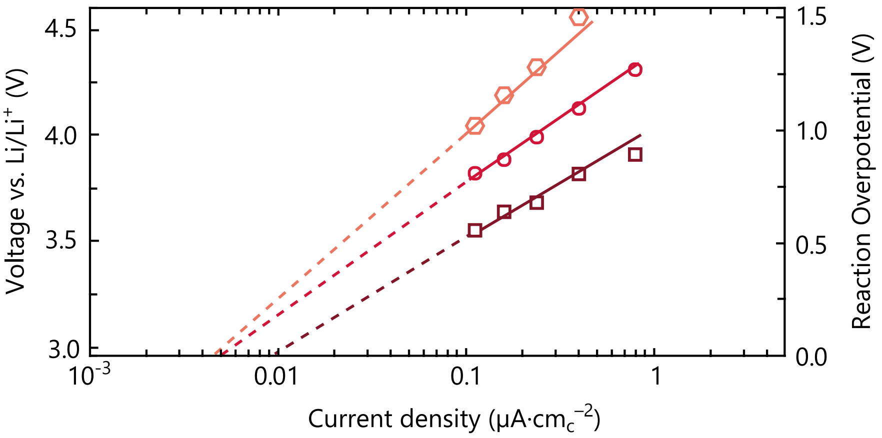

Figure 1.8: **Tafel slope dependence on Li_2O_2 crystallographic structure during charge, adapted from[66].** Pink hexagons correspond to commercial crystalline Li_2O_2, red circles to annealed Li_2O_2 and dark red squares to amorphous Li_2O_2.

Li_2O_2 electronic conductivity shows a particular dependence on the applied voltage. Higher potential was found by theory to result in reduced tunnelling barriers and easier charge transport in Li-deficient phases, notably by lithium vacancy formation as seen in Fig. 1.9[59,70,71]. The reduced conductivity at potentials found during discharge corroborate with low discharge capacities if a surface pathway prevails. On the other hand, higher conductivity at potentials corresponding to charge is in accord with low overpotentials at the charge onset. The presence of different morphologies would lead to several charge plateaus for Li_2O_2 oxidation, due to different charge transfer resistances.

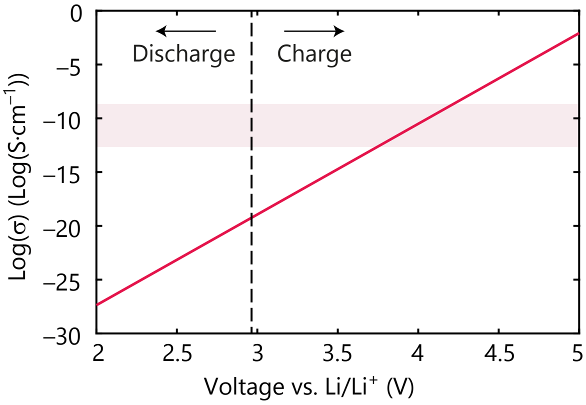

Figure 1.9: **Lithium peroxide electronic conductivity versus the cell potential, adapted from[59].** The light pink region represents an ohmic potential drop lower than 0.1 V for a 6 nm thick Li_2O_2 film. O_2/Li_2O_2 thermodynamic potential correspond to the dashed line.

Given the low conductivity of Li_2O_2, the interface at which charge transfer happens is of major importance. The reaction could proceed either at the cathode/Li_2O_2 or the Li_2O_2/electrolyte interfaces. The Li_2O_2/electrolyte interface is generally accepted as the reaction site during discharge via surface mechanism[48–50,72], in spite of contradictory results[73]. The reaction interface is more disputed during charge and leads to different interpretations of the overpotential rise, as illustrated in Fig. 1.10. Considering a Li_2O_2/electrolyte interface, Li_2O_2 poor conductivity will be limiting at all steps of charge[72,74,75]. If charge transfer occurs at the cathode/Li_2O_2 interface, the depletion will proceed preferentially at the electrode surface, reducing the contact interface between the discharge products and the electrode as well as contributing to reduced electron paths and increasing overpotential[48–50,73,76]. At the first stages of charge, mass transport of O_2 and Li^+ through the layer will be limiting in this case. As experiments seemingly support both assumptions, more thorough experiments are needed to unravel completely the reaction interface as its position appears related to the reaction pathway during discharge as well as the applied rate on charge[72]. The charge potential rise cannot, however, be fully accounted by an increasingly difficult charge transfer though Li_2O_2. The rise was mostly assigned to the formation of side products such as lithium carbonates[11,16,71,77].

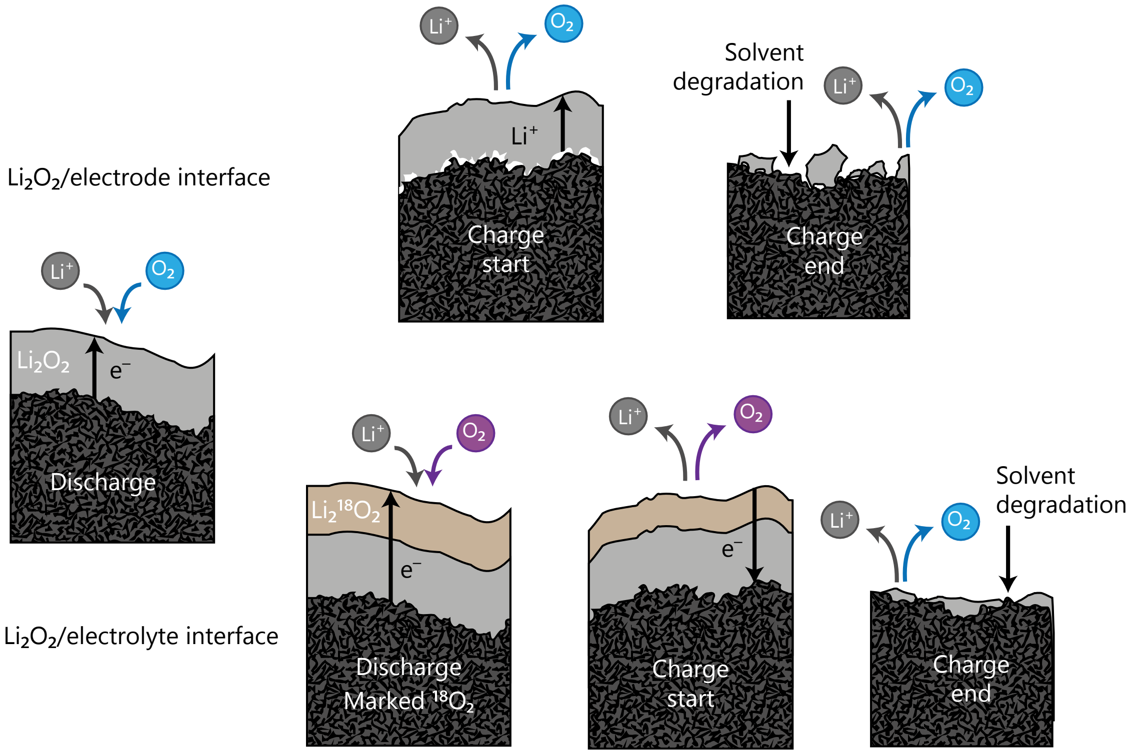

Figure 1.10: **Scheme of the reaction interfaces and the subsequent implications.** The Li_2O_2/electrode interface case is adapted from impedance spectrosopy results[48]. The Li_2O_2/electrolyte interface case is adapted from mass spectrometry results[72].

1.2.2 Electrodes

1.2.2.1 Cathode

Li-O_2 cells rely on the formation/decomposition of lithium peroxide. This reaction needs to proceed on a conductive matrix that can accommodate Li_2O_2. Peroxide will grow inside and fill the matrix pores; electrode materials with sufficient porosity are necessary to allow for significant Li_2O_2 formation, hence high capacity. Owing to its low cost, good conductivity, and adaptable surface geometry, carbon is the material of choice for Li-O_2 battery electrodes.

Carbon stability in Li-O_2 chemistry is, however, not perfect and was itself found to promote side reactions[58,77–79]. Using ^{13}C labelled carbon electrodes and in-situ as well as ex-situ mass spectrometry, CO_2 evolution was detected from deteriorated electrodes during charge. In contrast, electrodes in contact with Li_2O_2 or discharged release no notable CO_2 amount arising form the electrode[58]. Side products formation, hence, arise predominantly from electrolyte degradation during discharge. Electrode degradation commences on charge and accelerates as the overpotential rises, forming Li_2CO_3, as shown in Fig. 1.11(a)[58,77,78]. An aggravating factor is the presence of defects and hydrophilic moieties at the carbon surface, promoting electrode and electrolyte decompositions, as shown in Fig. 1.11(b)[58,79]. Another carbon cathode issue arises from polymer binders. Commonly used lithium-ion battery binders, as PVDF, are unfortunately not stable in Li-O_2 cells[80–83]. Nowadays, Nafion or PTFE are the binders of choice but their stability remains to be tested thoroughly towards aggressive chemicals formed in Li-O_2 cells[82–84].

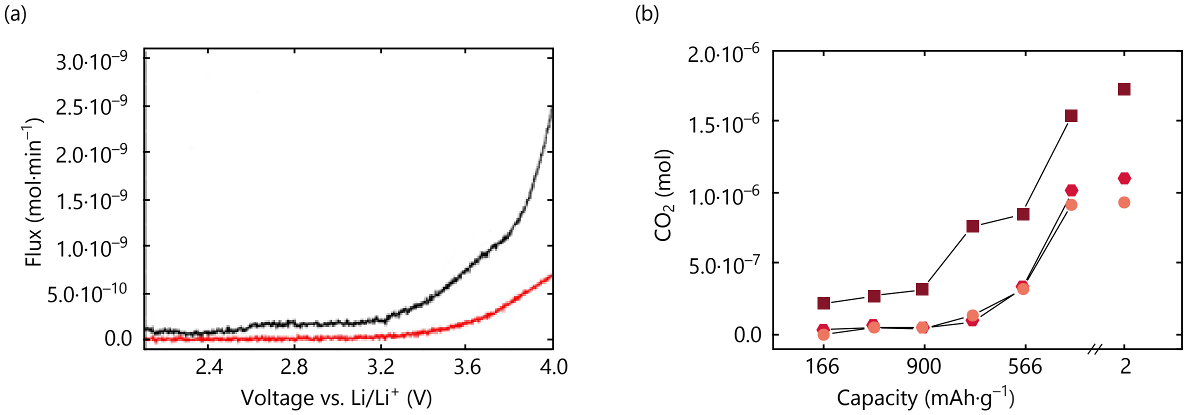

Figure 1.11: **Carbon electrode stability.** (a) In-situ CO_2 mass spectrometry during Li-O_2 cell charge, adapted from[58]. In red, $^{13}CO_2$ characterising side reactions form the electrode, and in black $^{12}CO_2$ characterising side reactions form the electrolyte. The results where obtained by DEMS with a DMSO electrolyte after a prior discharge to 2 V_{Li/Li^+}. (b) CO_2 evolution from Li_2CO_3 decomposition originating form the electrode decomposition in DMSO electrolyte at various stages of discharge and charge during the first cycle as well as after the second recharge, adapted from[58]. The pink circles represent hydrophobic carbon, the red hexagons commercial carbon, the dark red square hydrophilic carbon.

As a result of carbon instability, more stable materials have been tested as electrodes. To remain competitive, these materials should not catalyse electrolyte decomposition as well as keep a high porosity, a low density and price. Among the materials tested, Ti ceramics and nanoporous Au showed, for example, an improve cyclability and reduced side reactivity[21] [84,85]. If gold is naturally protected in Li-O_2 cell conditions, Ti materials as TiC or the metallic Magnéli phase Ti_4O_7 need a passivation layer[84–86]. This layer is likely formed by oxygen-deficient titanium oxide (TiO_{2-x}), enhancing the corrosion resistance of Ti materials. A similar ad-hoc passivation layer of ZnO or Au deposited on carbon increased its corrosion resistance. This method faces nevertheless passivation layer breaking after some cycling due to the deposition of Li_2O_2 below the passivation layer[87,88]. However, these material higher densities compared to carbon require a higher porosity to convey an interesting capacity.

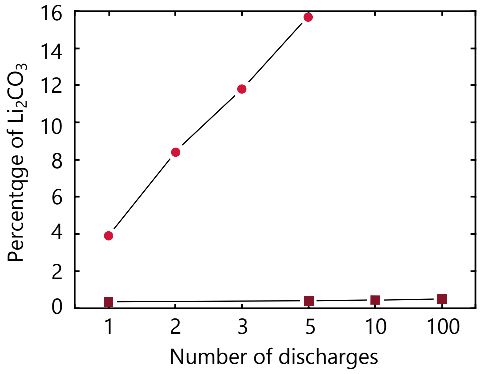

Figure 1.12: **Materials dependence on CO_2 evolution from Li_2CO_3 decomposition, adapted from[85].** Li_2CO_3 is formed by electrolyte decomposition (DMSO). The red hexagons represents a carbon cathode, the dark red squares a TiC cathode.

Considering the porosity, the influence of the electrode pore size has been investigated[89,90]. Several geometries and their impacts have been tested such as mesostructured carbon, carbon aerogels, or graphene-based electrodes[90–93]. Modelling have been used to verify the porosity significance[94]. The pathways to these pores, especially with nanomaterials, should not be neglected. At high current density, mass transport is limiting[93]. Li_2O_2 and side product formations could provoke clogging of small matrix pores. Higher pore size appears to enhance the lifetime of similarly constituted electrodes, as demonstrated in Fig. 1.13[89,90]. In a similar fashion, bigger molecules as additives also require access to the pore and a nano-grid electrode was proposed to facilitate their diffusion[95].

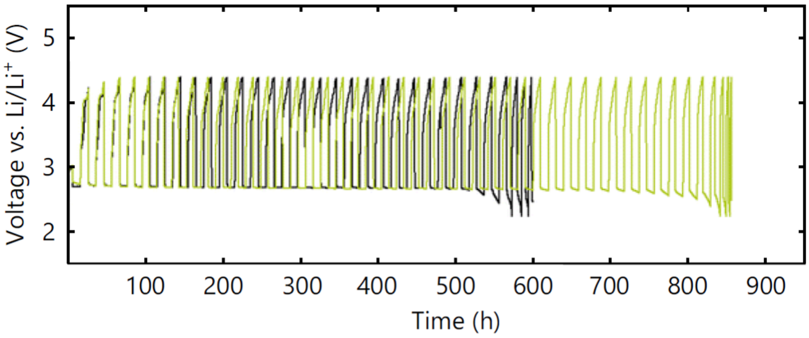

Figure 1.13: **Influence of pore size on Li-O_2 cells, adapted from[90].** In green, cycling of a large pore size carbon and in black, a small pore size carbon. The discharge capacity are limited to 1.0 mA·h·cm^{-2} and current fixed to 0.1 mA·cm^{-2}.

1.2.2.2 Anode

The cathode mostly limits the capacities with current lithium-ion technology. High capacity anode rise is, however, necessary to follow an increased cathode capacity. Anode technology with similar capacity to O_2 cathodes requires a "beyond-intercalation" approach. Lithium metal has a very good specific energy, a low density and the lowest electrochemical potential. Lithium metal anodes are, however, still not ready, despite in-depth mechanistic studies[96] [97].

The anode loses quickly coulombic efficiency with the formation of a so-called solid-electrolyte interphase (SEI). The SEI is notably formed by electrolyte decomposition products such as Li carbonates, LiOH or LiF[98–100]. These reactions can be due to decomposition of counter ions (PF_6^-, $TFSI^-$), impurities present in the electrolyte (H_2O, H^+), or the decomposition of the electrolyte solvent itself (O_2, carbonate, CO_2). The lithium passivation layer presents different mechanical resistances and tensile strengths depending on its composition, generally an inorganic core and an outer layer of organic chemicals, as schematically shown in Fig. 1.14[99].

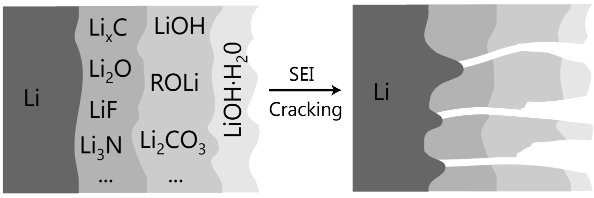

Figure 1.14: **SEI composition and formation of preferential deposition pathways through the SEI cracks, adapted from[99].**

In addition, lithium preferably grows as dendrites that lead to short circuits after some cycles which is hazardous due to flammable organic electrolytes. As a result of inhomogeneities, breaking of the SEI forms preferential deposition pathways, enhancing the tendency to produce dendrites[101]. This dendrite growth is favoured by the non-uniform electrical field distribution, accelerating deposition at the tip of the dendrites[102]. The pristine lithium surface of the dendrites is also subject to SEI reformation, increasing the side reactions. Lithium dendrites can disconnect from the anode due to parasitic reactivity, synonymous of dead weight and capacity loss[103]. Considering solid-state electrolyte, mossy or dentritic deposition can reduce electrode/electrolyte contact, increasing cell resistance and leading to quick cell death[104].

Since SEI formation appears inevitable, the formation of a compact and uniform layer, with good mechanical and electrical properties, is required to successfully use Li metal anodes. The presence of O_2 imposes specific stability requirements[96]. Even though lithium metal would require a separation from moisture and oxygenated species produced at the cathodes[105], a strong SEI remains a must-have to ensure long term cycling. The electrolyte constitution holds a strong influence on the SEI composition. As the solvent itself is not completely stable, it will change the composition of the SEI. The salts are not stable either, especially in contact with water impurities in the solvent, and can form LiF in case of PF_6^- or $TFSI^-$ cations[100,106]. LiF is actually a compact layer with good uniformity and strength improving the SEI stability but also brings a lower conductivity. Nitrate/azide based lithium salts are also employed to produce a stable SEI and have been tested in Li-O_2 cell conditions, as show in Fig. 1.15(a)[107–110]. NO_3^- enhances, furthermore, the solution pathway at the cathode and gets reduced at the Li anode to generate NO_2^- which facilitates Li_2O_2 oxidation by the oxidation mediator effect[37] [39]. Azides are known to quench reactive species formed in Li-O_2 batteries as it will be discussed in part 4.1[111]. Yet, nitrate based electrolytes suffer from lower conductivities compared to the $TFSI^-$ based one and these salts should be used as additives.

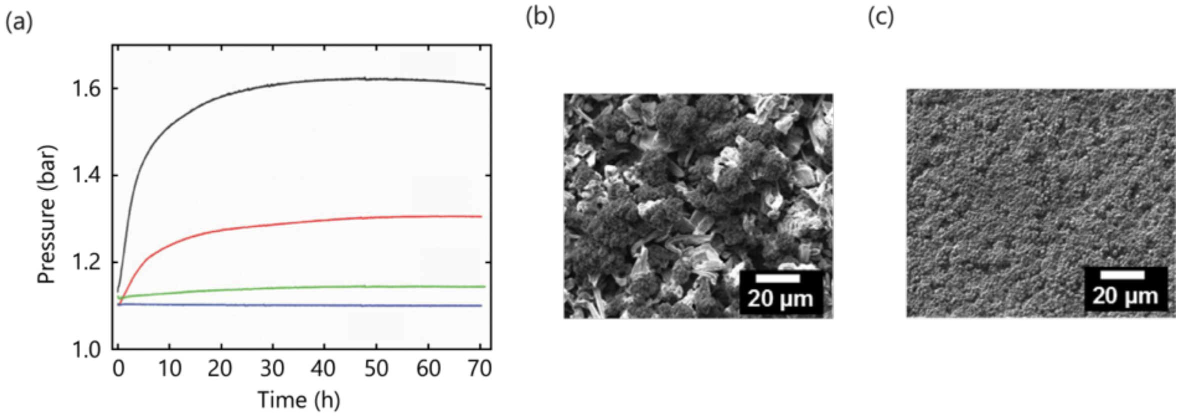

Figure 1.15: **Formation of a stable SEI.** (a) Pressure evolution at open-circuit voltage in a closed symmetric Li/Li cell, adapted from[107]. Pressure evolution indicates side reactions of the electrolyte with lithium metal. In black, evolution of cells with a N,N-dimethylacetamide electrolyte and no salt under argon; in red, the same electrolyte under oxygen atmosphere. In green, evolution of cells with a 1M $LiNO_3$ in N,N-Dimethylacetamide electrolyte under argon; In blue, the same electrolyte under oxygen atmosphere. (b) SEM image of a Li anode after 10th deposition at 0.1 $mA{\cdot}cm^{-2}$ with a 1 M $LiPF_6$ in propylene carbonate electrolyte, adapted from[112]. (c) SEM image of Li anode after 10th deposition at 0.1 $mA{\cdot}cm^{-2}$ with a 1 M $LiPF_6$ and 0.05 M $CsPF_6$ in propylene carbonate electrolyte, adapted from[112].

A proposed solution is to preform a SEI by plunging the lithium in a fluorinated solvent[113]. After this treatment, lithium metal was able to cycle in acetonitrile, a common solvent $Li-O_2$ chemistry. Another fashion to protect the anode is using a solid-state electrolyte as it will be discussed in 1.2.3. More exotic ways to reduce dendrites are investigated such as the formation of a self-healing electrostatic shield by incorporating Cs^+ or Na^+ ions, demonstrated in Fig. 1.15(b)-(c)[112] [114].

1.2.3 Electrolyte

Difficult criteria are to be met for $Li-O_2$ cell electrolyte, namely a sufficiently wide electrochemical window, formation of a stable passivation layer at the anode, a high conductivity, and chemical stability. The electrolyte in $Li-O_2$ cells holds, moreover, a major influence on the discharge and charge mechanisms. $Li-O_2$ chemistry induces very aggressive species in solution. For this reason, solvents such as ethers (particularly glymes)[115,116], sulfones[117], amides[107,109,118,119], or sulfoxides[21] replace carbonates usually used in lithium batteries[120]. Nitriles have likewise a good stability towards reduced oxygen species, the interest in them is, nevertheless, reduced due to their instability with lithium metal and low donor number[121].

The solution pathway enticed by higher achieved capacities, as described in part 1.2.1.1, favoured the use of high DN solvents. The solution pathway is, nonetheless, a double-edged sword. This pathway results in solvating more aggressive species for the electrolyte and increasing superoxide attack, as illustrated in Fig. 1.16[44]. A trade-off needs to be found between the longevity and capacity, high DN solvent being more susceptible to nucleophilic attack. To improve stability towards reduced O_2 species, solvents are designed to resist nucleophilic attack by avoiding any protons in alpha-position to heteroatoms. Among them, fully methylated glyme[122], hexamethylphosphoramide (HMPA)[123], or the fully methylated methoxy ketone 2,4-dimethoxy-2,4-dimethylpentan-3-one[124] were suggested to increase stability. Yet, such electrolytes are for the moment impeded by extreme toxicity (HMPA) or instability with a lithium metal. The choice of the salt equally influences the reaction mechanisms and should not only be chosen for their conductivity and stability towards lithium metal/oxygen species, as discussed in 1.2.1.1. The same reasoning goes with additives such as phenol, protic species or mediators.

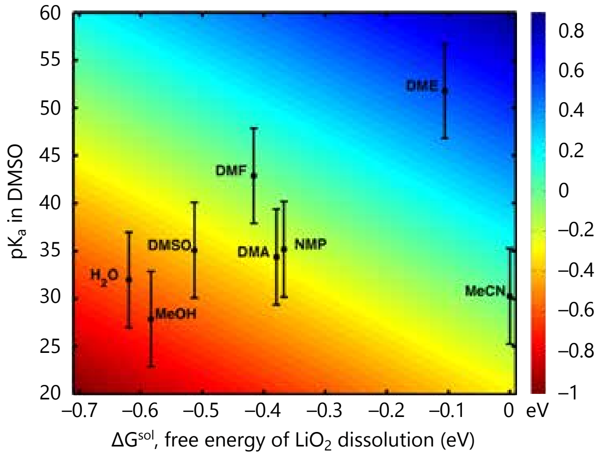

Figure 1.16: **Contour map of nucleophilic attack thermodynamic driving force for different solvents, adapted from[44].** The driving force is given in function of the Gibbs free energy for LiO_2 dissolution with MeCN as reference and the solvent pK_a in DMSO. Low dissolution energy denotes a tendency for the solution mechanism and low pK_a easier hydrogen abstraction

Ionic liquids, in addition to advantages such as a high electrochemical stability, present low volatility which is especially interesting for real applications with an airflow[7]. The oxygen reduction mechanism in ionic liquids appears to differ from conventional electrolytes, notably influenced by the weaker Lewis acidity of the ionic liquid cations, favouring superoxide solvation[125,126]. Unfortunately, O_2 solubility and diffusivity are low in ionic liquids due to their viscosity[127]. The ionic liquid chemical stabilities are also problematic for Li-O_2 applications, since common imidazolium based ionic liquids are not stable towards superoxide[128]. Pyrrolidinium or piperidinium based ionic liquids present a better compatibility with superoxide and lithium metal but still have insufficient reversibility and a tendency to parasitic chemistry[121,129–131]. Among other issues, higher price, possible stability issue towards lithium metal and lower Li ion solubility also speak in disfavour of ionic liquids[132].

Solid-state electrolytes are promising due to the external protection they offer to lithium metal from O_2 or H_2O. Dendrites growth can also be inhered by applying external pressure on the anode. Solid-state electrolytes comprise ceramics (perovskite, garnet, NASICON) and polymers. Solid-state electrolytes have, however, the detrimental characteristics of lower conductivities[133,134]. Li-air cells would specifically require the arrival of gaseous O_2 at the electrode surface, O_2 transport in solid being low. The solid-state electrolyte also prevents the solution pathway, leading to low capacities. The stability of polymer against reduced oxygen species is, moreover, problematic[133] [135]. Ceramics suffer from mechanical degradation due to their brittleness combined with volume changes of both electrodes[134].

A promising use of solid-state electrolytes is as separator between the oxygenated species/moisture and the lithium metal, necessary to prevent the anode corrosion. Solid-state electrolytes can separate anodic and cathodic compartments, avoiding cross-talk between the two electrodes[105,136]. Such methods can permit the use of additives in the cathode compartment that would not be stable in contact with lithium metal[137]. Solid-state electrolyte is then of major importance for long term cycling but not necessarily as direct electrolyte.

Work on Li-O_2 solid electrolytes is still at the beginning but researches are motivated by the possibility of flexible batteries and potential moisture and air protection of the anode[138,139].

1.2.4 Complete stack

Li-O_2 battery main advantage is often described as the Li_2O_2 theoretical capacity (1168 mA·h·g^{-1} [7]). Given the nature of "beyond-intercalation" batteries, achievable capacity is often misgiven as the capacity per gram of porous matrix; flattering numbers can then be obtained, between 1000 and 4000 mA·h·g^{-1}_{carbon}, compared to ~100–500 mA·h·g^{-1} for traditional technologies[5,6,140]. Limited discharge capacity, usually around 1000 mA·h·g^{-1}_{carbon}, limits as well the amount of side reactions, improves cyclability and may superficially still compare favourably with intercalation materials. The electrode mass is an accurate descriptor of the achievable capacity in intercalation materials; the host material mass and volume are well defined and relatively stable between discharge and charge states[6]. In Li-O_2 cells, no actual storage materials are present in the initial charged state and active material mass and volume definitions become fuzzier.

A more comparable descriptor of Li-O_2 electrode to intercalation materials is the concept of "super-host structure" representing the electrolyte filled porous cathode[6]. In Li-O_2 cells, the initial host material is not confined to the electrode but includes the electrolyte filling the pores. Discharge product formation displaces the electrolyte from the pores but it will still be present in the system and part of an extended host electrode definition. The concept of super-host electrode is elaborate in Fig. 1.17. Electrode porosity holds primary importance for the capacity. Besides being needed to accommodate a high amount of active storage materials, high porosity implies a larger electrolyte/electrode proportion. This additional electrolyte, in turn, diminishes the true specific capacity compared to lower porosity if the available pore space is not widely filled. A capacity given per mass of electrode alone can hence result in highly different "true" capacity depending on the initial porosity; only the "true" capacity based on the total super-host weight can be use to show a significant capacity improvement compared to intercalation materials, especially with limited capacity cycles.

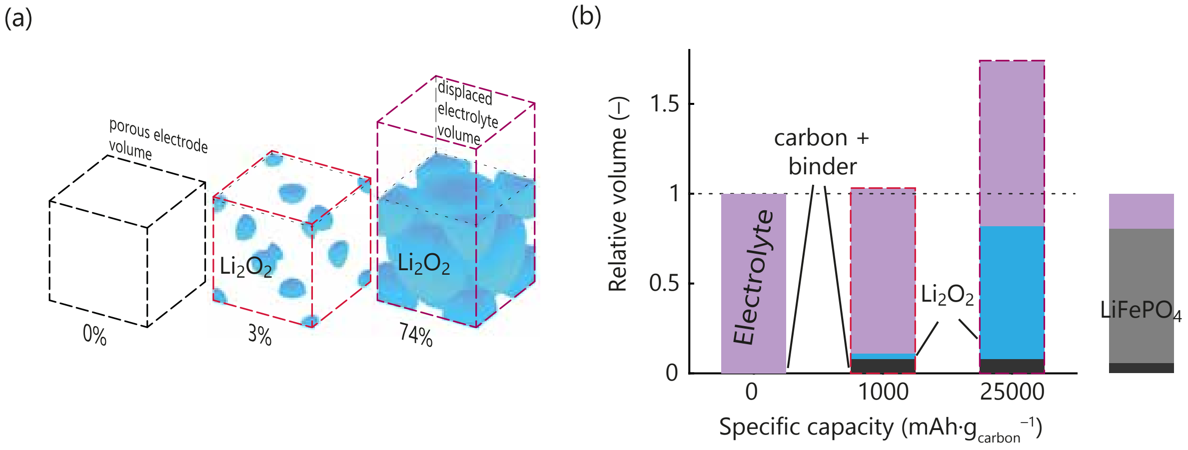

Figure 1.17: **Super-host structure, adapted from[6].** (a) Scheme of the super-host structure expansion at different Li_2O_2 filling degrees. (b) Relative volumes of each super-host component at different state of discharge. The insertion material $LiFePO_4$ at 74% volume occupation is given for comparison.

Only several easily obtained parameters are required to calculate "true" capacities. They are the electrode thickness, the mass fractions of all components (electrode, binder, and electrolyte), and their areal loading. Knowing the respective densities, the volume fractions can be obtained. From these data, it is straightforward to convert the capacity with respect to the porous matrix into "true" capacity per mass and volume of the total electrode including the displaced electrolyte. The maximum theoretical packing for Li_2O_2 is a 74% volume occupation assuming that the active material forms uniform spheres. Using an electrode with a 1:1 binder/carbon volume ratio, a starting porosity of 92% and an electrolyte with a 1.1 density yield a "true" capacity of ~700 $mA{\cdot}h{\cdot}g_{total}^{-1}$ and a volume occupation of 80%[6]. The results obtained are illustrated in Fig. 1.18(a).

Electrolyte/electrode ratio becomes even more predominant in the case of electrode materials such as porous Au or TiC, discussed in part 1.2.2.1. The specific capacity is naturally reduced considering their higher densities. An increased porosity reduces the high-density material proportion, hence, nearing its theoretical capacity to a lighter one, like carbon. The use of alternative cathode materials is therefore greatly dependent on their porosities as illustrated in Fig. 1.18(b).

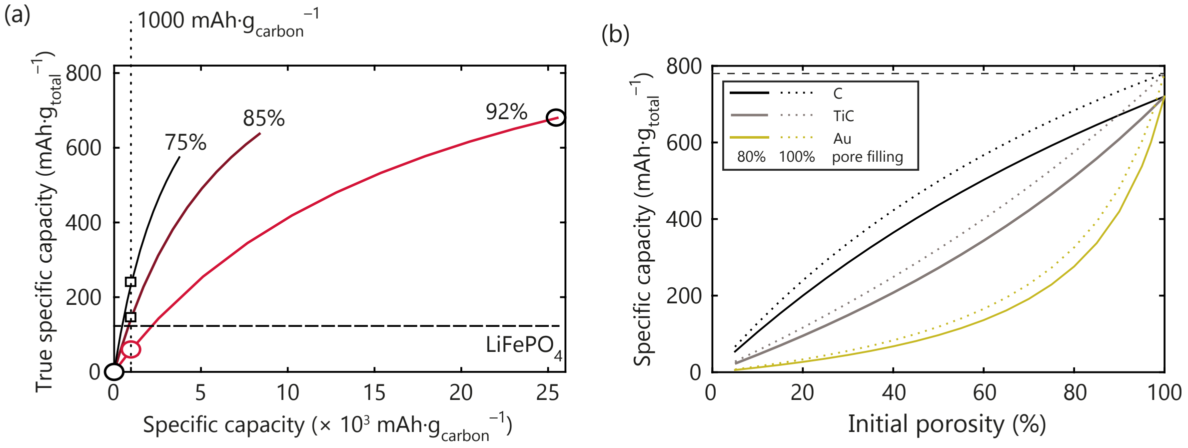

Figure 1.18: **Capacity based on the total mass of a super-host.** The calculation protocol is described in the main text. (a) Recalculated capacity at different initial matrix porosity (75%, 85% and 92 %), adapted from[6]. A 80% pore filling is used for calculations. The insertion material $LiFePO_4$ at 74% volume occupation is given for comparison in dashed black. (b) Recalculated "true" capacity in function of the inital electrode porosity and density given for either 80% (full line) or 100% (dotted line) Li_2O_2 volume occupation, adapted form[141].

Even though accounting for the mass and volume of the entire "super-host structure" results in lower achievable capacity, the Li-O_2 cathode can still achieve a significant amelioration compared to lithium-ion cells. The only requirements are high Li_2O_2 packing density and a small inactive/active material ratio. The Li-O_2 cathode is, however, not the only one to be subject to volume change during cycling. The lithium metal anode itself will change volume/mass upon lithium plating/stripping or the solid-electrolyte interphase formation[99,142]. This is often overlooked since lithium metal is a very efficient reservoir of lithium ions and imposes overdesigning lithium anode.

"True" cathode specific capacity is sufficient for Li-O_2 technology to hold promises at research scales; practical applications need to take into account specific cell designs[5]. Stack capacity depends notably on binders that should be kept at a minimum, current collectors, the cell housing and the stack housing[143]. The stack and cell housings are particularly important for Li-O_2 batteries where airflow to the cathode has to be ensured. Development of such technologies is still in its infancy. If current predictions are pessimistic, it is too early to judge on the final achievable capacity of a Li-O_2 stack[7].

1.3 Setbacks of metal-air technologies and suspected origins

1.3.1 Metrics characterising reversibility and the extent of side reactions

The biggest challenge faced by non-aqueous metal-air batteries is the large amount of side reactions, preventing long term cycling and maturing of the technology. Typical side products are lithium carbonates such as Li_2CO_3, Li formate and Li acetate[77,115,144]. The parasitic products subsequently lead to quick cell death due to pore and surface clogging as well as higher oxidation potentials[11,58]. The higher imposed potential results itself in an acceleration of side reactions[58]. Only a deep understanding of the reaction mechanisms and the development of accurate measurement methods will allow truly technological advancement and preventing cell degradation.

The first and foremost characteristic of reversible cells is an efficient redox chemistry of O_2. For Li-O_2 chemistry, the amount of oxygen and peroxide consumed/released compared to the capacity must comply with the Faraday law, given in Eq. 1.9, and a deviation characterises side reaction presence; stoichiometry implies strict e^-/O_2, e^-/Li_2O_2 and O_2/Li_2O_2 ratios described in Eq. 1.10 and Eq. 1.11. O_2 and Li_2O_2 are the only products in a perfectly reversible cell. No side reactivity results in a perfect coulombic yield, hence, all Li_2O_2 produced during discharge should readily be oxidized to O_2 during charge.

$$n = \frac{I \cdot t}{F \cdot z} \tag{1.9}$$

with n, the number of mole consumed/produced; I, the current (A); t, the time (s); F, the Faraday constant (96485 C·mol^{-1}); and z, the valency number.

$$\mathrm{O_2 + 2\,e^- + 2\,Li^+ \longleftrightarrow Li_2O_2} \tag{1.10}$$

$$\mathrm{e^-/O_2 = 2;\ e^-/Li_2O_2 = 2;\ O_2/Li_2O_2 = 1} \tag{1.11}$$

These conditions are not mutually inclusive and all of them should be met to achieved complete reversibility. During discharge, oxygen consumption is often close to the theoretical ratio of 2 e^-/O_2. Such oxygen consumption does not necessary result in a 2 e^-/Li_2O_2 ratio as side reactions might consume O_2. The observed side reactions are more severe during charge, represented by the orange gap between the O_2 production and Li_2O_2 consumption in Fig. 1.19. The clear lack of oxygen results in a deviation from the ideal trend of 2 e^-/O_2. This representation defines the major issue of metal-air batteries, far from ideal reactions due to parasitic reactions which are especially severe during charge.

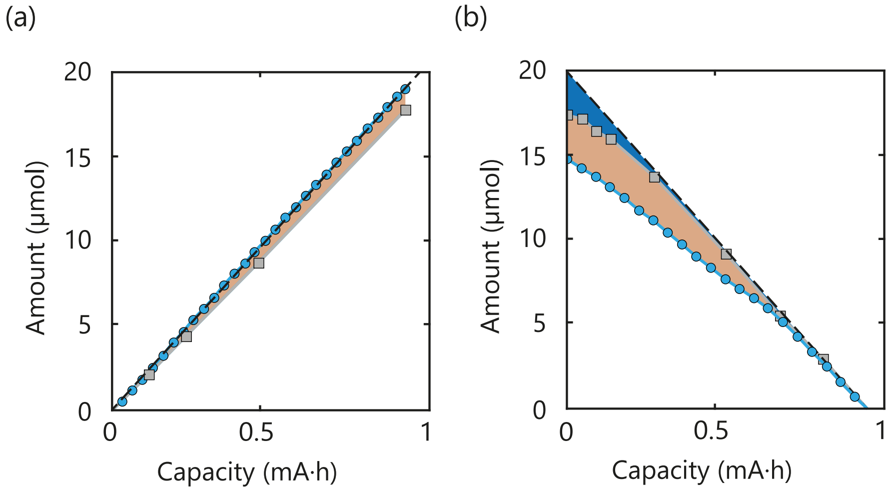

Figure 1.19: **Side reactivity characterised by Li_2O_2 and O_2 production/consumption over the capacity passed, adapted from[145].** O_2 amount evolution over the capacity passed is represented in light blue, Li_2O_2 in grey, the side reactions in orange are related to Li_2O_2 formation/dissolution and the side reactions due to parasitic oxidation of other species in blue. (a) Discharge, (b) Charge.

Analysis of the O_2 and Li_2O_2 productions is evermore crucial when limited discharge/charge capacity is used. Apart from biasing the faradic yield by reducing the amount of possible side reactions, the charge curves can falsely appear as reversible. Fig. 1.20 illustrates this point. Full discharge/charge curves are characterised by a plateau at a characteristic voltage corresponding to the reagent consumption with a rate imposed by the current. This plateau is followed by a sharp change at the end of the reaction due to insufficient reagent concentration at the electrode surface. It signifies the transition towards a new electrochemical reaction such as the solvent decomposition. In a limited capacity discharge case, a recharge at the same capacity should reach full consumption of the storage material and present a potential shift, except in the case of a complete absence of side reaction. The absence of potential rise indicates then the presence of side reactions. In a similar fashion, a side reaction at a potential close to the main reaction could appear as the main reaction such as for Li_2CO_3 oxidation during Li-O_2 batterie charge[11,58]. In the extreme case of the dark red curve in Fig. 1.20, the capacity is at least partly due to side reactivity, as indicated by the absence of peaks in the derivative scale. The faradic yield alone is thus not a good marker of reversibility.

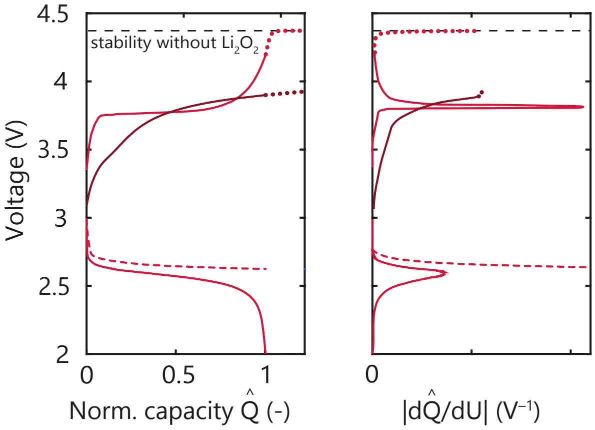

Figure 1.20: **Typical cycling curves of Li-O_2 cells, adapted from[141].** The dark red curves represent charge with high amount of side reactions. The full curves show cycling with voltage cut-off where the dashed curves shows capacity limited discharge and the dotted curves are extrapolation of the charge curves.

The need for more qualitative measurements gave rise to analytic protocols characterising side products as well as the consumptions/productions of O_2 and Li_2O_2 that will be reviewed more in depth in part 2.2.4.

It is important to consider metal-air batteries to be in their infancies. Most studies concerns indeed metal-O_2 chemistry and not metal-air. With the use of air, species such as CO_2 or H_2O, which are highly reactive with both the anode and the cathode, would increase the amount of side reactions[36,105,146]. Due to the lack of technological maturity with respect to air operation, the rest of the thesis will only focus on metal-O_2 side reactivity as the first step to eventually allow high reversibility in practical applications.

1.3.2 Reduced oxygen species as the source of side reactivity

Finding culprits for the crippling parasitic reactions of metal-O_2 cells have always been of major importance to unleash their potentials. Reduced oxygen species, formed during the reaction, were most easily and hence first identified as possible sources of side reactions due to their nucleophilicity, basicity and radical nature; species such as O_2^-, O_2^{2-}, HOO·, HOO^-, and HO· are prone to react with numerous organic molecules and are a possible source of parasitic chemistry[147,148]. Known reaction routes are for examples nucleophilic substitutions, H^+/H-atom abstraction or autoxidation. High polarity solvents are required to increase salt solubility; in view of their aprotic nature, solvents usually comprise electronegative moieties which are known attack sites and increase susceptibility to nucleophilic substitution[148]. For example, some common aprotic battery electrolytes such as carbonates are not stable with reduced oxygen species[120,149]. However, Alternative solvents, such as glyme, show increased stability[115,144].

Table 1.1: **Generic electrolyte side reactions with reduced oxygen species and molecular oxygen, adapted from[141].** The activation energies for the reactions are calculated by DFT. The followings are examples of solvents classed by pKa for O_2^- H^+ abstraction reaction. pKa < 30: Fluorinated esters, -$(CH_2$-$CF_2)_n$- , aliphatic dinitriles, alkyl imides; pKa > 30: acetonitrile, DMSO, N-alkyl amides and lactams, aliphatic ethers.

Reactant	Type of reaction	Reaction	E^{act} (kJ·mol^{-1})
O_2^-	nucleophilic substitution	$ROR' + O_2^- \longrightarrow RO^- + R'OO\cdot$	132[118] - 152[150] (DME) 121-193 with LiO_2[151] (DME derivative) 65[118] - 68[151] (PC) 96 with LiO_2[151] (PC) 105[118] (MeCN)
	H-atom abstraction	$RH + O_2^- \longrightarrow RO\cdot + HOO^-$	129[152] - 147[153] - 152[150] - 179[154] (DME)
	H^+ abstraction	$RH + O_2^- \longrightarrow R^- + HOO\cdot$	As first approx. pKa>30 is stable[155] [156] see legend for examples
Li_2O_2	nucleophilic substitution	$ROR' + Li_2O_2 \longrightarrow [RO^-Li^+] + [ROO^-Li^+]$	67[151] (PC) 135 - 192[157] (DME) 112[151] (DME derivative)
	H-atom abstraction	$RH + Li_2O_2 \longrightarrow R\cdot + [Li_2O_2\text{-}H\cdot]$	97-108 (Li-O-Li site)[157] (DME) 145 (O-O site)[157] (DME)
	H^+ abstraction	$RH + Li_2O_2^- \longrightarrow [R^-Li^+] + [HOO^-Li^+]$	112-154[157] (DME)
O_2	H-atom abstraction	$RH + O_2 \longrightarrow R\cdot + HOO\cdot$	163 (DME)[152]

An activation energy higher than 100 kJ·mol^{-1} appears too endothermic to greatly contribute as a significant parasitic reaction[118]. In contrast to carbonates, aliphatic ethers, commonly used in metal-air cells, appear to have minor reactivity with superoxide since the activation energies are close or above the 100 kJ·mol^{-1} threshold in Tab. 1.1. Furthermore, presence of Li^+, that coordinate with the solvent, stabilises it against H-abstraction by O_2^- and O_2[118,152,153]. K-O_2 cells can be cycled in DMSO reversibly for over thousands of cycles[23], as illustrated in Fig. 1.21; KO_2 being a source of superoxide anions, the long term cyclability of KO_2 demonstrates that the direct reactivity of superoxide is of minor importance for parasitic reactivity in metal-O_2 cells. Gas chromatography and cyclic voltammetry corroborate adapted solvent stabilities after contact with dissolve KO_2 by 18-crown-6 ether during one week[118]. This suggests low occurrence of direct superoxide reactivity with adapted solvents.

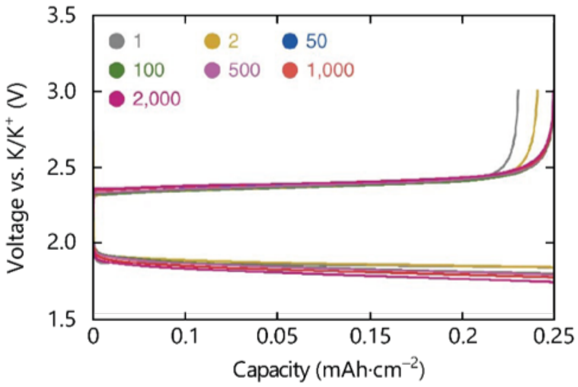

Figure 1.21: **Discharge/charge curves of a KO_2 cell for 2000 cycles at a current density of 2.0 mA·cm^{-2} and limited to 0.25 mA·h·cm^{-2}, adapted from[23].**

Setting aside superoxide, HOO·, HOO^-, and HO· are still good candidates as the source of unwanted reactivity. These species arise from proton source such as water or weak acids, with which O_2^- readily reacts according to Eq. 1.12[81,152].

$$
\begin{aligned}
&O_2^- + HA \longrightarrow HOO\cdot + A^- \\
&HOO\cdot + O_2^- \longrightarrow HOO^- + O_2 \\
&2\,HOO\cdot \longrightarrow H_2O_2 + O_2 \\
&HOO^- + H_2O_2 \longrightarrow O_2^- + HO\cdot + H_2O \\
&A^- + O_2 \longrightarrow O_2^- + A\cdot \\
&A\cdot + O_2 \longrightarrow AOO\cdot \\
&AOO\cdot + O_2^- \longrightarrow AOO^- + O_2
\end{aligned}
\tag{1.12}
$$

A proton source appears to be intertwined with nucleophilic attacks of the solvent; the parasitic chemistry in Li-O_2 actually increase with the addition of water[36]. The protonated reduced oxygen species are stronger reactants than the superoxide such as the HOO^- base[81]. The stronger base facilitates H-abstraction and the initiator leads to a radical chain reaction and solvent autoxidation. Water contamination can nevertheless not be assigned as solely responsible for side reactions. They are more abundant during charge than discharge, conflicting with the view of superoxide or protonated reduced oxygen species being solely responsible. The major difference between K-O_2 and Na/Li-O_2 is the relative thermodynamic properties of their respective superoxide and peroxide. Only KO_2 is thermodynamically more stable than its peroxide, as it will be discussed in part 2.3.3. We will show that the tendency to disproportionate of LiO_2 and NaO_2 is, in contrast, of prime importance for the formation of singlet oxygen, an excited molecular oxygen species.

Conclusion

Li-air technology is still in its infancy despite over a decade of intense research motivated by the promises of improved capacity. The new "beyond-intercalation chemistries" paradigm requires deep understanding of the reaction mechanisms, particularly the mechanism of parasitic chemistry, in order to ensure maturation of Li-air cells. The knowledge at the outset of my research work on Li-air chemistry was summarized in this chapter. While there is still some lack of deeper mechanistic understanding, recent insights provided a better awareness of the Li_2O_2 formation/disappearance processes and the associated parasitic chemistry.

The major advance in Li-O_2 chemistry understanding is the presence of superoxide disproportionation both on discharge and charge. This process leads to higher importance of the electrolyte composition which influences directly the discharge products morphology as well as the capacity achieved. As Li^+ and O_2^- solvations in the electrolyte increase, the processes shift between the extreme cases of a surface and solution mechanisms. In the first case, Li_2O_2 is formed via a second one e^- reduction at the electrode surface during discharge which leads to conformal coating of the electrode and low capacity. In the second case, superoxide is sufficiently soluble to diffuse away from the electrode surface and disproportionates to form larger particles which delay electrode passivation and lead to higher capacity. Li_2O_2 itself is an insulator which conductivity is now known to depend on its formation mechanism and the potential applied. The high overpotential encounter during charge is, however, mostly arising from the accumulation of side products due to electrode and electrolyte decompositions. The widely used carbon cathodes are increasingly degraded with the potential applied which results in carbonates formation. New materials are being developed to increase the cathode stability at the cost of weight increase. The anode is similarly problematic with instability towards organic and oxygenated species despite improve compatibility by means of specially designed SEI. Typical lithium-ion battery electrolytes are unstable in metal-air chemistry which gave rise to new organic solvent use, such as glyme, presenting higher robustness. Ionic liquids and solid-state electrolytes are concurrently developed but reveal themselves as currently unadapted to the metal-air chemistry.

Although there has been tremendous improvement of the Li-air cell cyclability, parasitic reactions stay their main hurdle. The achieved capacities per mass of cathode are often compared favourably to intercalation materials. This neglect the "beyond-intercalation" nature of the technology and the complete stack characteristic should be taken in consideration before any assessment. They might moreover be the results of limited capacity, potentially covering the parasitic chemistry contribution to the capacity. To determine the real reaction yield and reversibility, specific analytical methods have been developed such as pressure monitoring. Without such measurements, it is difficult to statute on improved performance claim due to the very nature of Li-air cells. The side reactions were mainly attributed to the presence of reduced oxygen species present during cell cycling. Superoxide species, yet, cannot explain the increased side reactions during charge. By DFT, it was moreover shown that the reduced oxygen species reactivity with adapted electrolyte is unlikely, comforted by the high stability achieved for K-O_2 cells. Recently, the very aggressive singlet oxygen was ascribed as a main source of side reactivity in Li-air chemistry.

Bibliography

[1] Y. K. Petit, E. Mourad, and S. A. Freunberger, "Encyclopedia of electrochemistry, section on batteries, ch. 19 lithium–oxygen batteries," in revision.

[2] D. Larcher and J.-M. Tarascon, "Towards greener and more sustainable batteries for electrical energy storage," *Nature chemistry*, vol. 7, no. 1, p. 19, 2015.

[3] M. S. Whittingham, "Ultimate limits to intercalation reactions for lithium batteries," *Chemical reviews*, vol. 114, no. 23, pp. 11 414–11 443, 2014.

[4] A. C. Luntz and B. D. McCloskey, "Nonaqueous Li–air batteries: a status report," *Chemical reviews*, vol. 114, no. 23, pp. 11 721–11 750, 2014.

[5] J. W. Choi and D. Aurbach, "Promise and reality of post-lithium-ion batteries with high energy densities," *Nature Reviews Materials*, vol. 1, no. 4, p. 16013, 2016.

[6] S. A. Freunberger, "True performance metrics in beyond-intercalation batteries," *Nature Energy*, vol. 2, p. 17091, 2017.

[7] K. G. Gallagher, S. Goebel, T. Greszler, M. Mathias, W. Oelerich, D. Eroglu, and V. Srinivasan, "Quantifying the promise of lithium–air batteries for electric vehicles," *Energy & Environmental Science*, vol. 7, no. 5, pp. 1555–1563, 2014.

[8] Z. Peng, S. A. Freunberger, L. J. Hardwick, Y. Chen, V. Giordani, F. Bardé, P. Novák, D. Graham, J.-M. Tarascon, and P. G. Bruce, "Oxygen reactions in a non-aqueous Li^+ electrolyte," *Angewandte Chemie International Edition*, vol. 50, no. 28, pp. 6351–6355, 2011.

[9] C. O. Laoire, S. Mukerjee, K. Abraham, E. J. Plichta, and M. A. Hendrickson, "Influence of nonaqueous solvents on the electrochemistry of oxygen in the rechargeable lithium-air battery," *The Journal of Physical Chemistry C*, vol. 114, no. 19, pp. 9178–9186, 2010.

[10] ——, "Elucidating the mechanism of oxygen reduction for lithium-air battery applications," *The Journal of Physical Chemistry C*, vol. 113, no. 46, pp. 20 127–20 134, 2009.

[11] B. D. McCloskey, R. Scheffler, A. Speidel, G. Girishkumar, and A. C. Luntz, "On the mechanism of nonaqueous Li–O_2 electrochemistry on C and its kinetic overpotentials: some implications for Li–air batteries," *The Journal of Physical Chemistry C*, vol. 116, no. 45, pp. 23 897–23 905, 2012.

[12] Y. Wang, N.-C. Lai, Y.-R. Lu, Y. Zhou, C.-L. Dong, and Y.-C. Lu, "A solvent-controlled oxidation mechanism of Li_2O_2 in lithium-oxygen batteries," *Joule*, vol. 2, no. 11, pp. 2364–2380, 2018.

[13] L. Johnson, C. Li, Z. Liu, Y. Chen, S. A. Freunberger, P. C. Ashok, B. B. Praveen, K. Dholakia, J.-M. Tarascon, and P. G. Bruce, "The role of LiO_2 solubility in O_2 reduction in aprotic solvents and its consequences for Li–O_2 batteries," *Nature chemistry*, vol. 6, no. 12, p. 1091, 2014.

[14] C. M. Burke, V. Pande, A. Khetan, V. Viswanathan, and B. D. McCloskey, "Enhancing electrochemical intermediate solvation through electrolyte anion selection to increase nonaqueous Li–O_2 battery capacity," *Proceedings of the National Academy of Sciences*, vol. 112, no. 30, pp. 9293–9298, 2015.

[15] Y. Zhang, X. Zhang, J. Wang, W. C. McKee, Y. Xu, and Z. Peng, “Potential-dependent generation of $O_2^-$and LiO_2 and their critical roles in O_2 reduction to Li_2O_2 in aprotic Li–O_2 batteries,” *The Journal of Physical Chemistry C*, vol. 120, no. 7, pp. 3690–3698, 2016.

[16] Z. Zhao, J. Huang, and Z. Peng, “Achilles’ heel of lithium–air batteries: lithium carbonate,” *Angewandte Chemie International Edition*, vol. 57, no. 15, pp. 3874–3886, 2018.

[17] P. G. Bruce, S. A. Freunberger, L. J. Hardwick, and J.-M. Tarascon, “Li–O_2 and Li–S batteries with high energy storage,” *Nature materials*, vol. 11, no. 1, p. 19, 2012.

[18] B. Dunn, H. Kamath, and J.-M. Tarascon, “Electrical energy storage for the grid: a battery of choices,” *Science*, vol. 334, no. 6058, pp. 928–935, 2011.

[19] M. Obrovac and V. Chevrier, “Alloy negative electrodes for Li-ion batteries,” *Chemical reviews*, vol. 114, no. 23, pp. 11 444–11 502, 2014.

[20] V. Chevrier and G. Ceder, “Challenges for Na-ion negative electrodes,” *Journal of The Electrochemical Society*, vol. 158, no. 9, pp. A1011–A1014, 2011.

[21] Z. Peng, S. A. Freunberger, Y. Chen, and P. G. Bruce, “A reversible and higher-rate Li-O_2 battery,” *Science*, vol. 337, no. 6094, pp. 563–566, 2012.

[22] P. Hartmann, C. L. Bender, M. Vraar, A. K. Dürr, A. Garsuch, J. Janek, and P. Adelhelm, “A rechargeable room-temperature sodium superoxide (NaO_2) battery,” *Nature materials*, vol. 12, no. 3, p. 228, 2013.

[23] G. Cong, W. Wang, N.-C. Lai, Z. Liang, and Y.-C. Lu, “A high-rate and long-life organic–oxygen battery,” *Nature materials*, vol. 18, no. 4, p. 390, 2019.

[24] S. Evers and L. F. Nazar, “New approaches for high energy density lithium–sulfur battery cathodes,” *Accounts of chemical research*, vol. 46, no. 5, pp. 1135–1143, 2012.

[25] D. Bresser, S. Passerini, and B. Scrosati, “Recent progress and remaining challenges in sulfur-based lithium secondary batteries – a review,” *Chemical communications*, vol. 49, no. 90, pp. 10 545–10 562, 2013.

[26] B. D. McCloskey, J. M. Garcia, and A. C. Luntz, “Chemical and electrochemical differences in nonaqueous Li–O_2 and Na–O_2 batteries,” *The journal of physical chemistry letters*, vol. 5, no. 7, pp. 1230–1235, 2014.

[27] Y. K. Petit and S. A. Freunberger, “Thousands of cycles,” *Nature materials*, vol. 18, no. 4, p. 301, 2019.

[28] C. L. Bender, P. Hartmann, M. Vraar, P. Adelhelm, and J. Janek, “On the thermodynamics, the role of the carbon cathode, and the cycle life of the sodium superoxide (NaO_2) battery,” *Advanced Energy Materials*, vol. 4, no. 12, p. 1301863, 2014.

[29] C. L. Bender, D. Schröder, R. Pinedo, P. Adelhelm, and J. Janek, “One- or two-electron transfer? The ambiguous nature of the discharge products in sodium–oxygen batteries,” *Angewandte Chemie International Edition*, vol. 55, no. 15, pp. 4640–4649, 2016.

[30] X. Ren and Y. Wu, “A low-overpotential potassium–oxygen battery based on potassium superoxide,” *Journal of the American Chemical Society*, vol. 135, no. 8, pp. 2923–2926, 2013.

[31] R. Cao, E. D. Walter, W. Xu, E. N. Nasybulin, P. Bhattacharya, M. E. Bowden, M. H. Engelhard, and J.-G. Zhang, “The mechanisms of oxygen reduction and evolution reactions in nonaqueous lithium–oxygen batteries,” *ChemSusChem*, vol. 7, no. 9, pp. 2436–2440, 2014.

[32] D. Aurbach, M. Daroux, P. Faguy, and E. Yeager, “The electrochemistry of noble metal electrodes in aprotic organic solvents containing lithium salts,” *Journal of electroanalytical chemistry and interfacial electrochemistry*, vol. 297, no. 1, pp. 225–244, 1991.

[33] D. G. Kwabi, V. S. Bryantsev, T. P. Batcho, D. M. Itkis, C. V. Thompson, and Y. Shao-Horn, “Experimental and computational analysis of the solvent-dependent O_2/Li^+-$O_2{}^-$ redox couple: standard potentials, coupling ctrength, and implications for lithium–oxygen batteries,” *Angewandte Chemie International Edition*, vol. 55, no. 9, pp. 3129–3134, 2016.

[34] V. Gutmann, “Solvent effects on the reactivities of organometallic compounds,” *Coordination Chemistry Reviews*, vol. 18, no. 2, pp. 225–255, 1976.

[35] C. Bondue, P. Bawol, A. Abd-El-Latif, P. Reinsberg, and H. Baltruschat, “Gaining control over the mechanism of oxygen reduction in organic electrolytes: the effect of solvent properties,” *The Journal of Physical Chemistry C*, vol. 121, no. 16, pp. 8864–8872, 2017.

[36] N. B. Aetukuri, B. D. McCloskey, J. M. García, L. E. Krupp, V. Viswanathan, and A. C. Luntz, “Solvating additives drive solution-mediated electrochemistry and enhance toroid growth in non-aqueous Li–O_2 batteries,” *Nature chemistry*, vol. 7, no. 1, p. 50, 2015.

[37] D. Sharon, D. Hirsberg, M. Salama, M. Afri, A. A. Frimer, M. Noked, W. Kwak, Y.-K. Sun, and D. Aurbach, “Mechanistic role of Li^+ dissociation level in aprotic Li–O_2 battery,” *ACS applied materials & interfaces*, vol. 8, no. 8, pp. 5300–5307, 2016.

[38] I. Gunasekara, S. Mukerjee, E. J. Plichta, M. A. Hendrickson, and K. Abraham, “A study of the influence of lithium salt anions on oxygen reduction reactions in Li-air batteries,” *Journal of The Electrochemical Society*, vol. 162, no. 6, pp. A1055–A1066, 2015.

[39] D. Sharon, D. Hirsberg, M. Afri, F. Chesneau, R. Lavi, A. A. Frimer, Y.-K. Sun, and D. Aurbach, “Catalytic behavior of lithium nitrate in Li-O_2 cells,” *ACS applied materials & interfaces*, vol. 7, no. 30, pp. 16 590–16 600, 2015.

[40] K. U. Schwenke, M. Metzger, T. Restle, M. Piana, and H. A. Gasteiger, “The influence of water and protons on Li_2O_2 crystal growth in aprotic Li-O_2 cells,” *Journal of The Electrochemical Society*, vol. 162, no. 4, pp. A573–A584, 2015.

[41] D. G. Kwabi, T. P. Batcho, S. Feng, L. Giordano, C. V. Thompson, and Y. Shao-Horn, “The effect of water on discharge product growth and chemistry in Li–O_2 batteries,” *Physical Chemistry Chemical Physics*, vol. 18, no. 36, pp. 24 944–24 953, 2016.

[42] C. Li, O. Fontaine, S. A. Freunberger, L. Johnson, S. Grugeon, S. Laruelle, P. G. Bruce, and M. Armand, “Aprotic Li–O_2 battery: influence of complexing agents on oxygen reduction in an aprotic solvent,” *The Journal of Physical Chemistry C*, vol. 118, no. 7, pp. 3393–3401, 2014.

[43] X. Gao, Z. P. Jovanov, Y. Chen, L. R. Johnson, and P. G. Bruce, “Phenol-catalyzed discharge in the aprotic lithium-oxygen battery,” *Angewandte Chemie*, vol. 129, no. 23, pp. 6639–6643, 2017.

[44] A. Khetan, A. Luntz, and V. Viswanathan, “Trade-offs in capacity and rechargeability in nonaqueous Li–O_2 batteries: solution-driven growth versus nucleophilic stability,” *The journal of physical chemistry letters*, vol. 6, no. 7, pp. 1254–1259, 2015.

[45] S. Kang, Y. Mo, S. P. Ong, and G. Ceder, “A facile mechanism for recharging Li_2O_2 in Li–O_2 batteries,” *Chemistry of Materials*, vol. 25, no. 16, pp. 3328–3336, 2013.

[46] B. D. Adams, C. Radtke, R. Black, M. L. Trudeau, K. Zaghib, and L. F. Nazar, “Current density dependence of peroxide formation in the Li–O_2 battery and its effect on charge,” *Energy & Environmental Science*, vol. 6, no. 6, pp. 1772–1778, 2013.

[47] D. G. Kwabi, M. Tuodziecki, N. Pour, D. M. Itkis, C. V. Thompson, and Y. Shao-Horn, “Controlling solution-mediated reaction mechanisms of oxygen reduction using potential and solvent for aprotic lithium–oxygen batteries,” *The journal of physical chemistry letters*, vol. 7, no. 7, pp. 1204–1212, 2016.

[48] J. Huang and B. Tong, “Probing the reaction interface in Li–O_2 batteries using electrochemical impedance spectroscopy: dual roles of Li_2O_2,” *Chemical Communications*, vol. 53, no. 83, pp. 11 418–11 421, 2017.

[49] J. Huang, B. Tong, Z. Li, T. Zhou, J. Zhang, and Z. Peng, “Probing the reaction interface in li-oxygen batteries using dynamic electrochemical impedance spectroscopy: Discharge–charge asymmetry in reaction sites and electronic conductivity,” *The journal of physical chemistry letters*, vol. 9, no. 12, pp. 3403–3408, 2018.

[50] A. Kushima, T. Koido, Y. Fujiwara, N. Kuriyama, N. Kusumi, and J. Li, “Charging/discharging nanomorphology asymmetry and rate-dependent capacity degradation in Li–oxygen battery,” *Nano letters*, vol. 15, no. 12, pp. 8260–8265, 2015.

[51] V. Viswanathan, K. S. Thygesen, J. Hummelshøj, J. K. Nørskov, G. Girishkumar, B. McCloskey, and A. Luntz, “Electrical conductivity in Li_2O_2 and its role in determining capacity limitations in non-aqueous Li-O_2 batteries,” *The Journal of chemical physics*, vol. 135, no. 21, p. 214704, 2011.

[52] K. B. Knudsen, T. Vegge, B. D. McCloskey, and J. Hjelm, “An electrochemical impedance spectroscopy study on the effects of the surface-and solution-based mechanisms in Li-O_2 cells,” *Journal of The Electrochemical Society*, vol. 163, no. 9, pp. A2065–A2071, 2016.

[53] J. Yang, D. Zhai, H.-H. Wang, K. C. Lau, J. A. Schlueter, P. Du, D. J. Myers, Y.-K. Sun, L. A. Curtiss, and K. Amine, “Evidence for lithium superoxide-like species in the discharge product of a Li–O_2 battery,” *Physical Chemistry Chemical Physics*, vol. 15, no. 11, pp. 3764–3771, 2013.

[54] Z. Li, S. Ganapathy, Y. Xu, J. R. Heringa, Q. Zhu, W. Chen, and M. Wagemaker, “Understanding the electrochemical formation and decomposition of Li_2O_2 and LiOH with operando X-ray diffraction,” *Chemistry of Materials*, vol. 29, no. 4, pp. 1577–1586, 2017.

[55] V. Viswanathan, J. Nørskov, A. Speidel, R. Scheffler, S. Gowda, and A. Luntz, “Li–O_2 kinetic overpotentials: Tafel plots from experiment and first-principles theory,” *The journal of physical chemistry letters*, vol. 4, no. 4, pp. 556–560, 2013.

[56] Y. Chen, S. A. Freunberger, Z. Peng, F. Bardé, and P. G. Bruce, “Li–O_2 battery with a dimethylformamide electrolyte,” *Journal of the American Chemical Society*, vol. 134, no. 18, pp. 7952–7957, 2012.

[57] R. Black, J.-H. Lee, B. Adams, C. A. Mims, and L. F. Nazar, “The role of catalysts and peroxide oxidation in lithium–oxygen batteries,” *Angewandte Chemie International Edition*, vol. 52, no. 1, pp. 392–396, 2013.

[58] M. M. Ottakam Thotiyl, S. A. Freunberger, Z. Peng, and P. G. Bruce, "The carbon electrode in nonaqueous Li–O_2 cells," *Journal of the American Chemical Society*, vol. 135, no. 1, pp. 494–500, 2012.

[59] M. D. Radin and D. J. Siegel, "Charge transport in lithium peroxide: relevance for rechargeable metal–air batteries," *Energy & Environmental Science*, vol. 6, no. 8, pp. 2370–2379, 2013.

[60] S. Ganapathy, B. D. Adams, G. Stenou, M. S. Anastasaki, K. Goubitz, X.-F. Miao, L. F. Nazar, and M. Wagemaker, "Nature of Li_2O_2 oxidation in a Li–O_2 battery revealed by operando X-ray diffraction," *Journal of the American Chemical Society*, vol. 136, no. 46, pp. 16 335–16 344, 2014.

[61] Y.-C. Lu and Y. Shao-Horn, "Probing the reaction kinetics of the charge reactions of nonaqueous Li–O_2 batteries," *The journal of physical chemistry letters*, vol. 4, no. 1, pp. 93–99, 2012.

[62] L. Luo, B. Liu, S. Song, W. Xu, J.-G. Zhang, and C. Wang, "Revealing the reaction mechanisms of Li–O_2 batteries using environmental transmission electron microscopy," *Nature nanotechnology*, vol. 12, no. 6, p. 535, 2017.

[63] Y. Mo, S. P. Ong, and G. Ceder, "First-principles study of the oxygen evolution reaction of lithium peroxide in the lithium-air battery," *Physical Review B*, vol. 84, no. 20, p. 205446, 2011.

[64] J. Hummelshøj, A. Luntz, and J. Nørskov, "Theoretical evidence for low kinetic overpotentials in Li-O_2 electrochemistry," *The Journal of chemical physics*, vol. 138, no. 3, p. 034703, 2013.

[65] D. Zhai, H.-H. Wang, J. Yang, K. C. Lau, K. Li, K. Amine, and L. A. Curtiss, "Disproportionation in Li–O_2 batteries based on a large surface area carbon cathode," *Journal of the American Chemical Society*, vol. 135, no. 41, pp. 15 364–15 372, 2013.

[66] Y. Zhang, Q. Cui, X. Zhang, W. C. McKee, Y. Xu, S. Ling, H. Li, G. Zhong, Y. Yang, and Z. Peng, "Amorphous Li_2O_2: chemical synthesis and electrochemical properties," *Angewandte Chemie International Edition*, vol. 55, no. 36, pp. 10 717–10 721, 2016.

[67] F. Tian, M. D. Radin, and D. J. Siegel, "Enhanced charge transport in amorphous Li_2O_2," *Chemistry of Materials*, vol. 26, no. 9, pp. 2952–2959, 2014.

[68] A. Dunst, V. Epp, I. Hanzu, S. Freunberger, and M. Wilkening, "Short-range Li diffusion vs. long-range ionic conduction in nanocrystalline lithium peroxide Li_2O_2 — the discharge product in lithium-air batteries," *Energy & environmental science*, vol. 7, no. 8, pp. 2739–2752, 2014.

[69] O. Gerbig, R. Merkle, and J. Maier, "Electron and ion transport in Li_2O_2," *Advanced materials*, vol. 25, no. 22, pp. 3129–3133, 2013.

[70] A. C. Luntz, V. Viswanathan, J. Voss, J. Varley, J. Nørskov, R. Scheffler, and A. Speidel, "Tunneling and polaron charge transport through Li_2O_2 in Li–O_2 batteries," *The Journal of Physical Chemistry Letters*, vol. 4, no. 20, pp. 3494–3499, 2013.

[71] J. Højberg, B. D. McCloskey, J. Hjelm, T. Vegge, K. Johansen, P. Norby, and A. C. Luntz, "An electrochemical impedance spectroscopy investigation of the overpotentials in Li–O_2 batteries," *ACS applied materials & interfaces*, vol. 7, no. 7, pp. 4039–4047, 2015.

[72] Y. Wang and Y.-C. Lu, "Isotopic labeling reveals active reaction interfaces for electrochemical oxidation of lithium peroxide," *Angewandte Chemie*, vol. 131, no. 21, pp. 7036–7040, 2019.

[73] J. Wang, Y. Zhang, L. Guo, E. Wang, and Z. Peng, "Identifying reactive sites and transport limitations of oxygen reactions in aprotic lithium-O_2 batteries at the stage of sudden death," *Angewandte Chemie International Edition*, vol. 55, no. 17, pp. 5201–5205, 2016.

[74] H. Zheng, D. Xiao, X. Li, Y. Liu, Y. Wu, J. Wang, K. Jiang, C. Chen, L. Gu, X. Wei *et al.*, "New insight in understanding oxygen reduction and evolution in solid-state lithium–oxygen batteries using an in situ environmental scanning electron microscope," *Nano letters*, vol. 14, no. 8, pp. 4245–4249, 2014.

[75] Y. Wang, Z. Liang, Q. Zou, G. Cong, and Y.-C. Lu, "Mechanistic insights into catalyst-assisted nonaqueous oxygen evolution reaction in lithium–oxygen batteries," *The Journal of Physical Chemistry C*, vol. 120, no. 12, pp. 6459–6466, 2016.

[76] Q. Peng, J. Chen, H. Ji, A. Morita, and S. Ye, "Origin of the overpotential for the oxygen evolution reaction on a well-defined graphene electrode probed by in situ sum frequency generation vibrational spectroscopy," *Journal of the American Chemical Society*, vol. 140, no. 46, pp. 15 568–15 571, 2018.

[77] B. McCloskey, A. Speidel, R. Scheffler, D. Miller, V. Viswanathan, J. Hummelshøj, J. Nørskov, and A. Luntz, "Twin problems of interfacial carbonate formation in nonaqueous Li–O_2 batteries," *The journal of physical chemistry letters*, vol. 3, no. 8, pp. 997–1001, 2012.

[78] B. D. McCloskey, A. Valery, A. C. Luntz, S. R. Gowda, G. M. Wallraff, J. M. Garcia, T. Mori, and L. E. Krupp, "Combining accurate O_2 and Li_2O_2 assays to separate discharge and charge stability limitations in nonaqueous Li–O_2 batteries," *The journal of physical chemistry letters*, vol. 4, no. 17, pp. 2989–2993, 2013.

[79] D. M. Itkis, D. A. Semenenko, E. Y. Kataev, A. I. Belova, V. S. Neudachina, A. P. Sirotina, M. Hävecker, D. Teschner, A. Knop-Gericke, P. Dudin *et al.*, "Reactivity of carbon in lithium–oxygen battery positive electrodes," *Nano letters*, vol. 13, no. 10, pp. 4697–4701, 2013.

[80] J. K. Papp, J. D. Forster, C. M. Burke, H. W. Kim, A. C. Luntz, R. M. Shelby, J. J. Urban, and B. D. McCloskey, "Poly(vinylidene fluoride) (PVDF) binder degradation in Li–O_2 batteries: a consideration for the characterization of lithium superoxide," *The journal of physical chemistry letters*, vol. 8, no. 6, pp. 1169–1174, 2017.

[81] V. S. Bryantsev, "Predicting the stability of aprotic solvents in Li-air batteries: pKa calculations of aliphatic C–H acids in dimethyl sulfoxide," *Chemical Physics Letters*, vol. 558, pp. 42–47, 2013.

[82] C. V. Amanchukwu, J. R. Harding, Y. Shao-Horn, and P. T. Hammond, "Understanding the chemical stability of polymers for lithium–air batteries," *Chemistry of Materials*, vol. 27, no. 2, pp. 550–561, 2015.

[83] E. Nasybulin, W. Xu, M. H. Engelhard, Z. Nie, X. S. Li, and J.-G. Zhang, "Stability of polymer binders in Li–O_2 batteries," *Journal of Power Sources*, vol. 243, pp. 899–907, 2013.

[84] D. Kundu, R. Black, E. J. Berg, and L. F. Nazar, "A highly active nanostructured metallic oxide cathode for aprotic Li–O_2 batteries," *Energy & Environmental Science*, vol. 8, no. 4, pp. 1292–1298, 2015.

[85] M. M. Ottakam Thotiyl, S. A. Freunberger, Z. Peng, Y. Chen, Z. Liu, and P. G. Bruce, "A stable cathode for the aprotic Li–O_2 battery," *Nature materials*, vol. 12, no. 11, p. 1050, 2013.

[86] A. Y. Kozmenkova, E. Y. Kataev, A. I. Belova, M. Amati, L. Gregoratti, J. Velasco-Vélez, A. Knop-Gericke, B. Senkovsky, D. V. Vyalikh, D. M. Itkis *et al.*, "Tuning surface chemistry of TiC electrodes for lithium–air batteries," *Chemistry of Materials*, vol. 28, no. 22, pp. 8248–8255, 2016.

[87] Y. Bae, D.-H. Ko, S. Lee, H.-D. Lim, Y.-J. Kim, H.-S. Shim, H. Park, Y. Ko, S. K. Park, H. J. Kwon *et al.*, "Enhanced stability of coated carbon electrode for Li-O_2 batteries and its limitations," *Advanced Energy Materials*, vol. 8, no. 16, p. 1702661, 2018.

[88] M. Marinaro, U. Riek, S. E. Moorthy, J. Bernhard, U. Kaiser, M. Wohlfahrt-Mehrens, and L. Jörissen, "Au-coated carbon cathodes for improved oxygen reduction and evolution kinetics in aprotic Li-O_2 batteries," *Electrochemistry Communications*, vol. 37, pp. 53–56, 2013.

[89] N. Ding, S. W. Chien, T. A. Hor, R. Lum, Y. Zong, and Z. Liu, "Influence of carbon pore size on the discharge capacity of Li–O_2 batteries," *Journal of Materials Chemistry A*, vol. 2, no. 31, pp. 12 433–12 441, 2014.

[90] J. Zeng, J. Amici, A. H. M. Videla, C. Francia, and S. Bodoardo, "Synthesis of mesoporous carbons and reduced graphene oxide and their influence on the cycling performance of rechargeable Li-O_2 batteries," *Journal of Solid State Electrochemistry*, vol. 21, no. 2, pp. 503–514, 2017.

[91] S. B. Ma, D. J. Lee, V. Roev, D. Im, and S.-G. Doo, "Effect of porosity on electrochemical properties of carbon materials as cathode for lithium-oxygen battery," *Journal of Power Sources*, vol. 244, pp. 494–498, 2013.

[92] B. Sun, X. Huang, S. Chen, P. Munroe, and G. Wang, "Porous graphene nanoarchitectures: an efficient catalyst for low charge-overpotential, long life, and high capacity lithium–oxygen batteries," *Nano letters*, vol. 14, no. 6, pp. 3145–3152, 2014.

[93] A. Kraytsberg and Y. Ein-Eli, "The impact of nano-scaled materials on advanced metal–air battery systems," *Nano Energy*, vol. 2, no. 4, pp. 468–480, 2013.

[94] A. Torayev, P. C. M. M. Magusin, C. P. Grey, C. Merlet, and A. A. Franco, "Importance of incorporating explicit 3D-resolved electrode mesostructures in Li–O_2 battery models," *ACS Applied Energy Materials*, vol. 1, no. 11, pp. 6433–6441, 2018.

[95] H.-D. Lim, H. Song, J. Kim, H. Gwon, Y. Bae, K.-Y. Park, J. Hong, H. Kim, T. Kim, Y. H. Kim *et al.*, "Superior rechargeability and efficiency of lithium–oxygen batteries: hierarchical air electrode architecture combined with a soluble catalyst," *Angewandte Chemie International Edition*, vol. 53, no. 15, pp. 3926–3931, 2014.

[96] J. Liu, Z. Bao, Y. Cui, E. J. Dufek, J. B. Goodenough, P. Khalifah, Q. Li, B. Y. Liaw, P. Liu, A. Manthiram *et al.*, "Pathways for practical high-energy long-cycling lithium metal batteries," *Nature Energy*, p. 1, 2019.

[97] M. D. Tikekar, S. Choudhury, Z. Tu, and L. A. Archer, "Design principles for electrolytes and interfaces for stable lithium-metal batteries," *Nature Energy*, vol. 1, no. 9, p. 16114, 2016.

[98] D. Aurbach, M. Daroux, P. Faguy, and E. Yeager, “Identification of surface films formed on lithium in propylene carbonate solutions,” *Journal of The Electrochemical Society*, vol. 134, no. 7, pp. 1611–1620, 1987.

[99] D. Aurbach, “Review of selected electrode–solution interactions which determine the performance of Li and Li ion batteries,” *Journal of Power Sources*, vol. 89, no. 2, pp. 206–218, 2000.

[100] J. Qian, W. Xu, P. Bhattacharya, M. Engelhard, W. A. Henderson, Y. Zhang, and J.-G. Zhang, “Dendrite-free Li deposition using trace-amounts of water as an electrolyte additive,” *Nano Energy*, vol. 15, pp. 135–144, 2015.

[101] G. Bieker, M. Winter, and P. Bieker, “Electrochemical in situ investigations of SEI and dendrite formation on the lithium metal anode,” *Physical Chemistry Chemical Physics*, vol. 17, no. 14, pp. 8670–8679, 2015.

[102] A. Aryanfar, D. Brooks, B. V. Merinov, W. A. Goddard III, A. J. Colussi, and M. R. Hoffmann, “Dynamics of lithium dendrite growth and inhibition: Pulse charging experiments and Monte Carlo calculations,” *The journal of physical chemistry letters*, vol. 5, no. 10, pp. 1721–1726, 2014.

[103] J.-i. Yamaki, S.-i. Tobishima, K. Hayashi, K. Saito, Y. Nemoto, and M. Arakawa, “A consideration of the morphology of electrochemically deposited lithium in an organic electrolyte,” *Journal of Power Sources*, vol. 74, no. 2, pp. 219–227, 1998.

[104] F. Orsini, A. Du Pasquier, B. Beaudoin, J. M. Tarascon, M. Trentin, N. Langenhuizen, E. De Beer, and P. Notten, “In situ scanning electron microscopy (SEM) observation of interfaces within plastic lithium batteries,” *Journal of power sources*, vol. 76, no. 1, pp. 19–29, 1998.

[105] B. G. Kim, J.-S. Kim, J. Min, Y.-H. Lee, J. H. Choi, M. C. Jang, S. A. Freunberger, and J. W. Choi, “A moisture- and oxygen- impermeable separator for aprotic Li-O_2 batteries,” *Advanced functional materials*, vol. 26, no. 11, pp. 1747–1756, 2016.

[106] X.-B. Cheng, R. Zhang, C.-Z. Zhao, F. Wei, J.-G. Zhang, and Q. Zhang, “A review of solid electrolyte interphases on lithium metal anode,” *Advanced Science*, vol. 3, no. 3, p. 1500213, 2016.

[107] V. Giordani, W. Walker, V. S. Bryantsev, J. Uddin, G. V. Chase, and D. Addison, “Synergistic effect of oxygen and $LiNO_3$ on the interfacial stability of lithium metal in a Li/O_2 battery,” *Journal of The Electrochemical Society*, vol. 160, no. 9, pp. A1544–A1550, 2013.

[108] G. G. Eshetu, X. Judez, C. Li, O. Bondarchuk, L. M. Rodriguez-Martinez, H. Zhang, and M. Armand, “Lithium azide as an electrolyte additive for all-solid-state lithium–sulfur batteries,” *Angewandte Chemie International Edition*, vol. 56, no. 48, pp. 15 368–15 372, 2017.

[109] W. Walker, V. Giordani, J. Uddin, V. S. Bryantsev, G. V. Chase, and D. Addison, “A rechargeable Li–O_2 battery using a lithium nitrate/N, N-dimethylacetamide electrolyte,” *Journal of the American Chemical Society*, vol. 135, no. 6, pp. 2076–2079, 2013.

[110] J. Uddin, V. S. Bryantsev, V. Giordani, W. Walker, G. V. Chase, and D. Addison, “Lithium nitrate as regenerable SEI stabilizing agent for rechargeable Li/O_2 batteries,” *The Journal of Physical Chemistry Letters*, vol. 4, no. 21, pp. 3760–3765, 2013.

[111] C. Schweitzer and R. Schmidt, “Physical mechanisms of generation and deactivation of singlet oxygen,” *Chemical reviews*, vol. 103, no. 5, pp. 1685–1758, 2003.

[112] F. Ding, W. Xu, X. Chen, J. Zhang, Y. Shao, M. H. Engelhard, Y. Zhang, T. A. Blake, G. L. Graff, X. Liu *et al.*, "Effects of cesium cations in lithium deposition via self-healing electrostatic shield mechanism," *The Journal of Physical Chemistry C*, vol. 118, no. 8, pp. 4043–4049, 2014.

[113] N. D. Trinh, D. Lepage, D. Aymé-Perrot, A. Badia, M. Dollé, and D. Rochefort, "An artificial lithium protective layer that enables the use of acetonitrile-based electrolytes in lithium metal batteries," *Angewandte Chemie International Edition*, vol. 57, no. 18, pp. 5072–5075, 2018.

[114] J.-l. Ma, F.-l. Meng, Y. Yu, D.-p. Liu, J.-m. Yan, Y. Zhang, X.-b. Zhang, and Q. Jiang, "Prevention of dendrite growth and volume expansion to give high-performance aprotic bimetallic Li-Na alloy–O_2 batteries," *Nature chemistry*, vol. 11, no. 1, p. 64, 2019.

[115] S. A. Freunberger, Y. Chen, N. E. Drewett, L. J. Hardwick, F. Bardé, and P. G. Bruce, "The lithium–oxygen battery with ether-based electrolytes," *Angewandte Chemie International Edition*, vol. 50, no. 37, pp. 8609–8613, 2011.

[116] K. R. Ryan, L. Trahey, B. J. Ingram, and A. K. Burrell, "Limited stability of ether-based solvents in lithium–oxygen batteries," *The Journal of Physical Chemistry C*, vol. 116, no. 37, pp. 19 724–19 728, 2012.

[117] F. Barde, Y. Chen, L. Johnson, S. Schaltin, J. Fransaer, and P. G. Bruce, "Sulfone-Based Electrolytes for Nonaqueous Li–O_2 Batteries," *The Journal of Physical Chemistry C*, vol. 118, no. 33, pp. 18 892–18 898, 2014.

[118] V. S. Bryantsev, V. Giordani, W. Walker, M. Blanco, S. Zecevic, K. Sasaki, J. Uddin, D. Addison, and G. V. Chase, "Predicting solvent stability in aprotic electrolyte Li–air batteries: nucleophilic substitution by the superoxide anion radical ($O_2^{\cdot-}$)," *The Journal of Physical Chemistry A*, vol. 115, no. 44, pp. 12 399–12 409, 2011.

[119] V. S. Bryantsev, J. Uddin, V. Giordani, W. Walker, D. Addison, and G. V. Chase, "The identification of stable solvents for nonaqueous rechargeable li-air batteries," *Journal of The Electrochemical Society*, vol. 160, no. 1, pp. A160–A171, 2013.

[120] S. A. Freunberger, Y. Chen, Z. Peng, J. M. Griffin, L. J. Hardwick, F. Bardé, P. Novák, and P. G. Bruce, "Reactions in the rechargeable lithium–O_2 battery with alkyl carbonate electrolytes," *Journal of the American Chemical Society*, vol. 133, no. 20, pp. 8040–8047, 2011.

[121] B. D. McCloskey, D. Bethune, R. Shelby, T. Mori, R. Scheffler, A. Speidel, M. Sherwood, and A. Luntz, "Limitations in rechargeability of Li-O_2 batteries and possible origins," *The journal of physical chemistry letters*, vol. 3, no. 20, pp. 3043–3047, 2012.

[122] B. D. Adams, R. Black, Z. Williams, R. Fernandes, M. Cuisinier, E. J. Berg, P. Novak, G. K. Murphy, and L. F. Nazar, "Towards a stable organic electrolyte for the lithium oxygen battery," *Advanced Energy Materials*, vol. 5, no. 1, p. 1400867, 2015.

[123] B. Zhou, L. Guo, Y. Zhang, J. Wang, L. Ma, W.-H. Zhang, Z. Fu, and Z. Peng, "A High-Performance Li–O_2 Battery with a Strongly Solvating Hexamethylphosphoramide Electrolyte and a LiPON-Protected Lithium Anode," *Advanced Materials*, vol. 29, no. 30, p. 1701568, 2017.

[124] D. Sharon, P. Sharon, D. Hirshberg, M. Salama, M. Afri, L. J. Shimon, W.-J. Kwak, Y.-K. Sun, A. A. Frimer, and D. Aurbach, "2, 4-dimethoxy-2, 4-dimethylpentan-3-one: an aprotic solvent designed for stability in Li–O_2 cells," *Journal of the American Chemical Society*, vol. 139, no. 34, pp. 11 690–11 693, 2017.

[125] C. J. Allen, S. Mukerjee, E. J. Plichta, M. A. Hendrickson, and K. Abraham, "Oxygen electrode rechargeability in an ionic liquid for the Li–air battery," *The Journal of Physical Chemistry Letters*, vol. 2, no. 19, pp. 2420–2424, 2011.

[126] C. J. Allen, J. Hwang, R. Kautz, S. Mukerjee, E. J. Plichta, M. A. Hendrickson, and K. Abraham, "Oxygen reduction reactions in ionic liquids and the formulation of a general ORR mechanism for Li–air batteries," *The Journal of Physical Chemistry C*, vol. 116, no. 39, pp. 20 755–20 764, 2012.

[127] M. C. Buzzeo, O. V. Klymenko, J. D. Wadhawan, C. Hardacre, K. R. Seddon, and R. G. Compton, "Voltammetry of oxygen in the room-temperature ionic liquids 1-ethyl-3-methylimidazolium bis ((trifluoromethyl)sulfonyl) imide and hexyltriethylammonium bis ((trifluoromethyl)sulfonyl)imide: one-electron reduction to form superoxide. steady-state and transient behavior in the same cyclic voltammogram resulting from widely different diffusion coefficients of oxygen and superoxide," *The Journal of Physical Chemistry A*, vol. 107, no. 42, pp. 8872–8878, 2003.

[128] M. Hayyan, F. S. Mjalli, M. A. Hashim, and I. M. AlNashef, "An investigation of the reaction between 1-butyl-3-methylimidazolium trifluoromethanesulfonate and superoxide ion," *Journal of Molecular Liquids*, vol. 181, pp. 44–50, 2013.

[129] S. Das, J. Højberg, K. B. Knudsen, R. Younesi, P. Johansson, P. Norby, and T. Vegge, "Instability of ionic liquid-based electrolytes in Li–O_2 batteries," *The Journal of Physical Chemistry C*, vol. 119, no. 32, pp. 18 084–18 090, 2015.

[130] L. Grande, E. Paillard, G.-T. Kim, S. Monaco, and S. Passerini, "Ionic liquid electrolytes for Li–air batteries: lithium metal cycling," *International journal of molecular sciences*, vol. 15, no. 5, pp. 8122–8137, 2014.

[131] G. Elia, J. Hassoun, W.-J. Kwak, Y.-K. Sun, B. Scrosati, F. Mueller, D. Bresser, S. Passerini, P. Oberhumer, N. Tsiouvaras *et al.*, "An advanced lithium–air battery exploiting an ionic liquid-based electrolyte," *Nano letters*, vol. 14, no. 11, pp. 6572–6577, 2014.

[132] Z. P. Rosol, N. J. German, and S. M. Gross, "Solubility, ionic conductivity and viscosity of lithium salts in room temperature ionic liquids," *Green Chemistry*, vol. 11, no. 9, pp. 1453–1457, 2009.

[133] M. Balaish, E. Peled, D. Golodnitsky, and Y. Ein-Eli, "Liquid-free lithium–oxygen batteries," *Angewandte Chemie International Edition*, vol. 54, no. 2, pp. 436–440, 2015.

[134] J. Janek and W. G. Zeier, "A solid future for battery development," *Nature Energy*, vol. 1, p. 16141, 2016.

[135] N. Bonnet-Mercier, R. A. Wong, M. L. Thomas, A. Dutta, K. Yamanaka, C. Yogi, T. Ohta, and H. R. Byon, "A structured three-dimensional polymer electrolyte with enlarged active reaction zone for Li–O_2 batteries," *Scientific reports*, vol. 4, p. 7127, 2014.

[136] S. H. Lee, J.-B. Park, H.-S. Lim, and Y.-K. Sun, "An advanced separator for Li–O_2 batteries: maximizing the effect of redox mediators," *Advanced Energy Materials*, vol. 7, no. 18, p. 1602417, 2017.

[137] B. J. Bergner, M. R. Busche, R. Pinedo, B. B. Berkes, D. Schröder, and J. Janek, "How to improve capacity and cycling stability for next generation Li–O_2 batteries: approach with a solid electrolyte and elevated redox mediator concentrations," *ACS applied materials & interfaces*, vol. 8, no. 12, pp. 7756–7765, 2016.

[138] T. Liu, Q.-C. Liu, J.-J. Xu, and X.-B. Zhang, “Cable-type water-survivable flexible Li-O_2 battery,” *Small*, vol. 12, no. 23, pp. 3101–3105, 2016.

[139] K. Zhang, S. Mu, W. Liu, D. Zhu, Z. Ding, and Y. Chen, “A flexible NASICON-type composite electrolyte for lithium-oxygen/air battery,” *Ionics*, vol. 25, no. 1, pp. 25–33, 2019.

[140] N. Nitta, F. Wu, J. T. Lee, and G. Yushin, “Li-ion battery materials: present and future,” *Materials today*, vol. 18, no. 5, pp. 252–264, 2015.

[141] N. Mahne, O. Fontaine, M. O. Thotiyl, M. Wilkening, and S. A. Freunberger, “Mechanism and performance of lithium–oxygen batteries–a perspective,” *Chemical science*, vol. 8, no. 10, pp. 6716–6729, 2017.

[142] R. Koerver, W. Zhang, L. de Biasi, S. Schweidler, A. O. Kondrakov, S. Kolling, T. Brezesinski, P. Hartmann, W. G. Zeier, and J. Janek, “Chemo-mechanical expansion of lithium electrode materials–on the route to mechanically optimized all-solid-state batteries,” *Energy & Environmental Science*, vol. 11, no. 8, pp. 2142–2158, 2018.

[143] J. Betz, G. Bieker, P. Meister, T. Placke, M. Winter, and R. Schmuch, “Theoretical versus practical energy: a plea for more transparency in the energy calculation of different rechargeable battery systems,” *Advanced Energy Materials*, vol. 9, no. 6, p. 1803170, 2019.

[144] B. D. McCloskey, D. S. Bethune, R. M. Shelby, G. Girishkumar, and A. C. Luntz, “Solvents’ critical role in nonaqueous lithium–oxygen battery electrochemistry,” *The Journal of Physical Chemistry Letters*, vol. 2, no. 10, pp. 1161–1166, 2011.

[145] A. C. Luntz and B. D. McCloskey, “Li–air batteries: importance of singlet oxygen,” *Nature Energy*, vol. 2, no. 5, p. 17056, 2017.

[146] S. R. Gowda, A. Brunet, G. Wallraff, and B. D. McCloskey, “Implications of CO_2 contamination in rechargeable nonaqueous Li–O_2 batteries,” *The journal of physical chemistry letters*, vol. 4, no. 2, pp. 276–279, 2012.

[147] D. T. Sawyer and J. S. Valentine, “How super is superoxide?” *Accounts of Chemical Research*, vol. 14, no. 12, pp. 393–400, 1981.

[148] D. Aurbach, B. D. McCloskey, L. F. Nazar, and P. G. Bruce, “Advances in understanding mechanisms underpinning lithium–air batteries,” *Nature Energy*, vol. 1, no. 9, p. 16128, 2016.

[149] V. S. Bryantsev and M. Blanco, “Computational study of the mechanisms of superoxide-induced decomposition of organic carbonate-based electrolytes,” *The Journal of Physical Chemistry Letters*, vol. 2, no. 5, pp. 379–383, 2011.

[150] B. Genorio, J. Staszak-Jirkovský, R. S. Assary, J. G. Connell, D. Strmcnik, C. E. Diesendruck, P. P. Lopes, V. R. Stamenkovic, J. S. Moore, L. A. Curtiss *et al.*, “Superoxide (electro)chemistry on well-defined surfaces in organic environments,” *The Journal of Physical Chemistry C*, vol. 120, no. 29, pp. 15 909–15 914, 2016.

[151] Z. Zhang, J. Lu, R. S. Assary, P. Du, H.-H. Wang, Y.-K. Sun, Y. Qin, K. C. Lau, J. Greeley, P. C. Redfern *et al.*, “Increased stability toward oxygen reduction products for lithium-air batteries with oligoether-functionalized silane electrolytes,” *The Journal of Physical Chemistry C*, vol. 115, no. 51, pp. 25 535–25 542, 2011.

[152] V. S. Bryantsev and F. Faglioni, “Predicting autoxidation stability of ether-and amide-based electrolyte solvents for Li-air batteries,” *The Journal of Physical Chemistry A*, vol. 116, no. 26, pp. 7128–7138, 2012.

[153] B. Liu, W. Xu, P. Yan, X. Sun, M. E. Bowden, J. Read, J. Qian, D. Mei, C.-M. Wang, and J.-G. Zhang, “Enhanced cycling stability of rechargeable Li–O_2 batteries using high-concentration electrolytes,” *Advanced Functional Materials*, vol. 26, no. 4, pp. 605–613, 2016.

[154] M. Carboni, A. G. Marrani, R. Spezia, and S. Brutti, “1,2-dimethoxyethane degradation thermodynamics in Li-O_2 Redox Environments,” *Chemistry–A European Journal*, vol. 22, no. 48, pp. 17 188–17 203, 2016.

[155] A. Khetan, H. Pitsch, and V. Viswanathan, “Solvent degradation in nonaqueous Li-O_2 batteries: oxidative stability versus H-abstraction,” *The journal of physical chemistry letters*, vol. 5, no. 14, pp. 2419–2424, 2014.

[156] V. S. Bryantsev, “Predicting the stability of aprotic solvents in Li-air batteries: pKa calculations of aliphatic C–H acids in dimethyl sulfoxide,” *Chemical Physics Letters*, vol. 558, pp. 42–47, 2013.

[157] R. S. Assary, K. C. Lau, K. Amine, Y.-K. Sun, and L. A. Curtiss, “Interactions of dimethoxy ethane with Li_2O_2 clusters and likely decomposition mechanisms for Li–O_2 batteries,” *The Journal of Physical Chemistry C*, vol. 117, no. 16, pp. 8041–8049, 2013.

Singlet oxygen in non-aqueous batteries, an affliction

Oxigen (sic), as you well know, is my hero as well as my foe.
Christian Friedrich Schonbein

Contents

Figures

Chapter based on Petit et al.[1]; Schafzahl, Petit et al.[2]; Mourad, Petit et al.[3]; Petit et al.[4]

Introduction

Metal-air batteries suffer from severe parasitic reactions preventing their long term cycling. Among other consequences, side reactions provoke electrolyte and electrode decompositions resulting in low efficiency, high overpotential and poor rechargeability due to side product accumulation. As described in the previous chapter, superoxide's reactivity does not suffice to explain such degradation in regards to the higher K-O_2 cyclability compared to Li-O_2 and Na-O_2 chemistries. Other culprits must be identified to underpin an improved metal-air cell cyclability. Considering the metal-air mechanisms, a likely reactive species would be excited oxygen. Due to the difficulty to detect it, its presence in metal-air devices was often overlooked despite its high reactivity. From peroxide chemical oxidation, singlet oxygen, the first electronically excited state of oxygen, can be produced[5–7]. Our group main reasoning, presented in this chapter, is the production of this aggressive species in metal-air devices and the consequent elucidation of its possible productions pathways.

Singlet oxygen, as an excited species, possesses a peculiar chemistry compared to its ground state counterpart. Singlet oxygen's reactivity lies in its electronic structures. In contrast to the triplet ground state, singlet oxygen has two paired electrons in its valence shell giving it a dienophile character. This particularity is made use of in organic chemistry. In the context of metal-air batteries, singlet oxygen was shown to react with and degrade cell components such as the electrolyte or the carbon electrode. Parasitic reactions could be, thus, partly attributed to $^1O_2$ if present in the cells.

To characterise and quantify the suspected $^1O_2$ presence in metal-air batteries, our group developed a number of adapted analytical methods. These analyses allow quantification in-situ or ex-situ of singlet oxygen and side reaction presences by a combination of techniques, i.e., high-performance liquid chromatography (HPLC), UV-vis spectrometry, mass spectrometry (MS), or pressure monitoring. The development of these methods relied on the production of photochemically produced $^1O_2$ at a controlled rate using a photo-sensitizer.

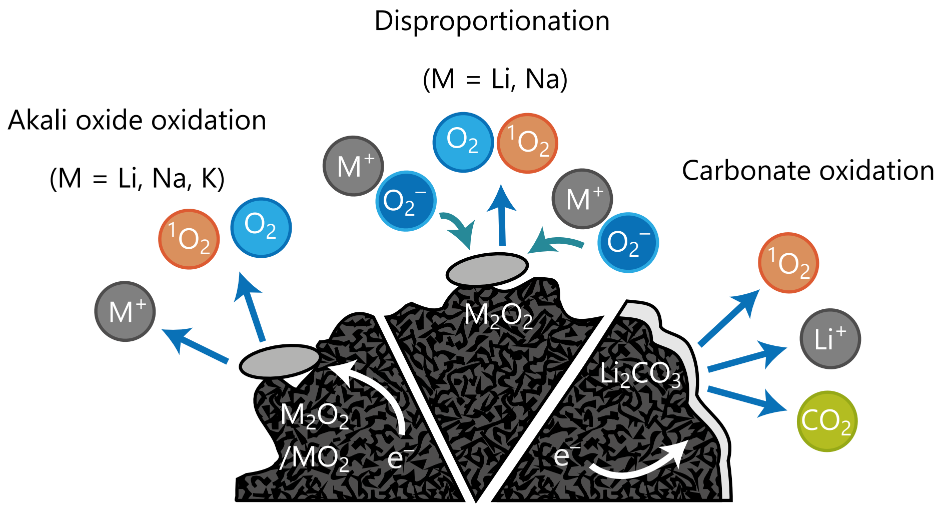

Figure 2.1: **Illustration of the identified singlet oxygen production pathways in metal-air batteries.**

The singlet oxygen presence will be demonstrated in metal-air as well as Li-based organic batteries and its production mechanisms described, either via electrochemical or chemical processes, as illustrated in Fig. 2.1. The formation of singlet oxygen is directly intertwined with the energy storage reactions in metal-air batteries. Its formation at high overpotentials can proceed by oxidation of either alkali oxide, at potentials sufficient to overcome the $^1O_2$ formation energy barrier, or lithium carbonate, a common by-products of lithium-based organic batteries. We have also shown experimentally $^1O_2$ formation via alkali superoxide disproportionation during this thesis, which is thermodynamically favoured for LiO_2 and NaO_2 and is partially responsible for NaO_2 decomposition at rest. The singlet oxygen role is important to understand the side reaction patterns in metal-air batteries as it will be presented in this chapter. The remainder of this thesis will try to unfold the singlet oxygen formation mechanisms more in depth.

2.1 Excited molecular oxygen as a source of side reactivity

2.1.1 Theoretical considerations

Oxygen redox chemistry is so crucial that the word oxidation was forged from this molecule. Cellular respiration, which shaped current animal evolution[8], relies on oxygen reduction in a similar fashion to metal-O_2 cells[9]. These reactions are based on the redox chemistry of ground state oxygen. The ground state of molecular dioxygen is a triplet state due to its open electron shell, in contrast to most molecules who have a closed shell (cf. the octet and eighteen-electron rules)[10]. The ground triplet state is denoted as $^3\Sigma_g^-$ in its molecular term symbol (3 is the total spin quantum number, Σ the projection of the orbital angular momentum along the internuclear axis and $^-$ the reflection symmetry along an arbitrary plane containing the internuclear axis). The $^3\Sigma_g^-$ state is characterised by two unpaired electrons with parallel spin in the valence shell, reducing electronic screening of the nucleus according to Hund's rule of maximum multiplicity[11,12]; the valence shell electrons are situated in the 2-π antibonding orbitals in the case of dioxygen ($\pi^*_{2p_x}$ and $\pi^*_{2p_y}$)[11] [13], as illustrated in Fig. 2.2. The ground state dioxygen is not the only state of molecular oxygen involved in biological processes[14,15]. Dioxygen can exist in excited states; the two lowest ones in energy are singlet states formed by the change of one electron spin at an energy of 94 and 157 kJ·mol^{-1} ($^1\Delta_g$ and $^1\Sigma_g^+$, respectively) above the ground state[13,16–18]. As singlet states, $^1\Delta_g$ and $^1\Sigma_g^+$ present two electron with opposite spins on their valence shell, as indicated in Fig. 2.2. The $^1\Delta_g$ state has both electrons situated on the same π^*_{2p} orbital where the $^1\Sigma_g^+$ has electrons on two different π^*_{2p} orbitals[6].

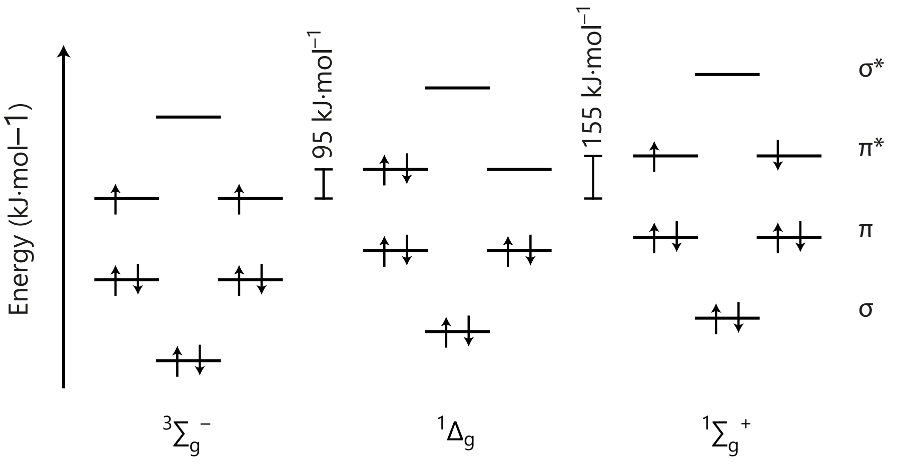

Figure 2.2: **Electronic configuration of the dioxygen valence shell at its ground state and two lower excited states ($^3\Sigma_g^-$, $^1\Delta_g$, and $^1\Sigma_g^+$).**

$^1\Delta_g$ and $^1\Sigma_g^+$ states decay towards the ground state at largely different kinetics, giving rise to their differing lifetimes[15]. $^1\Sigma_g^+$ quickly decay to the $^1\Delta_g$(/$^3\Sigma_g^-$) state(s)[15], with a lifetime of 7 secondes in absence of external perturbation (e.g. low pressure), 24 µs in dry air and less than to 1 ns in solution[15,17]. The $^1\Delta_g$ transition to the ground state is, however, spin forbidden[16]. The $^1\Delta_g$ state can be called a metastable species, with a lifetime of 45-72 minutes in absence of external perturbation, 86 ms in dry air and between approximatelly 10^{-6} up to 10^{-2} seconds in solution depending on the solvent[15,17,19]. The lifetime of the $^1\Delta_g$ state depends strongly on the nature of the solvent and notably the water content as well as the presence of protic moeties[15].

2.1.2 Singlet oxygen's reactivity

Due to the lifetime and formation mechanism difference between $^1\Delta_g$ and $^1\Sigma_g^+$, only the $^1\Delta_g$ state will be considered of concern in metal-air chemistry; $^1\Delta_g$ notation will hence be simplified as singlet oxygen or $^1O_2$ through the rest of this thesis. Singlet oxygen is highly reactive and its singlet nature allows direct two-electron reaction with singlet organic molecules that would be spin-forbidden for the ground state[20]. The chemistry of singlet oxygen is widely different, being dienophile, than its ground state who behave more as a diradical[5]. Several singlet oxygen reactions are well known and used in organic synthesis such as Diels–Alder [4+2] cycloaddition[13,21–23]. $^1O_2$ reactivity usually involves direct reaction with double bonds. Singlet oxygen is also known to oxidize heteratoms as organosulfur for example[24]. More recently, singlet oxygen was shown to selectively perform hydroperoxidation of ethereal hydrocarbons[25].

Given that the reactivity of reduced O_2 species and ground state O_2 is not sufficient to explain the observed parasitic chemistry in metal-O_2 cells, our group investigated $^1O_2$ as a source of side reactivity. Relatively stable organic electrolytes, such as glymes, still result in a typical pattern of side products such as Li_2CO_3, Li formate, and Li acetate over cycling[26]. To investigate whether $^1O_2$ presence would induce the same decompostion products, a typical lithium-air electrolyte, 0.1 M $LiClO_4$ in DME, was exposed to singlet oxygen during 30 minutes[27]. CO_2 evolution could not be detected by mass spectrometry during the experiment. However, a subsequent addition of H_3PO_4, to decompose possibly formed Li_2CO_3[28], led to a significant CO_2 release as shown in Fig. 2.3(a). Singlet oxygen is thus able to decompose the electrolyte and to produce Li_2CO_3. In addition, ^{1}H-NMR spectrum of the electrolyte dissolved in D_2O after $^1O_2$ exposure, presented in Fig. 2.3b, reveals the production of lithium carboxylates such as lithium formate and acetate. Thus, metal-air electrolytes can react with singlet oxygen to produce common side products found in these chemistries and could therefore explain their formations. Singlet oxygen reactions involve commonly formation of peroxide as discussed in the previous paragraph; it was then hypothesised that singlet oxygen generates ROOH, ROO· and R· species that initiate degradation at higher rates, as suggested in previous studies[29,30]. In contrast to triplet oxygen, singlet oxygen is capable to react by Diels–Alder [4+2] cycloaddition with the electrode carbon surface which leads to the formation of quinone moeties at the surface[31]. The formation of quinone at the surface could serve as the onset of further side reactions[31] and change the hydrophilicity of the carbon surface, reducing further the electrode stability as discussed in 1.2.2.1. Singlet oxygen can also react with common organic additives in metal-air batteries containing double bonds such as redox mediators[32].

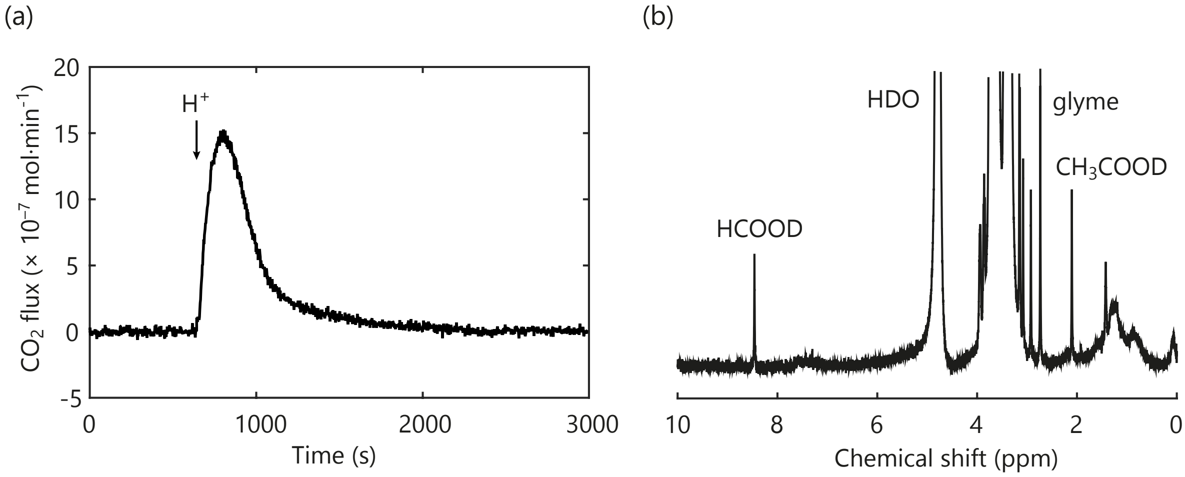

Figure 2.3: **Electrolyte reactivity towards $^1O_2$, adapted from[27].** (a) CO_2 evolution form Li_2CO_3 decomposition formed by O_2 saturated 0.1 M $LiClO_4$ in DME electrolyte exposure to $^1O_2$ for 30 minutes. (b) ^{1}H-NMR of the same electrolyte dissolved in D_2O after $^1O_2$ exposition.

2.2 Detecting singlet oxygen

2.2.1 Production of singlet oxygen

As singlet oxygen appears to be a possible source of metal-air side reactivity, it is necessary to detect and quantify it. To conceive and calibrate singlet oxygen analytical methods, controlled production must be achieved. Singlet oxygen cannot be produced chemically from its ground state, due to the spin forbidden transition. Singlet oxygen can, yet, be chemically produced from superoxide and peroxide[5–7]; such methods involve reactive species that could interfere with the detection of $^1O_2$ induced side reactivity alone. A more "soft" $^1O_2$ production is possible through photosensitizers. This production method is based on a sensitizer excitation by photons at a specific wavelength[15,16]. The excited sensitizer transfers the excess of energy to the ground state oxygen, forming its singlet state. Photosensitization of oxygen is especially efficient since oxygen transition form triplet to singlet state is lower in energy than most organic molecules that could quench the excited sensitizer and oxygen diffuses quickly in most media, increasing energy transfer chance[15]. Hence, the photosensitization main mechanism is quenching of the excited triplet state of the sensitizer by O_2[15,16]. Initially, the sensitizer is excited by photons to its singlet excited states, through a one photon transition. According to Kasha's rule, molecules in states above the lower excited state will deactivate through vibration until reaching the first excited singlet state (S_1)[16,33]. Intersystem crossing leads to the production of the first triplet state (T_1) of the sensitizer despite its spin forbidden nature[15,16,33]. Once formed, the T_1 state lifetime is long enough to allow for collision of the sensitizer with a ground state oxygen molecule, due to unfavoured decay by spin forbidden transition[16]. Upon collision, the sensitizer can transfer its energy excess to the oxygen as they are both in the triplet state, generating a singlet oxygen molecule and regenerating the ground state of the sensitizer. The photosensitization process is schematically shown in Fig. 2.4.

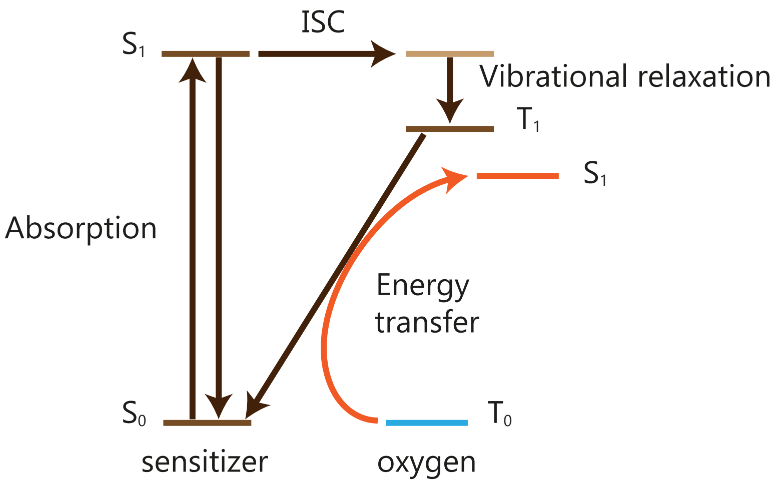

Figure 2.4: **Schematized electronic state transitions for photosensitized singlet oxygen production, adapted form[34].**

To allow for efficient photosensitization, a sensitizer must have high absorption at a specific wavelength, a T_1 state higher in energy than the transition of ground state oxygen to its singlet state, a good quantum yield of the triplet state with a long lifetime, and a good stability[16]. Several chemical groups were identified as good oxygen photosensitizers, such as organic dyes, porphyrins, phthalocyanines, tetrapyrroles, or transition metal complexes[16]. Palladium (II) *meso*-tetra(4-fluorophenyl-9-tetrabenzoporphyrin) (Pd_4F) has been used in metal-air battery environments to produce singlet oxygen and is relatively stable towards photobleaching and singlet oxygen[27,35].

2.2.2 Phosphorescence

Deexcitation of the singlet to the triplet state through photoemission is called phosphorescence. Singlet oxygen phosphorescence emits photons at the specific wavelength of ~1275 nm in the near-infrared that does not vary strongly with the solvent used[14,15,36]. Detection of photons at this specific wavelength allows to characterise the singlet oxygen presence as other species would usually release photons at shorter wavelengths[14]. The characteristic phosphorescence signal is nevertheless weak due to its low quantum yield and spin-forbidden nature[14,15,36]; its detection sensitivity is also strongly dependent on the solvent as singlet oxygen might be deactivated through other pathways. The spontaneous phosphorescence during the $^1O_2$ decay can be detected in operando in a Li-O_2 cell using a specifically designed cell based on a quartz cuvette[27]. The low sensibility of this method highlight, yet, the need for a more sensitive method as described in the following part to conclusively affirm the $^1O_2$ presence.

2.2.3 Use of a chemical trap

Singlet oxygen quantification can be improved using fluorescent probes. These probes are usually composed of a highly fluorescent chromophore, such as fluorescein, and a singlet oxygen trap, such as 9,10-diphenylanthracene (DPA)[14,37,38]. The chemical traps are most typically based on anthracenes which react selectively with $^1O_2$ to form their endoperoxides at high rates ($2{\cdot}10^7$ – $9{\cdot}10^8$ $\mathrm{mol{\cdot}L^{-1}{\cdot}s^{-1}}$ for 9,10-dimethylanthracene (DMA)[38]), as shown in Fig. 2.5(a). The anthracene endoperoxide formation via [4+2] cycloaddition results in a fluorescence change which can be sensitively detected. However, used fluorophores are not electrochemically stable in the required potential range for metal-air cells[27]. The actual singlet oxygen production can moreover be higher than the trap consumption as other decay routes are still present.

Anthracenes are themselves fluorescents albeit with a lower sensitivity than dedicated fluorophores. The detection is then based on decreasing absorbance, the endoperoxide being non-fluorescent as presented in Fig. 2.5(b)[27,37,38]. DMA and DPA reaction kinetics were compared in a Li-air electrolyte in presence of photogenerated $^1O_2$ to determined their usability as $^1O_2$ probes in the metal-O_2 environment[27]. DMA demonstrates a higher reaction rate, most likely arising from steric hindrance effect[27]. DMA and its endoperoxide are, moreover, stable in contact with triplet oxygen, superoxide, peroxide as well as lithium carbonate and electrochemically up to ~4 $V_{\mathrm{Li/Li^+}}$ on glassy carbon[27,39]. The DMA endoperoxide (DMA-O_2) production is hence specific to singlet oxygen in the metal-air chemistry and DMA a selective $^1O_2$ probe. DMA use as fluorescent probe requires, yet, a low starting concentration to achieve high sensitivity[27]. The DMA light emission decline, indicating $^1O_2$ production, is indeed more noticeable with a low probe starting amount; as the fluorescence intensity depends on the probe concentration, a higher proportion of DMA decay will results in a more sensitive measurement. A low probe concentration, however, increases the measurement noise and degrades the detection limits.

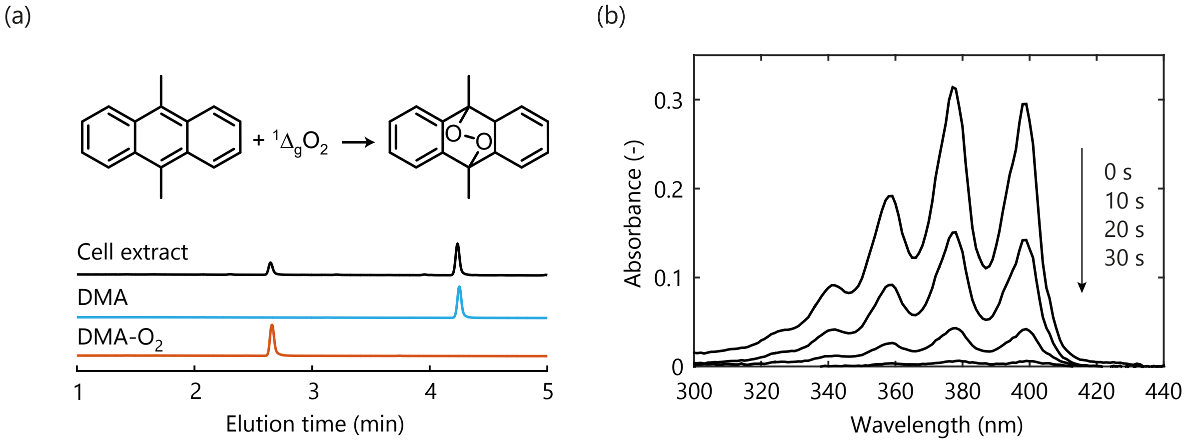

Figure 2.5: **Use of a chemical trap for singlet oxygen detection.** (a) DMA reaction to form its endoperoxide in presence of $^1O_2$ and the elution times in HPLC for DMA and DMA-O_2 compared to a HPLC measurement of a cell extract after cycling. (b) UV vis absorption spectra of DMA upon exposure to $^1O_2$ for different times, adapted from[27].

To improve $^1O_2$ detection sensitivity, ex-situ DMA/DMA-O_2 conversion measured by high-performance liquid chromatography (HPLC) permits the use of a near saturated electrolyte in DMA[27]. Using a specific procedure described more precisely in Appendix A.4, DMA and its endoperoxide present different elution times. Their respective amounts are quantified by the peak surface area compared to a control sample with known concentration, as illustrated in Fig. 2.5(a). This involves DMA and DMA-O_2 extraction from the electrolyte after electrochemical cycling by a more volatile solvent, such as DME, thanks to a Swagelock cell design shown in Appendix A.1. The extraction is followed by the evaporation of the volatile solvent and a subsequent dilution to reach a DMA/DMA-O_2 concentration of ~1 $mg{\cdot}mL^{-1}$ which is suitable for HPLC analysis.

2.2.4 Characterising side reaction

Side reactivity can be partly attributed to singlet oxygen if formed in metal-air batteries. As discussed in part 1.3.1, quantitative measurements of the species involved are necessary to conclude about the reversibility of a cell. Taking into consideration the gaseous nature of O_2, two specific methods have been developed to measure its consumption/release over time. The first one is operando electrochemical mass spectrometry (OEMS)[40–43]. In this case, the cell headspace is flushed to a mass spectrometer which allows for gas analysis. Quantification of the O_2 consumption requires the use of an invariable inert gas flow such as Ar together with a known proportion of O_2. Upon O_2 consumption, the Ar proportion will rise which permits to determine the relative fluxes. During charge, a pure Ar gas flow can be used to quantify of the gases produced. OEMS measurements give access to both O_2 consumption/formation rate as well as integral amounts of the different gases evolved. As another possibility to quantify gas production and consumption, the pressure in the closed headspace of a cell can be measured during charge/discharge; pressure change can be related to the gas evolution and in turn to the electron flux using the Faraday law (Eq. 1.9) and the ideal gas law (Eq. 2.1)[44,45], as shown in Fig. 2.6(a) and described more precisely in Appendix A.2. The nature of the gas is, however, unknown and CO_2 evolution on charge cannot be distinguished from O_2.

$$P \cdot V = n \cdot R \cdot T \tag{2.1}$$

with P, the pressure (Pa); V, the volume (m^3); n, the number of mole in the system; R, the ideal gas constant (8.314 $m^3 \cdot Pa \cdot K^{-1} \cdot mol^{-1}$); and T, the temperature (K).

The discharge product being a solid attached to a conductive matrix, only destructive ex-situ methods can be used to quantify the total amount in an electrode. Iodometric titration (Eq. 2.2) or $[Ti(O_2^{2-})]^{2+}$ complex spectrophotometry (Eq. 2.3) are, for example, destructive but quantitative measurements of the (su)peroxide quantity[46,47]. The amount of parasitic reactions can be evaluated by the carbonaceous products formed. These common side products in metal-O_2 cells can act be taken as a proxy for the total side reaction amounts[28,40,48–50]. Both organic and inorganic carbonaceous species are quantifiable through an ex-situ destructive method[28]. The addition of acid on a washed electrode provoke a CO_2 release from inorganic carbonate such as Li_2CO_3 (Eq. 2.4) and the addition of a Fenton's reagent evolve CO_2 from organic carbonates (Eq. 2.5), stable to the acid used at the right concentration. Mass spectrometry quantifies the CO_2 evolution for the two steps. We present a refined procedure, which combines both Li_2O_2 and carbonate quantification that is described in Appendices A.5 and A.6; in only one measurement both the amounts of Li_2O_2 and carbonaceous side reaction products are quantified[2], as illustrated in Fig. 2.6(b). The Fenton's reagent use requires washing electrodes to prevent reaction with the organic electrolyte. Analysing unwashed electrodes avoids possible removal of poorly attached Li_2O_2 and captures also dissolved species in the electrolyte. Two electrodes are then required for full characterisation. If more precise speciation of the carbonate products is necessary, their separate quantification can be obtained by ^{1}H-NMR of a D_2O solution after electrode immersion[46,51]. Altogether, these methods can capture the reversibility of a cell in its entirety. Despite the methods being explained here more thourougly for Li-O_2 chemistries, they can be applied for other non-aqueous metal-air batteries or the quantification of SEI components with simple adjustments[2,52].

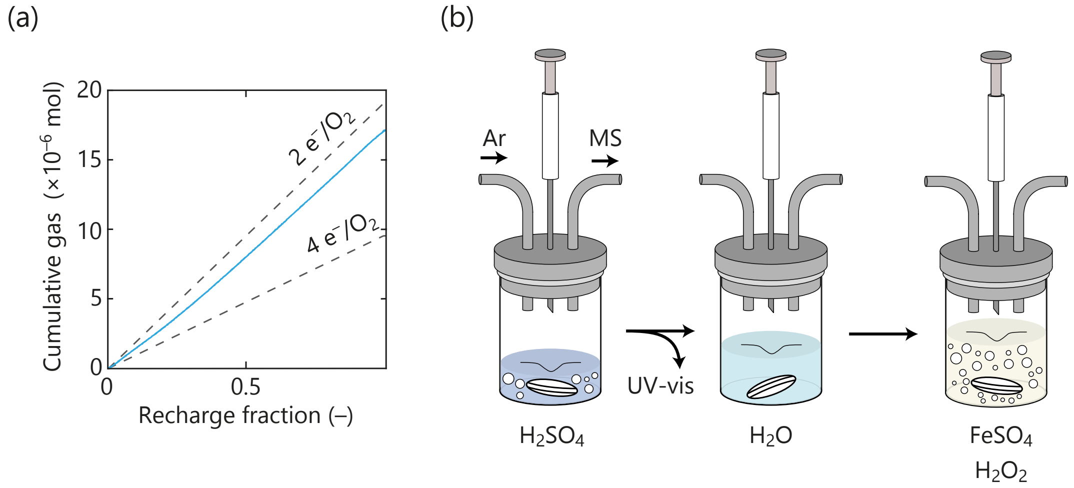

Figure 2.6: **Quantitative characterisations of (su)peroxide, carbonaceous compounds and O_2 evolution.** (a) Gas evolution during a Li-O_2 cell charge obtained by pressure monitoring in tetraglyme with 1M LiTFSI compared to theoretical yields of O_2, adapted from[4]. (b) Scheme of the Li_2O_2 and inorganic/organic carbonate quantifications by mass spectroscopy and UV-vis spectroscopy, adapted from[2].

Iodometric titration of Li_2O_2.

$$\begin{aligned}&Li_2O_2 + 2\,H_2O \longrightarrow 2\,LiOH + H_2O_2\\&H_2O_2 + 2\,KI + H_2SO_4 \longrightarrow I_2 + K_2SO_4 + 2\,H_2O\\&I_2 + 2\,Na_2S_2O_3 \longrightarrow Na_2S_4O_6 + 2\,NaI\end{aligned} \tag{2.2}$$

Photometric detection of Li_2O_2.

$$\begin{aligned}&Li_2O_2 + 2\,H_2O \longrightarrow 2\,LiOH + H_2O_2\\&TiOSO_4 + H_2O_2 \longrightarrow [Ti(O_2^{2-})]^{2+}\text{ complex}\end{aligned} \tag{2.3}$$

CO_2 evolution from inorganic carbonates by acidification.

$$CO_3^{2-} \rightleftharpoons HCO_3^{-} \rightleftharpoons CO_2 \tag{2.4}$$

The equilibrium highly favours CO_2 formation at high pH.

Fenton's regeant formation.

$$Fe^{2+} + H_2O \longrightarrow Fe^{3+} + OH\cdot + OH^{-} \tag{2.5}$$

Carboxylate radical decompositions by the Fenton's regeant give rise to CO_2 evolution.

Qualitative measurements, despite the loss of quantitative information, have the advantages to permit direct visualization of the charge/discharge processes or characterise specific products. Recent efforts address in-situ characterisation to understand the occuring reactions; TEM[53,54], X-ray and neutron tomography[55], XRD[56–58], XPS[59], Raman[60], IR spectroscopy[61] or AFM[62] are a few example of available techniques.

2.3 Formation mechanisms of singlet oxygen

2.3.1 Presence of singlet oxygen in metal-air batteries

The previously described analytical methods to detect singlet oxygen and side reactions are adapted to metal-air batteries, where singlet oxygen formation was suggested in an early stage of research[63]. In-situ measurements of singlet oxygen phosphorescence confirmed $^1O_2$ formation in Li-air chemistry at all stages of charge[27], as shown in Fig. 2.7. The absence of a detectable signal during discharge does not allow for a clear statement about $^1O_2$ absence because of the low sensitivity of the method. Similarly, EPR measurements showed production of singlet oxygen above 3.55 V_{Li/Li^+}[64].

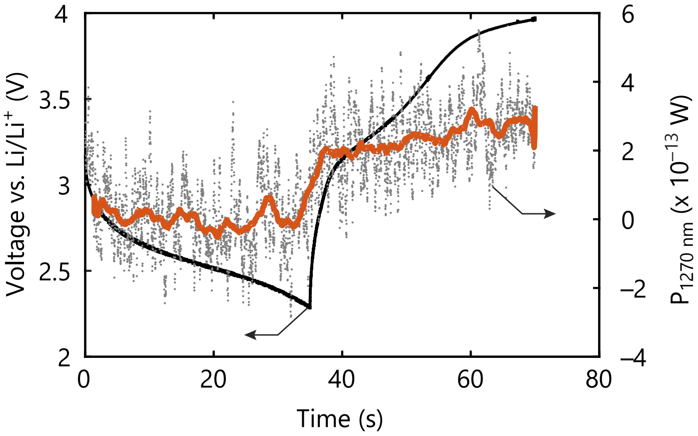

Figure 2.7: **In-situ detection of singlet oxygen during Li-O_2 cell cycling by phosphorescence, adapted from[27].** In black, the voltage profile during galvanostatic cycling of a Au-grid electrode in O_2 saturated 0.1 M $LiClO_4$ deuterated acetonitrile electrolyte with 1000 ppm D_2O. In light grey, the power of the optical emission at 1270 nm, related to $^1O_2$ phosphorescence. In orange, the moving average of the phosphorescence output.

DMA in-situ fluorescence monitoring during Li-air cell cycling shows clear consumption of the trap by singlet oxygen from the charge onset with improved sensitivity in a classical electrolyte (0.1 mol.L^{-1} $LiClO_4$ in TEGDME). The $^1O_2$ production rate increases with the overpotential during the charge, yet, no clear singlet oxygen production appears during discharge[27]. The addition of 1000 ppm of water as additive, known to increases the solution pathway and solvated superoxide[65], changes drastically the results as presented in Fig. 2.8(a). A slight DMA consumption can be seen also through the discharge in this case, indicating singlet oxygen formation at all stages of cycling[27]. The presence of water appears to enhance $^1O_2$ production, especially during discharge. Using a similar method in Na-O_2 cells showed production of singlet oxygen during NaO_2 oxidation in a similar fashion[52], as depicted in Fig. 2.8(b). The production of singlet oxygen does therefore not only occur in Li-O_2 chemistry but concerns metal-air batteries in general.

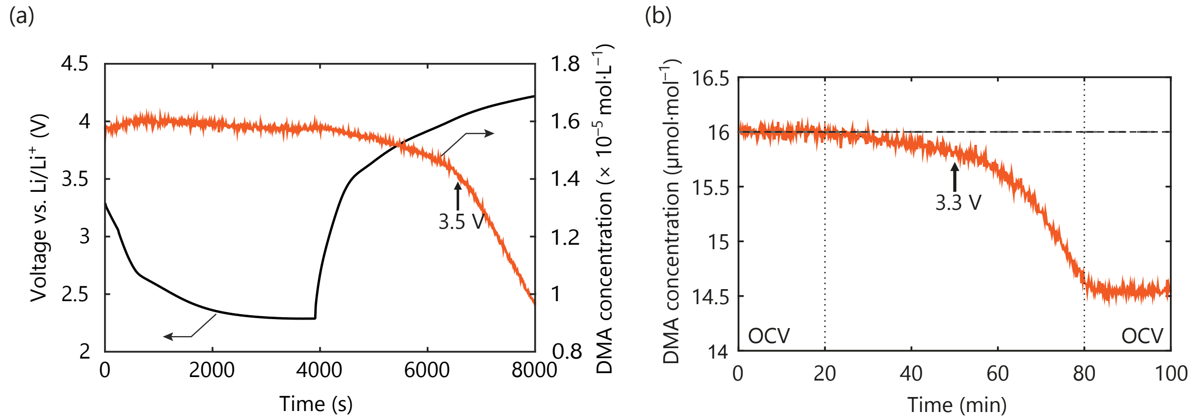

Figure 2.8: **In-situ detection of singlet oxygen by DMA fluorescence.** (a) $^1O_2$ detection by fluorescence spectroscopy in a Li-air cell, adapted from[27]. In black, the voltage profile of the Li-O_2 cell during galvanostatic cycling in O_2 saturated electrolyte containing 16 μM DMA, 0.1 M $LiClO_4$ and 1000 ppm H_2O in TEGDME at 25 mA·cm^{-2}. In orange, the DMA concentration evolution. (b) $^1O_2$ detection by fluoresence spectroscopy in a Na-air cell, adapted from[52]. In orange, the DMA concentration evolution during potentiostatic charge of a NaO_2 containing electrode. Prior to charge, the cathode was first discharged to 75 mA·h·cm^{-2} in a O_2 saturated electrolyte containing 0.5 M NaOTf and 40 ppm H_2O in diglyme and was transferred to the in-situ fluorescence setup containing the same electrolyte and 16 μM DMA as additive.

To clarify the singlet oxygen production during discharge even without H_2O additive in Li-air cells, HPLC characterisation of the DMA to DMA-O_2 conversion has been performed at different stages of discharge and recharge[27]. The results, shown in Fig. 2.9(a)-(b), present $^1O_2$ production during discharge, in accord with the in-situ measurements. Similarly, DMA-O_2 is produced during charge as well as discharge at smaller rate in Na-O_2 cells[52], as represented in Fig. 2.9(c)-(d).

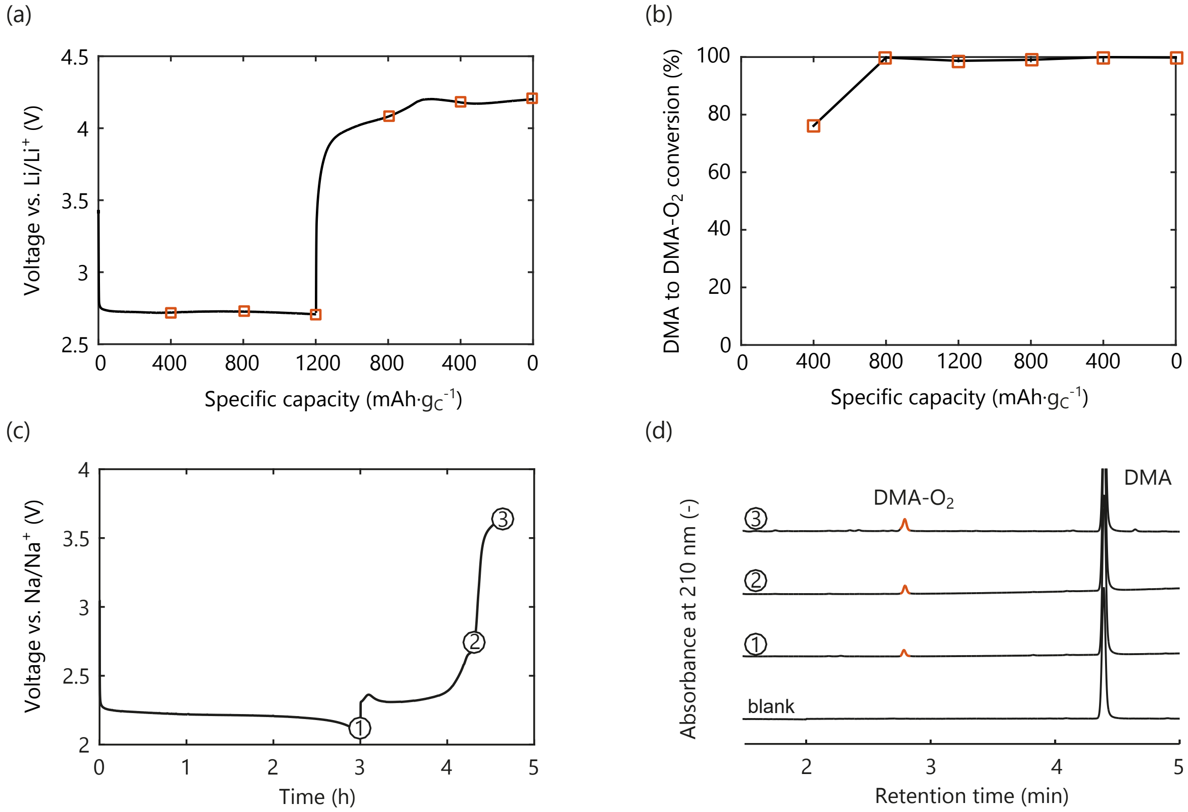

Figure 2.9: **Ex-situ detection of singlet oxygen by HPLC.** (a-b) $^1O_2$ detection by DMA-O_2 formation in Li-air cells, adapted from[27]. (a) The voltage profile of a porous carbon black electrode during cycling in a O_2 saturated 30 mM DMA, 0.1 M $LiClO_4$ TEGDME electrolyte at 70 mA·g_c^{-1}. The orange squares show the states of discharge/charge where samples for HPLC were taken. (b) DMA-O_2 yield indicating $^1O_2$ amount. (c-d) $^1O_2$ detection by DMA-O_2 formation in Na-air cells, adapted from[52]. (c) The voltage profile of a carbon paper electrode during cycling in a O_2 saturated 30 mM DMA, 0.5 M NaOTf and 40 ppm H_2O diglyme electrolyte at 90 mA·cm^{-2}. The numbered circles show the states of discharge/charge where samples for HPLC were taken. (d) HPLC runs corresponding to the numbered circles in (c) indicating in orange the DMA to DMA-O_2 conversion.

The $^1O_2$ formation rate displays striking similarity with the rate of side reactions illustrated in Fig. 1.19, namely a smaller rate during discharge and an increased rate as the charge progresses. DMA addition to the electrolyte reduces the production of carbonates through most of the cycling[27]. DMA effectiveness will be, however, reduced during cycling as it is consumed over time by $^1O_2$ trapping. To further confirm singlet oxygen influence on parasitic chemistry, OEMS measurements monitored the O_2 and CO_2 release during recharge of Li-air cells with or without DMA as additive, respectively from Li_2O_2 and Li_2CO_3 oxidation[27]. The DMA addition resulted in lower overpotentials through out charge which was attributed to a lower production of carbonates during discharge; carbonate accumulation and oxidation provoke in part the overpotential rise as described in part 1.2.1.3. The O_2 evolution follows more closely the theoretical yield with the DMA containing electrolyte which is accompanied by a greatly reduced CO_2 release. This indicates reduced parasitic reactivity both in discharge and charge via $^1O_2$ trapping. Given the reduction of side reactions in presence of a high DMA concentration and their augmentation once the DMA is consumed, $^1O_2$ can be ascribed as an important parasitic chemistry source in metal-air batteries.

2.3.2 Alkali oxide oxidation

As singlet oxygen is partially responsible for metal-air parasitic chemistry, the biggest hindrance to their cyclability, understanding its formation mechanisms is of prime importance. Chemical oxidation of alkali peroxides is a known production pathway for $^1O_2$[7]. The most direct formation mechanism in metal-air chemistries is then alkali oxide oxidation. Despite being unfavoured thermodynamically, singlet oxygen can be produced if the applied overpotential is high enough to overcome the energy barrier. The required energy to pass oxygen from its ground state to its singlet state is ~94 kJ·moL^{-1} or 0.97 eV[18]. Assuming this energy as a first estimate of the Gibbs free energy difference between the singlet and triplet state[27,64], a singlet oxygen potential threshold estimation is possible from the triplet state release according to the Eq. 2.6. The $^1O_2$ formation overpotential is then approximate as 0.97 V for the alkali superoxide (considering a 1 e$^-$ process) and 0.49 V for the alkali peroxide (2 e$^-$ process) above the potential for $^3O_2$ release. A direct two-electron reaction appears unlikely from the mechanism described in part 1.2.1.2. However, the hypothetical case of a direct two-electron oxidation is still useful to be discussed as an extreme case. The different potential thresholds for $^1O_2$ formation obtained from the thermodynamical potentials of the different alkali oxides are compiled in Tab. 2.1 and illustrated in Fig. 2.10. Potassium peroxide being unstable, its value is given only for completeness. The exact potential of the O_2/LiO_2 couple is not known since lithium superoxide is unstable[66]. The O_2/LiO_2 potential was nevertheless estimated around 2.57 V_{Li/Li^+}[66,67].

$$\begin{aligned} &\Delta_r G = n \cdot F \cdot E \qquad \text{in charge} \\ &E_{^1O_2} = E_{^3O_2} + \frac{\Delta_r G(^3O_2 \longrightarrow {}^1O_2)}{n \cdot F} \end{aligned} \tag{2.6}$$

with $\Delta_r G$, the Gibbs energy per mole of reaction (J·mol^{-1}); n, the number of e$^-$ transferred (mol); F, the Faraday constant (96485 C·mol^{-1}); and E, the reaction potential (V).

Table 2.1: **Potential of the O_2/MO_2 and O_2/M_2O_2 redox couples (with M = Li, Na, K) and the thresholds for $^1O_2$ production ($^3O_2/^1O_2$)**

Oxide	Li-O_2 (V_{Li/Li^+})	Na-O_2 (V_{Na/Na^+})	K-O_2 (V_{K/K^+})
superoxide	2.46/3.43[66], 2.61/3.58[67], 2.68/3.65[67]	2.28/3.25[68]	2.48/3.45[69]
peroxide	2.96/3.45[70]	2.33/2.82[68]	2.20/2.69[69]

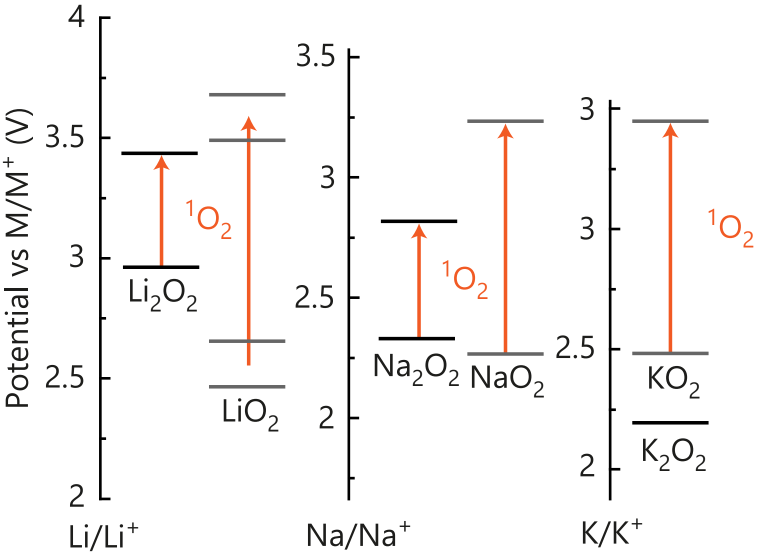

Figure 2.10: **Potential threshold of $^1O_2$ production by alkali oxide oxidation.** The orange arrow represent the 0.97/0.49 eV needed for $^1O_2$ formation via 1 and 2 e$^-$ extraction, respectively. The potential are given in Tab. 2.1.

These potential thresholds correspond to the onset of increased $^1O_2$ formation rate during charge both for Na-O_2 and Li-O_2 seen by in-situ fluorescence, presented in Fig. 2.8, as well as the detection start from in operando EPR[27,52,64]. Electrochemical oxidation of alkali oxides appears to be responsible for the $^1O_2$ formation at high overpotantials; this process is moreover not limited to lithium peroxide and continues with the oxidation of superoxide-like species formed during Li-O_2 cell charge, as discussed in part 1.2.1.2.

2.3.3 Disproportionation as source of singlet oxygen

Singlet oxygen was shown to form at all stages of cycling in Li-air and Na-air batteries, phenomenon that cannot be explained by direct alkali oxide oxidation alone[27,52]. Another reaction releasing oxygen while cycling Li-O_2 and Na-O_2 cells is the superoxide disproportionation towards peroxide, thermodynamically favoured as shown in Fig. 2.10. In agreement with Pearson's hard-soft acid-base concept, harder Lewis acidic cations such as Li$^+$ or Na$^+$ rather form peroxide, albeit with a lower driving force for the latter[49,71,72]. On the other hand, softer acidic Lewis cations such as K$^+$, TBA$^+$, or imidazolium are known to favour superoxide formation[69,73–78]. The relative Lewis acidity of these cations has been determined in literature by ^{13}C-NMR[79].

NaO$_2$ might appear kinetically stable due to the low disproportionation driving force (-12.2 kJ·mol^{-1} [66]), especially considering its enhanced stability during nucleation[80]; the discharge product in Na-O_2 chemistry is then often characterised as superoxide[47,81,82]. Resting of Na-O_2 cells after discharge, yet, showed severe superoxide degradation accompanied by the formation of peroxide and decomposition products such as carbonates, which is illustrated in Fig. 2.11(a)-(b)[49,50,71,72,83,84]. After discharge, resting of a Na-O_2 cathode in the same electrolyte containing in addition 30 mM of DMA exhibited DMA-O_2 formation over time, accompanied by Na$_2$CO$_3$ production. $^1O_2$ oxygen appears to be released during cell resting coinciding with degradation products formation as shown in Fig. 2.11(c)[52].

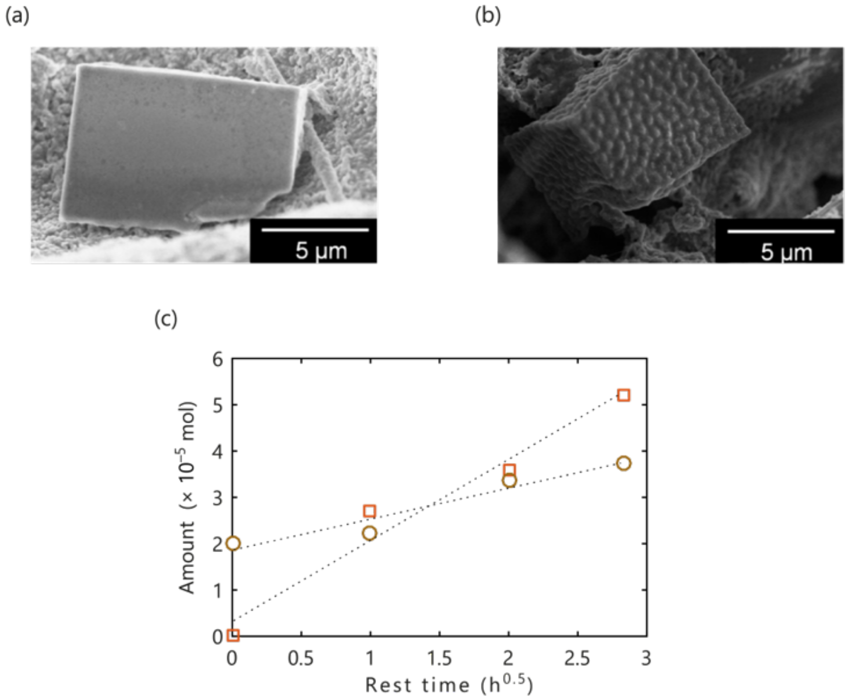

Figure 2.11: **NaO$_2$ degradation at rest.** (a) SEM image of Na-O$_2$ discharge products analysed directly after discharge. (b) SEM images of Na-O$_2$ discharge products analysed after 30 hours resting showing clear surface degradation. (c) DMA-O$_2$ (orange squares) and NaCO$_3$ (brown circles) production overtime during resting in a Na-O$_2$ cell. The cells were first discharged in a 0.5 M NaOTf and 40 ppm H$_2$O diglyme electrolyte. the washed cathodes were immersed in the same electrolyte containing additionally 30 mM DMA for a given amount of time before analysis.

KO$_2$ put in contact with water was shown to result in singlet oxygen production[85]. If KO$_2$ by itself is stable, the addition of protic species to superoxide could induce water assisted disproportionation with H$_2$O$_2$ as intermediate product despite contradictory results[27,52,86]. Poor NaO$_2$ chemical stability and parasitic chemistry at rest might arise partly from the superoxide disproportionation; NaO$_2$ can disporportionate via solvated superoxide despite lower solubility than LiO$_2$[71,72]. A parallel can be drawn between Li-air and Na-air chemistries with the formation of lithium superoxide or superoxide-like species at all stages of cycling.

To verify the production of $^1O_2$ via superoxide disproportionation, we have investigated more in-depth this reaction. Using KO$_2$ as stable superoxide, we modeled the disproportionation reaction in presence of different cations, as presented in Fig. 2.12 and further described in Appendix A.5[3]. We followed the reaction by mass spectrometry in a closed reactor with a headspace continuously purged. Disproportionation was initiated by injecting an electrolyte containing different cations, chosen for their different Lewis acidity (0.03 M DMA and 0.1 M Li$^+$, Na$^+$, K$^+$, or TBA$^+$ in TEGMDE) on a KO$_2$ powder. The electrolyte was further analysed by HPLC after reaction to quantify the $^1O_2$ production, as shown in the insert of Fig. 2.12 and detailed in Appendix A.4. As expected, disproportionation induced by Li$^+$ cations, the harder Lewis acid, quickly releases oxygen and the reaction reaches completion within 2 hours. Na$^+$ electrolyte addition to KO$_2$ powder also produces oxygen albeit at a slower rate and is still in progress after 2 hours. Slower rate is expected considering the lower driving force compare to Li$^+$. As for K$^+$ and TBA$^+$ cations, only negligible oxygen amounts evolve since peroxide formation is unfavoured. Li$^+$ induced disproportionation resulted in 93% $^3O_2$ and 2% $^1O_2$ of the theoretical amount obtain from Eq. 2.7, i.e., 1 mol O$_2$ per 2 mol KO$_2$. The Na$^+$

disproportionation reaches value further from the expected amount, as the reaction did not finish; Only 8% of the KO_2 have reacted of which 12% resulted in $^1O_2$, a higher amount than for Li^+. We found that disproportionation in presence of alkali cations yields significant fractions of $^1O_2$ with its fraction increasing for Na^+ compared to Li^+. K-O_2 cells show improved stability compare to Na-O_2 and Li-O_2, as discussed in part 1.3.2; increased side reactivity correlates hence with the presence of disproportionation and the evolution of $^1O_2$.

$$2\,O_2^{-} \longrightarrow O_2^{2-} + x\,{}^3O_2 + (1-x)\,{}^1O_2 \tag{2.7}$$

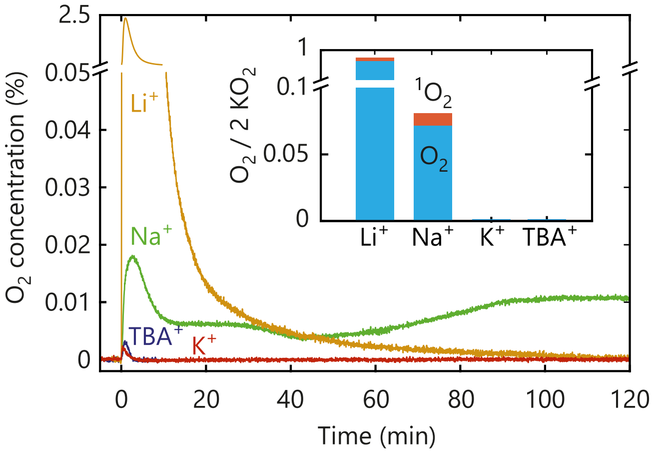

Figure 2.12: **Disproportionation as a source of singlet oxygen.** O_2 evolution induced by disproportionation overtime upon mixing KO_2 with TEGDME electrolytes containing 0.1 M of the indicated cations and 30 mM DMA. The insert shows the amount of evolved $^3O_2$ (as measured by MS) and $^1O_2$ (as measured by HPLC) after a reaction time of 2 hours.

2.3.4 More general importance of singlet oxygen for non-aqueous batteries

Li_2CO_3 is a common by-products in Li-air batteries but also in every organic lithium-based batteries[28,40,46,87,88]. Carbonate oxidation can proceed at potentials observed in Li-air batteries (E^0 = 3.82 V_{Li/Li^+} for Li_2CO_3[89,90]) and are held responsible for the increased overpotential during charge, as discussed in part 1.2.1.3[28,46,48,51,89,91,92]. If Li_2CO_3 oxidation could proceed via Eq. 2.8, only CO_2 release can be detected during Li_2CO_3 decompostion[89–91,93–95]; oxygen release is lacking and has been attributed to superoxide formation[90,93].

$$2\,Li_2CO_3 \longrightarrow 4\;Li^+ + 4\;e^- + 2\;CO_2 + O_2 \tag{2.8}$$

To explain the lack of oxygen release, $^1O_2$ formation instead of the ground state oxygen has been proposed[39]. The absence of oxygen detection could be explained by the singlet oxygen reactivity with cell components. Charging a prefilled electrode with chemical Li_2CO_3 in an electrolyte containing DMA (30 mM DMA and 0.1 M LiTFSI in DME) gave rise to DMA-O_2 formation, indicating $^1O_2$ production, above 3.8 V_{Li/li^+} as shown in Fig. 2.13[39]. The singlet oxygen release corresponds to more than 50% of the theoritical production, from Eq. 2.8, at all stages of charge above 3.8 V_{Li/li^+}; this value represents the low bound since part of the $^1O_2$ might react by other decay routes. As DMA-O_2 is only stable up to approximately 4 V_{Li/li^+}, the reduced $^1O_2$ production observed above 4.05 V_{Li/li^+} can rather be ascribed to DMA-O_2 oxidation[39].

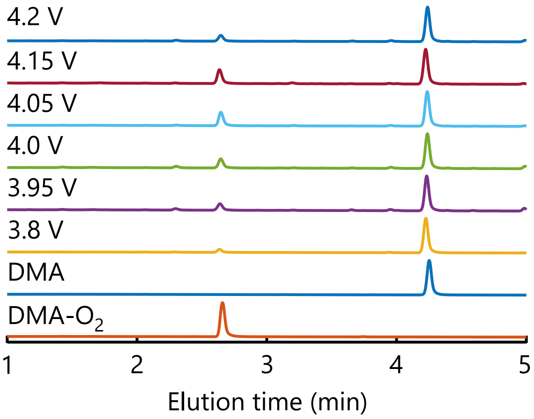

Figure 2.13: **Lithium carbonate oxidation as a source of singlet oxygen, adapted from[39].** The cells composed of a prefilled Li_2CO_3 carbon electrode were charged at a fixed potential to reach 0.64 mA·h in a DME electrolyte containing 0.03 M DMA and 0.1 M LiTFSI. HPLC runs of the electrolyte at different charge potentials show the production of singlet oxygen upon Li_2CO_3 oxidation.

Concurrently to alkali oxide oxidation, $^1O_2$ production at high overpotentials can proceed via carbonate oxidation; more precisely, Li_2CO_3 releases singlet oxygen during its oxidation[39]. As Li_2CO_3 is a common passivation agent, notably formed during the synthesis of transition metal oxides[95], singlet oxygen parasitic chemistry is not confined to metal-air batteries[96,97].

Conclusion

Singlet oxygen, owing to its chemical nature, is a highly reactive species able to degrade the battery components. $^1O_2$ formation is unquestionable in metal-air batteries and has serious mechanistic consequences. By means of adapted analytical methods, our group showed $^1O_2$ presence through all stages of cycling and corroborated the influence of $^1O_2$ on the metal-air cell degradation mechanisms. $^1O_2$ chemical traps stable in metal-air conditions, such as DMA, were shown to quantify the presence of singlet oxygen both in- or ex-situ. The reaction yields can be further determined by pressure monitoring, as the principal reagent/product is a gas (O_2). The missing O_2 evolution can hence at least partially be ascribed to the $^1O_2$ formation that will not be detected in the gas phase due to its reactivity. Finally we show that the reaction products can be quantified with one electrode alone using a combination of UV-vis spectroscopy and mass spectrometry. As the presence of $^1O_2$ can be related to the formation of side products, their characterisations are relevant indicators of its formation.

Using the aforementioned methods, singlet oxygen formation appears as intimately linked to the current discharge and charge mechanisms in metal-air batteries. It can form either directly by (su)peroxide or carbonate oxidation above a given potential threshold or, as proven through the course of this thesis, by superoxide disproportionation. The importance of singlet oxygen goes further than metal-air batteries. Formation of $^1O_2$ by Li_2CO_3 oxidation widens the necessity of $^1O_2$ mitigation means to most of the currently investigated Li-based cathode materials reaching high potentials. The $^1O_2$ formation mechanisms need to be better understood to control its production and to permit realistic cyclability of metal-air redox chemistries.

Reckoning the presence of $^1O_2$ in non-aqueous batteries, the rest of this manuscript will give in-depth mechanistic understanding of $^1O_2$ formation and means to alleviate its consequence which are both outcomes of this thesis. $^1O_2$ formation by alkali oxide or Li_2CO_3 oxidation in metal-air batteries could be avoided for example through the use of adapted catalyst or redox mediators, reducing the applied overpotential. The disproportionation reaction, yet, is spontaneous in Li^+ and Na^+ electrolytes and its mechanistic should be unravelled to understand $^1O_2$ production in metal-air batteries and to possibly bypass it through altered reaction mechanisms.

Bibliography

[1] Y. K. Petit, E. Mourad, and S. A. Freunberger, "Encyclopedia of electrochemistry, section on batteries, ch. 19 lithium–oxygen batteries," in revision.

[2] B. Schafzahl, E. Mourad, L. Schafzahl, Y. K. Petit, A. R. Raju, M. O. Thotiyl, M. Wilkening, C. Slugovc, and S. A. Freunberger, "Quantifying total superoxide, peroxide, and carbonaceous compounds in metal–O_2 batteries and the solid electrolyte interphase," *ACS Energy Letters*, vol. 3, no. 1, pp. 170–176, 2017.

[3] E. Mourad, Y. K. Petit, R. Spezia, A. Samojlov, F. F. Summa, C. Prehal, C. Leypold, N. Mahne, C. Slugovc, O. Fontaine *et al.*, "Singlet oxygen from cation driven superoxide disproportionation and consequences for aprotic metal–O_2 batteries," *Energy & Environmental Science*, vol. 12, no. 8, pp. 2559–2568, 2019.

[4] Y. K. Petit, C. Leypold, N. Mahne, E. Mourad, L. Schafzahl, C. Slugovc, S. M. Borisov, and S. A. Freunberger, "DABCOnium: an efficient and high-voltage stable singlet oxygen quencher for metal–O_2 cells," *Angewandte Chemie International Edition*, vol. 58, no. 20, pp. 6535–6539, 2019.

[5] E. McKeown and W. A. Waters, "The oxidation of organic compounds by "singlet" oxygen," *Journal of the Chemical Society B: Physical Organic*, pp. 1040–1046, 1966.

[6] M. Kasha and A. U. Khan, "The physics, chemistry, and biology, of singlet molecular oxygen," *Annals of the New York Academy of Sciences*, vol. 171, no. 1, pp. 5–23, 1970.

[7] Q. Li, F. Chen, W. Zhao, M. Xu, B. Fang, Y. Zhang, L. Duo, Y. Jin, and F. Sang, "A spectroscopic study on singlet oxygen production from different reaction paths using solid inorganic peroxides as starting materials," *Bulletin of the Korean Chemical Society*, vol. 28, no. 10, pp. 1656–1660, 2007.

[8] P. G. Falkowski, M. E. Katz, A. J. Milligan, K. Fennel, B. S. Cramer, M. P. Aubry, R. A. Berner, M. J. Novacek, and W. M. Zapol, "The rise of oxygen over the past 205 million years and the evolution of large placental mammals," *Science*, vol. 309, no. 5744, pp. 2202–2204, 2005.

[9] J. J. Zimmerman, A. von Saint André-von Arnim, and J. McLaughlin, "Cellular respiration," in *Pediatric Critical Care*, 2011, pp. 1058–1072.

[10] G. Parkin, "Valence, oxidation number, and formal charge: three related but fundamentally different concepts," *Journal of chemical education*, vol. 83, no. 5, p. 791, 2006.

[11] C. A. Coulson, "Representation of simple molecules by molecular orbitals," *Quarterly Reviews, Chemical Society*, vol. 1, no. 2, pp. 144–178, 1947.

[12] I. Levine, *Quantum Chemistry*. Pearson, 2014.

[13] D. Min and J. Boff, "Chemistry and reaction of singlet oxygen in foods," *Comprehensive reviews in food science and food safety*, vol. 1, no. 2, pp. 58–72, 2002.

[14] P. R. Ogilby, "Singlet oxygen: there is indeed something new under the sun," *Chemical Society Reviews*, vol. 39, no. 8, pp. 3181–3209, 2010.

[15] C. Schweitzer and R. Schmidt, "Physical mechanisms of generation and deactivation of singlet oxygen," *Chemical reviews*, vol. 103, no. 5, pp. 1685–1758, 2003.

[16] M. C. DeRosa and R. J. Crutchley, "Photosensitized singlet oxygen and its applications," *Coordination Chemistry Reviews*, vol. 233, pp. 351–371, 2002.

[17] S. Arnold, M. Kubo, and E. Ogryzlo, "Relaxation and reactivity of singlet oxygen," *Adv. Chem. Ser*, vol. 77, pp. 133–142, 1968.

[18] F. Wilkinson, W. P. Helman, and A. B. Ross, "Rate constants for the decay and reactions of the lowest electronically excited singlet state of molecular oxygen in solution. An expanded and revised compilation," *Journal of Physical and Chemical Reference Data*, vol. 24, no. 2, pp. 663–677, 1995.

[19] P. B. Merkel and D. R. Kearns, "Remarkable solvent effects on the lifetime of $^1\Delta_g$ oxygen," *Journal of the American Chemical Society*, vol. 94, no. 3, pp. 1029–1030, 1972.

[20] R. Y. Ho, J. F. Liebman, and J. S. Valentine, "Overview of the energetics and reactivity of oxygen," in *Active Oxygen in Chemistry*. Springer, 1995, pp. 1–23.

[21] H. H. Wasserman and J. L. Ives, "Singlet oxygen in organic synthesis," *Tetrahedron*, vol. 37, no. 10, pp. 1825–1852, 1981.

[22] P. D. Bartlett, G. D. Mendenhall, and A. P. Schaap, "Competitive modes of reaction of singlet oxygen," *Annals of the New York Academy of Sciences*, vol. 171, no. 1, pp. 79–88, 1970.

[23] A. A. Frimer, "The reaction of singlet oxygen with olefins: the question of mechanism," *Chemical Reviews*, vol. 79, no. 5, pp. 359–387, 1979.

[24] E. Clennan and A. Pace, "Advances in singlet oxygen chemistry," *TETRAHEDRON*, vol. 61, pp. 6665–6691, 10 2005.

[25] A. Sagadevan, K. C. Hwang, and M.-D. Su, "Singlet oxygen-mediated selective C–H bond hydroperoxidation of ethereal hydrocarbons," *Nature communications*, vol. 8, no. 1, p. 1812, 2017.

[26] S. A. Freunberger, Y. Chen, N. E. Drewett, L. J. Hardwick, F. Bardé, and P. G. Bruce, "The lithium–oxygen battery with ether-based electrolytes," *Angewandte Chemie International Edition*, vol. 50, no. 37, pp. 8609–8613, 2011.

[27] N. Mahne, B. Schafzahl, C. Leypold, M. Leypold, S. Grumm, A. Leitgeb, G. A. Strohmeier, M. Wilkening, O. Fontaine, D. Kramer *et al.*, "Singlet oxygen generation as a major cause for parasitic reactions during cycling of aprotic lithium–oxygen batteries," *Nature Energy*, vol. 2, no. 5, p. 17036, 2017.

[28] M. M. Ottakam Thotiyl, S. A. Freunberger, Z. Peng, and P. G. Bruce, "The carbon electrode in nonaqueous Li–O_2 cells," *Journal of the American Chemical Society*, vol. 135, no. 1, pp. 494–500, 2012.

[29] V. S. Bryantsev, V. Giordani, W. Walker, M. Blanco, S. Zecevic, K. Sasaki, J. Uddin, D. Addison, and G. V. Chase, "Predicting solvent stability in aprotic electrolyte Li–air batteries: nucleophilic substitution by the superoxide anion radical ($O_2{}^{\cdot-}$)," *The Journal of Physical Chemistry A*, vol. 115, no. 44, pp. 12 399–12 409, 2011.

[30] V. S. Bryantsev and F. Faglioni, "Predicting autoxidation stability of ether-and amide-based electrolyte solvents for Li–air batteries," *The Journal of Physical Chemistry A*, vol. 116, no. 26, pp. 7128–7138, 2012.

[31] K. Chaisiwamongkhol, C. Batchelor-McAuley, R. G. Palgrave, and R. G. Compton, "Singlet oxygen and the origin of oxygen functionalities on the surface of carbon electrodes," *Angewandte Chemie*, vol. 130, no. 21, pp. 6378–6381, 2018.

[32] W.-J. Kwak, H. Kim, Y. K. Petit, C. Leypold, T. T. Nguyen, N. Mahne, P. Redfern, L. A. Curtiss, H.-G. Jung, S. M. Borisov *et al.*, "Deactivation of redox mediators in lithium-oxygen batteries by singlet oxygen," *Nature communications*, vol. 10, no. 1, p. 1380, 2019.

[33] C. M. Marian, "Spin–orbit coupling and intersystem crossing in molecules," *Wiley Interdisciplinary Reviews: Computational Molecular Science*, vol. 2, no. 2, pp. 187–203, 2012.

[34] R. Bonnett, "Photosensitizers of the porphyrin and phthalocyanine series for photodynamic therapy," *Chemical Society Reviews*, vol. 24, no. 1, pp. 19–33, 1995.

[35] S. Borisov, G. Nuss, W. Haas, R. Saf, M. Schmuck, and I. Klimant, "New NIR-emitting complexes of platinum (II) and palladium (II) with fluorinated benzoporphyrins," *Journal of Photochemistry and Photobiology A: Chemistry*, vol. 201, no. 2-3, pp. 128–135, 2009.

[36] S. Nonell and C. Flors, "Steady-state and time-resolved singlet oxygen phosphorescence detection in the near-IR," *Compr Ser. Photoch*, vol. 2, pp. 7–26, 2016.

[37] N. Umezawa, K. Tanaka, Y. Urano, K. Kikuchi, T. Higuchi, and T. Nagano, "Novel fluorescent probes for singlet oxygen," *Angewandte Chemie International Edition*, vol. 38, no. 19, pp. 2899–2901, 1999.

[38] A. Gomes, E. Fernandes, and J. L. Lima, "Fluorescence probes used for detection of reactive oxygen species," *Journal of biochemical and biophysical methods*, vol. 65, no. 2-3, pp. 45–80, 2005.

[39] N. Mahne, S. E. Renfrew, B. D. McCloskey, and S. A. Freunberger, "Electrochemical oxidation of lithium carbonate generates singlet oxygen," *Angewandte Chemie International Edition*, vol. 57, no. 19, pp. 5529–5533, 2018.

[40] B. D. McCloskey, D. S. Bethune, R. M. Shelby, G. Girishkumar, and A. C. Luntz, "Solvents' critical role in nonaqueous lithium–oxygen battery electrochemistry," *The Journal of Physical Chemistry Letters*, vol. 2, no. 10, pp. 1161–1166, 2011.

[41] Z. Peng, S. A. Freunberger, Y. Chen, and P. G. Bruce, "A reversible and higher-rate Li-O_2 battery," *Science*, vol. 337, no. 6094, pp. 563–566, 2012.

[42] Y. Chen, S. A. Freunberger, Z. Peng, F. Bardé, and P. G. Bruce, "Li–O_2 battery with a dimethylformamide electrolyte," *Journal of the American Chemical Society*, vol. 134, no. 18, pp. 7952–7957, 2012.

[43] M. M. Ottakam Thotiyl, S. A. Freunberger, Z. Peng, Y. Chen, Z. Liu, and P. G. Bruce, "A stable cathode for the aprotic Li–O_2 battery," *Nature materials*, vol. 12, no. 11, p. 1050, 2013.

[44] B. D. McCloskey, D. Bethune, R. Shelby, T. Mori, R. Scheffler, A. Speidel, M. Sherwood, and A. Luntz, "Limitations in rechargeability of Li-O_2 batteries and possible origins," *The journal of physical chemistry letters*, vol. 3, no. 20, pp. 3043–3047, 2012.

[45] S. Das, J. Højberg, K. B. Knudsen, R. Younesi, P. Johansson, P. Norby, and T. Vegge, "Instability of ionic liquid-based electrolytes in Li–O_2 batteries," *The Journal of Physical Chemistry C*, vol. 119, no. 32, pp. 18 084–18 090, 2015.

[46] B. D. McCloskey, A. Valery, A. C. Luntz, S. R. Gowda, G. M. Wallraff, J. M. Garcia, T. Mori, and L. E. Krupp, "Combining accurate O_2 and Li_2O_2 assays to separate discharge and charge stability limitations in nonaqueous Li–O_2 batteries," *The journal of physical chemistry letters*, vol. 4, no. 17, pp. 2989–2993, 2013.

[47] P. Hartmann, C. L. Bender, J. Sann, A. K. Dürr, M. Jansen, J. Janek, and P. Adelhelm, "A comprehensive study on the cell chemistry of the sodium superoxide (NaO_2) battery," *Physical Chemistry Chemical Physics*, vol. 15, no. 28, pp. 11 661–11 672, 2013.

[48] B. McCloskey, A. Speidel, R. Scheffler, D. Miller, V. Viswanathan, J. Hummelshøj, J. Nørskov, and A. Luntz, "Twin problems of interfacial carbonate formation in nonaqueous Li–O_2 batteries," *The journal of physical chemistry letters*, vol. 3, no. 8, pp. 997–1001, 2012.

[49] I. Landa-Medrano, R. Pinedo, X. Bi, I. Ruiz de Larramendi, L. Lezama, J. Janek, K. Amine, J. Lu, and T. Rojo, "New insights into the instability of discharge products in Na–O_2 batteries," *ACS applied materials & interfaces*, vol. 8, no. 31, pp. 20 120–20 127, 2016.

[50] R. Black, A. Shyamsunder, P. Adeli, D. Kundu, G. K. Murphy, and L. F. Nazar, "The nature and impact of side reactions in glyme-based sodium–oxygen batteries," *ChemSusChem*, vol. 9, no. 14, pp. 1795–1803, 2016.

[51] S. A. Freunberger, Y. Chen, Z. Peng, J. M. Griffin, L. J. Hardwick, F. Bardé, P. Novák, and P. G. Bruce, "Reactions in the rechargeable lithium–O_2 battery with alkyl carbonate electrolytes," *Journal of the American Chemical Society*, vol. 133, no. 20, pp. 8040–8047, 2011.

[52] L. Schafzahl, N. Mahne, B. Schafzahl, M. Wilkening, C. Slugovc, S. M. Borisov, and S. A. Freunberger, "Singlet oxygen during cycling of the aprotic sodium–O_2 battery," *Angewandte Chemie International Edition*, vol. 56, no. 49, pp. 15 728–15 732, 2017.

[53] A. Kushima, T. Koido, Y. Fujiwara, N. Kuriyama, N. Kusumi, and J. Li, "Charging/discharging nanomorphology asymmetry and rate-dependent capacity degradation in Li–oxygen battery," *Nano letters*, vol. 15, no. 12, pp. 8260–8265, 2015.

[54] C. Yang, J. Han, P. Liu, C. Hou, G. Huang, T. Fujita, A. Hirata, and M. Chen, "Direct observations of the formation and redox-mediator-assisted decomposition of Li_2O_2 in a liquid-cell Li–O_2 microbattery by Scanning Transmission Electron Microscopy," *Advanced Materials*, vol. 29, no. 41, p. 1702752, 2017.

[55] F. Sun, R. Gao, D. Zhou, M. Osenberg, K. Dong, N. Kardjilov, A. Hilger, H. Markötter, P. M. Bieker, X. Liu *et al.*, "Revealing hidden facts of Li anode in cycled lithium–oxygen batteries through X-ray and neutron tomography," *ACS Energy Letters*, vol. 4, no. 1, pp. 306–316, 2018.

[56] Z. Li, S. Ganapathy, Y. Xu, J. R. Heringa, Q. Zhu, W. Chen, and M. Wagemaker, "Understanding the electrochemical formation and decomposition of Li_2O_2 and LiOH with operando X-ray diffraction," *Chemistry of Materials*, vol. 29, no. 4, pp. 1577–1586, 2017.

[57] S. Ganapathy, B. D. Adams, G. Stenou, M. S. Anastasaki, K. Goubitz, X.-F. Miao, L. F. Nazar, and M. Wagemaker, "Nature of Li_2O_2 oxidation in a Li–O_2 battery revealed by operando X-ray diffraction," *Journal of the American Chemical Society*, vol. 136, no. 46, pp. 16 335–16 344, 2014.

[58] J.-L. Shui, J. S. Okasinski, C. Chen, J. D. Almer, and D.-J. Liu, "In operando spatiotemporal study of Li_2O_2 grain growth and its distribution inside operating Li–O_2 batteries," *ChemSusChem*, vol. 7, no. 2, pp. 543–548, 2014.

[59] Y.-C. Lu, E. J. Crumlin, T. J. Carney, L. Baggetto, G. M. Veith, N. J. Dudney, Z. Liu, and Y. Shao-Horn, “Influence of hydrocarbon and CO_2 on the reversibility of Li–O_2 chemistry using in situ ambient pressure X-ray photoelectron spectroscopy,” *The Journal of Physical Chemistry C*, vol. 117, no. 49, pp. 25 948–25 954, 2013.

[60] F. S. Gittleson, W.-H. Ryu, and A. D. Taylor, “Operando observation of the gold–electrolyte interface in Li–O_2 batteries,” *ACS applied materials & interfaces*, vol. 6, no. 21, pp. 19 017–19 025, 2014.

[61] J. P. Vivek, N. G. Berry, J. Zou, R. J. Nichols, and L. J. Hardwick, “In situ surface-enhanced infrared spectroscopy to identify oxygen reduction products in nonaqueous metal–oxygen batteries,” *The Journal of Physical Chemistry C*, vol. 121, no. 36, pp. 19 657–19 667, 2017.

[62] R. Wen, M. Hong, and H. R. Byon, “In situ AFM imaging of Li–O_2 electrochemical reaction on highly oriented pyrolytic graphite with ether-based electrolyte,” *Journal of the American Chemical Society*, vol. 135, no. 29, pp. 10 870–10 876, 2013.

[63] J. Hassoun, F. Croce, M. Armand, and B. Scrosati, “Investigation of the O_2 electrochemistry in a polymer electrolyte solid-state cell,” *Angewandte Chemie International Edition*, vol. 50, no. 13, pp. 2999–3002, 2011.

[64] J. Wandt, P. Jakes, J. Granwehr, H. A. Gasteiger, and R.-A. Eichel, “Singlet oxygen formation during the charging process of an aprotic lithium–oxygen battery,” *Angewandte Chemie International Edition*, vol. 55, no. 24, pp. 6892–6895, 2016.

[65] N. B. Aetukuri, B. D. McCloskey, J. M. García, L. E. Krupp, V. Viswanathan, and A. C. Luntz, “Solvating additives drive solution-mediated electrochemistry and enhance toroid growth in non-aqueous Li–O_2 batteries,” *Nature chemistry*, vol. 7, no. 1, p. 50, 2015.

[66] C. L. Bender, P. Hartmann, M. Vraar, P. Adelhelm, and J. Janek, “On the thermodynamics, the role of the carbon cathode, and the cycle life of the sodium superoxide (NaO_2) battery,” *Advanced Energy Materials*, vol. 4, no. 12, p. 1301863, 2014.

[67] S. Kang, Y. Mo, S. P. Ong, and G. Ceder, “A facile mechanism for recharging Li_2O_2 in Li–O_2 batteries,” *Chemistry of Materials*, vol. 25, no. 16, pp. 3328–3336, 2013.

[68] C. L. Bender, D. Schröder, R. Pinedo, P. Adelhelm, and J. Janek, “One-or two-electron transfer? The ambiguous nature of the discharge products in sodium–oxygen batteries,” *Angewandte Chemie International Edition*, vol. 55, no. 15, pp. 4640–4649, 2016.

[69] X. Ren and Y. Wu, “A low-overpotential potassium–oxygen battery based on potassium superoxide,” *Journal of the American Chemical Society*, vol. 135, no. 8, pp. 2923–2926, 2013.

[70] B. D. McCloskey, R. Scheffler, A. Speidel, G. Girishkumar, and A. C. Luntz, “On the mechanism of nonaqueous Li–O_2 electrochemistry on C and its kinetic overpotentials: some implications for Li–air batteries,” *The Journal of Physical Chemistry C*, vol. 116, no. 45, pp. 23 897–23 905, 2012.

[71] C. Sheng, F. Yu, Y. Wu, Z. Peng, and Y. Chen, “Disproportionation of sodium superoxide in metal–air batteries,” *Angewandte Chemie*, vol. 130, no. 31, pp. 10 054–10 058, 2018.

[72] J. Kim, H. Park, B. Lee, W. M. Seong, H.-D. Lim, Y. Bae, H. Kim, W. K. Kim, K. H. Ryu, and K. Kang, “Dissolution and ionization of sodium superoxide in sodium-oxygen batteries,” *Nature communications*, vol. 7, p. 10670, 2016.

[73] W. Wang, N.-C. Lai, Z. Liang, Y. Wang, and Y.-C. Lu, "Superoxide stabilization and a universal KO_2 growth mechanism in potassium–oxygen batteries," *Angewandte Chemie International Edition*, vol. 57, no. 18, pp. 5042–5046, 2018.

[74] Y. Chen, Z. P. Jovanov, X. Gao, J. Liu, C. Holc, L. R. Johnson, and P. G. Bruce, "High capacity surface route discharge at the potassium-O_2 electrode," *Journal of Electroanalytical Chemistry*, vol. 819, pp. 542–546, 2018.

[75] L. Johnson, C. Li, Z. Liu, Y. Chen, S. A. Freunberger, P. C. Ashok, B. B. Praveen, K. Dholakia, J.-M. Tarascon, and P. G. Bruce, "The role of LiO_2 solubility in O_2 reduction in aprotic solvents and its consequences for Li–O_2 batteries," *Nature chemistry*, vol. 6, no. 12, p. 1091, 2014.

[76] C. O. Laoire, S. Mukerjee, K. Abraham, E. J. Plichta, and M. A. Hendrickson, "Elucidating the mechanism of oxygen reduction for lithium-air battery applications," *The Journal of Physical Chemistry C*, vol. 113, no. 46, pp. 20 127–20 134, 2009.

[77] C. J. Allen, J. Hwang, R. Kautz, S. Mukerjee, E. J. Plichta, M. A. Hendrickson, and K. Abraham, "Oxygen reduction reactions in ionic liquids and the formulation of a general ORR mechanism for Li–air batteries," *The Journal of Physical Chemistry C*, vol. 116, no. 39, pp. 20 755–20 764, 2012.

[78] C. V. Amanchukwu, H.-H. Chang, M. Gauthier, S. Feng, T. P. Batcho, and P. T. Hammond, "One-electron mechanism in a gel–polymer electrolyte Li–O_2 battery," *Chemistry of Materials*, vol. 28, no. 19, pp. 7167–7177, 2016.

[79] K. Abraham, "Electrolyte-directed reactions of the oxygen electrode in lithium-air batteries," *Journal of The Electrochemical Society*, vol. 162, no. 2, pp. A3021–A3031, 2015.

[80] S. Kang, Y. Mo, S. P. Ong, and G. Ceder, "Nanoscale stabilization of sodium oxides: implications for Na–O_2 batteries," *Nano letters*, vol. 14, no. 2, pp. 1016–1020, 2014.

[81] P. Hartmann, C. L. Bender, M. Vraar, A. K. Dürr, A. Garsuch, J. Janek, and P. Adelhelm, "A rechargeable room-temperature sodium superoxide (NaO_2) battery," *Nature materials*, vol. 12, no. 3, p. 228, 2013.

[82] N. Ortiz-Vitoriano, T. P. Batcho, D. G. Kwabi, B. Han, N. Pour, K. P. C. Yao, C. V. Thompson, and Y. Shao-Horn, "Rate-dependent nucleation and growth of NaO_2 in Na–O_2 batteries," *The journal of physical chemistry letters*, vol. 6, no. 13, pp. 2636–2643, 2015.

[83] T. Liu, G. Kim, M. T. Casford, and C. P. Grey, "Mechanistic insights into the challenges of cycling a nonaqueous Na–O_2 battery," *The journal of physical chemistry letters*, vol. 7, no. 23, pp. 4841–4846, 2016.

[84] S. Y. Sayed, K. P. Yao, D. G. Kwabi, T. P. Batcho, C. V. Amanchukwu, S. Feng, C. V. Thompson, and Y. Shao-Horn, "Revealing instability and irreversibility in nonaqueous sodium–O_2 battery chemistry," *Chemical Communications*, vol. 52, no. 62, pp. 9691–9694, 2016.

[85] A. U. Khan, "Direct spectral evidence of the generation of singlet molecular oxygen ($^1\Delta_g$) in the reaction of potassium superoxide with water," *Journal of the American Chemical Society*, vol. 103, no. 21, pp. 6516–6517, 1981.

[86] J. Aubry, J. Rigaudy, C. Ferradini, and J. Pucheault, "Search for singlet oxygen in the disproportionation of superoxide anion," *Journal of the American Chemical Society*, vol. 103, no. 16, pp. 4965–4966, 1981.

[87] K. Xu, "Electrolytes and interphases in Li-ion batteries and beyond," *Chemical reviews*, vol. 114, no. 23, pp. 11 503–11 618, 2014.

[88] P. Verma, P. Maire, and P. Novák, "A review of the features and analyses of the solid electrolyte interphase in Li-ion batteries," *Electrochimica Acta*, vol. 55, no. 22, pp. 6332–6341, 2010.

[89] W. Yin, A. Grimaud, F. Lepoivre, C. Yang, and J. M. Tarascon, "Chemical vs electrochemical formation of Li_2CO_3 as a discharge product in Li–O_2/CO_2 batteries by controlling the superoxide intermediate," *The journal of physical chemistry letters*, vol. 8, no. 1, pp. 214–222, 2016.

[90] S. Yang, P. He, and H. Zhou, "Exploring the electrochemical reaction mechanism of carbonate oxidation in Li–air/CO_2 battery through tracing missing oxygen," *Energy & Environmental Science*, vol. 9, no. 5, pp. 1650–1654, 2016.

[91] S. R. Gowda, A. Brunet, G. Wallraff, and B. D. McCloskey, "Implications of CO_2 contamination in rechargeable nonaqueous Li–O_2 batteries," *The journal of physical chemistry letters*, vol. 4, no. 2, pp. 276–279, 2012.

[92] J. Højberg, B. D. McCloskey, J. Hjelm, T. Vegge, K. Johansen, P. Norby, and A. C. Luntz, "An electrochemical impedance spectroscopy investigation of the overpotentials in Li–O_2 batteries," *ACS applied materials & interfaces*, vol. 7, no. 7, pp. 4039–4047, 2015.

[93] Z. Zhao, J. Huang, and Z. Peng, "Achilles' heel of lithium–air batteries: Lithium carbonate," *Angewandte Chemie International Edition*, vol. 57, no. 15, pp. 3874–3886, 2018.

[94] S. Meini, N. Tsiouvaras, K. U. Schwenke, M. Piana, H. Beyer, L. Lange, and H. A. Gasteiger, "Rechargeability of Li–air cathodes pre-filled with discharge products using an ether-based electrolyte solution: implications for cycle-life of Li–air cells," *Physical Chemistry Chemical Physics*, vol. 15, no. 27, pp. 11 478–11 493, 2013.

[95] S. E. Renfrew and B. D. McCloskey, "Residual lithium carbonate predominantly accounts for first cycle CO_2 and CO outgassing of Li-stoichiometric and Li-rich layered transition-metal oxides," *Journal of the American Chemical Society*, vol. 139, no. 49, pp. 17 853–17 860, 2017.

[96] T. Hatsukade, A. Schiele, P. Hartmann, T. Brezesinski, and J. Janek, "Origin of carbon dioxide evolved during cycling of nickel-rich layered NCM cathodes," *ACS applied materials & interfaces*, vol. 10, no. 45, pp. 38 892–38 899, 2018.

[97] J. Wandt, A. T. Freiberg, A. Ogrodnik, and H. A. Gasteiger, "Singlet oxygen evolution from layered transition metal oxide cathode materials and its implications for lithium-ion batteries," *Materials Today*, vol. 21, no. 8, pp. 825–833, 2018.

Cation influence on $^1O_2$ induced by disproportionation

For many centuries chemists labored to change lead into precious gold, and eventually found that precious uranium turned to lead without any human effort at all.
Isaac Asimov

Contents

Figures

Chapter based on Mourad, Petit et al.[1]

Introduction

Singlet oxygen presence in metal-air batteries has been established in the previous chapter. Considering its high reactivity, $^1O_2$ can be ascribed as a culprit for the severe parasitic reactions encountered in metal-air technologies. While singlet oxygen can be produced by direct oxidation of alkali oxide, it was also found during discharge in Li-O_2 cells and upon resting after discharge in Na-O_2 cells. Superoxide disproportionation, directly related to the formation of lithium and sodium peroxide as illustrated in Fig. 3.1, produce singlet oxygen. Disproportionation occurrence at all stages of cycling correspond well to the side reaction pattern observed. A sizeable part of the metal-air cell cyclability issue could hence be imputed to disproportionation. This reaction is indeed the only known mechanism capable of producing $^1O_2$ during discharge or at rest in Li/Na-O_2 chemistry.

The relationship of superoxide disproportionation with side reactivity imposes a strive to understand its underlying chemical mechanism. Disproportionation was already consider as a crucial process in lithium-air batteries through the so-called solution mechanism which is described in part 1.2.1.1. As (su)peroxides are insulating solids, they can quickly passivate the electrode surface, reducing the achievable capacities. Disproportionation allows for peroxide formation in solution resulting in higher capacities. A consequence is the search for enhanced solution pathway by the choice of electrolyte or additives use. Yet, $^1O_2$ production by disproportionation imposes a certain plight to the technology and only unravelling more in-depth mechanistic descriptors for this reaction will enable to unlock the full potential of metal-air batteries.

Disproportionation, as a chemical process, is greatly influenced by the media. In part 1.2.1.1, it was shown that the solvent or additives influence superoxide disproportionation by stabilizing its solvated state. Concerning $^1O_2$ production, we observed a higher singlet oxygen yield with Na^+ than with Li^+ in part 2.3.3, despite Na^+ lower Lewis acidity. The cations appear thus to have a strong influence on $^1O_2$ production induced by disproportionation.

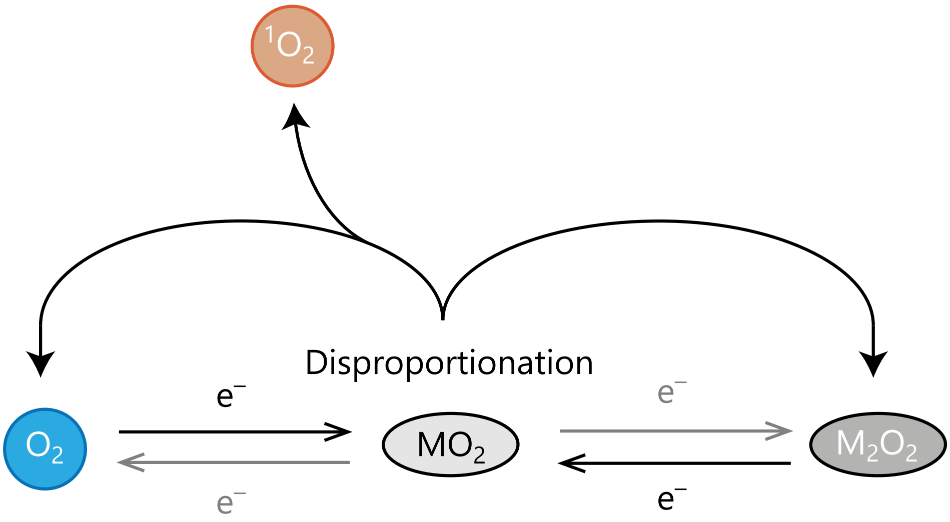

Figure 3.1: **Illustration of the disproportionation process in Li/Na-O_2 cells and the induced $^1O_2$ production.**

To decipher the cation influence on the disproportionation reaction, we put in place mechanistic descriptors confirmed both experimentally and by calculations. To do so, we first studied the disproportionation reaction of chemically produced solvated superoxide in presence of different cations and their influences. As the cation's Lewis acidity governs the disproportionation driving force (formation of solid peroxide), the cations studied covers a large range of Lewis acidity used in metal-air batteries such as alkali cations or typical ionic liquid cations. The results confirm that inversely to the driving force, the $^1O_2$ production increases with the presence of soft Lewis acid. While weakly Lewis acidic cations themselves would not drive superoxide disproportionation, their presences together with the strongly Lewis acidic Li^+ and Na^+ markedly increase $^1O_2$ formation.

Density functional theory (DFT) calculations were conducted in collaboration with Sapienza University to understand the reaction pathways in presence of different cations. As disproportionation evolves through LiO_2 clusters formation, here strictly modelled by dimers, these clusters can be formed in the singlet state with a certain energy cost. The presence of soft Lewis acidic cations appears to reduce the activation energy to the singlet state routes, enhancing the proportion of $^1O_2$ compared to $^3O_2$.

Li-O_2 cells were analysed further during discharge and charge to verify the presence of the disproportionation process as well as the influence of cations during actual cell cycling. The consumption/production of O_2 clearly showed presence of disproportionation and its influence on side product formation. The presence of weak Lewis acids increased the formation of carbonates on discharge where $^1O_2$ is produced by disproportionation in higher proportion. Presence of disporoportionation in metal-air cells has serious consequences, notably on electrolyte, additives and aimed discharge products that will be discussed more in-depth.

3.1 Disproportionation of chemically produced solvated superoxide

As disproportionation is a spontaneous chemical reaction, it can be studied outside a cell by means of the stable potassium superoxide as a chemical superoxide source. To characterise disproportionation chemistry, solvated superoxide occurs as a better proxy than KO_2 powder to avoid possible surface chemistry effects. KO_2 can be solvated by crown ether (such as 18-crown-6 or 1,4,7,10,13,16-hexaoxacyclooctadecane) in TEGDME[2]. In a similar fashion than discussed in part 2.3.3, disproportionation reactions could be characterised by the amount of $^3O_2$/$^1O_2$ release as well as Li_2O_2/Na_2O_2 yield and carbonate production. The disproportionation was driven by injecting TEGDME based electrolytes containing different cations into solvated KO_2. The reaction yield and carbonate amount were determined by coupling mass spectrometry and UV-vis spectroscopy after complete reaction according to the oxygen release, as described in Appendices A.5 and A.6.

The O_2, $^1O_2$, peroxide and carbonate productions via dissolved superoxide disproportionation in presence of different cations are given in Fig. 3.2. With the addition of a Li^+ electrolyte, the reaction yields similar amount of $^3O_2$ and $^1O_2$ than with solid KO_2 shown in part 2.3.3, i.e. ~93%$^3O_2$, ~2% $^1O_2$ and a correspondant ~93% peroxide. A Na^+ electrolyte addition gives in turn similar results than on solid KO_2, i.e., ~83%$^3O_2$, ~13% $^1O_2$ and a ~85% peroxide yield as the reaction reached completeness. Simulating proton sources by adding 0.1 M trifluoroacetic acid (F_3CCOOH) as additive to the lithium electrolyte, singlet oxygen production presents a slight increase with ~91% $^3O_2$/peroxide yields and ~3% $^1O_2$. Albeit shallow, this $^1O_2$ increase might indicate water assisted disproportionation and partly explain the increased $^1O_2$ production in Li-air cell with the addition of water[3].

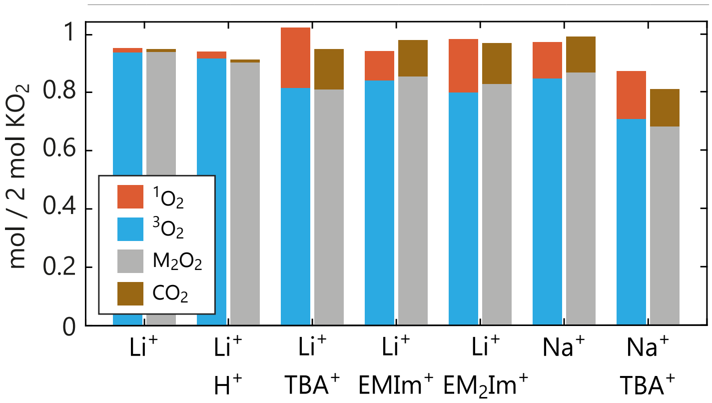

Figure 3.2: **O_2, $^1O_2$, peroxide, and carbonate productions via solvated superoxide disproportionation.** Solvated peroxide in TEGDME is obtained by mixing KO_2 powder in presence of an 18-crown-6 ether equimolar ratio in solution. To drive disproportionation and quantify singlet oxygen, a TEGDME electrolyte composed of 30 mM DMA, 0.5 M Li^+/Na^+ and either no additives, 0.1 M TBA^+, $EMIm^+$, EM_2Im^+ or F_3CCOOH is added to the dissolved O_2^-. The scale represent the theoretical yield of 1 mol O_2 and peroxide per 2 mol of KO_2 according to Eq. 2.7. The errors of the obtained values can be found in Appendix B.2.1

Rather than only testing pure Li^+ or Na^+ electrolytes, salt combinations to drive superoxide disproportionation in presence of soft Lewis acids were also tested. The chosen organic cations cover a different range of Lewis acidity, namely in descending Lewis acidity $EMIm^+$, EM_2Im^+, and TBA^+[4]. As described in parts 1.3.2 and 2.1.2, superoxide and singlet oxygen are prone to react with organic species and their stability was assessed beforehand. TBA^+

is known to be stable in contact with superoxide[5,6]. Imidazolium salt stabilities towards superoxide were tested by ^{1}H-NMR before and after 1 hour contact either with KO_2 powder or photochemically produced singlet oxygen according to Appendix A.3. On the one hand, the cations showed good stability towards singlet oxygen, as illustrated in Fig. 3.3(b)-(d). Singlet oxygen, being electrophile, appears mainly active towards electron-rich species[7]. On the other hand, imidazoliums are unstable with KO_2 with the appearance of decomposition products in the ^{1}H-NMR spectra as shown in Fig. 3.3(a)-(c). These results are in agreement with previous reports of instability[8].

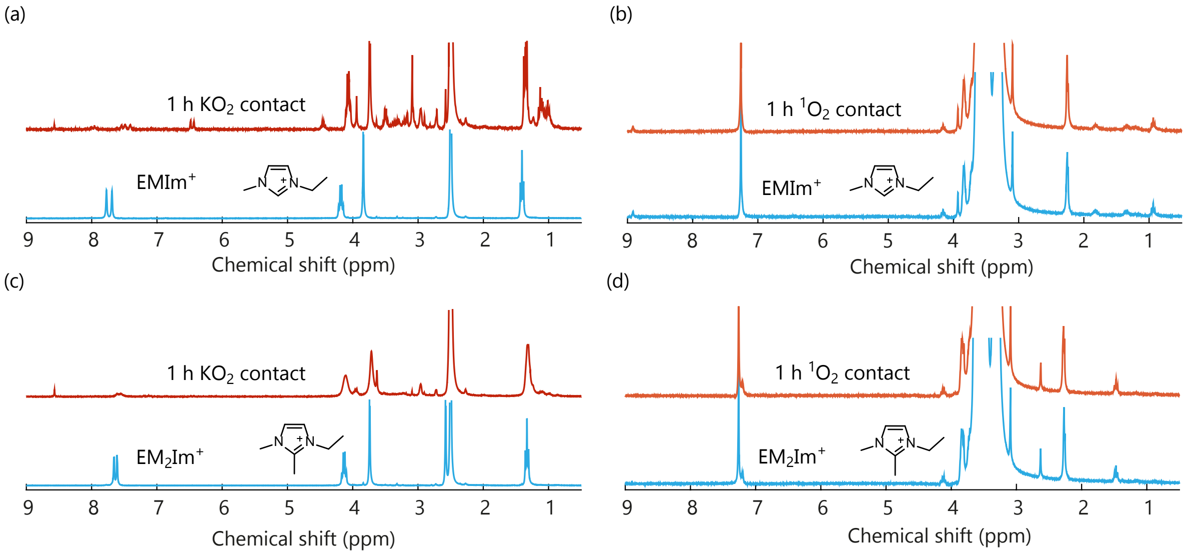

Figure 3.3: **The stability of imidazoliums in presence of KO_2 and $^1O_2$ by ^{1}H-NMR.** The spectra were recorded in $CDCl_3$. The first line characterises EMIm$^+$ and the second line EM$_2$Im$^+$. (a) and (c) show ^{1}H-NMR spectra of imidazoliums before and after 1 hour contact with KO_2 dissolved in TEGDME, in blue and red respectively. (b) and (d) show ^{1}H-NMR spectra of imidazoliums before and after 1 hour contact with $^1O_2$ in O_2 saturated TEGDME, in blue and orange respectively. $^1O_2$ was produced photochemically, according to a previously described method[3] and further described in Appendix A.3, by means of 1 μM Pd$_4$F and illumination at 643 nm.

Tertiary amines are known as $^1O_2$ quenchers that physically deactivate (quench) $^1O_2$ to $^3O_2$[9]. By their chemical nature, imidazoliums could partially quench singlet oxygen and reduce the detected amount by DMA-O_2 formation. At low imidazolium concentrations, the quenching effect is not expected to be significant as the amine quenching efficiency decreases with the oxidation potential of the species[9–11]; at high concentration, imidazolium salt showed an appreciable quenching effect. As a token of quenching efficiency, the consumption of DMA was measured by UV-vis spectroscopy in presence of photochemically produced $^1O_2$ with or without quencher addition. Competing reactions between the quencher and DMA with $^1O_2$ leads to a slower DMA consumption rate which indicates a good quenching efficiency compared to DMA reactivity. More details of this method are given in Appendix A.7. As shown in Fig. 3.4, 0.1 M EMIm$^+$ in TEGDME results in a much slower DMA decay than without additives. Hence, the amount of $^1O_2$ quenched during the experiment cannot be neglected. Imidazolium experiments were still conducted, keeping in mind that the $^1O_2$ yields presented are underestimated and a part of the side reactions induced by their instability with superoxide.

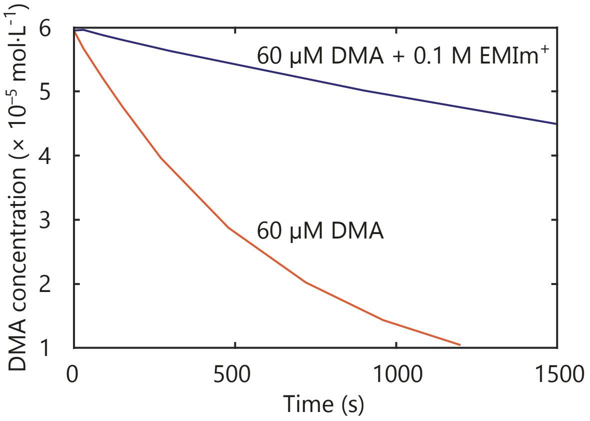

Figure 3.4: **$^1O_2$ quenching effect of imidazolium cation.** In orange, DMA concentration decay over time in presence of photochemically produced $^1O_2$ according to Appendix A.7. In purple, DMA concentration decay over time in presence of photochemically produced $^1O_2$ and 0.1 M $EmIm^+$. The decrease of the DMA reaction rate indicates other $^1O_2$ decay pathways such as quenching by $EMIm^+$. The electrolytes used were based on 60 µM DMA and 1 µM Pd_4F in TEGDME illuminated at 643 nm.

Disproportionation in presence of weak Lewis acidic cations enhanced noticeably the production of $^1O_2$ in Fig. 3.2. For Li^+ electrolyte, the value decreased to reaction yields close to the pure Na^+ electrolyte with ~80–85% yields for $^3O_2$ and Li_2O_2 accompanied by a growth of $^1O_2$ and carbonate yields (~10–20%). Mixture of Na^+ and TBA^+ results in a similar trends; $^3O_2$ and Na_2O_2 yields decreases to ~70% while $^1O_2$ reached ~16%. This similar trend with TBA^+ suggests that the presence of weaker Lewis acidic cations during disproportionation drives $^1O_2$. In any case, the increase of $^1O_2$ is always accompanied by an increase in carbonates, hence side product formation, as well as a decrease in $^3O_2$ and peroxide yields; these yields are moreover similar. The missing peroxide and the side-product formation appears well connected to the formation of $^1O_2$ as suggested before[3,12].

Disproportionation characterisations in presence of the different counter anions used in this study ($TFSI^-$ and ClO_4^-) show a similar trend for the same cations, as depicted in Fig. 3.5. The influence of the anions is then disregarded in the rest of this chapter since they possess rather similar acceptor numbers and should not affect the result conclusions[13,14], as discussed in part 1.2.1.1.

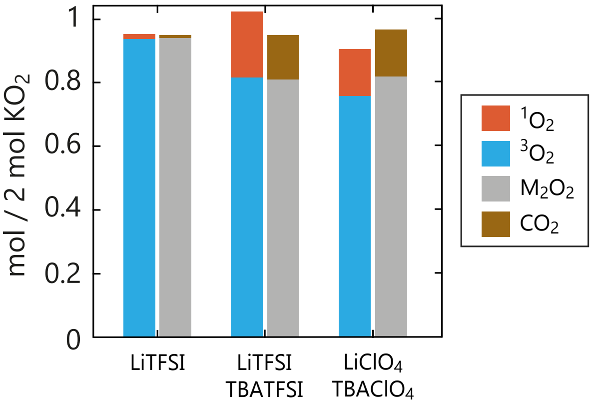

Figure 3.5: **Influence of the anions used during this study of disproportionation.** O_2, $^1O_2$, peroxide and carbonate productions via dissolved superoxide disproportionation using electrolytes with different counter anions. Dissolved peroxide in TEGDME is obtained by mixing KO_2 powder in presence of an 18-crown-6 ether equimolar ratio in solution. The electrolyte injected to drive disproportionation is either 0.5 M LiTFSI, or 0.2 M Li^+/TBA^+ (5:1 ratio) with $TFSI^-$ or ClO_4^- as counter ions. Despite the slight variance of the detected amounts, the same conclusion can be drawn upon cation influence.

3.2 Thermodynamic aspects of the cation influence

Weak Lewis acidic cations drive $^1O_2$ production; the reaction mechanism must thus be influenced by the cations present. To understand the relative disproportionation energies and their underlying reaction pathways, DFT calculations were performed. The different routes to $^3O_2$ and $^1O_2$ were scrutinized in presence of LiO_2 and NaO_2 as starting materials in presence of H^+, TBA^+, K^+ or Li^+/Na^+ respectively.

Energies were calculated for solvated species using the continuous C-PCM solvation model with a mean dielectric constant of $\epsilon = 7.28$ (resembling that of glyme as previously done[15]) and using the hybrid GGA DFT M06-2X functional. More details on the calculation method can be found in Appendix B.1. As disproportionation passes via at least formation of dimers over superoxide monomers[6,16,17], different pathways might arise through the formation of different superoxide dimer $M(O_2)_2M'$ (M being Li^+ or Na^+, and M' being Li^+, Na^+, K^+, H^+ or TBA^+). The dimers consequently release a O_2 molecule and a peroxide. After ion exchanges, which enegies can be found in Tab. B.1, M_2O_2 is obtained and precipitates as solid peroxide. The overall driving force is, in this case, the formation of solid M_2O_2(s) as previously shown in the case of Li chemistry both in gas and liquid phase[6,16] and illustrated in Fig. 3.6. As a side note, the calculations presented here presuppose that only superoxide dimers will be formed as a first approximation. The formation and disproportionation of more complex superoxide clusters might be favoured at longer terms and change the energy difference but the energy tendencies were hypothesised to be similar[17].

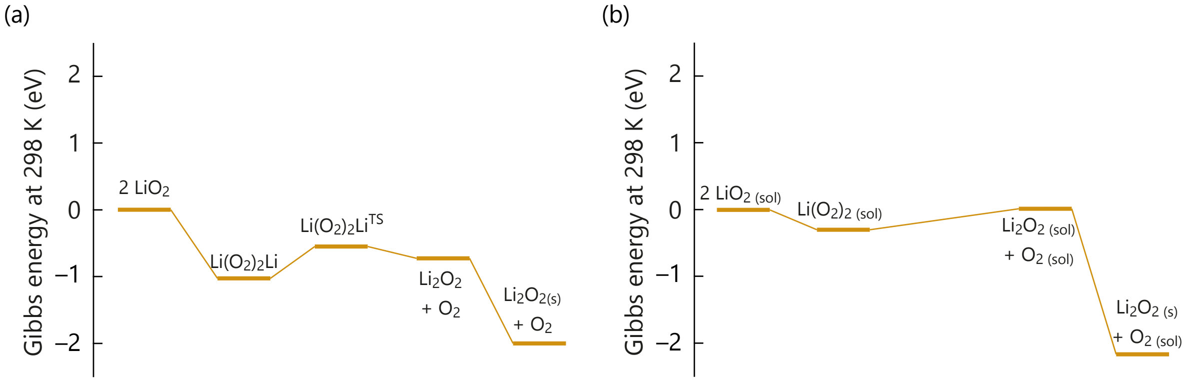

Figure 3.6: **Literature reported reaction free energy profiles for $^3O_2$ release from LiO_2 disproportionation in the gas phase[16] or solution phase[6].** The reaction pathways are adapted from the two previously cited publications. If unspecified (either solvated or solid state), the species are in the gas phase. As indicated by the energy profiles, the overall reaction driving force is the largely favoured peroxide precipitation.

As superoxide dimers can have different configurations[16], only the most stable structures collected after calculation will be considered in the following chapter. The considered dimer configurations are given in Fig. 3.7 and Tab. B.2. The reaction energies are presented taking the more favoured pure solvated alkali superoxide as reference (2 LiO_2 or 2 NaO_2). The energetic influence of cation additions and the new reaction pathways are more easily comparable with such scales. As discussed in part 1.3.2, activation energies beyond 1 eV (100 kJ.mol^{-1}) are considered to be sufficiently high to ensure low reaction kinetic at room temperature.

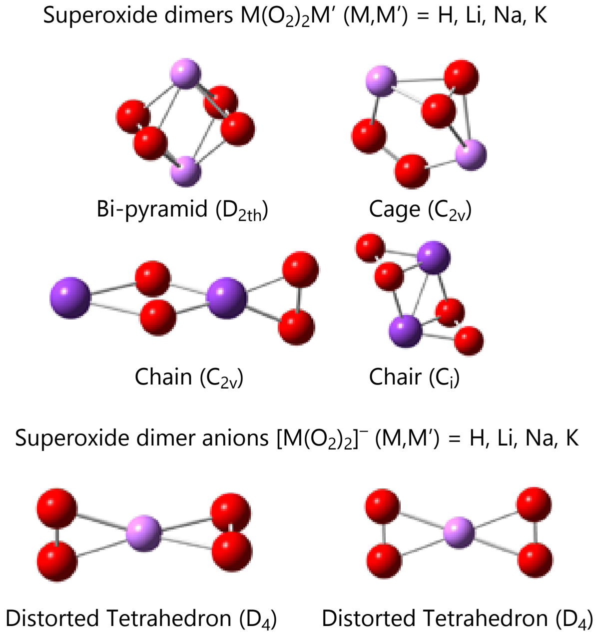
Superoxide dimers $M(O_2)_2M'$ (M,M') = H, Li, Na, K

Bi-pyramid (D_{2th}) Cage (C_{2v})

Chain (C_{2v}) Chair (C_i)

Superoxide dimer anions $[M(O_2)_2]^-$ (M,M') = H, Li, Na, K

Distorted Tetrahedron (D_4) Distorted Tetrahedron (D_4)

Figure 3.7: **Computed structures of neutral and negatively charge superoxide dimers ($M(O_2)_2M'$ and $M(O_2)_2^-$) with M and M' being H, Li, Na or K.**

The present model rests on superoxide dimer formations either in a triplet state or a singlet state, releasing $^3O_2$ and $^1O_2$ respectively, during disproportionation. The most simple pathway is the one of a pure Li^+ or Na^+ electrolyte presented in Fig. 3.8 and Fig. 3.9, in yellow and green respectively. The dimerization free energies are given in Tab. B.3 for the different cations. The pathway resulting in triplet oxygen with LiO_2 is similar to the one already accepted from literature and showed in Fig. 3.6(b)[6]. First, a $^3Li(O_2)_2Li$ dimer is form due to a slight stabilization compared to two LiO_2 monomers. The dimer then disproportionate in Li_2O_2 and $^3O_2$ in a second step despite being weakly endergonic by means of a strong driving force to precipitate and form the stabilized solid Li_2O_2 as a final product, as given in Tab. 3.1. Now considering the singlet oxygen pathway for pure Li^+ electrolyte, the consecutive steps are similar but the energy profile differently distributed. The most unfavourable step is the $^1Li(O_2)_2Li$ dimer formation with a ~1 eV thermodynamic barrier, the reaction being favourable for the rest of the reaction up to the formation Li_2O_2. The ~1 eV activation energy leads to a small formation occurrence despite the strongly favoured overall disproportionation.

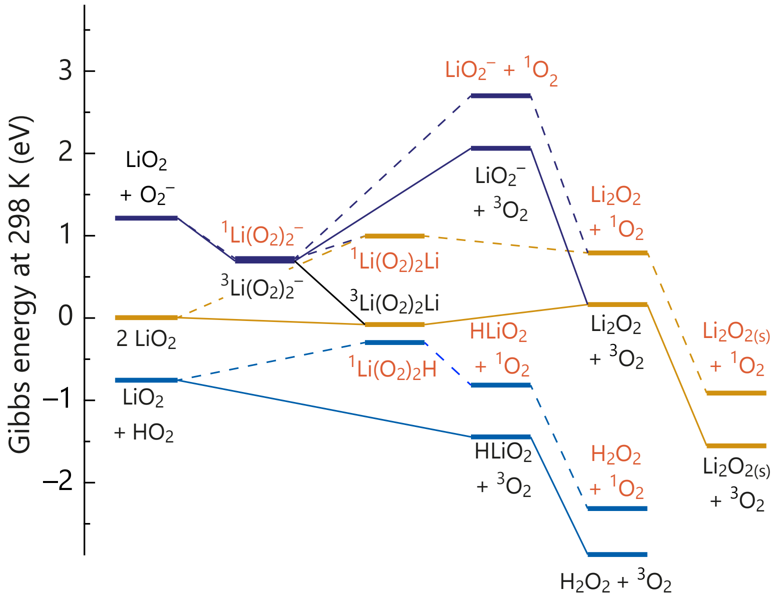

Figure 3.8: **Calculated free energy profiles for superoxide disproportionation in presence of Li⁺ and H⁺ traces.** The reaction forms peroxide and O_2, either in singlet (dashed line) or triplet state (full line). More details about the calculations can be found in Appendix B.1.

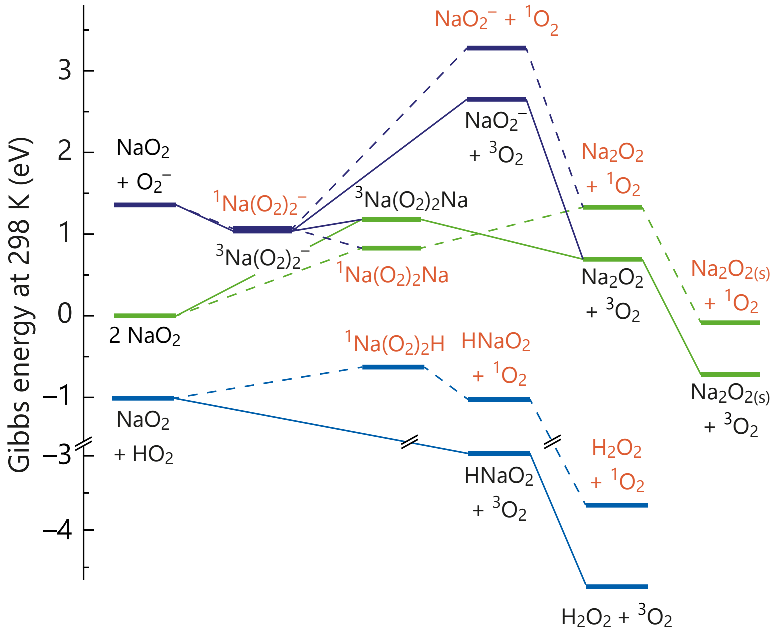

Figure 3.9: **Calculated free energy profiles for superoxide disproportionation in presence of Na⁺ and H⁺ traces.** The reaction forms peroxide and O_2, either in singlet (dashed line) or triplet state (full line). More details about the calculations can be found in Appendix B.1.

Table 3.1: **Precipitation free energy of solid alkali peroxides from solution phase at 298 K.**

Peroxide	$\Delta_r G^0_{298\,K}$ (eV)
$Li_2O_{2(solvated)} \longrightarrow Li_2O_{2(solid)}$	−1.71
$Na_2O_{2(solvated)} \longrightarrow Na_2O_{2(solid)}$	−1.40
$K_2O_{2(solvated)} \longrightarrow K_2O_{2(solid)}$	−2.31

Considering NaO_2, the overall disproportionation process results also in product stabilizations although less than for LiO_2. The dimer formation is, yet, energy costly for NaO_2 in both triplet and singlet states. Nevertheless, the singlet dimer is less endergonic than the triplet state with 0.83 eV compared to a 1.2 eV barrier. The $^1O_2$ disproportionation step is, however, unfavoured by 0.5 eV while $^3O_2$ release is exergonic by −0.5 eV. The total energy needed for Na^+ disproportionation towards $^1O_2$ is then more exergonic by ~0.1 eV compared to $^3O_2$. NaO_2 disproportionation is highly depend on the solvent use[18]. Solvated NaO_2 appears almost kinetically stable in high DN solvents while it disproportionates relatively fast in low DN solvents. A low DN solvent stabilize less the superoxide in solution as described in part 1.2.1.1 and might rise the solvated NaO_2 energy, decreasing at the same time the energy difference with the dimer formation. The endergonicity of the dimer formations for NaO_2 could partly explain its relative stability in Na-O_2 cells[19].

The experimental differences observed between LiO_2 and NaO_2 are in accord with the calculated single step barriers and overall driving forces. The low activation energy for LiO_2 results in fast disproportionation kinetic and low amount of $^1O_2$ due to the strong energy barrier difference between the singlet and triplet pathways. While NaO_2 singlet and triplet have more similar energy barriers, causing larger $^1O_2$ release, the comparably high exergonic character of sodium superoxide disproportionation imposes a slower reaction rate. The high driving force due to solid peroxide formation allows relatively high energy barrier to be overcome and form singlet oxygen by disproportionation.

The addition of protons opens new highly favoured disproportionation pathways in Li^+ electrolyte, as shown in Fig. 3.8. The HO_2 formation is by itself favoured and leads to the mixed $HLiO_2$ peroxide accompanied by a release of $^3O_2$ without forming an intermediate dimer; the reaction results in the more stable H_2O_2. Even though one might consider 2 HO_2 as a preferable state compared to mixed superoxides, H^+ is considered here as a contaminant in presence of a large Li^+ excess. The singlet reaction path still requires the $^1Li(O_2)_2H$ dimer formation via a 0.46 eV barrier, which releases $HLiO_2$ and $^1O_2$ in a −0.52 eV exergonic step that continue downhill to reach H_2O_2. Analogous results were obtained for the NaO_2–HO_2 pairing as illustrated in Fig. 3.9. As singlet path is exergonic, albeit less than for Li^+/Na^+ alone, and the triplet path highly favourable, only minor yields of $^1O_2$ can be expected by water induced disproportionation. This is in accord with experimental findings in Fig. 3.2, which shows very light additional $^1O_2$ production with proton traces compared to pure Li^+ electrolyte.

Disproportionation induces more $^1O_2$ production in presence of the weak Lewis acid TBA^+ as shown in Fig. 3.2 and Fig. 3.5. The main developed hypothesis is based on the weaker O_2^-–TBA^+ interaction than O_2^-–M^+ ($M = Li^+$ or Na^+)[5,20,21]; the asymmetric pairing of superoxide would destabilize intermediates, reduce the energy barriers, and hence make $^1O_2$ production more favourable. Computing the asymmetric $Li(O_2)_2TBA$ would be extremely difficult because of the large number of electrons. Considering the weak association of the O_2^-–TBA^+ ion pair even in low dielectric constant solvents like DME ($\Delta_{diss}G^0 = 0.44$ eV), $TBAO_2$ may be at first approximated by the free solvated O_2^- anion. O_2/LiO_2 and $O_2/TBAO_2$ standard potentials in DME differs by 1.24 V[21], which agrees well with the estimated 1.21 eV for the dissociation energy of LiO_2 to free O_2^- anions, as given in Tab. B.1. O_2^- does not have to form via dissociation of LiO_2 which would not result in appreciable O_2^- concentration; O_2^- may form as a transient species upon O_2^- generation before the initially formed O_2^- binds with Li^+[5,22]. O_2^- exist in Li^+/TBA^+ mixtures even in low DN solvent as MeCN, where LiO_2 dissociates particularly poorly[5]. In more strongly solvating electrolytes such as DMSO, O_2^- lifetime is long enough in 0.1 M Li^+, TBA^+ free, electrolyte to allow for some reversiblility to the O_2/O_2^- couple. Glyme used in this study lies between MeCN and DMSO in terms of

LiO_2 solvation strength. The Fig. 3.2 shows well that TBA^+ strongly impact disproportionation in mixtures with Na^+ or Li^+ and must hence influence the O_2^- binding states.

The DFT calculations shown in Fig. 3.8 and Fig. 3.9 confirm the suggested destabilizing mechanism, in presence of Li^+ and Na^+. The first step for Li^+ proceeds via formation of $^3Li(O_2)_2^-$ or $^1Li(O_2)_2^-$ dimers that are stabilized to a close value versus $LiO_2 + O_2^-$, -0.52 eV and -0.49 eV, respectively. Ongoing disproportionation pathways to the charged LiO_2^- peroxide species would face prohibitively high energy barriers in either states because of the large Li_2O_2 dissociation energy to $LiO_2^- + Li^+$. Yet, a more facile pathway is possible, as a $Li(O_2)_2^-$ dimer can easily proceed to an ion exchange to form a $Li(O_2)_2Li$ dimer. The disproportionation can then continue through the pure lithium disproportionation mechanism described previously. If the reaction route is then similar to that of a pure Li^+ electrolyte, the presence of TBA^+ decreases the barrier towards $^1O_2$; in any case, the most endergonic step is $^1Li(O_2)_2Li$ formation which pass from ~1 eV to a mere 0.27 eV in the case of the charged dimer. The proportion to each pathway is not given by the energy difference between $^1Li(O_2)_2Li$ and $^3Li(O_2)_2Li$, but the largest barrier in the respective free energy profiles; the smaller $^1Li(O_2)_2Li$ formation energy result in an acceleration of the singlet path. Analogously, the asymmetric $NaO_2 + O_2^-$ pairing passes via $Na(O_2)_2^-$ and $Na(O_2)_2Na$ dimers and the barrier towards $^1O_2$ decreases from 1.2 eV to 0.4 eV. The weak Lewis acid TBA^+ opens paths that facilitate the most unfavourable reaction steps and hence strongly enhance $^1O_2$ production.

Several recent works have proposed mixed alkali cation electrolytes for metal-O_2 cells to influence solution equilibria and possibly improve cell characteristics[23–27]. For completeness, LiO_2 with KO_2 as well as NaO_2 with KO_2 or LiO_2 disproportionation pathways have been calculated and are respectively illustrated in Fig. 3.10, Fig. 3.11 and Fig. 3.12. The asymmetric intermediates and peroxide products (LiO_2Na, NaO_2K, and LiO_2K) are not likely compared to the symmetric pathways. Disproportionation of mixed dimers is less favourable since more exergonic; Li_2O_2 or Na_2O_2 production will hence more likely involves ion exchange towards the stronger Lewis acid and further proceed via the symmetric cases described earlier.

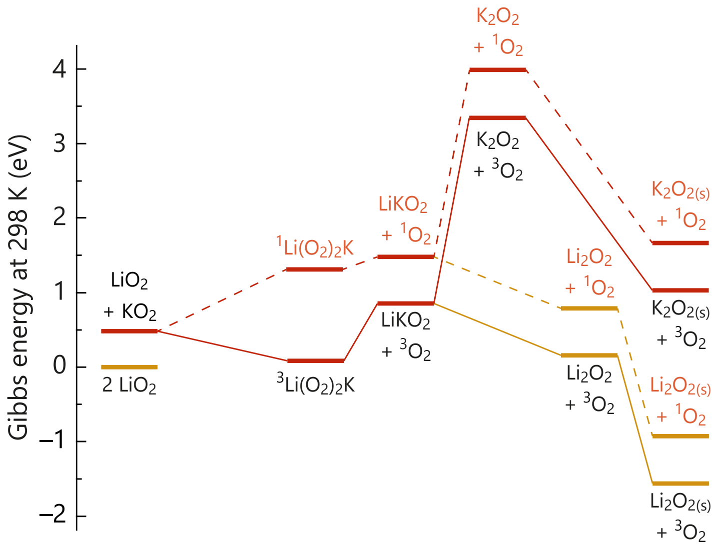

Figure 3.10: **Calculated free energy profiles for superoxide disproportionation in the presence of Li^+ and K^+.** The reaction forms peroxide and O_2, either in singlet (dashed line) or triplet state (full line). More details about the calculations can be found in Appendix B.1.

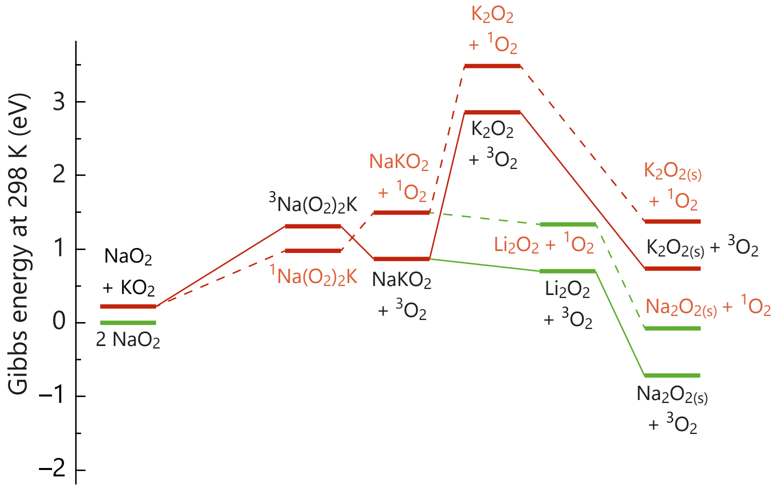

Figure 3.11: **Calculated free energy profiles for superoxide disproportionation in the presence of Na^+ and K^+.** The reaction forms peroxide and O_2, either in singlet (dashed line) or triplet state (full line). More details about the calculations can be found in Appendix B.1.

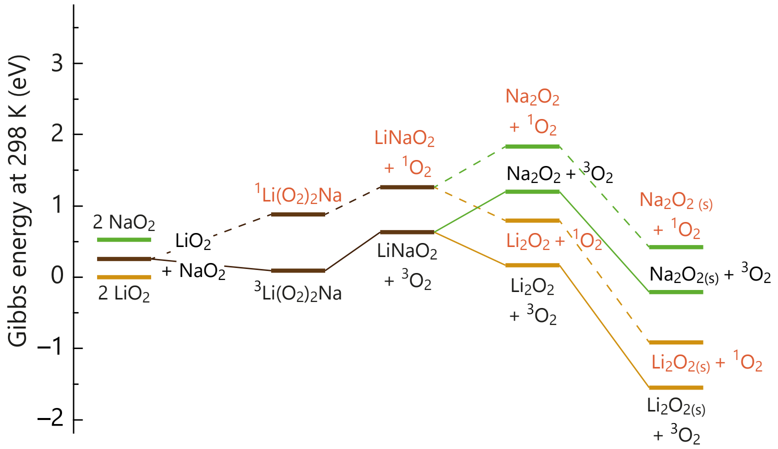

Figure 3.12: **Calculated free energy profiles for superoxide disproportionation in the presence of Li^+ and Na^+.** The reaction forms peroxide and O_2, either in singlet (dashed line) or triplet state (full line). More details about the calculations can be found in Appendix B.1.

3.3 Disproportionation during Li-O_2 cell cycling

Both chemical studies and DFT calculations show that $^1O_2$ production can be induced by superoxide disproportionation and is strongly enhance in the presence of weakly Lewis acidic cations. This phenomenon remains to be proven during cell operations. The reaction yield and $^1O_2$ as well as carbonate production have hence been characterised during Li-O_2 cell cycling with either pure Li^+ electrolyte or Li^+/TBA^+ mixtures. Li-O_2 chemistry was chosen since disproportionation is most significantly driven by thermodynamics in this case, as shown in fig. 2.12. The cells are composed of carbon black cathodes and TEGDME electrolytes containing 30 mM DMA with either only 0.1 M Li^+ or a total of 1 M salt with a Li^+/TBA^+ ratio of 1:9 or 1:99. The emphasis is put on TBA^+ as weak Lewis acid since it avoids the further complications of imidazolium instability with O_2^-.

3.3.1 Discharge

Considering first discharge, the cells were run at constant current and the gas consumption followed using a pressure transducer as shown in Fig. 3.13(a)-(b). The method is further described in Appendix A.2, assuming that the only gas varying is oxygen[28]. $^1O_2$, Li_2O_2, and carbonates were quantified after electrolyte and cathode extraction by a HPLC, MS and UV-vis spectroscopy combination as described in Appendices A.4, A.5 and A.6. The values are expressed in mol per 2 mol e^- passed in fig 3.13(c); An ideal reaction yields/consumes 1 mol Li_2O_2/O_2 per 2 mol e^- according to Eq. 2.7.

Discharge in pure Li^+ electrolyte resulted in a ratio of 1.98 e^-/O_2 in Fig. 3.13(a), close to the ideal ratio of 2 e^-/O_2, and a Li_2O_2 yield of 94%, both in accord with previous reports for similar cells[29] [28] [30] [31]. The $^1O_2$ yield is $\sim$ 3% and hence similar to the one found by chemical disproportionation with a similar electrolyte, illustrated in Fig. 3.2. Using a mixed electrolyte with Li^+:TBA^+ ratio of 1:9 (1:99), the reaction yield remarkably decreases in Fig. 3.13(a)-(b); The e^-/O_2 ratio and Li_2O_2 yield dropped to 1.74 (1.70) and 85% (81%), respectively. As the Li_2O_2 yield decreases, the amount of $^1O_2$ and carbonate follow an inverse trend which correlate well with the presence of $^1O_2$ and side reactions. Increasing $^1O_2$ yield together with decreasing Li_2O_2 yield as the electrolyte is changed from Li^+ to a Li^+/TBA^+ mixture mirrors the results obtain with dissolved superoxide in Fig. 3.2. The increase presence of TBA^+ results in a higher $TBAO_2$ occurrence and so $^1O_2$ production due to facilitate formation mechanism.

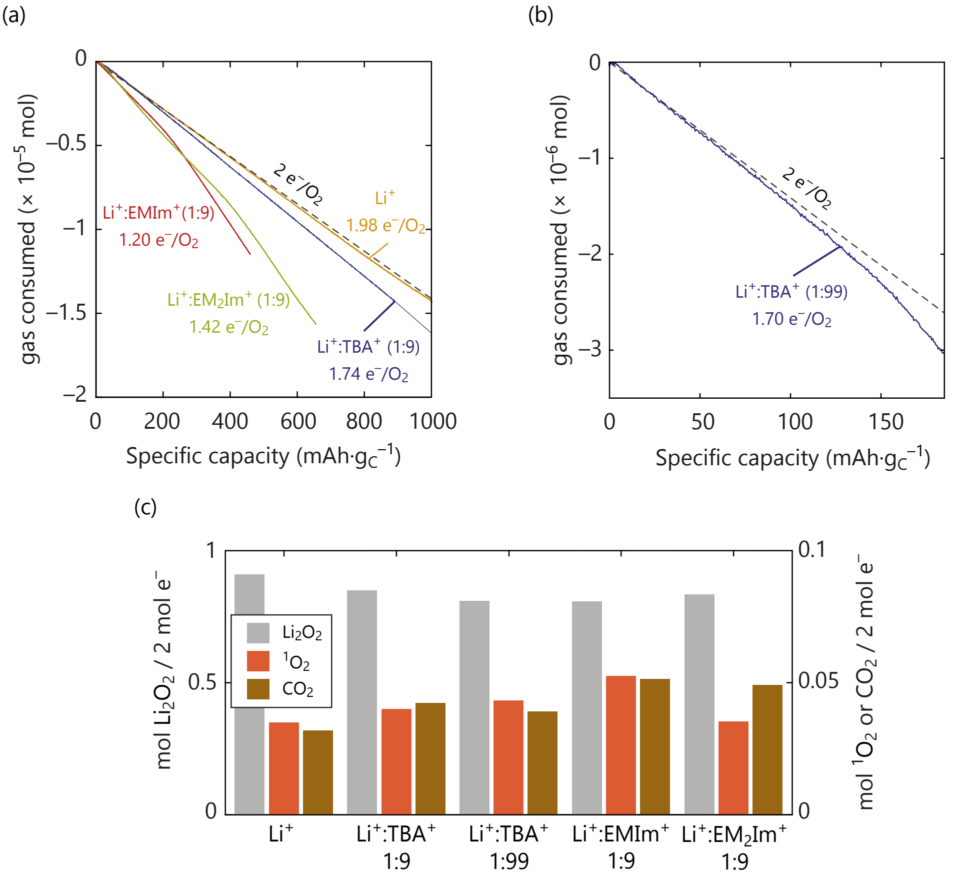

Figure 3.13: **Disproportionation and the influence of the cations during Li-O_2 cell discharges.** (a)-(b) Gas evolution during a Li-O_2 cell discharge with a carbon black cathode and LFP counter electrode at 100 mA·$g_c{}^{-1}$. The O_2 saturated TEGDME elecrolytes used are composed of 30 mM DMA and the studied cations. The dashed line represent the theoretical 2 e^-/O_2. (a) 0.1 Li^+ or a combined 1 M salt of Li^+/TBA^+, $Li^+/EMIm^+$, Li^+/EM_2Im^+ (1:9 ratio) and (b) Li^+/TBA^+ (1:99 ratio). (c) O_2, $^1O_2$, peroxide and carbonate productions during discharge of the aforementioned cells. The discharge curves associated can be found in Fig. B.2.

Deviation of the $e^-/{}^3O_2$ ratio from 2 does not necessarily arise from $^1O_2$; side reactions with the cations can also act as a O_2^- sink, preventing alkali peroxide formation. Discharge with imidazolium cations instead of TBA^+ (1:9 ratio) further corroborates their instability with lower e^-/O_2 ratios, 1.42 and 1.2 for EM_2Im^+ and $EMIm^+$, respectively. A part of the stronger deviation compared to TBA^+ can be attributed to the O_2^- reaction with the imidazolium cations, even though the $^1O_2$ still increase compare to pure Li^+ electrolyte. Given the known stability of TBA^+ with O_2^-, as discussed earlier, a direct reaction can be excluded as the sink causing the decrease to 1.74 (1.70) e^-/O_2. Instead, the lower ratio is in accord with TBA^+ enhancing the $^1O_2$ fraction from O_2^- disproportionation. The $^1O_2$ cannot be detected by the pressure transducer as it will react before.

The results during discharge are in good agreement with the chemical experiments presented in Fig. 3.2, which have shown that O_2^- disproportionation partly releases $^1O_2$ and that the $^1O_2$ fraction increases with the presence of weakly Lewis acidic cations such as TBA^+. Overall, the results indicate O_2^- disproportionation as the source of $^1O_2$ on discharge in Li-O_2 cells and at rest in Na-O_2 cells.

3.3.2 Charge

Intermediate $Li_{2-x}O_2$ or soluble superoxide species are produced during charge in Li-O_2 cells, as discussed in part 1.2.1.2[32–34]. They might undergo disproportionation to form Li_2O_2 and O_2. Through the same mechanism than during discharge, disproportionation induced $^1O_2$ could be formed and influenced by the cations present. To avoid influence of side products that would be formed at different rate during discharge depending on the electrolyte used, working electrodes filled with chemically produced Li_2O_2 were produced according to Appendix A.1. Similarly to discharge, the cells build with prefilled electrode were charged at constant current with TEGDME electrolytes that contained 30 mM DMA and either only Li^+ (0.1 M) or a Li^+/TBA^+ mixture (0.1:0.9 M). The $^3O_2$ and $^1O_2$ yields were measured by pressure monitoring and DMA conversion by HPLC after extraction as in part 3.3.1, assuming that the large majority of released gas is oxygen[28,30,35]. An ideal reaction yields 1 mol O_2 per 2 mol e^- according to Eq. 2.7 and as for discharge the value are expressed consequently in Fig. 3.14(e)-(f).

The charge voltage was first limited to 3.95 V_{Li/Li^+} since this voltage was reported to be the upper limit for quasi-equilibrium decomposition in TEGDME for similarly prefilled working electrodes[33]. Charge in pure Li^+ electrolyte shows high side reactivity with a 2.40 e^-/O_2 yield in Fig. 3.14(a), corresponding to ~83% of the expected O_2 evolution based on the charge passed, in good agreement with previous study[29–31]. This $^3O_2$ loss is accompanied by $^1O_2$ detection which can partially be accounted for side reactions. Changing for a Li^+/TBA^+ electrolyte in Fig. 3.14(c), Li_2O_2 oxidation drift even more from the theoritical yield with a 2.95 e^-/gas ratio and hence only ~68% of the expected O_2. Roughly doubled missing $^3O_2$ evolution goes along with the $^1O_2$ amount being more than doubled. Cells restricted to 3.45 V_{Li/Li^+} were also charged to exclude the possibility of $^1O_2$ evolution from a direct Li_2O_2 oxidation above ~3.5 V_{Li/Li^+}, as described in part 2.3.2. Albeit reduced sensitivity due to the lower capacity passed, similar trends are observed for both $^3O_2$ and $^1O_2$, as shown in Fig. 3.14(b)-(d).

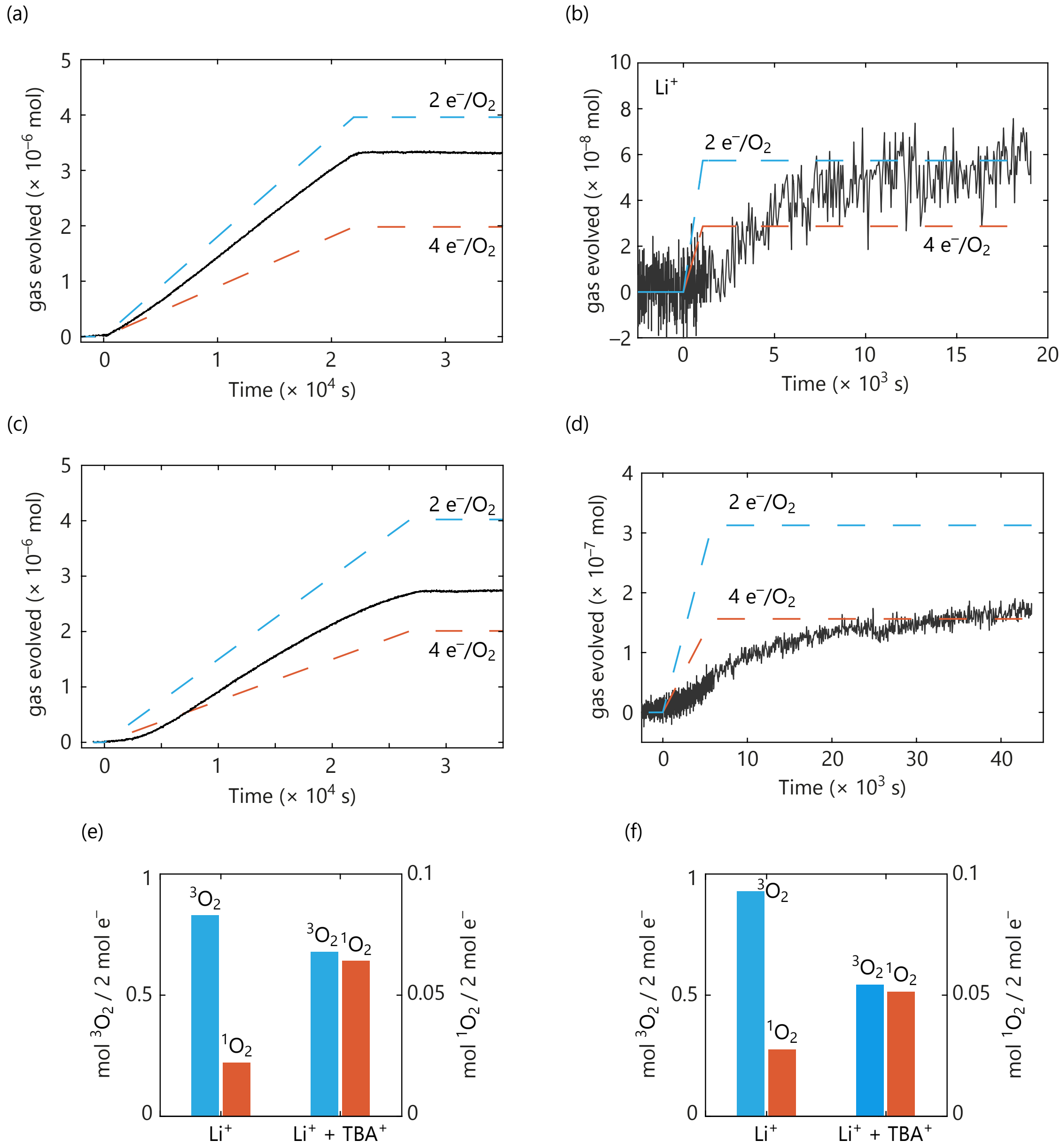

Figure 3.14: **Disproportionation and the influence of the cations during Li-O_2 cell charges.** (a)-(d) Gas evolution during a Li-O_2 cell charge. The O_2 saturated TEGDME elecrolytes used are composed of 30 mM DMA and 0.1 M Li^+ on the first row ((a)-(b)) or a combined 1 M salt of Li^+/TBA^+ (1:9 ratio) on the second row ((c)-(d)). The prefilled carbon black cathodes with chemically produced Li_2O_2 are charged at 10 mA·g_c^{-1} until reaching a cut off voltage of either 3.95 V_{Li/Li^+} ((a) and (c)) or 3.45 V_{Li/Li^+} ((b) and (d)). After charge, the cells were kept at open circuit voltage until pressure stabilization. The blue dashed lines represent the theoretical 2 e^-/O_2 and the orange ones 4 e^-/O_2. (e)-(f) O_2, $^1O_2$, peroxide and carbonate productions during discharge of the aforementioned cells either up to 3.95 V_{Li/Li^+} (e) or 3.45 V_{Li/Li^+} (f). The charge curves associated can be found in Fig. B.2.

3.3.3 Mechanistic consequences of disproportionation

Altogether, the DFT calculations, as well as chemical and electrochemical experiments show that superoxide disproportionation, driven by the higher stability of the peroxide with strong Lewis acids, generates in part $^1O_2$. Additional presence of weakly Lewis acidic cations increases the $^1O_2$ yield. As $^1O_2$ cannot be produced by direct oxidation below ~3.5 V_{Li/Li^+} in Li-O_2

cells, $^1O_2$ production below this potential threshold indicates disproportionation reaction, especially when influenced by the presence of weak Lewis acid such as TBA^+. Taken as an indicator for disproportionation, the presence of $^1O_2$ at all stages of cycling have sizeable consequences on the reaction mechanism in metal-air batteries, particularly on the second step pathways.

The correlation between missing $^3O_2$ evolution and the $^1O_2$ yield influenced by weakly Lewis acidic cations during discharge shows that a substantial part of the Li_2O_2 formation proceeds via disproportionation. As discussed in part 1.2.1.1, the disproportionation is favoured by solvents with high DN number and strongly coordinating Li^+ counter ions[36–38]. Disproportionation is, yet, occurring even with weakly coordinating anions or medium DN solvent, e.g, $TFSI^-$ and TEGDME. It is hence a crucial mechanism during discharge, especially at low overpotentials[5,39]. On Au(111) in DMSO, the calculated free energy of absorbed superoxide shows disproportionation to dominate direct reduction of superoxide to peroxide above 2 V_{Li/Li^+}[6].

As TBA^+ addition results in a continuous deviation from the $2e^-/O_2$ ratio in discharge, it could indicate that solvated superoxide is present at non negligeable concentration even at relatively high overpotentials as ion exchange with TBA^+ is unlikely according to Tab. B.1. At high overpotentials, absorbed superoxide could be formed by supersaturation at the vicinity of the electrode, especially in relatively low DN number solvent. Solid superoxide facilitated formation by supersaturation was already proposed for the formation of the less soluble NaO_2 and hinted as influence at high overpotentials in Li-O_2 chemistry[39–41]. The supersaturation effect could explain absence or low detection of solvated superoxide independently of the solvent used[5,39] and the $TBAO_2$ formation through all the discharge. A consequence of supersaturation would be an enhanced disproportionation rate at high overpotentials in the electrode vicinity, reducing solvated superoxide concentration far away from the electrode and its detection in solution.

Concerning the charge, the presence of $^1O_2$ below 3.5 V_{Li/Li^+} implies disproportionation to take place during charge in TEGDME. Formation of soluble superoxide and subsequent disproportionate was shown during charge in high DN number[33]. Soluble superoxide was yet not detected in lower DN solvent as TEGDME. As Li_2O_2 oxidation proceeds first via progressive delithiation as presented in part 1.2.1.2, the superoxide-like species formed were hypothesised to disproportionate[42]. Since PITT showed a quasi-equilibrium potential around 3.5 - 3.96 V_{Li/Li^+} in glymes[33,42], oxygen evolution must proceed via disproportionation at least for early stages of charge. The influence of TBA^+ on the $^1O_2$ yield seems to indicate at least partially soluble superoxide in vicinity of the electrode during charge even in TEGDME despite the absence of superoxide detection afar from the electrode.

Superoxide disproportionation is then a source for $^1O_2$ and parasitic chemistry during all steps of cell cycling in Li-O_2 cells. NaO_2 is also susceptible to disproportionate albeit at slower rate due to its lower driving force and solubility[41]. NaO_2 is yet subject to severe degradation and peroxide formation at rest which was correlated with $^1O_2$ release as discussed in part 2.3.3. Singlet oxygen at rest can arises by NaO_2 disproportionation, which also induces side reactions in Na-O_2 cells. Only KO_2 does not undergo disproportionation. The disproportionation reaction at least partially explains the higher stability of K-O_2 chemistry, especially in complete absence of protons[43], compared to lithium and sodium cells as discussed in part 1.3.2. Disproportionation is therefore an important process to understand side reactivity in metal-air batteries.

3.4 Direct consequences of singlet oxygen induced by disproportionation

Since $^1O_2$ formation is deeply rooted in the way current metal–O_2 cells operate, it has serious consequences on cell design, notably on the electrolyte. Weak Lewis acids are proposed as additives to enhance the solution mechanism, resulting in higher capacity as described in part 1.2.1.1[44,45]. Caution must be exercised with such additives as they could likewise drive $^1O_2$ production. The selected quaternary ammonium and imidazolium cations are prototypical motifs for the cations used so far in ionic liquid electrolytes for metal–O_2 cells, as discussed in part 1.2.3[8]. Imidazoliums can be ruled out as metal-O_2 electrolytes since they readily decompose with superoxide. As ionic liquid cations suitable for electrolytes are most typically weak Lewis acids, the effect can likely be generalized considering that the organic cations would boost $^1O_2$ production[8]. Favoured $^1O_2$ formation explains why quantitative studies of metal–O_2 chemistry with a broad variety of ionic liquids have shown worse parasitic chemistry on discharge and charge than molecular electrolytes, as described in part 1.2.3[30,46,47]. Protic additives drive $^1O_2$ formation insignificantly but may drive parasitic chemistry in other ways as by reacting with intermediate decomposition products. This is in accord with reports that found increased side reactions when water or other Brønsted acids were added[29,48,49].

Considering the discharge products itself, superoxide presence should be avoided as it favoures disproportionation in presence of Li^+ and Na^+ which leads to cell degradations through $^1O_2$ release. Cells based on metastable LiO_2 or NaO_2 have been proposed to reduce the cell overpotential[19,50]. Their practical feasibility faces high disproportionation rate during either low rate cycling or at rest since superoxides gradually convert to peroxide and side products over time.[18,41,51–54]. Lithium and sodium peroxide which are the thermodynamically stable products, as illustrated in Fig. 2.10 and Tab. 2.1, should be preferred. Peroxide based chemistry does not, however, prevent disproportionation during cycling; reaction pathways by-passing the superoxide formation step need to be developed. Solution to the disproportionation issue could be provided by catalyst on charge which stabilize superoxide-like cluster[55].

Conclusion

To conclude, we described a $^1O_2$ formation route at all stages of cycling and consequently a substantial reason for parasitic chemistry in non-aqueous metal–O_2 cells. We have shown that alkali superoxide disproportionation forms $^1O_2$ and detailed the underlying mechanistic pathways and its repercussions on metal-O_2 chemistries. The different side reactivity propensity of K-, Na- and Li-O_2 at least partly originates from the disproportionation susceptibility of the superoxide. As disproportionation is driven by the peroxide formation for hard Lewis acid as Li^+, Na^+ or H^+, KO_2 remains stable in absence of additives or pollutants.

If hard Lewis acids drive disproportionation, soft Lewis acids on the contrary facilitate the production of singlet oxygen. Superoxide disproportionation evolves oxygen via the formation of a superoxide cluster either in the triplet or singlet state. The presence of a weak Lewis acid, even if not driving disproportionation itself, results in a lower energy barrier to a singlet state superoxide dimer and causes experimentally higher $^1O_2$ production. Since H^+ as additives results in minor augmentation of the $^1O_2$ release, the previous $^1O_2$ formation mechanism based on water induced disproportionation can be revised to alkali oxide disproportionation. Furthermore, the promising ionic liquid based electrolytes are not necessarily indicated in the case of metal-air batteries. Ionic liquids are based on soft Lewis acidic cations that would enhance $^1O_2$ formation and suffer greatly from degradations. In the same vein, weakly Lewis acid additives should be used with caution.

From our results, disproportionation is active and superoxide is at least partly present in solvated state during every reaction steps. This results in a significant degradation route in metal–O_2 cells, especially in Li^+/Na^+ containing electrolytes. The formation of metastable NaO_2 as discharge products is hence synonymous with significant degradation during rest due to low disproportionation rate. Similarly, advocating the solution pathway in Li-O_2 cell owing to solvated superoxide for increased capacity is a double edged sword since it favours $^1O_2$ formation. As $^1O_2$ production is inevitable in the current understanding of Na/Li-O_2 chemistries, its consequences must be mitigated. Singlet oxygen quenchers appear therefore well indicated to deactivate $^1O_2$ before the occurrence of parasitic reactions with the cell components.

Bibliography

[1] E. Mourad, Y. K. Petit, R. Spezia, A. Samojlov, F. F. Summa, C. Prehal, C. Leypold, N. Mahne, C. Slugovc, O. Fontaine *et al.*, “Singlet oxygen from cation driven superoxide disproportionation and consequences for aprotic metal–O_2 batteries,” *Energy & Environmental Science*, vol. 12, no. 8, pp. 2559–2568, 2019.

[2] J. S. Valentine and A. B. Curtis, “Convenient preparation of solutions of superoxide anion and the reaction of superoxide anion with a copper (II) complex,” *Journal of the American Chemical Society*, vol. 97, no. 1, pp. 224–226, 1975.

[3] N. Mahne, B. Schafzahl, C. Leypold, M. Leypold, S. Grumm, A. Leitgeb, G. A. Strohmeier, M. Wilkening, O. Fontaine, D. Kramer *et al.*, “Singlet oxygen generation as a major cause for parasitic reactions during cycling of aprotic lithium–oxygen batteries,” *Nature Energy*, vol. 2, no. 5, p. 17036, 2017.

[4] K. Abraham, “Electrolyte-directed reactions of the oxygen electrode in lithium-air batteries,” *Journal of The Electrochemical Society*, vol. 162, no. 2, pp. A3021–A3031, 2015.

[5] L. Johnson, C. Li, Z. Liu, Y. Chen, S. A. Freunberger, P. C. Ashok, B. B. Praveen, K. Dholakia, J.-M. Tarascon, and P. G. Bruce, “The role of LiO_2 solubility in O_2 reduction in aprotic solvents and its consequences for Li–O_2 batteries,” *Nature chemistry*, vol. 6, no. 12, p. 1091, 2014.

[6] Y. Zhang, X. Zhang, J. Wang, W. C. McKee, Y. Xu, and Z. Peng, “Potential-dependent generation of O_2^- and LiO_2 and their critical roles in O_2 reduction to Li_2O_2 in aprotic Li–O_2 batteries,” *The Journal of Physical Chemistry C*, vol. 120, no. 7, pp. 3690–3698, 2016.

[7] I. Saito, T. Matsuura, and K. Inoue, “Formation of superoxide ion via one-electron transfer from electron donors to singlet oxygen,” *Journal of the American Chemical Society*, vol. 105, no. 10, pp. 3200–3206, 1983.

[8] M. Hayyan, M. A. Hashim, and I. M. AlNashef, “Superoxide ion: generation and chemical implications,” *Chemical reviews*, vol. 116, no. 5, pp. 3029–3085, 2016.

[9] C. Schweitzer and R. Schmidt, “Physical mechanisms of generation and deactivation of singlet oxygen,” *Chemical reviews*, vol. 103, no. 5, pp. 1685–1758, 2003.

[10] A. P. Darmanyan, W. S. Jenks, and P. Jardon, “Charge-transfer quenching of singlet oxygen O_2 $(^1\Delta_g)$ by amines and aromatic hydrocarbons,” *The Journal of Physical Chemistry A*, vol. 102, no. 38, pp. 7420–7426, 1998.

[11] Y. K. Petit, C. Leypold, N. Mahne, E. Mourad, L. Schafzahl, C. Slugovc, S. M. Borisov, and S. A. Freunberger, “DABCOnium: an efficient and high-voltage stable singlet oxygen quencher for metal–O_2 cells,” *Angewandte Chemie International Edition*, vol. 58, no. 20, pp. 6535–6539, 2019.

[12] L. Schafzahl, N. Mahne, B. Schafzahl, M. Wilkening, C. Slugovc, S. M. Borisov, and S. A. Freunberger, “Singlet oxygen during cycling of the aprotic sodium–O_2 battery,” *Angewandte Chemie International Edition*, vol. 56, no. 49, pp. 15 728–15 732, 2017.

[13] W. Linert, A. Camard, M. Armand, and C. Michot, “Anions of low Lewis basicity for ionic solid state electrolytes,” *Coordination Chemistry Reviews*, vol. 226, no. 1-2, pp. 137–141, 2002.

[14] M. Schmeisser, P. Illner, R. Puchta, A. Zahl, and R. van Eldik, "Gutmann donor and acceptor numbers for ionic liquids," *Chemistry–A European Journal*, vol. 18, no. 35, pp. 10 969–10 982, 2012.

[15] M. Carboni, A. G. Marrani, R. Spezia, and S. Brutti, "1, 2-dimethoxyethane degradation thermodynamics in Li-O_2 redox environments," *Chemistry–A European Journal*, vol. 22, no. 48, pp. 17 188–17 203, 2016.

[16] V. S. Bryantsev, M. Blanco, and F. Faglioni, "Stability of lithium superoxide LiO_2 in the gas phase: computational study of dimerization and disproportionation reactions," *The Journal of Physical Chemistry A*, vol. 114, no. 31, pp. 8165–8169, 2010.

[17] U. Das, K. C. Lau, P. C. Redfern, and L. A. Curtiss, "Structure and stability of lithium superoxide clusters and relevance to Li–O_2 batteries," *The journal of physical chemistry letters*, vol. 5, no. 5, pp. 813–819, 2014.

[18] C. Sheng, F. Yu, Y. Wu, Z. Peng, and Y. Chen, "Disproportionation of sodium superoxide in metal–air batteries," *Angewandte Chemie*, vol. 130, no. 31, pp. 10 054–10 058, 2018.

[19] P. Hartmann, C. L. Bender, M. Vraar, A. K. Dürr, A. Garsuch, J. Janek, and P. Adelhelm, "A rechargeable room-temperature sodium superoxide (NaO_2) battery," *Nature materials*, vol. 12, no. 3, p. 228, 2013.

[20] C. J. Allen, J. Hwang, R. Kautz, S. Mukerjee, E. J. Plichta, M. A. Hendrickson, and K. Abraham, "Oxygen reduction reactions in ionic liquids and the formulation of a general ORR mechanism for Li–air batteries," *The Journal of Physical Chemistry C*, vol. 116, no. 39, pp. 20 755–20 764, 2012.

[21] D. G. Kwabi, V. S. Bryantsev, T. P. Batcho, D. M. Itkis, C. V. Thompson, and Y. Shao-Horn, "Experimental and computational analysis of the solvent-dependent O_2/Li^+-O_2^- redox couple: standard potentials, coupling strength, and implications for lithium–oxygen batteries," *Angewandte Chemie International Edition*, vol. 55, no. 9, pp. 3129–3134, 2016.

[22] Z. Peng, S. A. Freunberger, L. J. Hardwick, Y. Chen, V. Giordani, F. Bardé, P. Novák, D. Graham, J.-M. Tarascon, and P. G. Bruce, "Oxygen reactions in a non-aqueous Li^+ electrolyte," *Angewandte Chemie International Edition*, vol. 50, no. 28, pp. 6351–6355, 2011.

[23] W. Yu, H. Wang, L. Qin, J. Hu, L. Liu, B. Li, D. Zhai, and F. Kang, "Controllable electrochemical fabrication of KO_2-decorated binder-free cathodes for rechargeable lithium–oxygen batteries," *ACS applied materials & interfaces*, vol. 10, no. 20, pp. 17 156–17 166, 2018.

[24] I. Landa-Medrano, I. R. de Larramendi, and T. Rojo, "Modifying the ORR route by the addition of lithium and potassium salts in Na-O_2 batteries," *Electrochimica Acta*, vol. 263, pp. 102–109, 2018.

[25] C. Li, Z. Qian, Y. Ma, P. Zuo, C. Du, H. Huo, and G. Yin, "Bifunctional electrolyte additive KI to improve the cycling performance of Li–O_2 batteries," *New Journal of Chemistry*, vol. 42, no. 21, pp. 17 311–17 316, 2018.

[26] I. Landa-Medrano, M. Olivares-Marín, B. Bergner, R. Pinedo, A. Sorrentino, E. Pereiro, I. Ruiz de Larramendi, J. Janek, T. Rojo, and D. Tonti, "Potassium salts as electrolyte additives in lithium–oxygen batteries," *The Journal of Physical Chemistry C*, vol. 121, no. 7, pp. 3822–3829, 2017.

[27] J.-l. Ma, F.-l. Meng, Y. Yu, D.-p. Liu, J.-m. Yan, Y. Zhang, X.-b. Zhang, and Q. Jiang, "Prevention of dendrite growth and volume expansion to give high-performance aprotic bimetallic Li-Na alloy–O_2 batteries," *Nature chemistry*, vol. 11, no. 1, p. 64, 2019.

[28] B. D. McCloskey, A. Valery, A. C. Luntz, S. R. Gowda, G. M. Wallraff, J. M. Garcia, T. Mori, and L. E. Krupp, “Combining accurate O_2 and Li_2O_2 assays to separate discharge and charge stability limitations in nonaqueous Li–O_2 batteries,” *The journal of physical chemistry letters*, vol. 4, no. 17, pp. 2989–2993, 2013.

[29] N. B. Aetukuri, B. D. McCloskey, J. M. García, L. E. Krupp, V. Viswanathan, and A. C. Luntz, “Solvating additives drive solution-mediated electrochemistry and enhance toroid growth in non-aqueous Li–O_2 batteries,” *Nature chemistry*, vol. 7, no. 1, p. 50, 2015.

[30] B. D. McCloskey, D. Bethune, R. Shelby, T. Mori, R. Scheffler, A. Speidel, M. Sherwood, and A. Luntz, “Limitations in rechargeability of Li-O_2 batteries and possible origins,” *The journal of physical chemistry letters*, vol. 3, no. 20, pp. 3043–3047, 2012.

[31] B. D. McCloskey, J. M. Garcia, and A. C. Luntz, “Chemical and electrochemical differences in nonaqueous Li–O_2 and Na–O_2 batteries,” *The journal of physical chemistry letters*, vol. 5, no. 7, pp. 1230–1235, 2014.

[32] S. Ganapathy, B. D. Adams, G. Stenou, M. S. Anastasaki, K. Goubitz, X.-F. Miao, L. F. Nazar, and M. Wagemaker, “Nature of Li_2O_2 oxidation in a Li–O_2 battery revealed by operando X-ray diffraction,” *Journal of the American Chemical Society*, vol. 136, no. 46, pp. 16 335–16 344, 2014.

[33] Y. Wang, N.-C. Lai, Y.-R. Lu, Y. Zhou, C.-L. Dong, and Y.-C. Lu, “A solvent-controlled oxidation mechanism of Li_2O_2 in lithium-oxygen batteries,” *Joule*, vol. 2, no. 11, pp. 2364–2380, 2018.

[34] S. Kang, Y. Mo, S. P. Ong, and G. Ceder, “A facile mechanism for recharging Li_2O_2 in Li–O_2 batteries,” *Chemistry of Materials*, vol. 25, no. 16, pp. 3328–3336, 2013.

[35] B. D. McCloskey, D. S. Bethune, R. M. Shelby, G. Girishkumar, and A. C. Luntz, “Solvents’ critical role in nonaqueous lithium–oxygen battery electrochemistry,” *The Journal of Physical Chemistry Letters*, vol. 2, no. 10, pp. 1161–1166, 2011.

[36] D. Aurbach, B. D. McCloskey, L. F. Nazar, and P. G. Bruce, “Advances in understanding mechanisms underpinning lithium–air batteries,” *Nature Energy*, vol. 1, no. 9, p. 16128, 2016.

[37] H.-D. Lim, B. Lee, Y. Bae, H. Park, Y. Ko, H. Kim, J. Kim, and K. Kang, “Reaction chemistry in rechargeable Li–O_2 batteries,” *Chemical Society Reviews*, vol. 46, no. 10, pp. 2873–2888, 2017.

[38] D. Sharon, D. Hirsberg, M. Salama, M. Afri, A. A. Frimer, M. Noked, W. Kwak, Y.-K. Sun, and D. Aurbach, “Mechanistic role of Li^+ dissociation level in aprotic Li–O_2 battery,” *ACS applied materials & interfaces*, vol. 8, no. 8, pp. 5300–5307, 2016.

[39] D. G. Kwabi, M. Tuodziecki, N. Pour, D. M. Itkis, C. V. Thompson, and Y. Shao-Horn, “Controlling solution-mediated reaction mechanisms of oxygen reduction using potential and solvent for aprotic lithium–oxygen batteries,” *The journal of physical chemistry letters*, vol. 7, no. 7, pp. 1204–1212, 2016.

[40] N. Ortiz-Vitoriano, T. P. Batcho, D. G. Kwabi, B. Han, N. Pour, K. P. C. Yao, C. V. Thompson, and Y. Shao-Horn, “Rate-dependent nucleation and growth of NaO_2 in Na–O_2 batteries,” *The journal of physical chemistry letters*, vol. 6, no. 13, pp. 2636–2643, 2015.

[41] J. Kim, H. Park, B. Lee, W. M. Seong, H.-D. Lim, Y. Bae, H. Kim, W. K. Kim, K. H. Ryu, and K. Kang, “Dissolution and ionization of sodium superoxide in sodium–oxygen batteries,” *Nature communications*, vol. 7, p. 10670, 2016.

[42] Y.-C. Lu and Y. Shao-Horn, “Probing the reaction kinetics of the charge reactions of nonaqueous Li–O_2 batteries,” *The journal of physical chemistry letters*, vol. 4, no. 1, pp. 93–99, 2012.

[43] G. Cong, W. Wang, N.-C. Lai, Z. Liang, and Y.-C. Lu, “A high-rate and long-life organic–oxygen battery,” *Nature materials*, vol. 18, no. 4, p. 390, 2019.

[44] X. Gao, Z. P. Jovanov, Y. Chen, L. R. Johnson, and P. G. Bruce, “Phenol-catalyzed discharge in the aprotic lithium-oxygen battery,” *Angewandte Chemie*, vol. 129, no. 23, pp. 6639–6643, 2017.

[45] C. Li, O. Fontaine, S. A. Freunberger, L. Johnson, S. Grugeon, S. Laruelle, P. G. Bruce, and M. Armand, “Aprotic Li–O_2 battery: influence of complexing agents on oxygen reduction in an aprotic solvent,” *The Journal of Physical Chemistry C*, vol. 118, no. 7, pp. 3393–3401, 2014.

[46] S. Das, J. Højberg, K. B. Knudsen, R. Younesi, P. Johansson, P. Norby, and T. Vegge, “Instability of ionic liquid-based electrolytes in Li–O_2 batteries,” *The Journal of Physical Chemistry C*, vol. 119, no. 32, pp. 18 084–18 090, 2015.

[47] M. Piana, J. Wandt, S. Meini, I. Buchberger, N. Tsiouvaras, and H. A. Gasteiger, “Stability of a pyrrolidinium-based ionic liquid in Li-O_2 cells,” *Journal of The Electrochemical Society*, vol. 161, no. 14, pp. A1992–A2001, 2014.

[48] K. U. Schwenke, M. Metzger, T. Restle, M. Piana, and H. A. Gasteiger, “The influence of water and protons on Li_2O_2 crystal growth in aprotic Li-O_2 cells,” *Journal of The Electrochemical Society*, vol. 162, no. 4, pp. A573–A584, 2015.

[49] D. G. Kwabi, T. P. Batcho, S. Feng, L. Giordano, C. V. Thompson, and Y. Shao-Horn, “The effect of water on discharge product growth and chemistry in Li–O_2 batteries,” *Physical Chemistry Chemical Physics*, vol. 18, no. 36, pp. 24 944–24 953, 2016.

[50] J. Lu, Y. J. Lee, X. Luo, K. C. Lau, M. Asadi, H.-H. Wang, S. Brombosz, J. Wen, D. Zhai, Z. Chen *et al.*, “A lithium–oxygen battery based on lithium superoxide,” *Nature*, vol. 529, no. 7586, p. 377, 2016.

[51] I. Landa-Medrano, R. Pinedo, X. Bi, I. Ruiz de Larramendi, L. Lezama, J. Janek, K. Amine, J. Lu, and T. Rojo, “New insights into the instability of discharge products in Na–O_2 batteries,” *ACS applied materials & interfaces*, vol. 8, no. 31, pp. 20 120–20 127, 2016.

[52] R. Black, A. Shyamsunder, P. Adeli, D. Kundu, G. K. Murphy, and L. F. Nazar, “The nature and impact of side reactions in glyme-based sodium–oxygen batteries,” *ChemSusChem*, vol. 9, no. 14, pp. 1795–1803, 2016.

[53] T. Liu, G. Kim, M. T. Casford, and C. P. Grey, “Mechanistic insights into the challenges of cycling a nonaqueous Na–O_2 battery,” *The journal of physical chemistry letters*, vol. 7, no. 23, pp. 4841–4846, 2016.

[54] S. Y. Sayed, K. P. Yao, D. G. Kwabi, T. P. Batcho, C. V. Amanchukwu, S. Feng, C. V. Thompson, and Y. Shao-Horn, “Revealing instability and irreversibility in nonaqueous sodium–O_2 battery chemistry,” *Chemical Communications*, vol. 52, no. 62, pp. 9691–9694, 2016.

[55] Y. Wang, Z. Liang, Q. Zou, G. Cong, and Y.-C. Lu, “Mechanistic insights into catalyst-assisted nonaqueous oxygen evolution reaction in lithium–oxygen batteries,” *The Journal of Physical Chemistry C*, vol. 120, no. 12, pp. 6459–6466, 2016.

Deactivation of singlet oxygen by physical quenchers

Water will never quench your thirst for knowledge.
Anthony T. Hincks

Contents

Figures

Chapter based on Petit et al.[1]

Introduction

Oxides are a prominent research subject as new cathode materials for non-aqueous alkali battery technologies, either as intercalation materials based on transition metal oxides or as direct alkali oxides in metal–O_2 batteries[2–7]. Beside their promises for higher energy storage, oxide based cathodes suffer from side reactions and understanding their reactivities is the key for increased battery lifetime. Metal-O_2 technologies are particularly inhibited by a quick and crippling fade in capacity, which is discussed in 1.3.2. To allow these technologies to reach their full potentials, side reaction origins must be understood and subdued.

The side reactions plaguing metal–O_2 cells have been solely ascribed to superoxide reactivity for an enduring time but superoxide's reactivity is not sufficient to explain such extended degradations, as explained in part 1.3.2. In the ch. 2 and 3, we have shown that singlet oxygen is currently an inevitable source of side reactions at all stages of cycling in Na and Li cells. Singlet oxygen's high reactivity was shown to correlate with the amount of side products in metal-air batteries whose accumulation increases the overpotential and reduces cell cyclability. Singlet oxygen reactivity is moreover not confined to metal-air chemistry as it forms from parasitic products, as discussed in ch. 2. Finding countermeasures against $^1O_2$ is thus of major importance to achieve long term cycling with non-aqueous alkali batteries.

O_2 quenchers can bring the answer to the $^1O_2$ mitigation question. Chemical traps such as DMA, described in the previous chapters, react preferentially with $^1O_2$ and prevent further side reactions by forming their endoperoxides[8]. To sustain the extend lifetime required for a battery, very high concentration of chemical traps would have to be used which would consequently form a high amount of inactive species in the electrolytes. Since the use of chemical traps is unrealistic in batteries, physical quenchers that deactivate $^1O_2$ to $^3O_2$ without being consumed, as schemed in Fig. 4.1, appears well indicated. Efficient quenchers need, yet, to sustain the aggressive conditions found in metal-O_2 batteries and particularly the charging potentials.

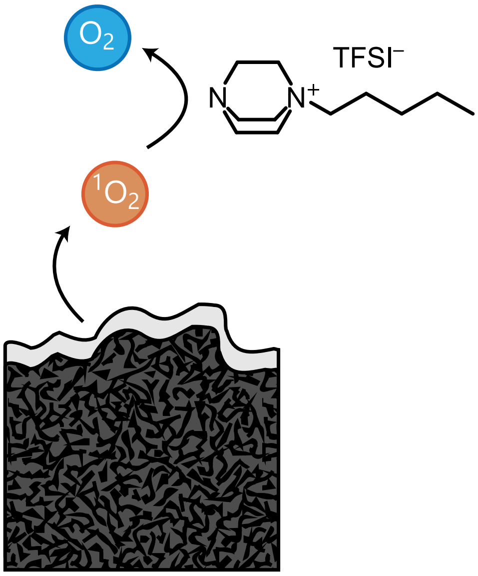

Figure 4.1: **Illustration of the quenching process by PeDTFSI in electrochemical cells.**

We present here PeDTFSI, a ionic liquid formed by monoalkylating the known quencher DABCO[8–10], as an efficient quencher in metal-O_2 batteries. PeDTFSI has a sufficiently reduced electron density at the remaining lone pair to raise its oxidative stability beyond the DABCO one. We show that the higher solubility of PeDTFSI in glymes, a common solvent in metal-O_2 batteries, counterbalances its reduced molar efficiency arising from its increased oxidation potential[9,11]. To do so, we followed the consumption of DMA in the presence of $^1O_2$ by UV-vis spectroscopy. The DMA consumption rate will be decreased by competitive $^1O_2$ deactivation pathways, e.g. physical quenching. Quenchers as additives in Li-O_2 electrolytes result in reduced parasitic products and increased reaction yield during both discharge and charge. Besides providing a means to mitigate $^1O_2$ in batteries, this study established clearly $^1O_2$ as a main degradation source in metal-O_2 cells considering the influence of $^1O_2$ quenchers on parasitic reactions.

4.1 Physically quenching singlet oxygen

Processes in the living nature suggest substantial answers to the $^1O_2$ mitigation issue in electrochemical devices. Singlet oxygen is found in biological systems that use O_2 redox chamistry for energy storage[11,12]. Natural systems evolved to counteract negative effects of this harmful chemical. Amongst possible solutions, the most commons are chemical trapping and physical quenching agents, such as tocopheroles and carotenes[11,12]. Chemist have synthesized molecules with similar effect, e.g. the previously discussed DMA that traps $^1O_2$ by forming its endoperoxide[13,14]. These traps, yet, directly react at high rates with $^1O_2$ to form innocuous species. Their consumptions render chemical traps inadequate in battery technologies where a high number of cycles needs to be sustained.

Physically deactivating $^1O_2$ to its ground state is preferred since the quencher is not consumed and no new inactive products accumulate. Several physical quenching mechanisms can convert $^1O_2$ excess energy into heat[11,13]. They are namely, in increasing reaction kinetics order, electronic-to-vibrational energy transfer (e.g. $^1O_2$ quenching by solvents), charge transfer induced quenching (e.g. tertiary aliphatic amines), and electronic energy transfer (unsuitable for electrochemical systems, e.g. carotenes in biologic systems)[11]. The fastest quenching mechanism suitable for electrochemical systems proceeds, hence, via a charge transfer (CT) mechanism. In the CT mechanism, the quencher (Q) and $^1O_2$ form a singlet encounter complex ($^1(Q^1O_2)_{EC}$), followed by the formation of a singlet charge transfer complex ($^1(Q^1O_2)_{CT}$), in which the electronic charge is partially transferred to the oxygen. Energy is then released during the intersystem crossing (isc) to the triplet ground state complex ($^3(Q^3O_2)_{CT}$), which dissociates to Q and $^3O_2$[11,15], as described in Eq. 4.1.

$$Q + {}^1O_2 \rightleftharpoons {}^1(Q^1O_2)_{EC} \rightleftharpoons {}^1(Q^1O_2)_{CT} \xrightarrow[\text{isc}]{} {}^3(Q^3O_2)_{CT} \rightleftharpoons Q + {}^3O_2 \tag{4.1}$$

Charge transfer quenching is favoured in the case of electron-rich quenchers, such as amines. 1,4-diazabicyclo [2.2.2]octane (DABCO, Fig. 4.2(a)) has been suggested for $^1O_2$ quenching as early as 1968 and was shown to be effective in aprotic media[8–10]. Amines have been widely investigated and it was found that the partial charge transfer causes the quenching efficiency to correlate logarithmically with the ionization potential and hence the oxidation potential[11,15]. The quenching efficiency by the CT mechanism drops by a factor of $\sim 10^4$ per volt of increased oxidation potentials for amines. The well known quenchers DABCO and LiN_3 are oxidized at $\sim 3.6\ V_{Li/Li^+}$[9–11,16], whereas $\sim 4.2\ V_{Li/Li^+}$ are typically required to recharge Li–O_2 cells[17–19]. The other non-aqueous metal-air batteries present a lower overpotential during charge and so the oxidative stability of the quencher should be settled for Li-O_2 chemistry[7,20–22]. Another challenge in batteries is the reduced quenching activity due to cation interactions with strongly Lewis basic amines[11]. To be suitable under metal-air battery conditions, an amine quencher should then have low Lewis basicity, raised oxidation stability (to around $4.2\ V_{Li/Li^+}$), be chemically stable, counterbalance the inevitably lower molar quenching efficiency by high solubility in the solvent media and ultimately be compatible with a lithium metal anode. Herein, we show that monoalkylating the diamine DABCO to its onium salt (here 1-pentyl-1,4-diazabicyclo[2.2.2]octan-1-ium TFSI or PeDTFSI, presented in Fig. 4.2b) achieves all these goals.

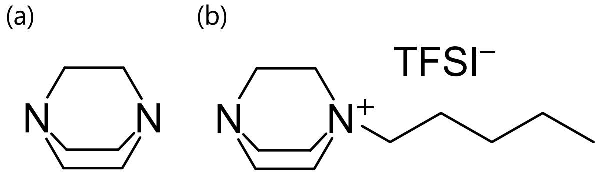

Figure 4.2: **Structure of the used $^1O_2$ quenchers.** (a) DABCO (1,4-diazabicyclo[2.2.2]octane), (b) PeDTFSI (1-pentyl-1,4-diazabicyclo[2.2.2]octan-1-ium TFSI).

4.2 A quencher adapted for lithium-air batteries

According to a literature procedure detailed in Appendix C.2, a pentyl DABCOnium (PeDTFSI) species counterbalanced by a bis(trifluoromethanesulfonyl)imide ($TFSI^-$) anion was synthesized[23]. PeDTFSI is an ionic liquid with a melting point of 43 °C (PeDTFSI characterisations are detailed in Fig. C.3) and is widely miscible with glymes, a common metal-air battery electrolyte, fulfilling the high solubility requirement. Concerning the low Lewis basicity criterion, its donor number (DN) was determined to be 12.5 by ^{23}Na-NMR shift as depicted in Fig. C.4. The commonly used TEGDME has a similar Lewis basicity with a DN of 12, which is much lower than other common solvents such as DMSO (DN=30) or tertiary amines such as triethylamine (DN=61) and 1,2-diaminoethane (DN=55), as expressed in Tab. C.1[24]. We verified the chemical stability of DABCO and PeDTFSI in presence of superoxide, peroxide and $^1O_2$ by ^{1}H-NMR spectroscopy to assess their usability in metal-air batteries. The procedure is further described in Appendix A.10 and the resulting ^{1}H-NMR spectra are illustrated in Fig. 4.3 for PeDTFSI and Fig. C.6 for DABCO.

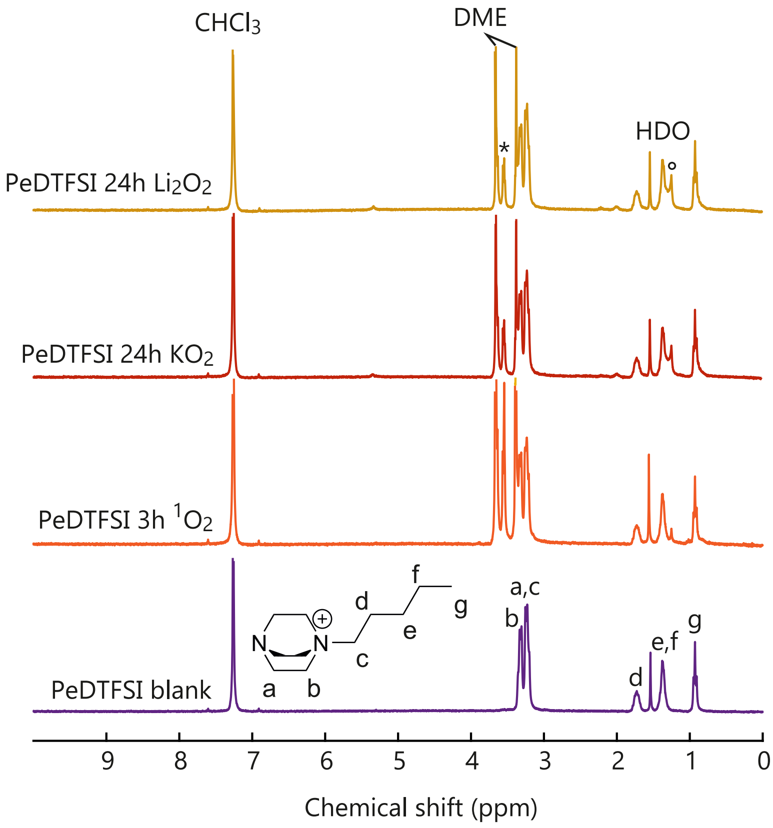

Figure 4.3: **Stability of PeDTFSI in contact with $^1O_2$, KO_2, and Li_2O_2 by ^{1}H-NMR.** The spectra were recorded in $CDCl_3$. The ^{1}H-NMR spectra characterise PeDTFSI (in purple), PeDTFSI after 3h contact with $^1O_2$ (in orange), PeDTFSI after 24h contact with KO_2 (in red), and PeDTFSI after 24h contact with Li_2O_2 (in yellow). The * denotes a residue from DME evaporation, which amounts to a content of 1 ppm in the DME; the ° denotes H from grease. $^1O_2$ was produced photochemically, according to a previously described method[8] and further described in Appendix A.3, by means of 1 μM Pd_4F and illumination at 643 nm.

Cyclic voltammetry was used to determine the electrochemical stability window of the quenchers, as shown in Fig. 4.4. Monoalkylating DABCO diminishes the electronegativity of the tertiary amine and raises its oxidation onset by approximately 0.6 V. The oxidation stability increase from ~3.6 V_{Li/Li^+} for DABCO to ~4.2 V_{Li/Li^+} for PeDTFSI and hence is sufficiently high for Li-O_2 cells. Onset of reduction is in either case around 0.5 V_{Li/Li^+} permitting its use for every O_2 cathodes[7,20–22,25]. Regarding the lithium metal anode, a symmetrical Li/Li cells with a TEGDME electrolyte composed of 1 M LiTFSI and 380 mM PeDTFSI could sustain 5 hours plating/deplating at |131| μA with low overpotentials upon cycling, as pictured in Fig. C.5. Since recent researches advocate for additives unstable with lithium metal as mediators, the use of additives might require anyway the use of solid sate separators[26].

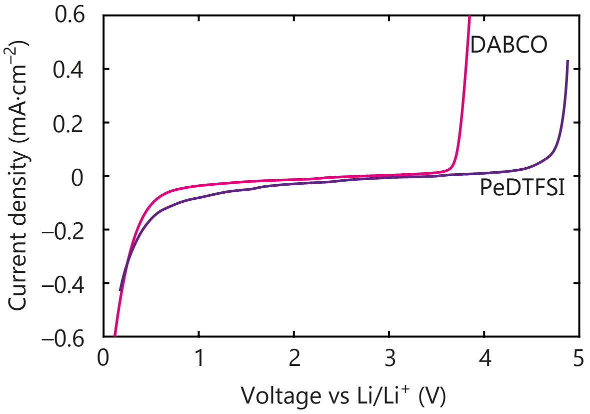

Figure 4.4: **Cyclic voltammetry of DABCO (in light purple) and PeDTFSI (in dark purple).** The cyclic voltammetries were performed at a glassy carbon disk electrode in a TEGDME electrolyte containing 0.1 M LiTFSI and 2 mM of the quenchers at a scan rate of 50 mV·s^{-1}.

To verify the quenching efficiency of PeDTFSI despite its higher oxidation potential, we monitored the disappearance rate of the $^1O_2$ trap DMA by UV-vis spectroscopy in presence of quenchers during continuous photochemical $^1O_2$ generation[13,27]: This protocol is further detailed in Appendix A.7 and the results depicted in Fig. 4.5. Like in part 3.1, a slower DMA decay rate in presence of quenchers, due to competitive reactions, is taken as a token of the quencher activity. $^1O_2$ was generated photochemically at a constant rate by illuminating O_2 saturated TEGDME containing 1 μM Pd4F photosensitizer[8] [27] [28], 80 μM DMA and either the tested quencher or no additives. In order to compare the different rates, the $^1O_2$ production should be constant. The quencher should hence not deactivate the excited triplet state of the sensitizer itself, responsible for the conversion of $^3O_2$ into $^1O_2$, effect described in part 2.2.1. By measuring the excited sensitizer lifetime, described in Appendix C.3.4, we verified the negligible influence of the studied quenchers compared to quenching by molecular oxygen and thus on the $^1O_2$ generation rate.

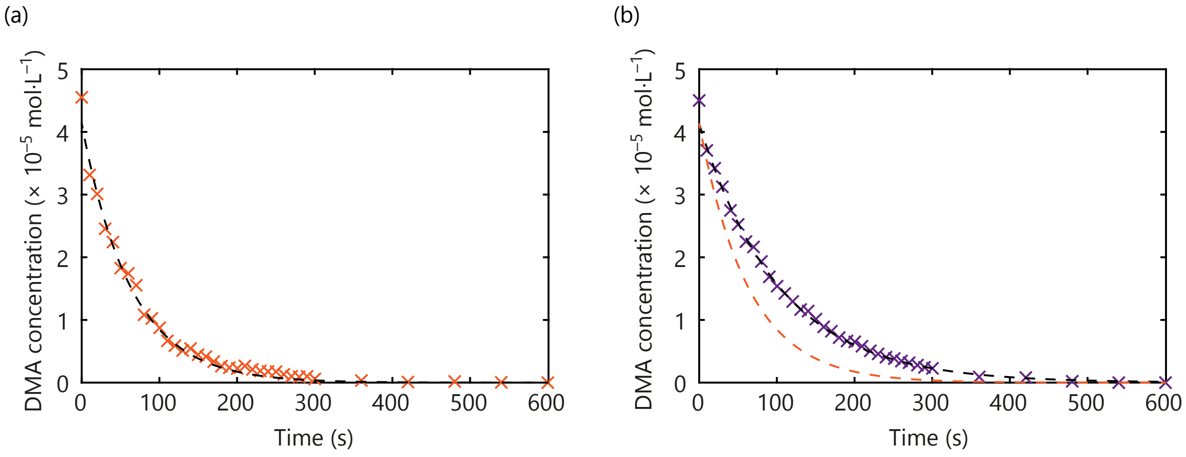

Figure 4.5: **DMA decay over time in presence of photochemically produced $^1O_2$ with or without DABCO.** (a) DMA consumption without quencher (in orange) and the first-order kinetic fit (in black) (b) DMA in presence of 40 μM DABCO (in purple), the first-order kinetic fit (in dashed black) and the DMA without quencher fitted (in orange). The electrolytes used are based one 40 μM DMA and 1 μM Pd_4F in O_2 saturated TEGDME illuminated at 643 nm, as described more lengthy in Appendix A.7. The dashed lines are the exponential fit of DMA consumption.

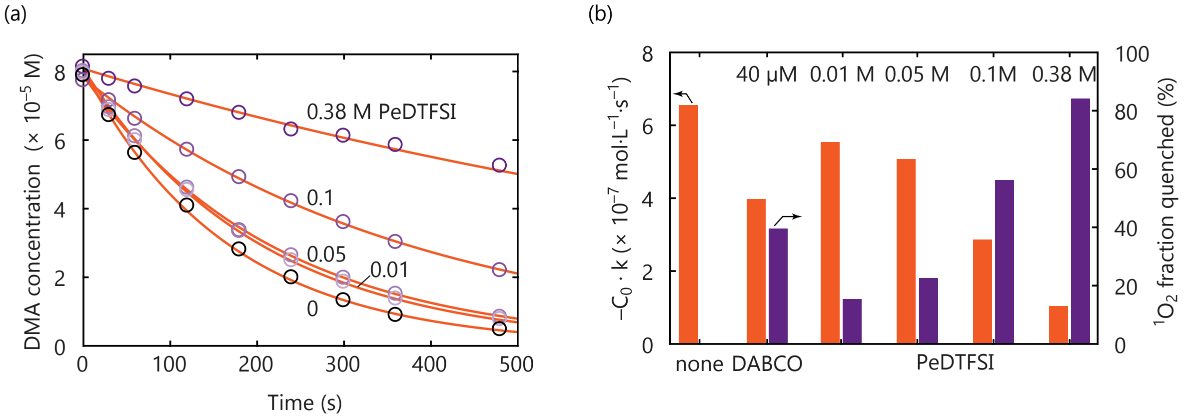

Figure 4.6: **Comparison of the quenching efficiency and the influence of the quencher concentration.** (a) DMA concentration evolution over time in presence of photochemically produced $^1O_2$ with or without PeDTFSI at various concentrations to determine the quenching efficiency. The electrolytes used are based on 80 µM DMA, the noted concentration of PeDTFSI and 1 µM Pd_4F in O_2 saturated TEGDME illuminated at 643 nm, as described more lengthy in Appendix A.7. The lines are the exponential fit of DMA consumption. (b) Quenching efficiency expressed as DMA decay rates and $^1O_2$ fraction quenched for 40 µM DABCO and various PeDTFSI concentrations.

The obtained DMA concentration decays show a clear correlation with the PeDTFSI concentration used in Fig. 4.6(a), verifying that higher concentrations allow to circumvent the lower molar activity of PeDTFSI. The DMA decay can be fitted by a pseudo first-order reaction kinetic according to Eq. A.8, considering the $^1O_2$ concentration as constantly replenished to the same level[13]; Examples of fitted decays can be found in Fig. 4.5. The obtained rate at t_0 can then be compared to characterise the quenching efficiency and the $^1O_2$ fraction quenched as given by the ratio between the rate of DMA alone and in quencher presence at a given concentration, presented in Fig. 4.6(b). As expected from their respective oxidation potentials, DABCO presents a higher molar quenching efficiency with roughly halved the

DMA decay rate at only 40 μM; On the other hand, PeDTFSI concentration had to be increased to the mM range for a comparable effect. With 0.01, 0.05, 0.1, and 0.38 mM, the quenched $^1O_2$ fractions were 9, 23, 56, and 86 %, respectively. Owing to its high solubility, PeDTFSI can thus compensate its lower efficiency to achieve quenching of the vast majority of $^1O_2$.

4.3 Quencher influence on side reactivity

Ultimately, a suitable quencher needs to effectively decrease the amount of $^1O_2$ related parasitic chemistry in metal-air batteries. We chose the Li–O_2 cell to demonstrate the impact of PeDTFSI since amongst Li–, Na–, and K–O_2 cells, Li–O_2 present the highest $^1O_2$ production rate and shows the most severe side reactions as depicted in part 1.3.2 and ch. 2. The deviation from the theoretical yield was measured by pressure monitoring assuming that the large majority of the released gases is oxygen[17] [29] [30]. Reaction products (Li_2O_2 and carbonates) were characterised by a combination of UV-Vis spectroscopy and MS whereas the $^1O_2$ production was obtained by the ratio of DMA/DMA-O_2 thanks to HPLC measurements after the electrolyte extraction. The methods are further described in Appendices A.4, A.6, and A.5. Li–O_2 cells were constructed with activated carbon cathodes and TEGDME electrolytes containing 1 M LiTFSI, 30 mM DMA and either no quencher, 60 mM DABCO, or 60, 120, and 380 mM PeDTFSI according to Appendix A.1.

4.3.1 Discharge

Considering first the $^3O_2$ consumption, cells discharged at 100 mA·g_c^{-1} up to 1000 mA·h·g_c^{-1} present a light deviation within 2% of the ideal value of 2 e^-/O_2 with a slight improvement in presence of a quencher in Fig. 4.7(a), in accord with other reports[17,20,27,29,31]. In a similar fashion, Li_2O_2 yields, shown in Fig. 4.7(b), stay unchanged by the presence of quenchers at ~95%. The presence of quenchers is not expected to change significantly the reaction mechanism of the cell and hence to strongly influence the Li_2O_2 or e^-/O_2 yield during discharge. Deactivating already formed $^1O_2$ should solely influence the side product amount and $^1O_2$ trapped by DMA in solution. Consequently, the amount of unquenched $^1O_2$ directly correlates with the quantity of carbonaceous side products formed in Fig. 4.7(b). The presence of 60 mM DABCO additive cuts down both the singlet oxygen trapped in solution and the side products by roughly a factor of 4. The same concentration of PeDTFSI reduces the side products only by half, as a result of its lower molar quenching efficiency. With 380 mM PeDTFSI, however, the side products were cut to 14% of the value without quencher whether a smaller amount than for 60 mM DABCO. PeDTFSI hence effectively reduces $^1O_2$ related parasitic chemistry on discharge owing to its high solubility.

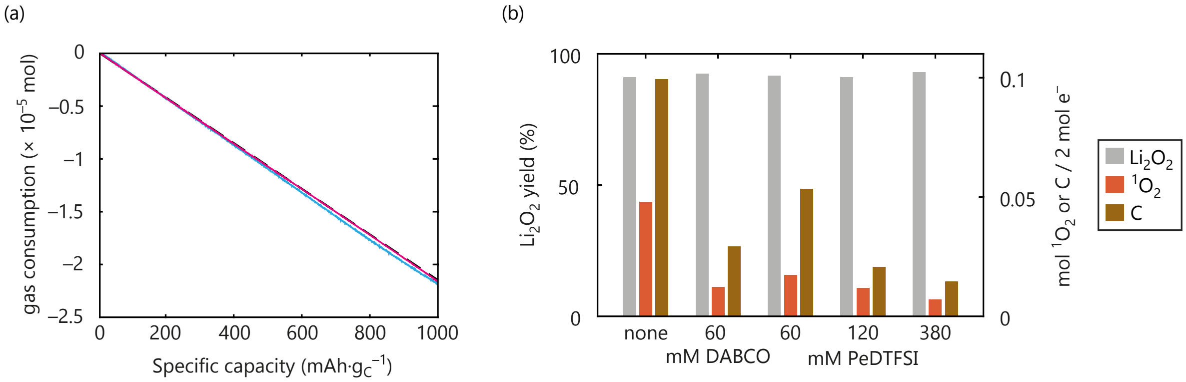

Figure 4.7: **Quencher influence on Li-O_2 cell discharges.** (a) Gas consumption during a Li-O_2 cell discharge with a carbon black cathode and LFP counter electrode discharged at 100 mA·g_c^{-1} to 1000 mA·h·g_c^{-1} in a TEGDME electrolyte containing 1 M LiTFSI, 30 mM DMA and either no quencher (blue) or 0.38 M PeDTFSI (purple). The dashed line represents the theoretical consumption of 2 e^-/O_2. The method is detailed in Appendix A.2. (b) O_2, $^1O_2$, peroxide and carbonate productions during discharge of Li-O_2 cells with or without quenchers. The cells are composed of a carbon black cathode and LFP counter electrode in a TEGDME electrolyte containing 1 M LiTFSI and the mentioned quencher concentration and discharged at 100 mA·g_c^{-1} to 1000 mA·h·g_c^{-1}.

4.3.2 Charge

Turning to cell recharge, we assessed the effect of a quencher on the gas evolution rate measured using the pressure in the cell headspace. As DABCO has already been shown to reduce $^1O_2$ related parasitic chemistry on charge within the limited oxidative stability of 3.6 V_{Li/Li^+} [8], focus was given to a quencher-free cell and a 380 mm PeDTFSI containing cell. Cells were first discharged in the same conditions than the discharge study and then recharged at 100 mA·g_c^{-1} to a cut-off voltage of 4.6 V_{Li/Li^+} and depicted in Fig. 4.8(a)-(b).

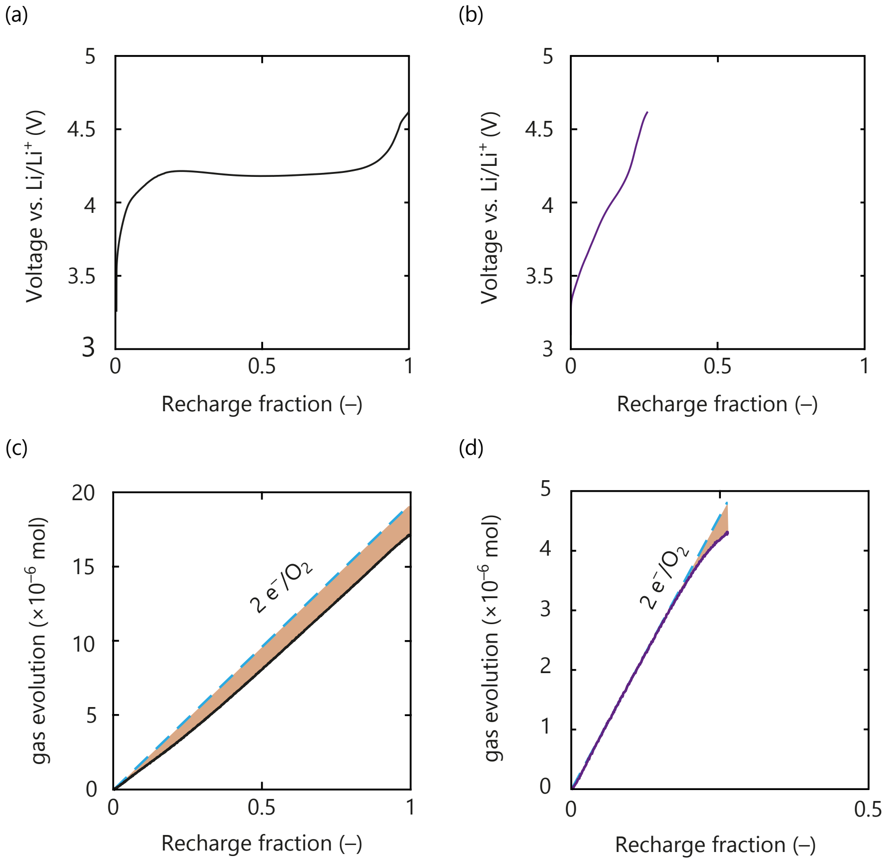

Figure 4.8: **Quencher influence on Li-O_2 cell charges.** The O_2 saturated TEGDME electrolytes used are composed of 1 M LiTFSI on the first column ((a)-(c)) and an additional 0.38 M PeDTFSI on the second column ((b)-(d)). (a)-(b) Voltage profiles during recharge of cells with a carbon black cathode and LFP counter electrode at 100 mA·g_c^{-1} to a cut-off voltage of 4.6 V_{Li/Li^+} after a discharge to 1000 mA·h·g_c^{-1}. (c)-(d) Gas evolution during a Li-O_2 cell charge of the aforementioned cells (in black without quencher and in purple with 0.38 M PeDTSFI). The blue dashed lines represent the theoretical 2 e^-/O_2 and the orange areas represent the parasitic reactions. The method is detailed in Appendix A.2.

For the quencher-free cell in Fig. 4.8(a)-(c), the voltage rises within a few percents of the recharge capacity towards to a plateau at ~4.2 V_{Li/Li^+} before it further rises steeply close to the end of recharge. The gas evolution remains, from the onset of charge, significantly below the theoretical value of 2 e^-/O_2, as previously observed in literature[17,20,29]. This deviation indicate e^- extraction from side products, i.e. Li_2CO_3[10], and possible reaction of released O_2 species with cell components rather than evolving as O_2. In contrast, the cell with PeDTFSI evolves O_2 at the ideal rate of 2 e^-/O_2 up to approximately 4.2 V_{Li/Li^+}, namely the PeDTFSI oxidation stability threshold; From this voltage onwards, part of the e^- exchanged are due to PeDTFSI oxidation. A 2 e^-/O_2 reaction yield establishes that all the electrons are extracted from Li_2O_2 rather than partly from side products and any $^1O_2$ formed is quenched to $^3O_2$ in order to be detected in the headspace. $^1O_2$ being evolved from the onset of charge in Li-O_2 cells from disproportionation[8,27], $^1O_2$ suppression can only arise via PeDTFSI quenching since the quencher is not expected to change the charging mechanism. It should be noted that the capacity at the cut-off with the electrolyte containing 380 mM PeDTFSI corresponds to only 23% of the formed Li_2O_2 during discharges, which balances with the 77% left in the electrode after recharge measured by Li_2O_2 titration.

4.3.3 Consequences

The addition of quenchers as additive results in a substantial decrease in side product formation both on discharge and charge. The quencher effectiveness to reduce parasitic reactions established clearly $^1O_2$ as one of the major degradation pathway in metal-air batteries. A reduction to 14% of the original carbonate formation on Li-O_2 cell discharge with high quencher concentration shows that disproportionation might arise as a culprit for 86% of the cell degradation during discharge, accentuating the importance of the disproportionation mechanism elucidated in the ch. 3. Quenching $^1O_2$ from the disproportionation reaction can explain the slightly improved e^-/O_2 yield since the $^1O_2$ released by disproportionation is recovered in the headspace as $^3O_2$ instead of reacting with cell components. As the $^1O_2$ formation rate is accelerated with the charge overpotential[8], quencher use is evermore important during Li-O_2 charge.

During Li-O_2 cell charge without quencher, the quickly increasing voltage is partly related to increasingly difficult electron transfer, as the Li_2O_2 content decreases, and mainly to the accumulation of side products with higher oxidation potentials[32–35]. Considering the case with quenchers, the near theoretical yield through most of the recharge indicates that rising voltage is not caused by side-product formation. Together with the much lower amounts of side products at the end of discharge, the continued $^1O_2$ elimination on charge also avoids more side products to be formed during recharge. This is reflected in the slower overpotential rise compared to the quencher-free cell. Accounting for the 77% Li_2O_2 left in at the electrode vicinity at the charge end with PeDTFSI, rising voltage can be related to increasingly difficult electron transport from the electrode surface to remote Li_2O_2 and subsequent loss of contact as charging proceeds. PeDTFSI is amphoteric, Lewis basic at the tertiary N atom and Lewis acidic at the quaternary N atom, which could possibly solubilize the LiO_2 intermediate and favour the solution discharge pathway. Difficulties in recharging cells with additives favouring the solution mechanism are already recognized[5,36–38].

The advantages of quencher additives are not limited to Li-O_2 batteries but to all battery chemistries where $^1O_2$ formation occurs. NaO_2 disproportionation at rest, accompanied by $^1O_2$ release, is responsible for high degradations in Na-O_2 cells, as demonstrated in part 2.3.3 and ch. 3. Quencher additives should be able to reduce this effect. The PeDTFSI quencher presented here is only a first attempt to adapt singlet oxygen quenchers to battery chemistries. Singlet oxygen evolution from layered transition metal oxides at high potential would require an even more improved oxidative stability[39,40]. Nevertheless, our study assesses the importance of singlet oxygen reactivity in non-aqueous batteries and its mitigation through quencher additives.

Conclusion

In conclusion, $^1O_2$ is partly responsible for side reactions and requires adequate mitigation strategies in non-aqueous alkali batteries. Physically quenching $^1O_2$ appears as a good solution to counter its production in batteries, permitting deactivation to its ground state before side reaction occurrences. We show that PeDTFSI, the monoalkylated form of the diamine 1,4-diazabicyclo[2.2.2]octane (DABCO), is an efficient $^1O_2$ quencher with sufficient voltage and chemical stability. Quaternizing one of the nitrogen atoms raises the oxidation stability of the remaining tertiary nitrogen from 3.6 V_{Li/Li^+} to approximately 4.2 V_{Li/Li^+}. Despite the lower molar efficiency of PeDTFSI, its high miscibility with glymes permits an effective $^1O_2$ quenching at high concentrations.

We have demonstrated the efficiency of PeDTFSI with Li–O_2 cathodes, where the quencher greatly reduces the parasitic chemistry. PeDTFSI's influence on parasitic chemistries settles the importance of $^1O_2$ in metal-O_2 batteries and the influence of side products on the Li-O_2 cell overpotential during charge. On a wider perspective, partly quaternized diamines are suitable to tune the oxidation potential of $^1O_2$ quenchers. $^1O_2$ is also known to evolve from layered transition metal cathodes and upon oxidizing Li_2CO_3, a common impurity of cathode materials. Quenchers stable under high voltages are, hence, relevant to control $^1O_2$ related reactivity and long-term cyclability of many currently studied cathodes. As transition metal cathodes can produced singlet oxygen at higher potentials than 4.2 V_{Li/Li^+}[39], alternative quenchers might arise in the future. Nevertheless, this study presents a first definition of quencher potential in oxide based cathodes and their design.

Enhanced solution pathway mechanism in Li-O_2 increases the discharge capacity but also leads to difficulties to reach full recharge. Complete oxidation of the Li_2O_2 formed during discharge could not be achieved with PeDTFSI addition. Such cells are now recognized to require oxidation mediators for full charge[5]. As mediators change the mechanism of the reaction, singlet oxygen production via mediators ought to be studied in more details.

Bibliography

[1] Y. K. Petit, C. Leypold, N. Mahne, E. Mourad, L. Schafzahl, C. Slugovc, S. M. Borisov, and S. A. Freunberger, "DABCOnium: an efficient and high-voltage stable singlet oxygen quencher for metal–O_2 cells," *Angewandte Chemie International Edition*, vol. 58, no. 20, pp. 6535–6539, 2019.

[2] Q. Liu, Z. Hu, M. Chen, C. Zou, H. Jin, S. Wang, S.-L. Chou, and S.-X. Dou, "Recent progress of layered transition metal oxide cathodes for sodium-ion batteries," *Small*, p. 1805381, 2019.

[3] P. Rozier and J. M. Tarascon, "Li-rich layered oxide cathodes for next-generation li-ion batteries: chances and challenges," *Journal of The Electrochemical Society*, vol. 162, no. 14, pp. A2490–A2499, 2015.

[4] H. Kim, D.-H. Seo, A. Urban, J. Lee, D.-H. Kwon, S.-H. Bo, T. Shi, J. K. Papp, B. D. McCloskey, and G. Ceder, "Stoichiometric layered potassium transition metal oxide for rechargeable potassium batteries," *Chemistry of Materials*, vol. 30, no. 18, pp. 6532–6539, 2018.

[5] D. Aurbach, B. D. McCloskey, L. F. Nazar, and P. G. Bruce, "Advances in understanding mechanisms underpinning lithium–air batteries," *Nature Energy*, vol. 1, no. 9, p. 16128, 2016.

[6] P. Hartmann, C. L. Bender, M. Vraar, A. K. Dürr, A. Garsuch, J. Janek, and P. Adelhelm, "A rechargeable room-temperature sodium superoxide (NaO_2) battery," *Nature materials*, vol. 12, no. 3, p. 228, 2013.

[7] G. Cong, W. Wang, N.-C. Lai, Z. Liang, and Y.-C. Lu, "A high-rate and long-life organic–oxygen battery," *Nature materials*, vol. 18, no. 4, p. 390, 2019.

[8] N. Mahne, B. Schafzahl, C. Leypold, M. Leypold, S. Grumm, A. Leitgeb, G. A. Strohmeier, M. Wilkening, O. Fontaine, D. Kramer *et al.*, "Singlet oxygen generation as a major cause for parasitic reactions during cycling of aprotic lithium–oxygen batteries," *Nature Energy*, vol. 2, no. 5, p. 17036, 2017.

[9] C. Ouannes and T. Wilson, "Quenching of singlet oxygen by tertiary aliphatic amines. Effect of DABCO (1,4-diazabicyclo[2.2.2]octane)," *Journal of the American Chemical Society*, vol. 90, no. 23, pp. 6527–6528, 1968.

[10] N. Mahne, S. E. Renfrew, B. D. McCloskey, and S. A. Freunberger, "Electrochemical oxidation of lithium carbonate generates singlet oxygen," *Angewandte Chemie International Edition*, vol. 57, no. 19, pp. 5529–5533, 2018.

[11] C. Schweitzer and R. Schmidt, "Physical mechanisms of generation and deactivation of singlet oxygen," *Chemical reviews*, vol. 103, no. 5, pp. 1685–1758, 2003.

[12] P. R. Ogilby, "Singlet oxygen: there is indeed something new under the sun," *Chemical Society Reviews*, vol. 39, no. 8, pp. 3181–3209, 2010.

[13] F. Wilkinson, W. P. Helman, and A. B. Ross, "Rate constants for the decay and reactions of the lowest electronically excited singlet state of molecular oxygen in solution. an expanded and revised compilation," *Journal of Physical and Chemical Reference Data*, vol. 24, no. 2, pp. 663–677, 1995.

[14] A. Gomes, E. Fernandes, and J. L. Lima, "Fluorescence probes used for detection of reactive oxygen species," *Journal of biochemical and biophysical methods*, vol. 65, no. 2-3, pp. 45–80, 2005.

[15] A. P. Darmanyan, W. S. Jenks, and P. Jardon, "Charge-transfer quenching of singlet oxygen O_2 ($^1\Delta_g$) by amines and aromatic hydrocarbons," *The Journal of Physical Chemistry A*, vol. 102, no. 38, pp. 7420–7426, 1998.

[16] D. Shanmukaraj, S. Grugeon, S. Laruelle, G. Douglade, J.-M. Tarascon, and M. Armand, "Sacrificial salts: Compensating the initial charge irreversibility in lithium batteries," *Electrochemistry Communications*, vol. 12, no. 10, pp. 1344–1347, 2010.

[17] B. D. McCloskey, D. Bethune, R. Shelby, T. Mori, R. Scheffler, A. Speidel, M. Sherwood, and A. Luntz, "Limitations in rechargeability of Li-O_2 batteries and possible origins," *The journal of physical chemistry letters*, vol. 3, no. 20, pp. 3043–3047, 2012.

[18] Y.-C. Lu, B. M. Gallant, D. G. Kwabi, J. R. Harding, R. R. Mitchell, M. S. Whittingham, and Y. Shao-Horn, "Lithium–oxygen batteries: bridging mechanistic understanding and battery performance," *Energy & Environmental Science*, vol. 6, no. 3, pp. 750–768, 2013.

[19] B. D. Adams, R. Black, Z. Williams, R. Fernandes, M. Cuisinier, E. J. Berg, P. Novak, G. K. Murphy, and L. F. Nazar, "Towards a stable organic electrolyte for the lithium oxygen battery," *Advanced Energy Materials*, vol. 5, no. 1, p. 1400867, 2015.

[20] B. D. McCloskey, J. M. Garcia, and A. C. Luntz, "Chemical and electrochemical differences in nonaqueous Li–O_2 and Na–O_2 batteries," *The journal of physical chemistry letters*, vol. 5, no. 7, pp. 1230–1235, 2014.

[21] C. L. Bender, P. Hartmann, M. Vraar, P. Adelhelm, and J. Janek, "On the thermodynamics, the role of the carbon cathode, and the cycle life of the sodium superoxide (NaO_2) battery," *Advanced Energy Materials*, vol. 4, no. 12, p. 1301863, 2014.

[22] X. Ren and Y. Wu, "A low-overpotential potassium–oxygen battery based on potassium superoxide," *Journal of the American Chemical Society*, vol. 135, no. 8, pp. 2923–2926, 2013.

[23] M. Yoshizawa-Fujita, K. Johansson, P. Newman, D. R. MacFarlane, and M. Forsyth, "Novel lewis-base ionic liquids replacing typical anions," *Tetrahedron letters*, vol. 47, no. 16, pp. 2755–2758, 2006.

[24] V. Gutmann, "Solvent effects on the reactivities of organometallic compounds," *Coordination Chemistry Reviews*, vol. 18, no. 2, pp. 225–255, 1976.

[25] Z. Peng, S. A. Freunberger, Y. Chen, and P. G. Bruce, "A reversible and higher-rate Li-O_2 battery," *Science*, vol. 337, no. 6094, pp. 563–566, 2012.

[26] B. J. Bergner, M. R. Busche, R. Pinedo, B. B. Berkes, D. Schroöder, and J. Janek, "How to improve capacity and cycling stability for next generation Li–O_2 batteries: approach with a solid electrolyte and elevated redox mediator concentrations," *ACS applied materials & interfaces*, vol. 8, no. 12, pp. 7756–7765, 2016.

[27] E. Mourad, Y. K. Petit, R. Spezia, A. Samojlov, F. F. Summa, C. Prehal, C. Leypold, N. Mahne, C. Slugovc, O. Fontaine *et al.*, "Singlet oxygen from cation driven superoxide disproportionation and consequences for aprotic metal–O_2 batteries," *Energy & Environmental Science*, vol. 12, no. 8, pp. 2559–2568, 2019.

[28] S. Borisov, G. Nuss, W. Haas, R. Saf, M. Schmuck, and I. Klimant, "New NIR-emitting complexes of platinum (II) and palladium (II) with fluorinated benzoporphyrins," *Journal of Photochemistry and Photobiology A: Chemistry*, vol. 201, no. 2-3, pp. 128–135, 2009.

[29] B. D. McCloskey, A. Valery, A. C. Luntz, S. R. Gowda, G. M. Wallraff, J. M. Garcia, T. Mori, and L. E. Krupp, “Combining accurate O_2 and Li_2O_2 assays to separate discharge and charge stability limitations in nonaqueous Li–O_2 batteries,” *The journal of physical chemistry letters*, vol. 4, no. 17, pp. 2989–2993, 2013.

[30] B. D. McCloskey, D. S. Bethune, R. M. Shelby, G. Girishkumar, and A. C. Luntz, “Solvents’ critical role in nonaqueous lithium–oxygen battery electrochemistry,” *The Journal of Physical Chemistry Letters*, vol. 2, no. 10, pp. 1161–1166, 2011.

[31] N. B. Aetukuri, B. D. McCloskey, J. M. García, L. E. Krupp, V. Viswanathan, and A. C. Luntz, “Solvating additives drive solution-mediated electrochemistry and enhance toroid growth in non-aqueous Li–O_2 batteries,” *Nature chemistry*, vol. 7, no. 1, p. 50, 2015.

[32] B. D. McCloskey, R. Scheffler, A. Speidel, G. Girishkumar, and A. C. Luntz, “On the mechanism of nonaqueous Li–O_2 electrochemistry on C and its kinetic overpotentials: some implications for Li–air batteries,” *The Journal of Physical Chemistry C*, vol. 116, no. 45, pp. 23 897–23 905, 2012.

[33] B. McCloskey, A. Speidel, R. Scheffler, D. Miller, V. Viswanathan, J. Hummelshøj, J. Nørskov, and A. Luntz, “Twin problems of interfacial carbonate formation in nonaqueous Li–O_2 batteries,” *The journal of physical chemistry letters*, vol. 3, no. 8, pp. 997–1001, 2012.

[34] Z. Zhao, J. Huang, and Z. Peng, “achilles’ heel of lithium–air batteries: lithium carbonate,” *Angewandte Chemie International Edition*, vol. 57, no. 15, pp. 3874–3886, 2018.

[35] J. Højberg, B. D. McCloskey, J. Hjelm, T. Vegge, K. Johansen, P. Norby, and A. C. Luntz, “An electrochemical impedance spectroscopy investigation of the overpotentials in Li–O_2 batteries,” *ACS applied materials & interfaces*, vol. 7, no. 7, pp. 4039–4047, 2015.

[36] X. Gao, Y. Chen, L. Johnson, and P. G. Bruce, “Promoting solution phase discharge in Li–O_2 batteries containing weakly solvating electrolyte solutions,” *Nature materials*, vol. 15, no. 8, p. 882, 2016.

[37] X. Gao, Z. P. Jovanov, Y. Chen, L. R. Johnson, and P. G. Bruce, “Phenol-catalyzed discharge in the aprotic lithium-oxygen battery,” *Angewandte Chemie*, vol. 129, no. 23, pp. 6639–6643, 2017.

[38] Y. Zhang, L. Wang, X. Zhang, L. Guo, Y. Wang, and Z. Peng, “High-capacity and high-rate discharging of a coenzyme Q10-catalyzed Li–O_2 battery,” *Advanced Materials*, vol. 30, no. 5, p. 1705571, 2018.

[39] J. Wandt, A. T. Freiberg, A. Ogrodnik, and H. A. Gasteiger, “Singlet oxygen evolution from layered transition metal oxide cathode materials and its implications for lithium-ion batteries,” *Materials Today*, vol. 21, no. 8, pp. 825–833, 2018.

[40] S. E. Renfrew and B. D. McCloskey, “Quantification of surface oxygen depletion and solid carbonate evolution on the first cycle of $LiNi_{0.6}Mn_{0.2}Co_{0.2}O_2$ electrodes,” *ACS Applied Energy Materials*, 2019.

Oxidation mediators for metal-air battery recharge

> *Each problem that I solved became a rule, which served afterwards to solve other problems.*
> René Descartes

Contents

Figures

Chapter based on Petit et al.[1]; Kwak, Petit[2]; Mourad†, Petit†et al.[3]

Introduction

Owing to their high capacity per mass and volume, alkali oxides provide an attractive energy storage. Unfortunately, alkali oxides are also wide-bandgap insulators, preventing efficient charge transport as described in part 1.2.1.3; the oxide's high resistivity hampers pores filling, limits discharge capacity and causes high charging voltages even at low rates[4–11]. Deeply discharged Li-O_2 cathodes through the solution pathway are filled with large Li_2O_2 particles with several 100 nm in size[5,8,10–13]. Oxidizing them on charge is relatively easy at the charge onset for Li_2O_2 directly in contact with the porous electrode[14–16]. Li_2O_2 more remote from the electrode surface, however, loses contact as charging proceeds, an effect seen with additives such as PeDTFSI in part 4.3.2, causing rising voltage and incomplete charge. The problems caused by the insulating nature of oxide, e.g Li_2O_2, particles being disconnected and parasitic chemistry are interrelated and particularly severe on charge[4–8,10,17–26]. Parasitic reactions on discharge form side products such as carbonates, which are hard to oxidize and may release $^1O_2$ as explain previouly. More of these side products form on charge with increasing rate as the charge voltage rises, self-amplifying the processes[19,20,27,28].

Since growth/dissolution of Li_2O_2 occurs at its surface, Li^+ and e^- transport into/out of the bulk particle are not required. The restriction of Li_2O_2's role to charge storage could be enabled by diffusion of available Li^+ and e^- at its surface through the electrolyte. Relocating the charge transport away from the peroxide circumvents, moreover, the issue of detached peroxide formed during discharge. The reactions could proceed away from the electrode and no discharge products would be lost. Bypassing alkali oxide for ion and electron transport may, in turn, enable high-power metal-O_2 cells. The main problem is the e^- transfer thought the electrolyte. During discharge, the charge transport can be assured by superoxide through the disproportionation process which correlates with higher discharge capacities as seen in part 1.2.1.1 and ch. 3. Disproportionation, yet, does not permit recharge of particles formed away from the electrode and is slow or not favoured for Na-O_2 and K-O_2 cells.

Redox mediators address the charge transport between the e^- conductor and O_2 or oxide distant from the electrode in a more controlled fashion[5,7,9,18,22,23,27,29–33]. Mediators act by being reduced/oxidized at the e^- conductor, diffusing through the electrolyte and reducing O_2 or oxidizing alkali oxide at low overpotentials, thereby being regenerated themselves. By switching electrode reactions to mediators reduction/oxidation, the peroxide becomes a convenient way to store charge which enables higher power batteries; the only requirements are faster reaction kinetic and mediators diffusion than the reaction through the highly resistive alkali oxides. Oxidation mediators allow, in principle, charging at nearly zero overpotential and a wide variety of mediators have been studied based on their redox potentials as well as O_2 evolution efficiency in Li-O_2 cells. First attempts were also done for Na-O_2 cells[5,9,18,22,23,29–34]. As the main concern is the formation of side products during charge and disconnect alkali oxides, this thesis will only focus on oxidation mediators. While numerous mediators are known in literature, little is known on the actual mediated oxidation mechanisms and their relations with parasitic chemistry. Oxidation mediators may also induce side reactions, if for example the oxidized mediators can oxidized the electrolyte solvent[9,27,29,35]. Since chemical oxidation of peroxides and superoxides in non-aqueous media by, e.g., chlorine or ferrocenium has been found to generate $^1O_2$, mediators may themselves contribute to its production[36–40]. The elementary steps during the mediated Li_2O_2 oxidation pathways and governing factors leading to $^3O_2$ or $^1O_2$ are yet to be described. Only knowing them in detail may allow designing mediators for $^1O_2$-free Li-O_2 battery recharge.

Using the methods previously described in this thesis, we decipher in this chapter the mechanism of mediated alkali peroxide/superoxide oxidation and identify pathways that lead to $^1O_2$. In a first step, one-electron mediated oxidation generates a superoxide intermediate from peroxide. The second step can either proceed via superoxide disproportionation or superoxide oxidation by mediators as depicted in Fig. 5.1. $^1O_2$ is hence not suppressed by oxidation mediators as it can form by disproportionation or oxidation at potentials higher than the thermodynamic threshold discussed in ch. 2. For low redox potential mediators, the $^1O_2$ amount is determined by the relative kinetics of the two pathways. We found that disproportionation cannot be neglected with commonly used mediators and, thus, $^1O_2$ production. Once the $^1O_2$ presence is established, the stability of oxidation mediators towards $^1O_2$ needs to be assessed. By using UV-vis spectroscopy, we found mediator degradations at significant rates when in contact with $^1O_2$. Mediators with quenching moieties, e.g. tertiary amines presented in ch. 4, display increased robustness most likely by deactivating singlet oxygen to its triple state and such moieties are consequently desirable for oxidation mediators. Chemical stability of mediators is also an essential parameter to ensure efficiency through long term cycling. We show that commonly used mediators, e.g. TEMPO or Fc, do not reform their reduced forms in contact with alkali oxide despite some O_2 release. Even low voltage mediators can spontaneously form highly oxidizing species in the case of mediators with multiples oxidation degrees, e.g. TDPA, resulting in $^1O_2$ evolution by mediated alkali oxide oxidation. The results establish the main characteristic desirable for oxidation mediators to avoid degradation and achieve good cyclability, i.e chemical stability, fast superoxide oxidation kinetic, and good $^1O_2$ quenching efficiency.

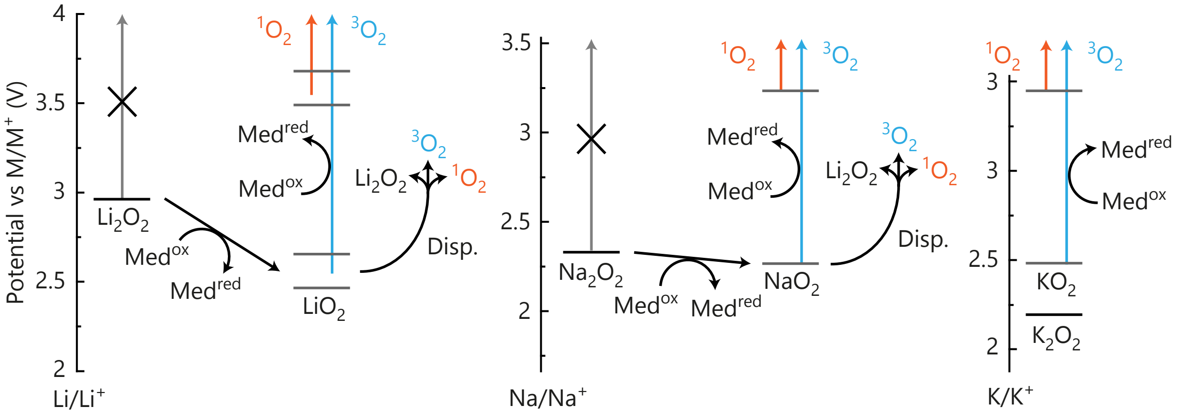

Figure 5.1: **Mediated alkali (su)peroxide oxidation mechanisms.** The crossed arrow represent

5.1 Oxidation mediators in metal-air batteries

Oxidation mediators are meant to be oxidized at the electrode and to oxidize in turn the alkali oxides, giving back the reduced mediator. The oxidation mediator being solvated any peroxide surface in contact with the solution can be subject to the reaction. Irrespective of the alkali oxide thickness or deposition geometry, the reaction potential is fixed by the mediator itself, if sufficient pristine carbon surface is present. By choosing appropriate mediators with a redox potential just above the O_2/MO_2 potential (M= Li_2, Na or K), e.g. 2.96 V_{Li/Li^+} for lithium based cells, nearly zero overpotential during charge is in principle possible. The promises of these soluble mediators on charge are tremendous for the field and numerous studied searched for appropriate mediators amongst either organic, organometallic or halide molecules[22,29,30,41]. Common given criteria are the molecule redox potential, a fast reaction kinetic to achieve a fast charging rate, to reduce the production of side products as well as stability in the Li-O_2 environment. Unless an impermeable separator is used, it also needs to be compatible with the lithium metal anode. Organic mediators have most widely been investigated owing to their variability[9,29].

While the exact mechanism was unknown, the reaction kinetic has been in first approximation decomposed into two steps. These are a heterogeneous oxidation of the mediators at the electrode surface (k_0) followed by the heterogeneous oxidation of Li_2O_2 by the oxidized mediators according to the overall reaction given in Eq. 5.1. Due to the lack of more precise mechanistic knowledge, divergent views have emerged in the literature. On the one hand, apparent rate constants (k_{app}) of the overall reactions at Li_2O_2 surface were determined using scanning electrochemical microscopy and compared to the k_0 obtained by cyclic voltammetry on glassy carbon for a wide range of mediators with potential ranging from ~3.1 to 3.85 V_{Li/Li^+}[31]. Since no clear dependence between k_0 and k_{app} appeared, it was concluded that the reaction between mediators and Li_2O_2 is an inner-sphere process and mostly governed by the sterics of the redox molecules. From the obtained k_{app}, it was calculated that, even for the slowest mediator, the apparent kinetic appears fast enough to sustain with a porous Li_2O_2 filled electrode a current density as high as ~100 $mA{\cdot}cm^{-2}$[31]. On the other hand, differential electrochemical mass spectrometry (DEMS) experiment showed a clear correlation between the onset potential for O_2 evolution and the mediator oxidation potential, a behaviour interpreted through an outer-sphere mechanism using Marcus theory and Nernst law[42]. O_2 evolution was moreover found to start at low mediator concentration (e.g. 10^{-5} M for TTF).

$$Li_2O_2 + 2\,Med^{ox} \longrightarrow 2\,Li^+ + 2\,Med^{red} + O_2 \tag{5.1}$$

As the apparent rate constants seem relatively high even for the slowest mediators and taking into account the wide range of potentials covered by organic molecules, the main criterion emerges as the influence on parasitic chemistry. Literature shows, yet again, discrepancies. Using mediators, online electrochemical mass spectrometry and pressure monitoring experiments showed an improved e^-/O_2 ratio[18] [23]. Other studies showed mediated oxidation of chemical Li_2O_2 that deviates from the theoretical 2 e^-/O_2 ratio, instability of some mediators in presence O_2, or presence of CO_2 production by action of mediators below the Li_2CO_3 oxidation potential. All these phenomena indicate the presence of side reactions[22,42].

The reactivity of some mediators could be explained by oxidation of the solvent rather than Li_2O_2, resulting in irreversibility[9] [27,29,35]. A mechanistic study rationalized this effect by comparing the position of the singly occupied molecular orbital of the oxidized mediators to the highest occupied molecular orbital of the solvent[9]. The stability of the mediators is especially problematic due to their often organic nature, and thus easily degradable at the contact with the lithium metal anode and potentially with singlet oxygen.

5.2 Mediated oxidation mechanism and singlet oxygen formation

The mediated alkali peroxide oxidation is commonly described by the overall reaction (Eq. 5.2)[5,7,9,18,23,29–34]. The exact mechanism of mediated alkali peroxide oxidation and pathways to $^1O_2$ have to be elucidate before designing mediators that allow for $^1O_2$-free metal-O_2 battery recharge. A previous study, yet, hinted the decomposition of the oxidation reaction in two individual steps based on DEMS experiment[42]. To decipher the mechanism, we hence hypothesized that mediated oxidation may follow two possible pathways. In the first case, oxidation could proceed via a direct two-electron oxidation as described in Eq. 5.1 with M^+ representing the alkali ions. In the second case, the overall oxidation could first proceed by the formation of superoxide species (noted MO_2 or superoxide through the rest of this chapter) through a mediated one-electron step according to Eq. 5.3. Once superoxide species are formed, the reaction can either continue with a second one-electron mediated oxidation described in Eq. 5.4 or by disproportionation as described in Eq. 5.5.

$$M_2O_2 + 2\,Med^{ox} \xrightarrow[k_{app}]{} 2\,M^+ + 2\,Med^{red} + O_2 \tag{5.2}$$

$$M_2O_2 + Med^{ox} \xrightarrow[k_1]{} M^+ + Med^{red} + MO_2 \tag{5.3}$$

$$MO_2 + Med^{ox} \xrightarrow[k_2]{} M^+ + Med^{red} + O_2 \tag{5.4}$$

$$MO_2 + MO_2 \xrightarrow[k_{disp}]{} M_2O_2 + x\,^3O_2 + (1-x)\,^1O_2 \tag{5.5}$$

5.2.1 Mediated oxidation pathways

Two $^1O_2$ production pathways emerge from the hypothetized elementary steps, either via disproportionation, as described in ch. 3, or via alkali oxide oxidation above a potential threshold (e.g. 3.45 V_{Li/Li^+} for Li_2O_2 and ~3.55 V_{Li/Li^+} for MO_2 with M = Li, Na, K), as described in part 2.3.2. Mediated alkali oxide oxidation could produce $^1O_2$ in accord with previous works. Its production was report from the reaction between O_2– and oxidized mediator with sufficiently high redox potentials such as Fc^+ (3.56 V_{Li/Li^+}, measured by CV in Fig. D.1 and Tab. D.1)[38–40]. Using a mediator with a potential below the $^1O_2$ potential threshold (MBT_2, 3.1 V_{Li/Li^+} measured by CV in Fig. D.1 and Tab. D.1) and a mediator above ($TEMPO^+$, 3.76 V_{Li/Li^+} measured by CV in Fig. D.1 and Tab. D.1), we performed characterisation of the $^3O_2$ and $^1O_2$ released upon oxidation of Li_2O_2 and KO_2 powders. The oxygen yield determinations are based on a combination of MS, UV-vis spectroscopy and HPLC, similarly to part 3.1 and further described in Appendices A.4, A.5, and A.6. KO_2 was used as stable substitute to LiO_2 due to its stability and similar redox potential. The mediators were chemically oxidized beforehand to avoid the presence of lithium ions in the superoxide case according to the procedure described in Appendix D.1. The results are illustrated in Fig. 5.2 and expressed in O_2 mol per 2 Med^{ox} for Li_2O_2 and O_2 mol per Med^{ox} for KO_2 corresponding to the theoritical yields given in Eq. 5.2 and Eq. 5.4.

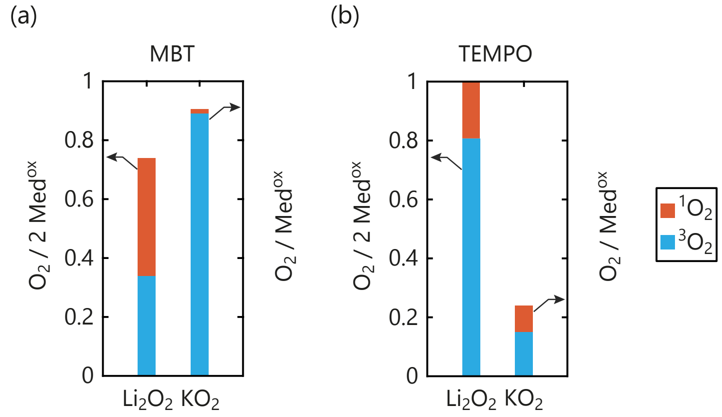

Figure 5.2: **$^3O_2$ and $^1O_2$ yields upon mediated peroxide and superoxide oxidations by MBT_2 and $TEMPO^+$.** $^3O_2$ and $^1O_2$ evolutions obtained by addition of 10 mM (a) MBT_2 or (b) $TEMPO^+$ in TEGDME to an excess of Li_2O_2 or KO_2.

$^1O_2$ formation from KO_2 and Li_2O_2 oxidation with $TEMPO^+$ indicates well that singlet oxygen can be produced via mediated alkali oxide oxidation. As KO_2 does not disproportionate in absence of more Lewis acidic cations, the important presence of $^1O_2$ can be safely associated with the superoxide oxidation. Singlet oxygen, yet, cannot be produced directly by mediators below ~3.5 V_{Li/Li^+} and its presence can then be used as a proxy for disproportionation as in part 3.3.3. Li_2O_2 oxidation with MBT_2 is accompanied by a clear release of singlet oxygen and a negligible one with KO_2, indicating LiO_2 disproportionation even in presence of mediators. If Li_2O_2 were oxidized by a direct two-electron process, no $^1O_2$ would be expected with Li_2O_2 and if singlet oxygen were produced by direct oxidation then it should also be formed with KO_2. The presence of disproportionation indicates hence a reaction in two steps as for non-mediated charge. Direct two-electron oxidation appears additionally unlikely since a trimolecular process with two mediators hitting the same surface spot at the same time would be required. Similarly, Na_2O_2 mediated oxidation occurs in two steps with superoxide as intermediate; The results are shown in Appendix E.3.4.

5.2.2 Mediated oxidation kinetics

The use of low potential oxidation mediators hence does not prevent disproportionation and subsequent $^1O_2$ formation. Oxidation mediators could reduce the disproportionation importance, and hence the $^1O_2$ yield, since there is competing kinetics between MO_2 disproportionation and mediated oxidation. To separate the influence of each kinetic, we measured the rate of the overall reaction between the mediators and Li_2O_2 (Eq. 5.2, k_{app}), the rate of the superoxide oxidation (Eq. 5.4, k_2) and the disproportionation rate (Eq. 5.5, k_{disp}) for a wide range of mediators ($TDPA^+$, MBT_2, $TMPD^+$, $DMPZ^+$, Fc^+, I_2[9,31,33,35]) covering potential from 3.09 to 3.63 V_{Li/Li^+} which are determined in Fig. D.1 and Tab. D.1.

Mediators were found to be all UV-vis active and their reaction rates were measured using their absorbance change starting at a known initial concentration. The oxidized mediator solutions were brought in contact with an excess of Li_2O_2 (k_{app}) or KO_2 (k_2) in pellet shapes with known surface area under agitation, exemplified by DMPZ in Fig. 5.3 and given in Fig. D.2 for the other mediators. The concentration decays overtime were then fitted and the rate at the initial time used to calculate the reaction kinetics according to a pseudo first-order reaction in first approximation. The initial rate was used to neglected side reaction influences as the reaction proceeds (e.g. by $^1O_2$ action or disproportionation as Li^+

will be released upon Li_2O_2 oxidation). The mediators were oxidized chemically to avoid the presence of Li^+ and parallel disproportionation of KO_2, as described in ch. 3. The methods are detailed in A.8. Measurements via UV-vis spectroscopy are also beneficial over scanning electrochemical microscopy to measure kinetics. They allow to detect possible side reactions not reforming the reduced mediators and probe the reactions on the surface as a whole[31]. The disproportionation rate (k_{disp}) was measured by pressure monitoring in a closed vessel after injection of 0.5 M a LiTFSI TEGDME electrolyte onto KO_2 pellets under similar condition according to Appendix A.9. The pressure evolution was then fitted by a second-order reaction kinetic represented by the Eq. 5.5, Eq. A.9, Eq. A.10 and Eq. A.11 and illustrated in Fig. 5.4. It can be noted that the obtained rates are minimal rates as the production of $^1O_2$ could not be detected by means of pressure measurements. We showed previously in ch. 3 that weak Lewis acids highly influences the disproportionation reaction and increased the $^1O_2$ production. Oxidized mediators are weakly Lewis acidic and their possible influences on disproportionation were modelled by measuring disproportionation in presence of a 0.5 M LiTFSI/0.5 M TBATFSI mixture in TEGDME. The presence of TBA^+ results in a more than 2.5 fold disproportionation rate increase.

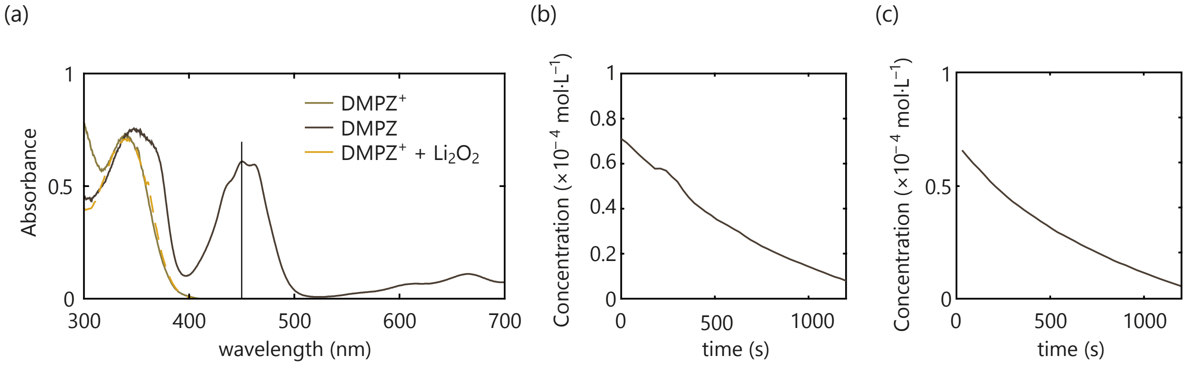

Figure 5.3: **Mediated oxidation rate with $DMPZ^+$ obtained by UV-vis spectroscopy.** (a) UV-Vis spectra of DMPZ (brown), $DMPZ^+$ (light brown) and $DMPZ^+$ after reaction on Li_2O_2 (dashed yellow). The black line denotes the wavelength used for kinetic measurements (450 nm). (b)-(c) $DMPZ^+$ concentration over time in contact with (b) KO_2 or (c) Li_2O_2 pellets

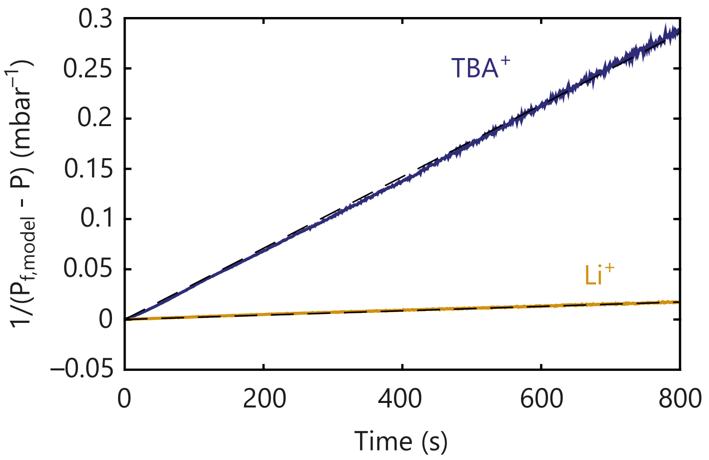

Figure 5.4: **Pressure evolution during KO_2 disproportionation in presence of Li^+ or Li^+/TBA^+ TEGDME electrolytes.** Electrolytes contained either 0.5 M LiTFSI (yellow) or 0.5 M LiTFSI and 0.5 M TBATFSI (purple). The fit obtained by Eq. A.11 are given in black dashed lines.

The overall reaction rate between the oxidized mediator and Li_2O_2 is composed of several elementary step which have been elucidated in the previous part. First, the reaction proceeds via a one-electron oxidation according to Eq. 5.3 (k_1), followed by either a second one electron oxidation or disproportionation. Areal mediated oxidation rates must be recalculated by assuming a mediator concentration ($v = k \cdot C_{mediator}$), here 10 mM, to be compared to the areal disproportionation rate (v_{disp}) at the solid superoxide surface. The initial disproportionation rate could then be compared to the mediator kinetics in Fig. 5.5; The range of v_{disp} values between pure Li^+ and Li^+/TBA^+ allows to determine the dominant kinetics and hence the major O_2 evolution pathway from superoxide in presence of a specific mediator. The k_{app} kinetics values obtained appears moreover similar to the ones obtained by SECM in the literature as shown in Fig. D.2.3[31].

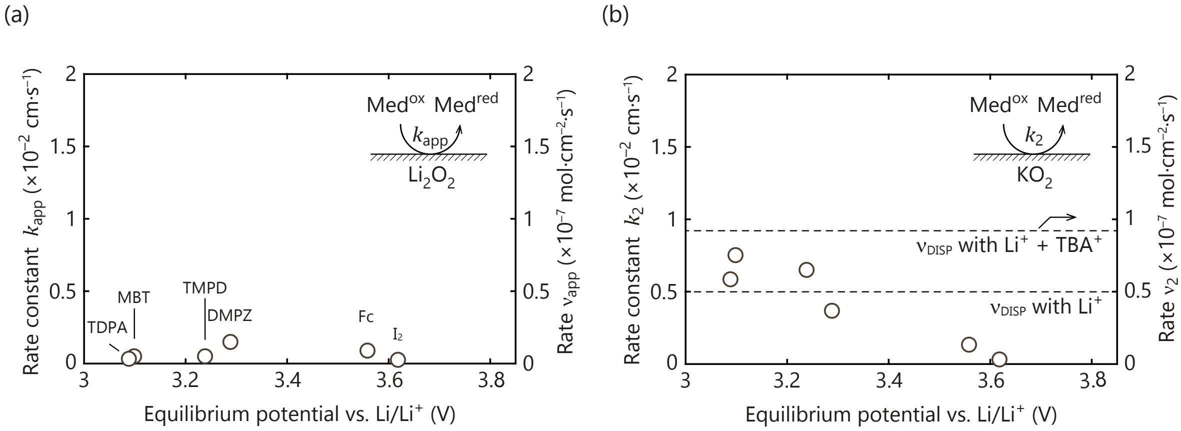

Figure 5.5: **Kinetics of mediated (su)peroxide oxidation and superoxide disproportionation.** Kinetic constants k (left axis) and reaction rates v assuming a 10 mM concentration (right axis) in TEGDME for the reaction between oxidized mediators and the Li_2O_2 surface (a) and the KO_2 surface (b) obtained by UV-vis spectroscopy. Superoxide disproportionation rates in presence of 0.5 M LiTFSI or 0.5 M LiTFSI and 0.5 M TBATFSI are indicated by dashed line in (b).

O_2 evolution is clearly dominated by disproportionation for mediators with redox potential above 3.5 V_{Li/Li^+}. For high potential oxidation mediators, the disproportionation rate in pure Li^+ electrolyte appears more than 3 times faster than mediated superoxide oxidation for a 10 mM concentration. The results are more nuanced for lower redox potential with mediated superoxide oxidation rates similar or slightly higher to disproportionation in pure Li^+ electrolyte. The disproportionation in the presence of TBA^+ as a model for soft Lewis acids, yet, stays faster than the mediated oxidation at a 10 mM concentration. Disproportionation is, similarly than for non-mediated cell, at least one of the main pathways to $^1O_2$ formation, especially in presence of weak Lewis acids such as oxidized mediators. The kinetics of the second step, be it oxidation or disproportionation, appears much faster than the overall reaction rate on Li_2O_2. The rate limiting reaction step is thus the first electron oxidation to form superoxide from peroxide.

5.2.3 Consequences

The presence of singlet oxygen permits to reveal the oxidation reaction mechanism which is summarized in Fig. 5.1. $^1O_2$ formation below 3.4 V_{Li/Li^+} from Li_2O_2 oxidation indicates the presence of disproportionation and hence of superoxide. Direct two-electron oxidation of Li_2O_2 or Na_2O_2, as described in more details in part 5.2.1 and Appendix E.3.4, may thus be excluded. The superoxide production is moreover the rate limiting step of the reaction and should be optimized to allow for fast reaction kinetic. By superoxide, we do not imply any particular species as it may, for example, be a Li-deficient solid solution $Li_{2-x}O_2$ phase or dissolved $LiO_{2(sol)}$ which have been proposed for non-mediated peroxide oxidation[4,6,12,24,25].

After superoxide formation, O_2 can subsequently evolve through two competing pathway, a second mediated oxidation or disproportionation. $^1O_2$ presence has been shown to result in important degradations in metal-air batteries in previous chapters (ch. 2 and 4). Mediated metal-air cells are no stranger to $^1O_2$ existence. Singlet oxygen can be formed by superoxide oxidation above ~3.55 V_{Li/Li^+} irrespective of direct or mediated electron transfer. High potential mediators show significant deficiencies in $^3O_2$ release, especially in contact with KO_2. In this case, the absence of strong Lewis cations inhibits the disproportionation reaction and $^1O_2$ must arise from the direct oxidation pathway.

Disproportionation yields $^1O_2$, especially in presence of weak Lewis acids as discussed in ch. 3. Widely $^1O_2$-free cells by mediated recharge are theoretically possible with low redox potential mediators since mediated superoxide oxidation would not results in $^1O_2$ release. The mediators should, yet, present sufficiently high superoxide oxidation kinetics to outpace and prevent parallel disproportionation. For the wide range of mediators tested here, $^1O_2$ induced by disproportionation is inevitable as its kinetic is at least comparable to the mediator ones at a 10 mM concentration. Efforts should hence be direct towards designing mediators with a fast superoxide oxidation kinetic and a low redox potential to reduce the $^1O_2$ yield during charge.

5.3 Reactivity of oxidation mediators with singlet oxygen

Among possible oxidation mediators, organic molecules have received special attention due to their variety and tunable oxidation potential via synthesis within the same chemical class[23]. Their organic natures, yet, make them susceptible to degradation by singlet oxygen, formed at all stages of cycling as discussed in ch. 2. Singlet oxygen is known for being dienophile and mediators possessing double bonds should be particularly sensitive to its presence, e.g. DMPZ, TTF, MPT or TMPD[9,22,31]. The presence of oxidation mediators does not necessarily prevent $^1O_2$ formation as explained in part 5.2. Since Li_2O_2 oxidation proceeds via superoxide formation, singlet oxygen can be formed by disproportionation even with low redox potential mediators. The reactivity of organic oxidation mediators towards $^1O_2$ needs to be assessed to ensure efficient effect during extended cycling and understand mechanisms favouring their stability.

Redox mediators may be reactive not only with $^1O_2$ but potentially to other oxygenated species present in metal-air battery chemistry, i.e., O_2, O_2^- and peroxide. We thus investigated the stability of some redox mediators towards these species. Among possibly reactive mediators, tetrathiafulvalene (TTF) and dimethylphenazine (DMPZ) were selected and shown in Fig. 5.6. Both TTF and DMPZ present good oxidative stability towards TEGDME, a common solvent in metal-air batteries[9]. TTF was also chosen for historical reason, being one of the first mediators proposed[22], and DMPZ due to its low redox potential[9]. TTF and DMPZ also contain heteroatoms that may influence their stability, sulfur or nitrogen respectively. As singlet oxygen is a known electrophile[43], we investigated the stability of both the reduced and oxidized states of the mediators to examine the impact of oxidation state on their reactivity[43].

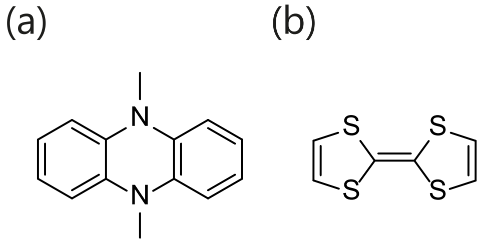

Figure 5.6: **Structure of the studied mediators.** (a) DMPZ (b) TTF.

5.3.1 Oxidation mediators in the reduced state

To determine the mediator stability, ^1H-NMR spectra in DMSO-d_6 were recorded for each mediator after 24 hours in presence of the oxygen species as described in A.10. By comparing with the pure substance ^1H-NMR spectrum in Fig. 5.7, neither dissolved O_2, dissolved O_2^- or Li_2O_2 reacts perceptibly with the studied mediators as previously reported in the case of DMPZ and O_2[9].

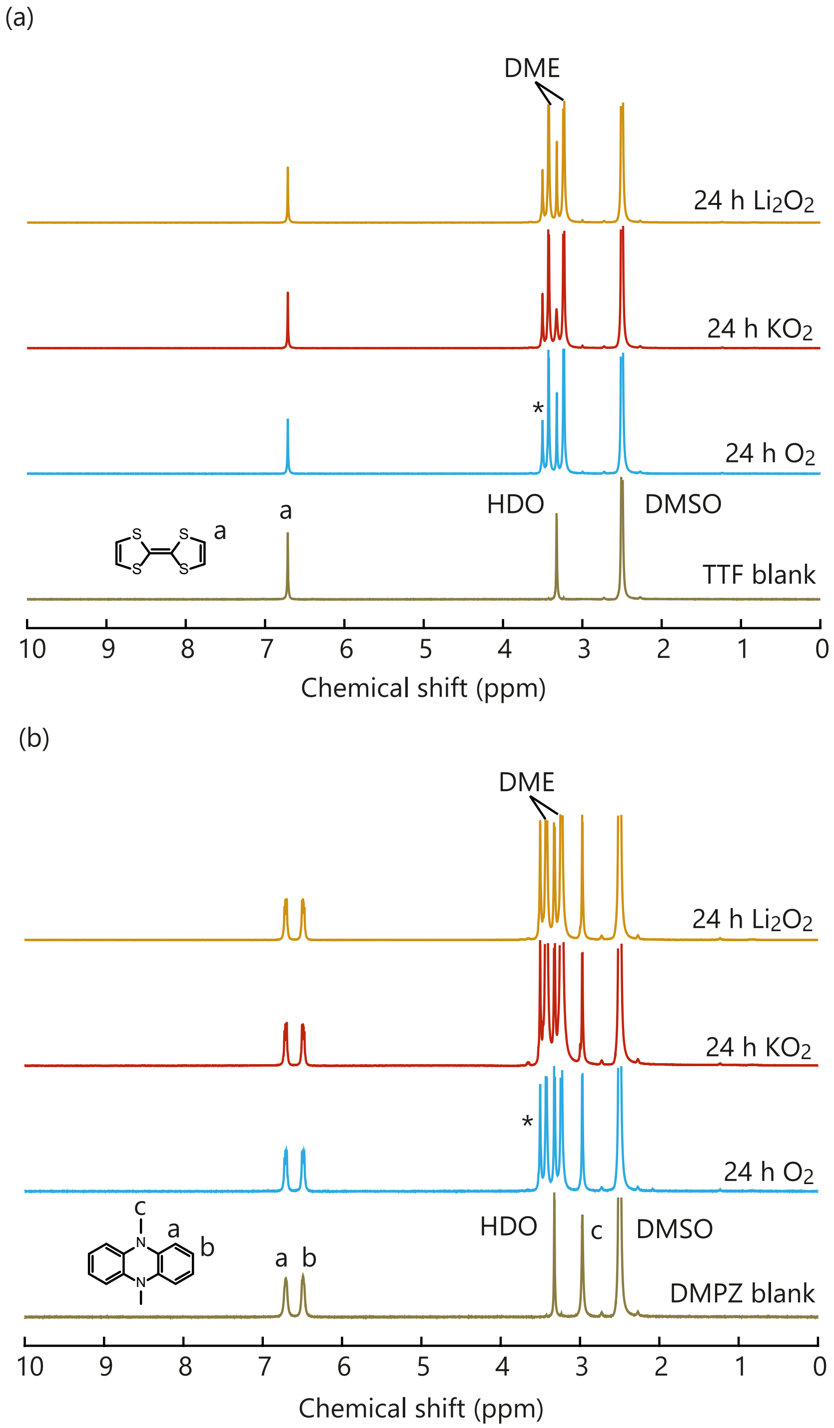

Figure 5.7: **Stability of DMPZ and TTF in contact with O_2, KO_2 and Li_2O_2 by ^{1}H-NMR.** The spectra were recorded in DMSO-d_6. ^{1}H-NMR spectra for (a) DMPZ and (b) TTF. The DMSO peak is taken as internal reference for quantitative comparison of spectra. The * denotes a residue from DME evaporation, which amounts to a content of 1 ppm in the DME.

As other oxygen species do not appears to react with the mediators, we investigate their stability against photochemically produced $^1O_2$ by means of Pd_4F and illumination at 643 nm, as described in part 2.2.1 and more in details in Appendix A.3. ^{1}H-NMR analys of the solutions were conducted after 3 hours illumination and show the mediator disappearances in Fig. 5.8. In the TTF case, the reactivity is clearly represented by the apparition of new peaks in the NMR spectrum; these new peaks indicate the formation of 1,3-dithiol-2-one, shown in insert of Fig. 5.8, in accord with a similar mechanism proposed in the literature[44]. Concerning the DMPZ, the NMR peak intensities decreased by ~40% according to the calculated integrals. The absence of new peaks may indicate that DMPZ decomposition ultimately forms inorganic products or evolves as gases. Nevertheless, the ^{1}H-NMR spectra unequivocally show organic mediators to react with $^1O_2$ despite their stability with other oxygenated species.

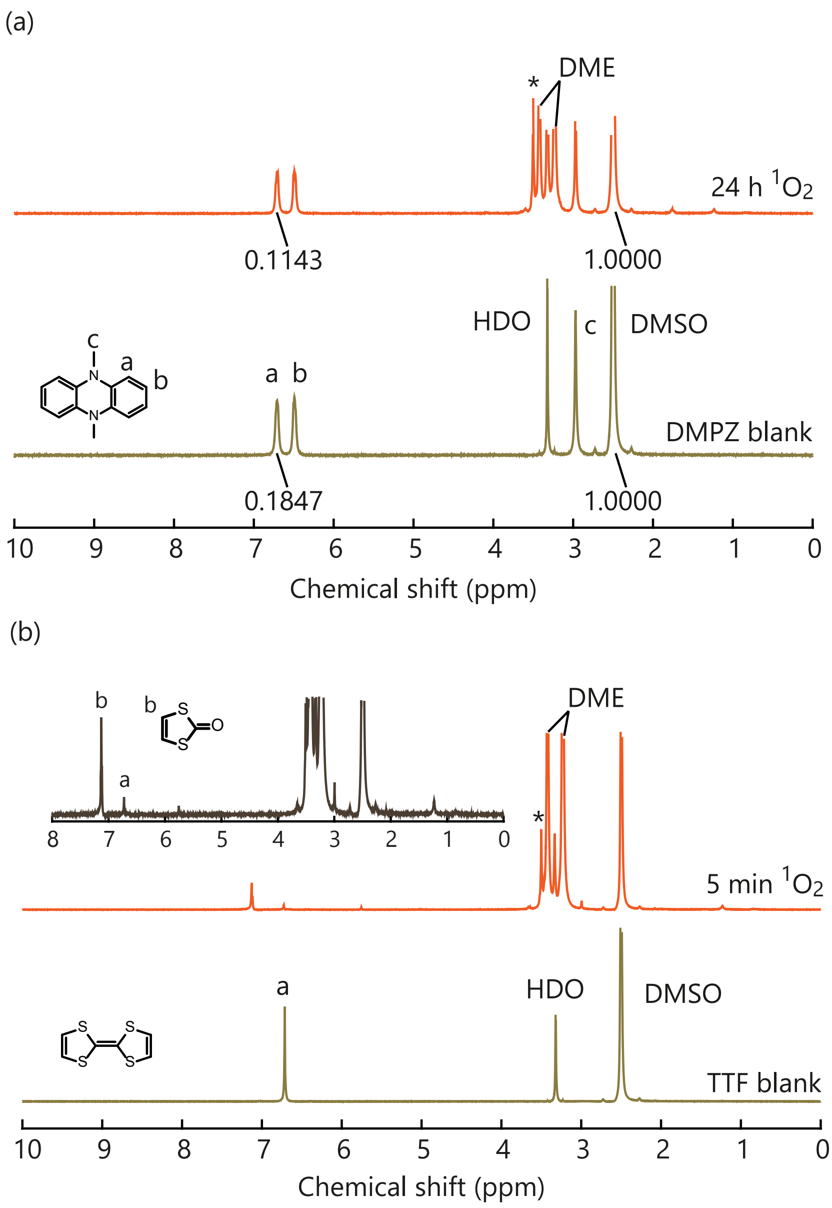

Figure 5.8: **Stability of DMPZ and TTF in contact with $^1O_2$ by ^{1}H-NMR.** The spectra were recorded in DMSO-d$_6$. ^{1}H-NMR spectra for (a) DMPZ after 3 hours exposure to $^1O_2$ and (b) TTF after 5 minutes exposure. The 1,3-dithiol-2-one ^{1}H-NMR spectrum is given in insert of (b) for comparison to the TTF ^{1}H-NMR spectrum after contact with $^1O_2$. The integrals are given for the peaks in (a). The DMSO peak is taken as internal reference for quantitative comparison of spectra. The * denotes a residue from DME evaporation, which amounts to a content of 1 ppm in the DME.

The concentration changes of DMPZ and TTF were monitored in-situ by UV-vis spectroscopy in presence of photochemically generated $^1O_2$. A mediator concentration of 60 μM in TEGDME has been determined as a suitable concentration for UV-vis spectroscopy beforehand and was used through out the rest of this study if not mentioned otherwise. The main absorbance peaks of each mediator were found to decrease over time accompanied by the appearance of new peaks, indicating side products formation with $^1O_2$, as illustrated in Fig. 5.9(a)-(c). TTF is much more reactive than DMPZ with a noticeable reaction in a few seconds where DMPZ necessitate a few hours. To illustrate clearly the different reaction rates, the change of the main absorbance peaks denoting either the disappearance of the mediators or the appearance of side products are given over $^1O_2$ exposure time in Fig. 5.9(b)-(d). TTF shows high reaction rate and fully decompose over approximately 30 s, revealed by the peaks evolution end. DMPZ is more robust and presents a decay of approximately one-thirds after 3 hours; the peak indicating side products stays stable after a bit more than 30 minutes, indicating formation of UV-vis inactive or gaseous species in accord with the ^{1}H-NMR spectra. Although reactivity with O_2, O_2^-, or Li_2O_2 over extended time cannot be completely dismissed, the mediators' reactivity with $^1O_2$ seems much more problematic, especially considering the possible presence of singlet oxygen at all stages of cycling.

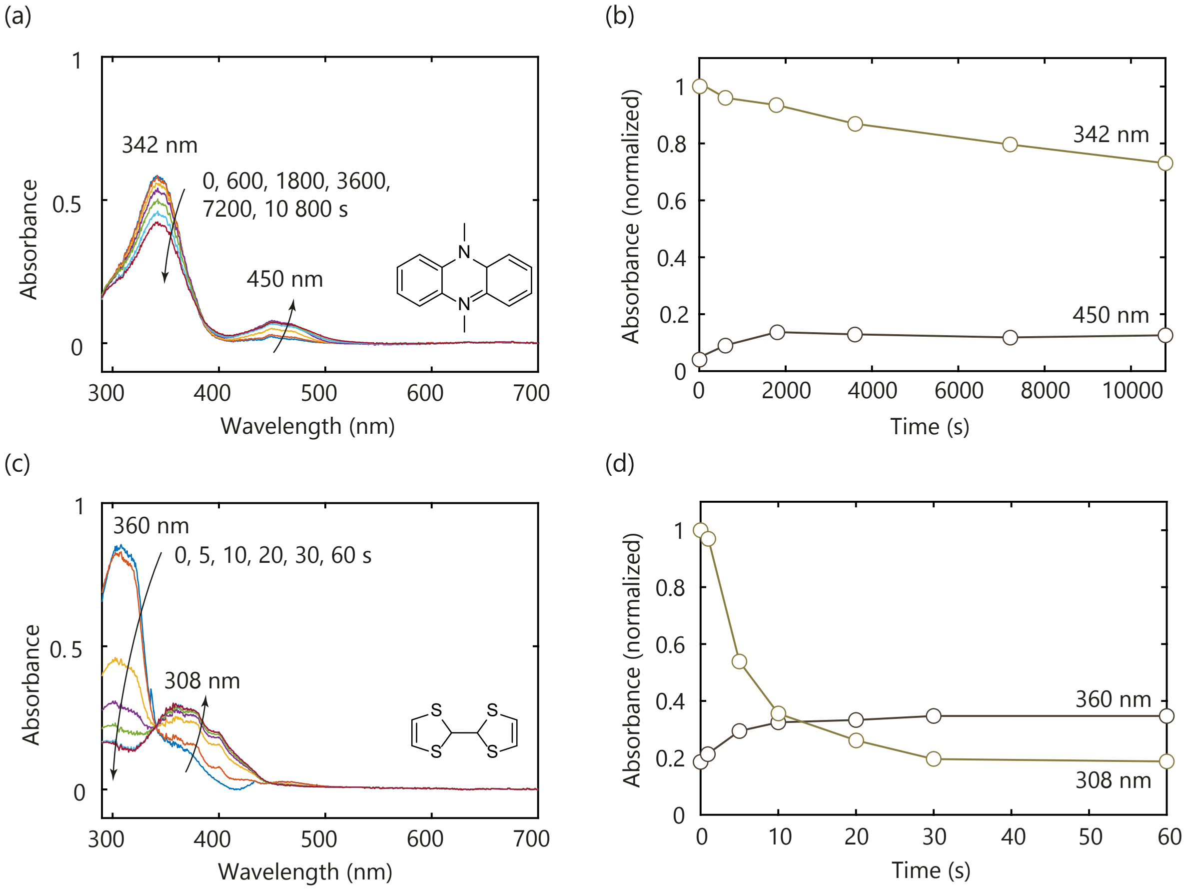

Figure 5.9: **Evolution of DMPZ and TTF concentrations in contact with $^1O_2$ over time by UV-vis spectroscopy.** (a)-(c) UV-Vis spectra of DMPZ (a) and TTF (c) in 0.1 M LiTFSI/TEGDME electrolyte upon $^1O_2$ exposure after substraction of the sensitizer signal. (b)-(d) Absorbance changes over time normalized to the initial value upon exposure to $^1O_2$ for (b) DMPZ and (d) TTF at the mentioned wavelength.

5.3.2 Oxidation mediators in the oxidized state

Since $^1O_2$ reactivity is associated to "ene" or "diene" reaction[45–48], the lower electronegativity of the oxidized mediators might results in increased stability. To verify this assumption, the oxidized form of the mediators at a concentration of ~250 μM were exposed to $^1O_2$ similarly to the previous paragraph and their evolutions followed by UV-vis spectroscopy, as depicted in Fig. 5.10(a)-(c). The details about the electrochemical oxidation procedure can be found in Appendix D.1. Both oxidized mediators present degradation albeit at slower rates than their reduced forms.

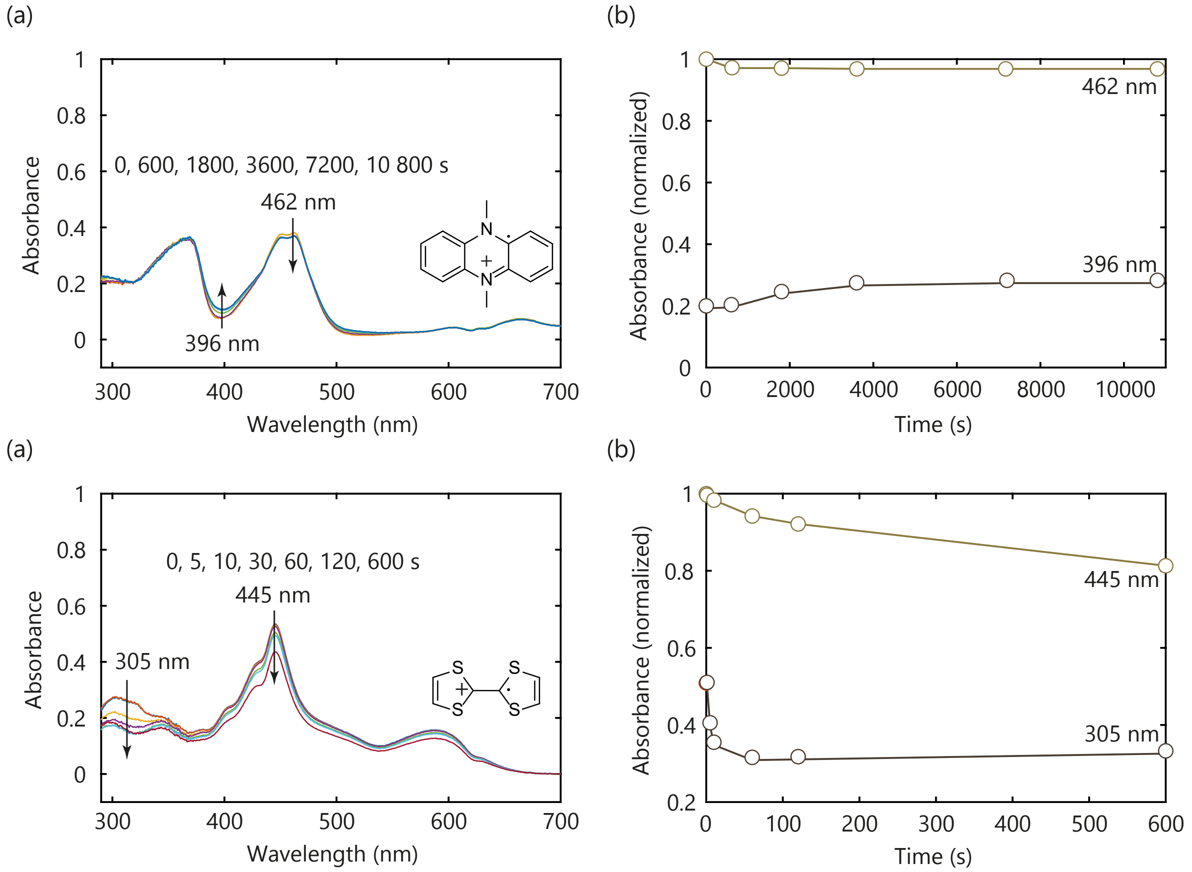

Figure 5.10: **Evolution of DMPZ$^+$ and TTF$^+$ concentrations in contact with $^1O_2$ over time by UV-vis spectroscopy.** (a)-(c) UV-Vis spectra of DMPZ$^+$ (a) and TTF$^+$ (c) in 0.1 M LiTFSI/TEGDME electrolyte upon $^1O_2$ exposure after substraction of the sensitizer signal. (b)-(d) Absorbance change over time normalized to the initial value upon exposure to $^1O_2$ for (b) DMPZ$^+$ and (d) TTF$^+$ at the mentioned wavelength.

DMPZ$^+$ shows a decrease of the 450 nm peak and increasing absorbance between 400 and 500 nm, which indicates the formation of degradation products over $^1O_2$ exposure time. Comparing now the rates of the reduced and oxidized forms from Fig. 5.9(b) and Fig. 5.10(b) respectively, after more than 3 hours illumination DMPZ$^+$ exhibits less than 5% degradation whereas the DMPZ only remains at 65% of its initial concentration. Likewise, TTF$^+$ is more stable than its reduced form but is still more reactive than DMPZ$^+$. TTF$^+$, yet, does not display clear degradation products peaks but rather a quick absorbance decrease in the 300 nm range and more gradual decrease through the rest of the spectrum. The spectrum change can nevertheless be attributed to mediator deactivation reactions. The TTF$^+$ reaction rate is more complicated to extract in light of the absence of clear peak trends. By taking the main absorbance peak at 445 nm, TTF$^+$ has reacted up to approximately one-third of its initial concentration within 10 minutes; for comparison, TTF was fully decomposed after ~30 s and is in other words roughly 150 times more reactive.

5.3.3 Consequences

Singlet oxygen is the main danger to organic mediators in metal-air batteries. Mediator reactivity with O_2, O_2^- and O_2^{2-} is comparatively smaller, if present at all. This high reactivity arises from the presence of double bond and oxidable heteroatoms such as sulfur[45–49]. The electrophilic nature of $^1O_2$ protects the oxidized state of the mediators compared to their reduced state. Even though oxidized mediators are more robust towards $^1O_2$, oxidation mediators are designed to be in their reduced forms during most of the cycling and the mediators as a whole would still be subject to severe deactivation in presence of $^1O_2$. As presented in ch. 4, singlet oxygen is one of the main sources of side reactivity in metal-air batteries and this is, hence, also applicable to organic additives. Design of new mediators should aim to reduce $^1O_2$ driven reactivity and present increased stability. We can draw conclusions from the different reaction rates between the TTF/TTF^+ and the $DMPZ/DMPZ^+$ couples. TTF/TTF^+ react much faster than their respective DMPZ counterparts. Mediators, as DMPZ or TDPA, may quench $^1O_2$ similarly to DABCO by dint of tertiary amines moieties and low oxidation potential[9,22,31]; The quenching mechanism of tertiary amines by charge transfer is described in part 4.1. Singlet oxygen quenching might explain the different reactivity between DMPZ and TTF and its effect will be described more in-depth in the following chapter. Quenching ability is nonetheless desirable for mediators since it would enhance their stability towards $^1O_2$. By tuning the quenching efficiency, even more robust mediators could be theoretically synthesized.

Despite its higher stability, DMPZ still reacts at non-negligible rate with $^1O_2$ and might not be sufficiently stable for long term cycling in Li-O_2 batteries. The necessity of $^1O_2$ mitigation is, thus, still required even for mediated metal-air cells. A combination of oxidation mediators with adapted physical quenchers, such as PeDTFSI described in ch. 4, can still be required to achieve long-time cycling and avoid $^1O_2$ related degradations. Even if mediators decrease the required oxidation potential threshold for effective quenchers, increases in potential were still observed after cycling in mediated cells due to the inevitable formation of carbonates after some cycles. Using quenchers that are stable through all the electrochemical window used in metal-air cells allows, thus, to prevent possible quencher degradation upon extensive cycling.

5.4 Oxidation mediators' chemical stability

The instability of organic mediators towards the highly reactive $^1O_2$ has been assessed in the previous part. The chemical stability of mediators is, yet, another important criterion for concrete usability in metal-O_2 cells. Fc^+ is for example known to be unstable in presence of $^3O_2$[50]. If mediators are chemically unstable, cell deterioration could be accelerated by inactive species build-up and possible further side reactions. The change in UV-vis signal of the oxidized mediator allows to verify the reformation of its reduced form once brought in contact with peroxide or superoxide as described in part 5.2.1. The mediator chemical instability towards oxygenated species can hence be easily verified and assesses efficient metal-O_2 mediator design.

5.4.1 Stability toward alkali oxides

Among the tested mediators, Fc^+ and $TEMPO^+$ showed non-exponential consumption over time accompanied by the absence of reduced mediators peaks appearing which hint the presence of side reactions. To verify their stability, the mentioned oxidized mediators were exposed to an excess of KO_2 or Li_2O_2 powders over 12 hours under agitation in Ar atmosphere and analysed by UV-vis spectroscopy. The resultant spectra are showed in Fig. 5.11. Both mediators do not reform their reduced state upon prolonged contact but new peaks emerge, indicating side products formation. Consumption of the Fc^+ mediators and oxygen release can be shown by UV-vis spectroscopy and mass spectrometry as described in part 5.2.1 and illustrated in Fig. D.2 and Fig. 5.11. Side products are, yet, formed during the alkali oxide oxidation rather than the reduced form of the mediator despite apparent reactivity. The spectral features of TEMPO and $TEMPO^+$ in conjunction with the formation of side products upon exposing $TEMPO^+$ to Li_2O_2 and KO_2 did not allow for reliable kinetic measurements using UV-Vis spectroscopy. Mass spectrometry measurements in Fig. 5.11(c)-(d) shows, however, clear O_2 production upon reaction with $TEMPO^+$ despite absence of TEMPO reformation in Fig. 5.11(b). The chemical stability of the mediator ought hence to be tested beforehand as they could appear active but are actually consumed during the reaction; Their use would result in accumulation of degradation products and the impossibility to sustain a high number of cycles.

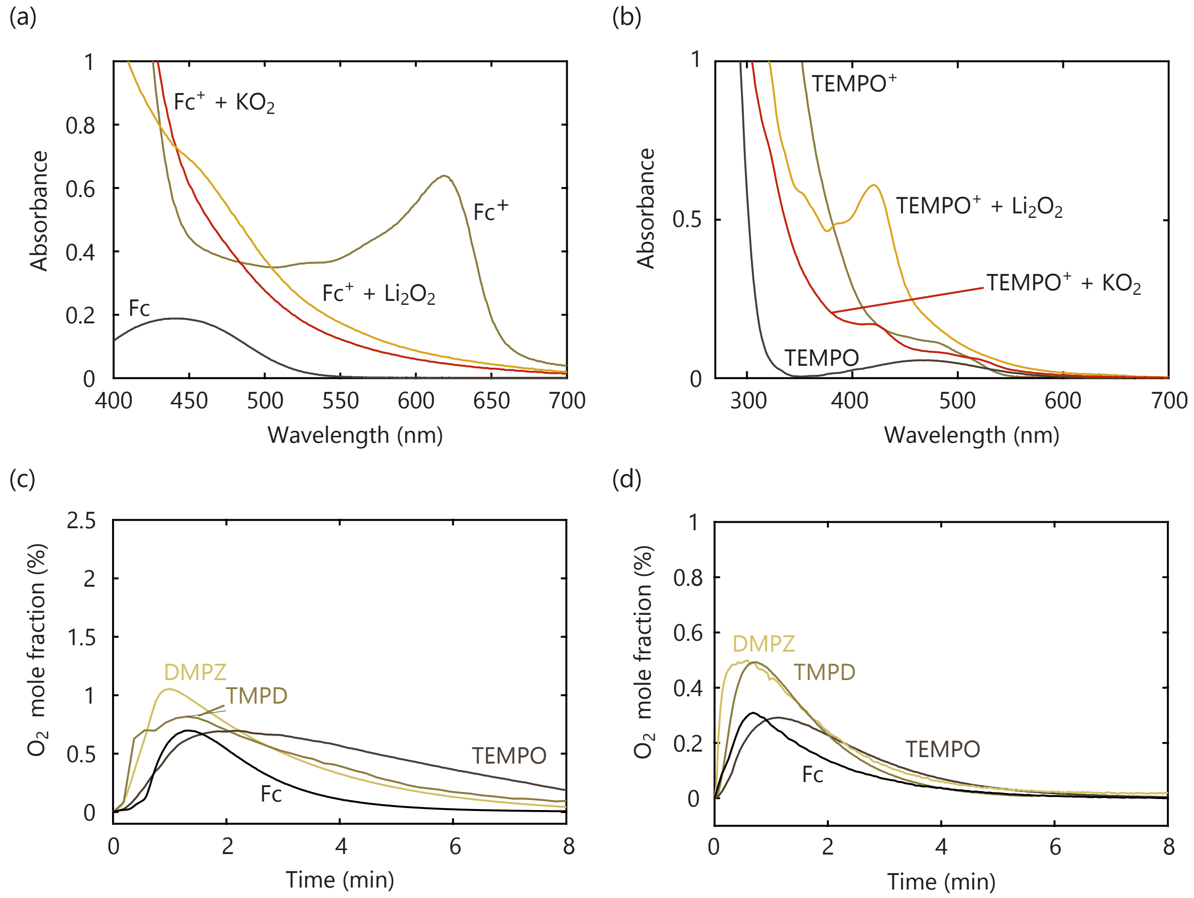

Figure 5.11: **Fc^+ and $TEMPO^+$ reactivity towards Li_2O_2 and KO_2.** UV-Vis spectra in 0.1 M LiTFSI TEGDME of 1 mM Fc, 1 mM $Fc^+BF_4^-$ or 1 mM $Fc^+BF_4^-$ after stirring for 12 h under Ar with an excess of Li_2O_2 or KO_2 powder, respectively, followed by filtering. (b) UV-Vis spectra in 0.1 M LiTFSI TEGDME of 5 mM TEMPO, 5 mM $TEMPO^+BF_4^-$ before or after stirring for 12 h under Ar with an excess of Li_2O_2 or KO_2 powder, respectively, followed by filtering. (c)-(d) $^3O_2$ evolution over time by MS upon mixing an excess of (c) Li_2O_2 or (d) KO_2 powder with 1 mM of the indicated oxidized mediators in TEGDME. For Li_2O_2 the electrolyte contained 0.1 M LiTFSI.

5.4.2 Oxidation state stability

TDPA presents also peculiar characteristics. TDPA induced O_2 evolution characterised by MS, UV-vis spectroscopy and HPLC, as described in part 5.2.1 and Appendices A.4, A.5, and A.6 shows significant $^3O_2$ deficiency and non-negligible $^1O_2$ production for both Li_2O_2 and KO_2 oxidation which is illustrated in Fig. 5.12. Considering the TDPA's low redox potential of 3.09 V_{Li/Li^+} and presence of potentially quenching amine moieties, only a small proportion of singlet oxygen should be formed with peroxide and none with superoxide in absence of disproportionation.

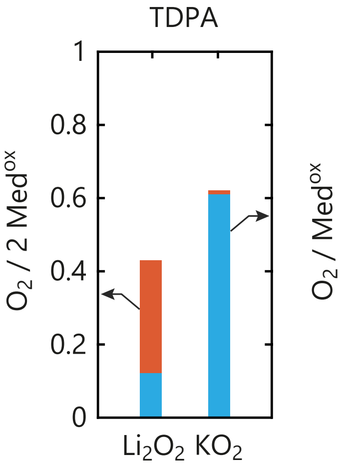

Figure 5.12: **$^3O_2$ and $^1O_2$ yield upon mediated peroxide and superoxide oxidation by TDPA$^+$.** $^3O_2$ and $^1O_2$ evolution obtained by the addition of 10 mM TDPA$^+$ in TEGDME to an excess of Li_2O_2 or KO_2 powder.

We hence hypothesized spontaneous formation of TDPA^{2+}. The TDPA$^+$/TDPA^{2+} couple has a redox potential of ~3.5 V_{Li/Li^+} and could yield $^1O_2$ by alkali oxide oxidation as it is similar to the potential threshold of $^1O_2$ given in part 2.3.2[33]. To demonstrate this assumption, TDPA$^+$ was produced electrochemically at a potential just sufficient for TDPA oxidation (3.15 V_{Li/Li^+} or $E^0_{TDPA/TDPA^+}$ + 60 mV), but well below the TDPA$^+$ oxidation potential. The oxidation was conducted to reach half conversion of the TDPA present on a glassy carbon electrode in a 0.1 M LiTFSI DME electrolyte. The resulting solution was separated by thin-layer chromatography (TLC) on an Al_2O_3 plate with ethyl acetate/ethanol (1/1) as eluent. The TLC plate, shown in Fig. 5.13(a), exhibits three different species after separation. The three differently coloured spots were separately analysed by UV-Vis spectroscopy and compared with simulated spectra of TDPA, TDPA$^+$ and TDPA^{2+} in Fig. 5.13(b)-(c). The DFT calculation details are given in Appendix D.2.4. One of the species shows the characteristic absorbance peaks associated with the modelled TDPA^{2+} whereas the others correspond to TDPA and TDPA$^+$. The UV-vis spectra hence confirm the spontaneous formation of TDPA^{2+} from a mixture of TDPA, TDPA$^+$ and LiTFSI in glyme in O_2 atmosphere. The results highlight that mediators with a redox couple below 3.5 V_{Li/Li^+} can still produce singlet oxygen by alkali oxide oxidation if highly oxidizing further oxidation steps exist and form spontaneously. Newly designed mediators should hence be carefully tested to verify their chemical stabilities, e.g. by testing for presence of $^1O_2$ after KO_2 oxidation in absence of disproportionation.

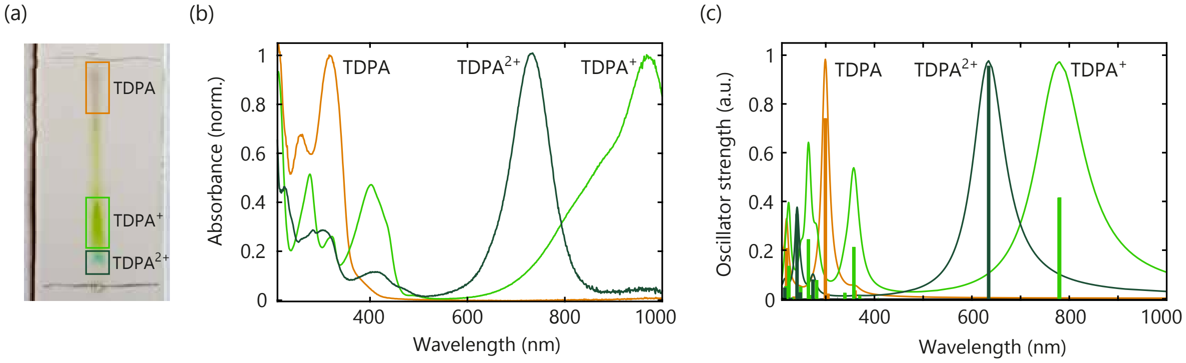

Figure 5.13: **$TDPA^+$ stability and spontaneous formation of highly oxidizing $TDPA^{2+}$** (a) Thin-layer chromatogram (TLC) of a partially oxidized TDPA solution under O_2, showing spontaneous occurrence of $TDPA^{2+}$ in a TDPA/$TDPA^+$ solution. (b) Respective UV-Vis spectra of the framed spots in (a) after dissolving them in methanol and normalized to the most intense peak. (c) Simulated UV-Vis spectra of TDPA, $TDPA^+$, and $TDPA^{2+}$ in methanol according to Appendix D.2.4. The stems show non-normalized oscillator strengths whereas the envelopes are normalized to the most intense peaks.

Conclusion

In conclusion, oxidation mediators hold the colossal promise of low overpotential recharge at fast rates and have been intensely studied on their own right. Disconnecting the electronic and ionic transports from the insulting alkali oxide allows to remove one of the reasons for high overpotentials during charge. Oxidation mediators pin, indeed, the charge potential to their own redox potential. Given that low potentials may be attained, oxidation mediators were suggested to avoid side reactions although data did not consistently show a clear reduction of side product formation. Despite the wide range of mediators tested in metal-O_2 cells, mechanistic descriptors of the reaction were lacking to provide efficient design rules and to achieve truly efficient mediation. While there were previous attempts to describe the mediated oxidation mechanism, kinetic influence, or stability, we could show clearly the presence of competing reaction steps within the mediated oxidation process and the importance of the mediator stability, especially towards singlet oxygen which is already identified as a main sources of degradation in non-mediated cells.

Using $^1O_2$ presence as a marker for disproportionation below the thermodynamic threshold for $^1O_2$ induced by alkali oxide oxidation, we showed that the mediated oxidation proceeds in different elementary steps. The first one is a one-electron extraction forming superoxide species. Once formed, the superoxide can either be oxidized via another one-electron step or disproportionate as described for non-mediated cells. This result is of high importance considering $^1O_2$. We have established before that disproportionation yields $^1O_2$, especially in presence of weak Lewis acids such as oxidized mediators. Cells using mediators with a redox potential below the $^1O_2$ threshold are hence not immune to $^1O_2$ production during charge. The relative importance of the two pathways is dictated by the competition of their respective kinetic. A high rate of mediated superoxide oxidation could allow to bypass the disproportionation reaction and hence $^1O_2$ by using mediators with low redox potential. Our results show, however, that current mediators do not present sufficiently high kinetics to sufficiently suppress disproportionation. The second electron extraction or disproportionation are, yet, not the overall rate limiting steps. With high reaction rates in mind, mediators should also have high reaction kinetic with peroxide. The mediation kinetics are hence of prime importance, not only for high power batteries, but also for the parasitic chemistry.

Since oxidation mediators do not necessarily prevent the presence of $^1O_2$, we assessed their reactivity with this very aggressive species. The majority of the proposed mediators are organic molecules owing to their wide variety and adaptability through adapted synthesis. $^1O_2$ is, however, a known electrophile and can react with double bonds. DMPZ and TTF, taken as typical examples of mediators, showed clear reactivity with $^1O_2$ at significant rates. The oxidized forms of the mediators present increased stability due to their reduced electron density but still noticeably react albeit at slower rates. DMPZ is markedly more resistant to $^1O_2$ contact than TTF. This robustness can in part be ascribed to the presence of tertiary amines moieties that are known to physically quench $^1O_2$ to its ground state. The low redox potential of the mediators should allow for relatively high molar efficiency as described in ch. 4. The presence of quenching moieties is hence desirable in oxidation mediators to increase their stability in long term cycling since the presence of singlet oxygen appears currently inevitable. The addition of an external quencher, e.g. PeDTFSI, can act as a safeguard and prevent deactivation of the mediators and unwanted accumulation of side products in the cell.

The chemical stability of oxidation mediators should moreover not be overlooked. Fc^+ and $TEMPO^+$ showed substantial degradations in contact with alkali oxides. Despite irreversibly, the aforementioned mediators react with alkali oxides, release O_2 and could appear as efficient mediators. Their action would nevertheless be constrained to a few cycles as they would be consumed over time. The chemical stability of mediators with several oxidation states can also be questioned. $TDPA^+$ in a Li^+ electrolyte was shown to form spontaneously the high redox potential $TDPA^{2+}$. $TDPA^{2+}$ can then induce $^1O_2$ formation from alkali oxide oxidation as its potential is close to the thermodynamic threshold. Determination of the mediator's chemical stability is then a prerequisite before its use in a metal-O_2 cell. The conclusions drawn here from the reaction mechanisms could be further used to provide design rules for future oxidation mediators.

Bibliography

[1] Y. K. Petit, E. Mourad, and S. A. Freunberger, "Encyclopedia of electrochemistry, section on batteries, ch. 19 lithium–oxygen batteries," in revision.

[2] W.-J. Kwak, H. Kim, Y. K. Petit, C. Leypold, T. T. Nguyen, N. Mahne, P. Redfern, L. A. Curtiss, H.-G. Jung, S. M. Borisov *et al.*, "Deactivation of redox mediators in lithium-oxygen batteries by singlet oxygen," *Nature communications*, vol. 10, no. 1, p. 1380, 2019.

[3] E. Mourad, Y. K. Petit, C. Leypold, A. Windischbacher, D. Mijailovic, C. Slugovc, S. M. Borisov, E. Zojer, S. Brutti, O. Fontaine, and S. A. Freunberger, "Mechanism of mediated alkali peroxide oxidation reveals strategies to suppress singlet oxygen formation," in revision.

[4] Y.-C. Lu, B. M. Gallant, D. G. Kwabi, J. R. Harding, R. R. Mitchell, M. S. Whittingham, and Y. Shao-Horn, "Lithium–oxygen batteries: bridging mechanistic understanding and battery performance," *Energy & Environmental Science*, vol. 6, no. 3, pp. 750–768, 2013.

[5] D. Aurbach, B. D. McCloskey, L. F. Nazar, and P. G. Bruce, "Advances in understanding mechanisms underpinning lithium–air batteries," *Nature Energy*, vol. 1, no. 9, p. 16128, 2016.

[6] Y. Wang, N.-C. Lai, Y.-R. Lu, Y. Zhou, C.-L. Dong, and Y.-C. Lu, "A solvent-controlled oxidation mechanism of Li_2O_2 in lithium-oxygen Batteries," *Joule*, vol. 2, no. 11, pp. 2364–2380, 2018.

[7] Y. Ko, H. Park, B. Kim, J. S. Kim, and K. Kang, "Redox mediators: A solution for advanced lithium–oxygen batteries," *Trends in Chemistry*, 2019.

[8] X. Gao, Y. Chen, L. Johnson, and P. G. Bruce, "Promoting solution phase discharge in Li–O_2 batteries containing weakly solvating electrolyte solutions," *Nature materials*, vol. 15, no. 8, p. 882, 2016.

[9] H.-D. Lim, B. Lee, Y. Zheng, J. Hong, J. Kim, H. Gwon, Y. Ko, M. Lee, K. Cho, and K. Kang, "Rational design of redox mediators for advanced Li–O_2 batteries," *Nature Energy*, vol. 1, no. 6, p. 16066, 2016.

[10] N. B. Aetukuri, B. D. McCloskey, J. M. García, L. E. Krupp, V. Viswanathan, and A. C. Luntz, "Solvating additives drive solution-mediated electrochemistry and enhance toroid growth in non-aqueous Li–O_2 batteries," *Nature chemistry*, vol. 7, no. 1, p. 50, 2015.

[11] T. Liu, J. T. Frith, G. Kim, R. N. Kerber, N. Dubouis, Y. Shao, Z. Liu, P. C. Magusin, M. T. Casford, N. Garcia-Araez, and C. P. Grey, "The effect of water on quinone redox mediators in nonaqueous Li-O_2 batteries," *Journal of the American Chemical Society*, vol. 140, no. 4, pp. 1428–1437, 2018.

[12] S. Ganapathy, B. D. Adams, G. Stenou, M. S. Anastasaki, K. Goubitz, X.-F. Miao, L. F. Nazar, and M. Wagemaker, "Nature of Li_2O_2 oxidation in a Li–O_2 battery revealed by operando X-ray diffraction," *Journal of the American Chemical Society*, vol. 136, no. 46, pp. 16 335–16 344, 2014.

[13] D. G. Kwabi, M. Tuodziecki, N. Pour, D. M. Itkis, C. V. Thompson, and Y. Shao-Horn, "Controlling solution-mediated reaction mechanisms of oxygen reduction using potential and solvent for aprotic lithium–oxygen batteries," *The journal of physical chemistry letters*, vol. 7, no. 7, pp. 1204–1212, 2016.

[14] B. D. McCloskey, R. Scheffler, A. Speidel, G. Girishkumar, and A. C. Luntz, "On the mechanism of nonaqueous Li–O_2 electrochemistry on C and its kinetic overpotentials: some implications for Li–air batteries," *The Journal of Physical Chemistry C*, vol. 116, no. 45, pp. 23 897–23 905, 2012.

[15] V. Viswanathan, J. Nørskov, A. Speidel, R. Scheffler, S. Gowda, and A. Luntz, "Li–O_2 kinetic overpotentials: Tafel plots from experiment and first-principles theory," *The journal of physical chemistry letters*, vol. 4, no. 4, pp. 556–560, 2013.

[16] Y. Chen, S. A. Freunberger, Z. Peng, F. Bardé, and P. G. Bruce, "Li–O_2 battery with a dimethylformamide electrolyte," *Journal of the American Chemical Society*, vol. 134, no. 18, pp. 7952–7957, 2012.

[17] J. W. Choi and D. Aurbach, "Promise and reality of post-lithium-ion batteries with high energy densities," *Nature Reviews Materials*, vol. 1, no. 4, p. 16013, 2016.

[18] Z. Liang and Y.-C. Lu, "Critical role of redox mediator in suppressing charging instabilities of lithium–oxygen batteries," *Journal of the American Chemical Society*, vol. 138, no. 24, pp. 7574–7583, 2016.

[19] B. McCloskey, A. Speidel, R. Scheffler, D. Miller, V. Viswanathan, J. Hummelshøj, J. Nørskov, and A. Luntz, "Twin problems of interfacial carbonate formation in nonaqueous Li–O_2 batteries," *The journal of physical chemistry letters*, vol. 3, no. 8, pp. 997–1001, 2012.

[20] B. D. McCloskey, D. Bethune, R. Shelby, T. Mori, R. Scheffler, A. Speidel, M. Sherwood, and A. Luntz, "Limitations in rechargeability of Li-O_2 batteries and possible origins," *The journal of physical chemistry letters*, vol. 3, no. 20, pp. 3043–3047, 2012.

[21] T. Liu, G. Kim, M. T. Casford, and C. P. Grey, "Mechanistic insights into the challenges of cycling a nonaqueous Na–O_2 battery," *The journal of physical chemistry letters*, vol. 7, no. 23, pp. 4841–4846, 2016.

[22] Y. Chen, S. A. Freunberger, Z. Peng, O. Fontaine, and P. G. Bruce, "Charging a Li–O_2 battery using a redox mediator," *Nature chemistry*, vol. 5, no. 6, p. 489, 2013.

[23] B. J. Bergner, A. Schürmann, K. Peppler, A. Garsuch, and J. Janek, "TEMPO: a mobile catalyst for rechargeable Li-O_2 batteries," *Journal of the American Chemical Society*, vol. 136, no. 42, pp. 15 054–15 064, 2014.

[24] Y.-C. Lu and Y. Shao-Horn, "Probing the reaction kinetics of the charge reactions of nonaqueous Li–O_2 batteries," *The journal of physical chemistry letters*, vol. 4, no. 1, pp. 93–99, 2012.

[25] S. Kang, Y. Mo, S. P. Ong, and G. Ceder, "A facile mechanism for recharging Li_2O_2 in Li–O_2 batteries," *Chemistry of Materials*, vol. 25, no. 16, pp. 3328–3336, 2013.

[26] J. Wang, Y. Zhang, L. Guo, E. Wang, and Z. Peng, "Identifying reactive sites and transport limitations of oxygen reactions in aprotic lithium-O_2 batteries at the stage of sudden death," *Angewandte Chemie International Edition*, vol. 55, no. 17, pp. 5201–5205, 2016.

[27] C. M. Burke, R. Black, I. R. Kochetkov, V. Giordani, D. Addison, L. F. Nazar, and B. D. McCloskey, "Implications of 4 e^- oxygen reduction via iodide redox mediation in Li–O2 batteries," *ACS Energy Letters*, vol. 1, no. 4, pp. 747–756, 2016.

[28] M. M. Ottakam Thotiyl, S. A. Freunberger, Z. Peng, and P. G. Bruce, "The carbon electrode in nonaqueous Li–O_2 cells," *Journal of the American Chemical Society*, vol. 135, no. 1, pp. 494–500, 2012.

[29] J.-B. Park, S. H. Lee, H.-G. Jung, D. Aurbach, and Y.-K. Sun, “Redox mediators for Li–O_2 batteries: status and perspectives,” *Advanced Materials*, vol. 30, no. 1, p. 1704162, 2018.

[30] V. Pande and V. Viswanathan, “Criteria and considerations for the selection of redox mediators in nonaqueous Li–O_2 batteries,” *ACS Energy Letters*, vol. 2, no. 1, pp. 60–63, 2016.

[31] Y. Chen, X. Gao, L. R. Johnson, and P. G. Bruce, “Kinetics of lithium peroxide oxidation by redox mediators and consequences for the lithium–oxygen cell,” *Nature communications*, vol. 9, no. 1, p. 767, 2018.

[32] X. Gao, Y. Chen, L. R. Johnson, Z. P. Jovanov, and P. G. Bruce, “A rechargeable lithium–oxygen battery with dual mediators stabilizing the carbon cathode,” *Nature Energy*, vol. 2, no. 9, p. 17118, 2017.

[33] D. Kundu, R. Black, B. Adams, and L. F. Nazar, “A highly active low voltage redox mediator for enhanced rechargeability of lithium–oxygen batteries,” *ACS central science*, vol. 1, no. 9, pp. 510–515, 2015.

[34] I. Landa-Medrano, I. Lozano, N. Ortiz-Vitoriano, I. R. de Larramendi, and T. Rojo, “Redox mediators: a shuttle to efficacy in metal–O_2 batteries,” *Journal of Materials Chemistry A*, vol. 7, no. 15, pp. 8746–8764, 2019.

[35] G. Leverick, M. Tuodziecki, R. Tatara, F. Bardé, and Y. Shao-Horn, “Solvent-Dependent Oxidizing Power of LiI Redox Couples for Li-O_2 Batteries,” *Joule*, vol. 3, no. 4, pp. 1106–1126, 2019.

[36] Q. Li, F. Chen, W. Zhao, M. Xu, B. Fang, Y. Zhang, L. Duo, Y. Jin, and F. Sang, “A spectroscopic study on singlet oxygen production from different reaction paths using solid inorganic peroxides as starting materials,” *Bulletin of the Korean Chemical Society*, vol. 28, no. 10, pp. 1656–1660, 2007.

[37] ——, “Singlet oxygen production in the reaction of potassium superoxide with chlorine,” *Chemistry letters*, vol. 36, no. 4, pp. 496–497, 2007.

[38] E. A. Mayeda and A. J. Bard, “Production of singlet oxygen in electrogenerated radical ion electron transfer reactions,” *Journal of the American Chemical Society*, vol. 95, no. 19, pp. 6223–6226, 1973.

[39] S. Senthil Kumar and A. J. Bard, “Background Emission of Electrogenerated Chemiluminescence during Oxidation of Tri-n-propylamine from the Dimeric $^1\Delta_g$ State of O_2,” *Analytical chemistry*, vol. 85, no. 1, pp. 292–295, 2012.

[40] W. Ando, Y. Kabe, S. Kobayashi, C. Takyu, A. Yamagishi, and H. Inaba, “Formation of sulfinyl oxide and singlet oxygen in the reaction of thianthrene cation radical and superoxide ion,” *Journal of the American Chemical Society*, vol. 102, no. 13, pp. 4526–4528, 1980.

[41] B. D. McCloskey and D. Addison, “A viewpoint on heterogeneous electrocatalysis and redox mediation in nonaqueous Li-O_2 batteries,” 2016.

[42] P. P. Bawol, P. Reinsberg, C. J. Bondue, A. A. Abd-El-Latif, P. Königshoven, and H. Baltruschat, “A new thin layer cell for battery related DEMS-experiments: the activity of redox mediators in the Li–O_2 cell,” *Physical Chemistry Chemical Physics*, vol. 20, no. 33, pp. 21 447–21 456, 2018.

[43] I. Saito, T. Matsuura, and K. Inoue, “Formation of superoxide ion via one-electron transfer from electron donors to singlet oxygen,” *Journal of the American Chemical Society*, vol. 105, no. 10, pp. 3200–3206, 1983.

[44] X. Zhang, F. Lin, and C. S. Foote, “Sensitized photooxygenation of 6-heteroatom-substituted fulvenes: primary products and their chemical transformations,” *The Journal of Organic Chemistry*, vol. 60, no. 5, pp. 1333–1338, 1995.

[45] D. Min and J. Boff, “Chemistry and reaction of singlet oxygen in foods,” *Comprehensive reviews in food science and food safety*, vol. 1, no. 2, pp. 58–72, 2002.

[46] H. H. Wasserman and J. L. Ives, “Singlet oxygen in organic synthesis,” *Tetrahedron*, vol. 37, no. 10, pp. 1825–1852, 1981.

[47] P. D. Bartlett, G. D. Mendenhall, and A. P. Schaap, “Competitive modes of reaction of singlet oxygen,” *Annals of the New York Academy of Sciences*, vol. 171, no. 1, pp. 79–88, 1970.

[48] A. A. Frimer, “The reaction of singlet oxygen with olefins: the question of mechanism,” *Chemical Reviews*, vol. 79, no. 5, pp. 359–387, 1979.

[49] E. Clennan and A. Pace, “Advances in singlet oxygen chemistry,” *Tetrahedron*, vol. 61, pp. 6665–6691, 2005.

[50] J. Hurvois and C. Moinet, “Reactivity of ferrocenium cations with molecular oxygen in polar organic solvents: decomposition, redox reactions and stabilization,” *Journal of Organometallic Chemistry*, vol. 690, no. 7, pp. 1829–1839, 2005.

Designing oxidation mediators to suppress $^1O_2$ formation

In the middle of every difficulty lies opportunity.
Albert Einstein

Contents

Figures

Chapter based on Mourad†, Petit†et al.[1]

Introduction

The oxidation mediator is a promising approach to reduce metal-air cells overpotential and to permit fast reaction rates during charge[2–5]. Oxidation mediators, yet, do not prevent the highly reactive $^1O_2$ presence. We show in the previous chapter that mediated alkali peroxide oxidation proceeds via two consecutive steps. The first and rate limiting step is a one-electron oxidation to produce superoxide species that can either disproportionate or be further oxidized. $^1O_2$ can hence either be produced via disproportionation or by oxidation at high overpotential (e.g. ~3.55 V_{Li/Li^+} for O_2^-). $^1O_2$ was shown previously to be a main degradation pathway in metal-air batteries. Its presence is especially problematic since the widely studied organic mediators quickly react with $^1O_2$, leading to their deactivation and accumulation of side products. The chemical stability of the mediators might furthermore be problematic as its reduced state is not necessarily reformed after reaction with peroxide or superoxide.

Oxidation mediator optimization is hence of main interest to achieve efficient and sustained mediation. Refined mediators still forecast reduced side reactions and fast charge rates. To do so, a mediator should have fast reaction rate on both peroxide and superoxide. The former one allowing fast reaction rate, being the slowest step, whereas the latter could reduce the superoxide portion undergoing disproportionation. The disproportionation and superoxide oxidation rates are competing for O_2 release; a fast enough oxidation would result in suppressed disproportionation and $^1O_2$ yield. Oxidation mediators with $^1O_2$ quenching moieties showed moreover increase stability and could guarantee low cell degradation in presence of a small disproportionation proportion. In addition, chemical stability against peroxide, superoxide and $^3O_2$ of newly proposed mediators should be insured before any further long term cyclability claims.

Considering the aforementioned observations, design rules can be drawn for efficient mediators, i.e. a high chemical stability, a high quenching efficiency, a redox potential lower than the $^1O_2$ thermodynamic threshold and high oxidation rates on peroxide and superoxide. We study in this chapter more in-depth the influence and underlying mechanism of these parameters using a wide range of mediators as well as a newly proposed class of mediators represented in Fig. 6.1, organic hydrazines, i.e., N-N bridged pyrrolidines and piperidines (BP). Organic hydrazines present the advantages to have an easily tunable redox potential, which we will show the kinetic to depend on, and quenching moieties[6]. The reasons and mechanisms of efficient mediation will hence be deciphered, allowing oxidation mediators to progress further and possibly unlock $^1O_2$-free fast charge in metal-O_2 technologies.

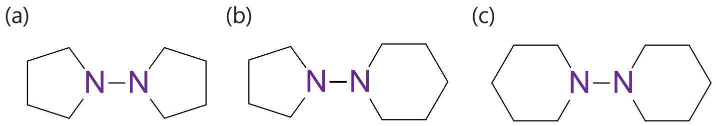

Figure 6.1: **Structure of the organic hydrazines proposed as oxidation mediators.** (a) 1,1'-bipyrrolidine (BP55), (b) 1-(pyrrolidin-1-yl)piperidine (BP56) and (c) 1,1'-bipiperidine (BP66). The quenching moieties are highlighted in purple.

To do so, we first determined the redox potential of several members of the organic hydrazine class proposed as mediators as well as their chemical stability after prolonged contact with KO_2, Li_2O_2 and $^3O_2$. After ensuring sufficient stability, the BP mediator reaction rates with O_2^- and O_2^{2-} were measured by UV-vis spectroscopy as described in the previous chapter. The 1,1'-bipyrrolidine (BP55) mediator was revealed to have an unusually high reaction kinetic and could greatly reduce disproportionation occurrence. To assess the efficiency of organic hydrazine mediators and verify our design rules, we measured $^3O_2$ and $^1O_2$ yields for a wide range of mediators by MS and HPLC. We were able to correlate the mediator redox potential to the superoxide reaction kinetic using Marcus theory. Accordingly, the reaction kinetics decrease for high potentials and hence possess a maximum that should be aimed by future oxidation mediators. Maximizing the mediator reaction rate was shown to reduced the $^1O_2$ evolution. Organic hydrazines have moreover tertiary amine quenching groups[6]; Presence of quenching moieties reduces the presence of $^1O_2$ during mediated oxidation and we will show that the quenching efficiency depends on the redox potential of the mediators and their chemical nature, as already discussed in part 5.3.3. Finally, the overall $^1O_2$ and $^3O_2$ yield tendencies can be best grasped through Sankey diagrams of relative rates, relating the relative rates to the $^3O_2$/$^1O_2$ evolution yields. BP55 demonstrates the feasibility and draws the path to efficient oxidation mediators that could reduce $^1O_2$ occurrence during metal-O_2 cell charges at high rates.

6.1 Organic hydrazines as oxidation mediators

Oxidation mediator reactivity described in the previous chapter requires to obey new criteria to achieve long term cycling. We hence studied a new class of mediators, organic hydrazines, to provide more in-depth a mechanism description of mediated oxidation for achieving $^1O_2$-free charge. Organic hydrazines present the advantage to have quenching moieties and easily tunable redox potentials in order to optimize the mediated oxidation kinetic. The redox potential of the molecules is fixed by the substituents of the amines. Different organic hydrazines were hence synthesized and selected for their redox potential. Before further characterisations of the mediator influences, we assessed their chemical stability and reaction kinetic to compare them to the previously studied mediators.

6.1.1 Electrochemical characteristics

To test organic hydrazines as mediators, synthesis methods were first developed and can be found in Appendix E.2. As the cycle size can be easily tuned, organic hydrazines can present a wide range of redox potential. Mediator redox potentials were determined by cyclic voltammetry using a 2 mM mediator in 0.1 M LiTFSI TEGDME electrolyte at a scan rate of 100 mV·s^{-1} on a glassy carbon electrode, which are depicted in Fig. 6.2. 1,1'-bipyrrolidine (BP55), 1-(pyrrolidin-1-yl)piperidine (BP56) and 1,1'-bipiperidine (BP66) were selected with potential of 3.2 V_{Li/Li^+}, 3.46 V_{Li/Li^+}, 3.76 V_{Li/Li^+} respectively. These three mediators cover a similar potential range as commonly proposed mediators presented in part 5.2.2. BP55 has a potential below the $^1O_2$ formation potential which is close to the one of TMPD (3.24 V_{Li/Li^+}) and DMPZ (3.29 V_{Li/Li^+}). BP56 potential is situated close to the thermodynamic threshold for $^1O_2$ (~3.55 V_{Li/Li^+}) and to mediators with lower kinetics such as Fc. Finally, BP66 has the same potential as TEMPO and can be used to characterise mediators with high potentials that would produce large $^1O_2$ amount by mediated oxidation.

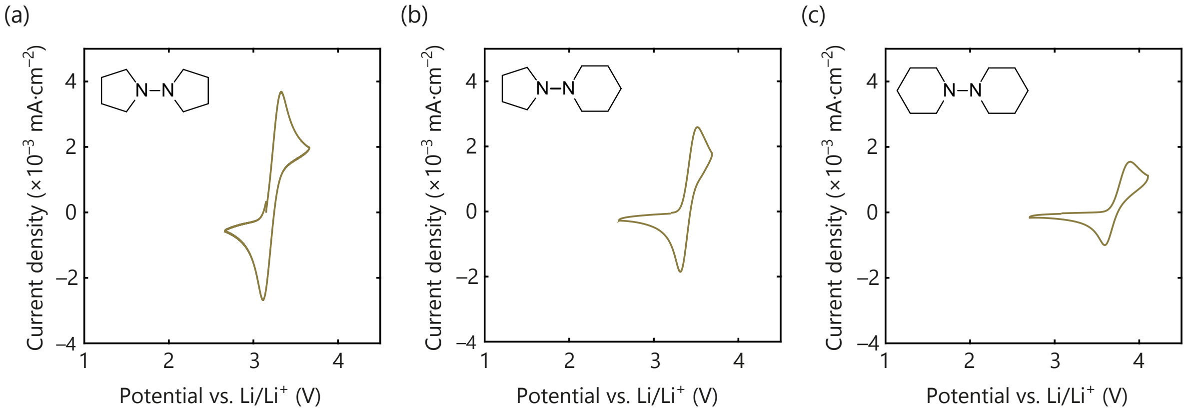

Figure 6.2: **Cyclic voltammetry of the organic hydrazines proposed as oxidation mediators.** The cyclic voltammetries were measured using 2 mM of (a) BP55 (b) BP56 or (c) BP66 in 0.1 M LiTFSI in TEGDME as electrolyte at a scan rate of 100 mV·s^{-1} on a glassy carbon electrode.

Given their potential, the selected amines can be used to scrutinize the presence of a two step mediation with sodium peroxide (2.87, 3.13, 3.43 V_{Na/Na^+}, respectively for BP55, BP56 and BP66). As described in Appendix E.3.4, the $^1O_2$ occurrence pattern advocates for superoxide formation via two sequential one-electron transfers rather than direct two-electron reaction, irrespective to the alkali peroxide nature. The design rules suggested in the main text are, hence, applicable to both non-aqueous Na-O2 and Li-O2 chemistries.

6.1.2 Chemical stability

Once organic hydrazines of significance were chosen, their chemical stability in contact with dissolved O_2, O_2^- and O_2^{2-} needed to be verified. Chemical stability is necessary to provide long term cyclability and we verify that the determined reaction rates are related to the oxidation reactions. We recorded ^{1}H-NMR spectra of BP55, BP56 and BP66 in CH_3CN-d_3 after synthesis or after a 24 hour immersion in O_2 saturated electrolyte. BP55$^+$, BP56$^+$ and BP66$^+$ oxidized chemically, according to Appendix E.1, were bring in contact with an excess of KO_2 or Li_2O_2 for a 12 hours period and subsequently analysed by ^{1}H-NMR to certify the reformation of their reduced forms rather than producing side products. The spectra of the mediators in similar concentrations can be found in Fig. 6.3. The mediators show sufficient chemical stability excepted BP55 in the presence of dissolved molecular oxygen. Although BP55 is, thus, not compatible with an actual metal-O_2 cell, it can still be used to discuss the mediator mechanism as the performed measurements involve much shorter times than 24 hours, after which BP55 is still detected albeit in a lower amount. This assumption was verified by UV-vis experiments where the oxidized organic hydrazine spectra were measured before and after reactions with an excess of KO_2 or Li_2O_2 during 12 hours and compared to the reduced form spectra. The oxidized BP mediators produce back their reduced form after alkali oxide oxidation in similar concentration as illustrated in Fig. 6.4. This indicates that, in the time range studied, BP55 is stable enough. The other mediator UV-vis studies are given in Appendix E.3.3.

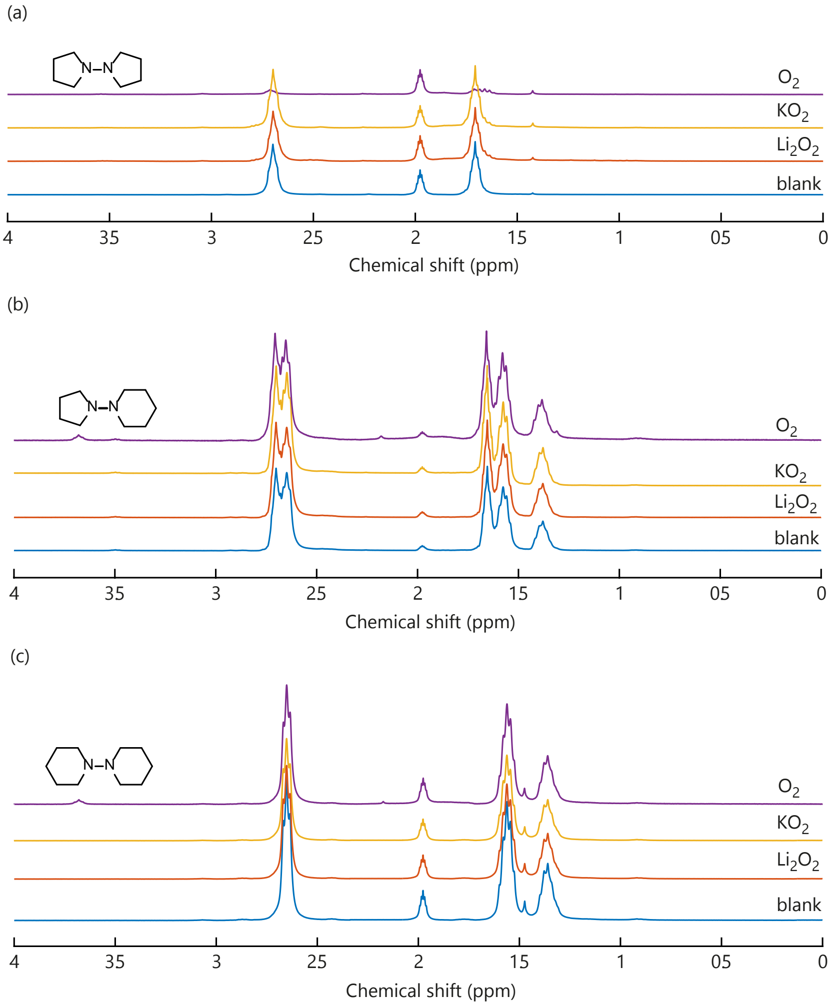

Figure 6.3: **Stability of the BP mediators in contact with O_2, KO_2 and Li_2O_2 by ^{1}H-NMR.** The spectra were recorded in DMSO-d_6. NMR spectra of the reduced mediators as synthesized (labelled blank) or after contact with O_2 for 24 hours and of oxidized mediators after contact with Li_2O_2 or KO_2. The mediators are (a) BP55, (b) BP56 and (c) BP66. Oxidized mediators were dissolved in CH_3CN-d3, the solution stirred with several mg KO_2 or Li_2O_2 for 12 hours and filtered before the measurements.

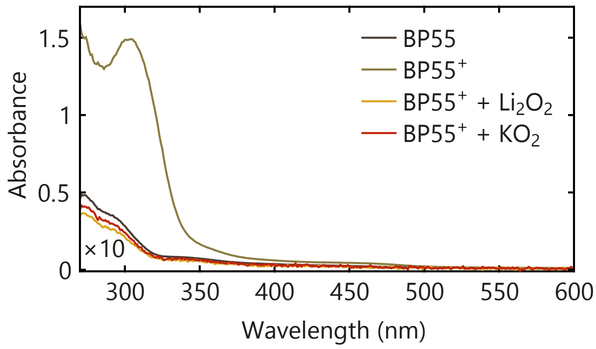

Figure 6.4: **$BP55^+$ conversion upon contact with Li_2O_2 or KO_2.** UV-vis spectra of BP55, $BP55^+$ and $BP55^+$ after contact with Li_2O_2 or KO_2 for 12 hours.

6.1.3 Oxidation kinetics

Owing to their sufficient stabilities, BP mediators can be used to assess correlations between mediator redox potentials and oxidation kinetics since they are based on similar chemical motifs. Large mediator kinetic on superoxide is of prime importance to avoid $^1O_2$ during charge by competing with disproportionation. Fast reaction with peroxide is also desirable to enable an overall fast charge rate. Determining the underlying parameters of mediated charge kinetics may hence allow for $^1O_2$-free and fast paced charging. The reactions rates on both Li_2O_2 and KO_2 have been determined by UV-vis spectroscopy according to the method described in Appendix A.8. The concentrations used are in a similar range as during the chemical stability UV-vis spectroscopy experiments assuring negligible side reactions. The decays in oxidized mediator concentration were then fitted by a first-order reaction rate to obtain the kinetic rate constant and compared to the previously obtained kinetics in ch. 5. The rates for 10 mM of mediators and reaction rate constants measured are depicted in Fig. 6.5.

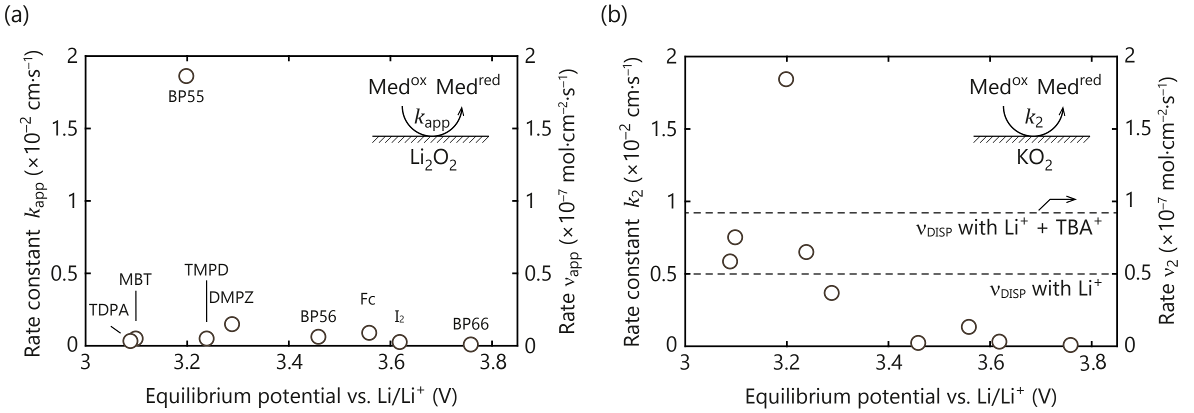

Figure 6.5: **Kinetics of mediated (su)peroxide oxidation including BP mediators and superoxide disproportionation.** Kinetic constants k (left axis) and reaction rates v assuming a 10 mM concentration (right axis) in TEGDME for the reaction between oxidized mediators and the Li_2O_2 surface (a) and the KO_2 surface (b) obtained by UV-vis spectroscopy. Superoxide disproportionation rates in presence of 0.5 M LiTFSI or 0.5 M LiTFSI and 0.5 M TBATFSI are indicated by dashed lines in (b).

The mediator kinetics show a clear dependence on the mediator redox potentials. As previously observed, the kinetics of mediators with redox potentials above ~3.2 V_{Li/Li^+} decay with growing potential. The kinetics of low redox potential mediators, yet, increase with the potential; This results in a maximum rate at ~3.2 V_{Li/Li^+} for superoxide oxidation, represented by BP55. The kinetic trend is, thus, rather surprisingly not proportional to the potential and hence the driving force with respect to the O_2/Li_2O_2 potential. The kinetics obtained with BP55 present remarkable characteristics. The mediated oxidation kinetics on Li_2O_2 and KO_2 are similar which indicates very fast overall reaction, roughly five times faster than the second fastest (DMPZ). Maximized mediator kinetics should, hence, be able to increase tremendously the charging rate in metal-O_2 batteries. The superoxide reaction kinetic of BP55 is moreover almost twice as fast as disproportionation in the presence of TBA$^+$ ions. By optimizing oxidation mediator designs, it is, thus, possible to outspeed the disproportionation rate and reduce the $^1O_2$ occurrence.

6.2 Designing efficient oxidation mediators

Oxidation mediators have mostly been studied for their redox potential, stability with the electrolyte or chemical nature[7–9]. In the ch. 5, we showed that an oxidation mediator must, in addition to being chemically stable, present a high stability towards $^1O_2$ and a high reaction kinetic towards superoxide to allow for long term cyclability. The mediator oxidation kinetics appears to be govern by their redox potential but not in a simple fashion with growing kinetics as the driving force increases. The origin of this dependence needs to be understood to design fast and efficient mediators for metal air-batteries. Mediator quenching abilities seem to be correlated with the O_2 robustness and must be rationalized. Only clarifying these effects can provide efficient oxidation mediator design rules which are of prime interest for future mediators and metal-air batteries development.

6.2.1 Kinetics and Marcus Theory

Finding a relationship of oxidation mediator kinetics with their redox potentials has been attempted previously by scanning electrochemical microscopy but no clear correlation was determined and the reaction was defined as only dependent on the chemical nature of the mediators, in particular steric hindrance of the redox centre[9]. BP mediator kinetics which are given in part 6.1.3, yet, present a clear potential dependence despite similar chemical natures.

A differential electrochemical mass spectrometry study found, on the contrary, a dependency of the potential for the oxygen evolution onset, and hence the kinetic, with the mediator redox potentials. The trend was shown to follow an outer-sphere mechanism according to Marcus theory[10]. As Marcus theory predicts a kinetic maximum, the physics behind its parameters would provide a guideline to achieve fast mediated oxidation rate and reduce disproportionation importance. Our UV-vis measured kinetics can be decomposed in two specific zones. At first, there is an increasing kinetic with increasing potential. Beyond a maximum at ~3.2 V_{Li/Li^+} for superoxide oxidation, the electron transfer rate decreases with growing potential. Such counterintuitive behaviour is predicted for homogeneous electron transfer by the Marcus theory and termed the "inverted region"[11,12]. Marcus theory based kinetic exhibits an exponential character similar to an Arrehnius law but with a quadratic dependence on the reaction driving force according to Eq. 6.1.

$$k_{ET} = Z_{el} \cdot \exp(\frac{-\Delta G^{\ddagger}}{R \cdot T}) = Z_{el} \cdot \exp(\frac{-(\lambda + \Delta G^0)^2}{4 \cdot \lambda \cdot R \cdot T}) \tag{6.1}$$

with k_{ET}, the electron transfer rate constant (cm·s^{-1}); Z_{el}, the collision factor (cm·s^{-1}); $\Delta G^{\ddagger}$, the activation free energy (J·mol^{-1}); ΔG^0, the Gibbs free energy (J·mol^{-1}); λ, the total reorganization energy (J·mol^{-1}); R, the ideal gas constant (J·K^{-1}·mol^{-1}); and T, the temperature (K). The activation free energy is hence given by $\Delta G^{\ddagger} = \frac{(\lambda + \Delta G^0)^2}{4 \cdot \lambda}$ where ΔG^0 is the reaction driving force and λ represents the energy required to change the nuclear configurations of the reactants and solvent to produce the product states[11,12].

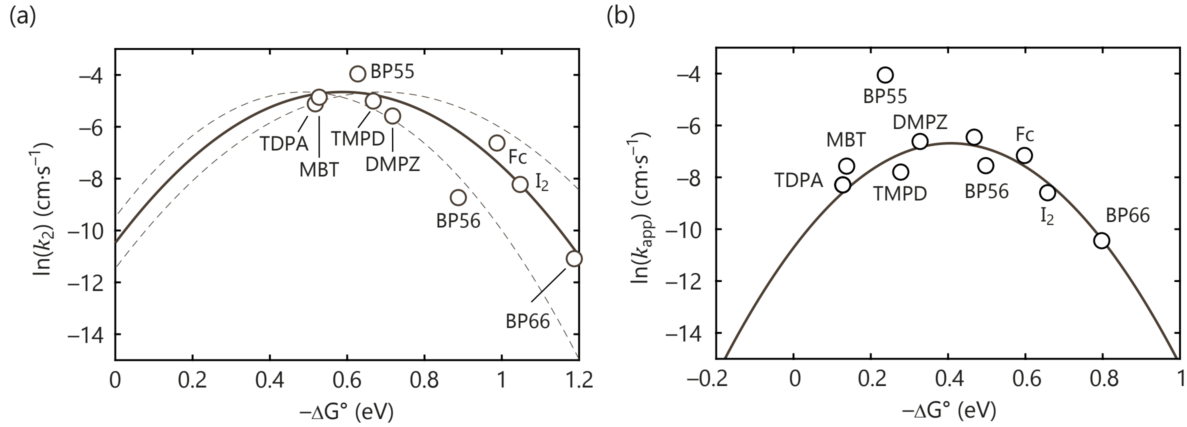

Figure 6.6: **Mediated (su)peroxide oxidation kinetics relationship with Gibbs free energy.** (a) Dependency of k_2 to ΔG^0 and associated fit according to Eq. 6.1 resulting in Z_{el} = 9.5·10^{-3} cm·s^{-1} and λ = 0.58 eV. The dashed parabolas are obtained for $\lambda \pm 0.1$ eV. (b) Dependency of k_{app} to ΔG^0 and associated fit according to Eq. 6.1 resulting in Z_{el} = 1.2·10^{-3} cm·s^{-1} and λ = 0.41 eV.

Marcus theory for electron transfer described in Eq. 6.1 is usually only valid for homogeneous reactions and does not apply to redox molecules reacting at metallic conductor surfaces[11,13]. Alkali oxides are, however, wide band-gap insulators and may justify this formalism. Considering Z_{el} as a constant in our experiments as first approximation, we could adequately fits the measured superoxide oxidation kinetic (k_2) as a function of the driving force($-\Delta G^0 = (E^0_{med} - E^0_{O_2/Li_2O_2}) \cdot F$) in Fig. 6.6(a).

Similarly, the overall reaction (k_{app}) also follows the same trend, albeit with larger deviations in Fig. 6.6(b); these deviations originate from k_{app} being a compound rate of different elementary steps. The use of Marcus theory formalism is thus justified in this case. Marcus theory implications give guidelines on the choice of the oxidation mediator. The electron transfer efficiency maximum is achieved for $\lambda = -\Delta G^O$ according Eq. 6.1 which corresponds to a barrier-less electron transfer ($\Delta G^\ddagger = 0$) as illustrated in Fig. 6.7. The other cases result in lower kinetics and the appearance of the inverted region in case of $-\Delta G^O >$ lambda. Z_{el} and λ provide mechanistic tools to maximize the reaction kinetics and avoid $^1O_2$ productions.

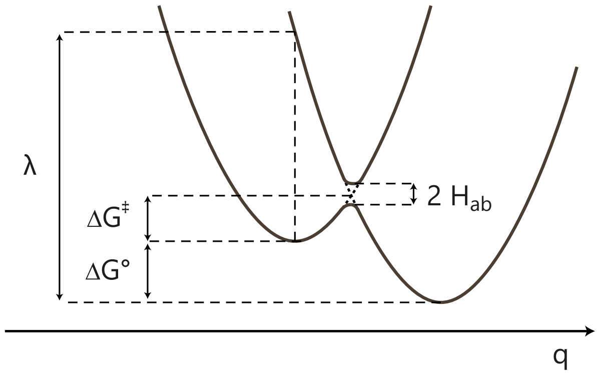

Figure 6.7: **Scheme of donor-acceptor orbitals and Marcus theory parameters.** $\Delta G^\ddagger$, ΔG^0, and λ meanings are given in Eq. 6.1. H_{ab} represents the donor-acceptor coupling and q the reaction coordinate.

The total reorganization energy can be decomposed between reorganisation in the solid phase ($\lambda_{M_2O_2}/\lambda_{MO_2}$) and reorganisation of the redox mediator ($\lambda_{mediator}$). Each reorganization energy depends itself on inner and outer parameters. The outer energy (λ_o) is attributed to the reorganization of the solvent shell whereas the inner energy (λ_i) represents the energy required to change the reactant oxidation state[11,12]. λ is hence composed of four contributions for mediated alkali oxide oxidation, according to Eq. 6.2 in the case of superoxide. The reorganisation during mediated oxidation can be further broken down. Electron transfer involves firstly the oxide bond breaking λ_{i,MO_2}, followed by the solvation of M^+ and O_2 in the liquid phase. The outer reorganization energy of the superoxide can then be described as $\lambda_{o,MO_2} = \lambda_{M^+,sol} + \lambda_{O_2,sol}$.

$$\lambda = \lambda_{i,MO_2} + \lambda_{o,MO_2} + \lambda_{i,mediator} + \lambda_{o,mediator} \tag{6.2}$$

A critical consequence of mediators obeying a Marcus behaviour is that all redox mediators can be described by the same kinetic maximum corresponding to a λ of 0.58 eV for superoxide (i.e. E^0_{med} ~3.2 V_{Li/Li^+}) irrespective to their chemical nature. λ is thus dominated by the oxide reorganisation energy which outweighs the mediator contributions. From an energetic point of view, the dominance of λ_{MO_2} results from a higher energy required to break the oxide bond and to solvate M^+ as well as O_2 than for the mediator reduction per se. Mediators with similar redox potential such as $TDPA^+$ and MBT_2 or Fc^+ and I_2 yield comparable kinetics despite considerable chemical differences, supporting this assumption. As little as mediator reorganization energies appear to be, they could account for small deviations that we modelled by fitting with $\lambda = \lambda_{maximum} \pm 0.1$ eV which enclose most of the obtained kinetics.

The mediator reorganization energy is not of prime importance at first but still influences the kinetic albeit in smaller range. The mediated oxidation kinetics depend, thus, mostly on the redox potential of the mediators rather than their chemical structure and their solvation energy. The electrolyte should be choosen to influence the M^+ and O_2 solvation as described in part 1.2.1.1. The solvent was shown to have an influence on the Li_2O_2 oxidation onset potential and hypothetized to facilitate mediated oxidation[14,15]. Further deviations might arise from Z_{el} modulation between the different mediators. This is supported by $BP55^+$ having enhanced kinetics compared to the Marcus theory predictions with a constant collision factor. Z_{el} is influenced by complex physico-chemical properties such as the donor-acceptor coupling, i.e. the diabatic character of the electron tranfer, and was deemed out of scope in this study[12,16,17]. Overall, our first approximation of the Marcus theory to mediated alkali superoxide oxidation predicts a maximum kinetic around 3.2 V_{Li/Li^+} that should be aimed by future oxidation mediators. This maximum may, however, depend on the solvent; an effect that remains to be studied. The reaction kinetic could be even more maximized with proper tuning of the overall reorganisation energy or the collision factor.

6.2.2 Importance of mediator quenching efficiency

The nature of the relationship between the reaction kinetic and the mediator redox potentials being resolve, the remaining question is the influence of the mediator on $^1O_2$ production. We hence characterised $^3O_2$ and $^1O_2$ releases upon mediated peroxide and superoxide oxidation for the same wide range of mediators used for kinetic determinations in part 6.1.3 by a combination of MS, UV-vis spectroscopy and HPLC according to Appendices A.4, A.5, and A.6. The results are depicted in Fig. 6.8, scaled to the theoretical O_2 yield.

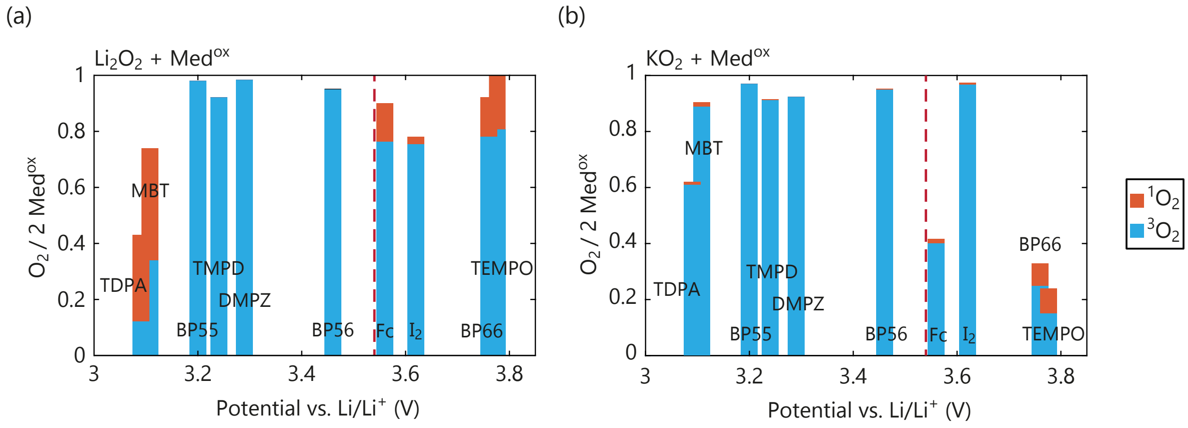

Figure 6.8: **$^3O_2$ and $^1O_2$ yields upon mediated peroxide and superoxide oxidations for a wide selection of mediators.** $^3O_2$ and $^1O_2$ evolutions obtained by the addition of 10 mM oxidized mediators in TEGDME to an excess of (a) Li_2O_2 or (b) KO_2. The bars are positioned according to the redox potential of the respective mediators. The red dashed line indicates the thermodynamic thresholds for $^1O_2$ evolution from LiO_2 oxidation.

Considering first the mediators with a potential above ~3.5 V_{Li/Li^+}, a significant lack of $^3O_2$ evolution can be noticed accompanied with $^1O_2$ for both peroxide and superoxide oxidations. This confirms $^1O_2$ generation by mediated alkali oxide oxidation above the $^1O_2$ potential threshold in addition to disproportionation. Similarly, TDPA$^+$ can form spontaneously TDPA^{2+} which has a redox potential around ~3.5 V_{Li/Li^+} as shown in part 5.4.2. TDPA^{2+} formation results in $^1O_2$ production from superoxide in absence of disproportionation. I_2 shows, yet, improved efficiency in absence of disproportionation during superoxide oxidation whereas the others give lower yields. Both I_2 and I^- are molecules known for their $^1O_2$ quenching efficiency by means of heavy-atom colliders effect[18–20]. The quenching character of I^-/I_2 might explain the observed difference as $^1O_2$ can only be formed in the vicinity of the iodide by mediated oxidation followed by a potential $^1O_2$ quenching whereas disproportionation would dominate in presence of Li$^+$ ions.

Using mediators below ~3.5 V_{Li/Li^+} can only lead to $^1O_2$ evolution through disproportionation. As described for MBT_2 in part 5.2.1, only a negligible $^1O_2$ amount is produced upon KO_2 oxidation, hence in absence of disproportionation. Li_2O_2 oxidation, yet, yields different behaviour between MBT_2 and BP55$^+$, TMPD$^+$, DMPZ$^+$ or BP56$^+$. The low $^1O_2$ amount during peroxide oxidation compared to MBT_2 can be explained by a reduced disproportionation proportion for the fast kinetic BP55$^+$. The other mediators, however, possess similar or lower kinetics than MBT_2. We do not exclude possible undetected side reaction or influence of the MBT^-/MBT_2 couples on disproportionation. The quenching proprieties of the mediators can additionally be the origin of deviations as for the I_3^-/I_2 couples.

To compare the $^1O_2$ quenching efficiency of different mediators, the quenching rate constants can be used. We either determined the quenching rates using the UV-vis spectroscopy protocol already discussed in ch. 4 and given in Appendix A.7 in the case of DMPZ or TDPA or were obtained from literature[6,18,19,21]. To take into account the influence of the electrolyte, the quenching rate of DABCO was used as a reference in first approximation, being a well known and studied quencher. The rates were then converted to the theoritical rates in acetonitrile using this reference quencher. The resulting quenching rate contants are given as a function of the mediator redox potentials in Fig. 6.9. The line with a slope of 10^4/V is added as a guide since the quenching efficiency depends on the oxidation potential of the molecule for the charge transfer mechanism, as discussed in part 4.1 and observed for the BP mediators. The quenching efficiency may nevertheless significantly differ between chemical classes[20,22].

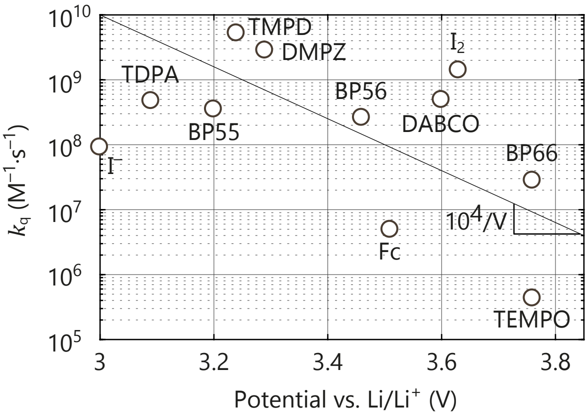

Figure 6.9: **$^1O_2$ quenching rate constants of mediators as a function of their redox potential in acetonitrile.**

I_2 presents indeed a highly improved quenching rate constant compared to the other high potential mediators which may partly be responsible for the higher $^3O_2$ yield. DMPZ has one of the best $^1O_2$ quenching efficiencies which may also contribute to its improved stability with $^1O_2$, in addition to the relatively unfavoured decomposition reactions[23]. This high quenching ability is accompanied by a negligible amount $^1O_2$ release and high $^3O_2$ yield during alkali oxide oxidation. The search for improved mediator stability with $^1O_2$ advocates for low potential mediators and the occurrence of quenching moieties on the molecule such as tertiary amines. The $^1O_2$ quenching rates of future mediators ought thus to be determined in addition to quantify the stability of the mediators in contact with $^1O_2$.

6.2.3 Consequences for oxidation mediators

$^1O_2$ has crucial consequences on metal-air parasitic chemistry. To achieved $^1O_2$-free mediated cells, the main parameters to optimize are the mediator kinetics and quenching efficiencies. The oxidation kinetics are mostly governed by the mediator potentials with an optimum at ~3.2 V_{Li/Li^+} and decreasing values below and above, according to the Marcus theory. The maximum kinetic could be more refined through complex physico-chemical parameters. Next to the the mediator redox potential influencing the quenching ability as shown for the BP mediators, the chemical nature of the mediators is also of prime importance. The chemical class of the mediator should hence be mostly selected to provide an efficient $^1O_2$ quenching rather than for their alkali oxide oxidation efficiency. Sankey diagrams reveal themselves as a helpful representation of these complex interactions, given for BP55, DMPZ and BP66 in Fig. 6.10 as examples for low and high redox potential mediators. The diagrams for the other studied mediators are given in Appendix E.3.5

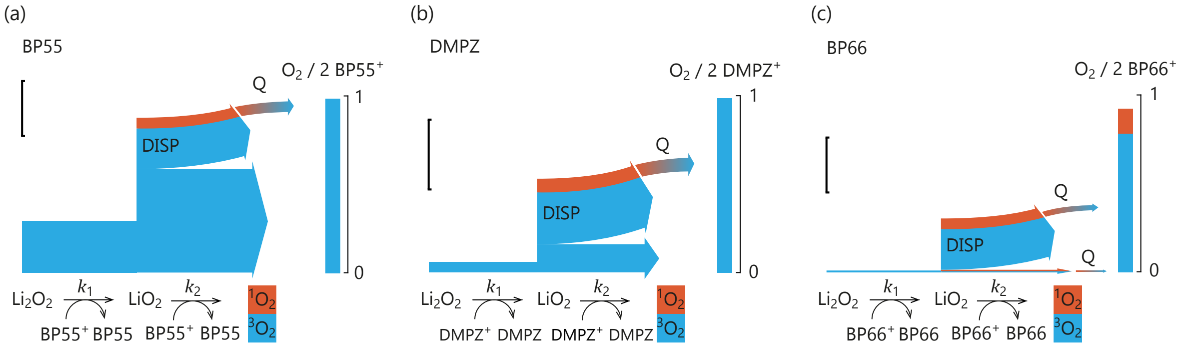

Figure 6.10: **Sankey plots of relative reaction rates during mediated Li_2O_2 oxidation for selected mediators.** The width of the arrows is proportional to the rate assuming 10 mM of (a) BP55$^+$, (b) DMPZ$^+$ and (c) BP66$^+$. The vertical scale bar corresponds to 1×10^{-7} mol·cm^{-2}·s^{-1}. $^1O_2$ quenching by the mediator is denoted by Q. The $^3O_2$ and $^1O_2$ yields per 2 equivalent of oxidized mediators are given at the right of each panel.

In our Sankey diagrams, the width of the arrows are proportional to the rates of the individual steps and the bar graph at the right shows the shares of $^3O_2$ and $^1O_2$ obtained. The diagrams allow for easily comparing the different step rates for a mediator and between the mediators. The quenching influence can be seen via the bar graph and lower $^1O_2$ amount than expected. To approximate the first one-electron transfer kinetic (k_1) which cannot directly be measured, the relationship between the different reaction steps must first be discussed. A strongly dominant disproportionation rate leads to negligible second one-electron transfer, as for high potential mediators (illustrated by the BP66 in Fig. 6.10(c)). In this case, the overall mediator consumption observed by k_{app} is overwhelmingly due to the first electron transfer and can be approximate as k_1. As the second one-electron transfer rate is getting closer to disproportionation rate for low potential mediators, e.g. DMPZ in Fig. 6.10(b), the second one-electron reaction is non negligible any more and some mediators will be consumed during the second one-electron transfer. We approximated k_1 in this case by k_{app} as disproportionation is still dominant and the overall reaction rate is much smaller than k_2. This indicates that k_1 is largely slower than the other two process and so susceptible to a smaller absolute error. BP55 is the exception with a faster second electron transfer rate than the disproportionation in Fig. 6.10(a). The obtained k_2 is moreover similar to the k_{app} of the overall reaction. In the extreme case, disproportionation would be negligible as the second electron transfer would be sufficiently fast to consume every superoxide intermediates formed in the first step. The overall consumption rate would hence be only be composed of the two one-electron steps, as the second e^- transfer will immediately follow the first one. k_{app} can then be equally divided between k_1 and k_2 in this case. We chose to represent BP55 as this extreme case with $k_1 = k_{app}/2$. In reality, as disproportionation is not negligible even for this mediator, k_1 might be larger to the one shown which is the lower range of the first electron transfer kinetic. For all mediators, nevertheless, the combined disproportionation and second electron transfer is faster than the first one which indicates that the first electron extraction is the rate limiting step of mediated peroxide oxidation.

An estimated proportion of disproportionation compared to superoxide oxidation rate can be visualized with Sankey diagrams and be related to the amount of singlet oxygen. It arises from the BP55 diagram that fast second electron transfer may suppress, but cannot fully eliminate $^1O_2$ production. The absence of significant $^1O_2$ detection or lack of $^3O_2$ for BP55 or DMPZ on Li_2O_2 suggests that the mediators' ability to quench $^1O_2$ is a indeed a requirement for future mediators. Sankey diagram could then be used to compare future mediator kinetics and O_2 yields. We propose, finally, as criteria for an efficient mediator design, in addition to chemical stability, a maximized kinetic using the Marcus theory and a maximized $^1O_2$ quenching efficiency via the chemical nature of the mediators. As shown by the BP55 results, only abiding by these rules may allow a fast reaction rate, minimized $^1O_2$ occurrence and as finality improved metal-O_2 charge.

Conclusion

To conclude, we deciphered in the previous chapter the mechanism of mediated alkali peroxide and superoxide oxidation which explains $^1O_2$ generation. Highly reactive $^1O_2$ should be avoided by all means to achieve long term cyclability. $^1O_2$ can evolve form mediated oxidation above a potential threshold of ~3.5 V_{Li/Li^+} and thus high redox potential mediators are to be avoided. As the mediated oxidation is composed of a two step oxidation, the initially formed superoxide is exposed to disproportionation and subsequent $^1O_2$ production. Only high mediated oxidation rates could decrease the proportion of disproportionation and must be aimed for.

We could show that the oxidation rates go through a maximum at ~3.2 V_{Li/Li^+} for superoxide and decrease at lower and higher potential. Such behaviour is described by the Marcus inverted region which predicts a quadratic dependency of the kinetics with the reaction driving force. A kinetic trend following Marcus theory has serious consequences. We could derive that the mediator chemical nature is of secondary importance next to its redox potential considering the reaction kinetic. The overall reorganisation energy is dominated by the oxide reorganisation energy which should be studied more deeply to optimize the reaction kinetic. Small deviations nevertheless can be ascribed to the chemical nature of the mediator and complex physico-chemical parameters, such as the donor-acceptor coupling, that could be further optimized in future oxidation mediators. The maximum kinetic obtained was sufficiently high to overcome the disproportionation rate and hence to efficiently reduce the $^1O_2$ production. The reaction rates on peroxide and superoxide were moreover similar with BP55. This indicates that the overall reaction rate can also be optimized as the peroxide rate is significantly slower for the other mediators.

Using Sankey diagrams, disproportionation appears as an inevitable process which can only be diminished by high superoxide reaction kinetics. The presence of quenching moieties appears thus very desirable for oxidation mediators. The highest $^3O_2$ yields were observed with mediators incorporating a quenching moiety such as tertiary amines. The quenching efficiency shows a rough dependence on the mediator potential and additionally depends highly on the mediator chemical class. If the chemical nature of the mediator does not influence greatly the reaction kinetic, this one should be chosen to provide an efficient $^1O_2$ quenching. We showed in the previous chapter that quenching moieties furthermore confer a higher resistivity to oxidation mediator deactivation induced by $^1O_2$.

The design rules drawn from the uses of organic hydrazines as oxidation mediators can be sum up in three parameters. First, a high chemical stability is needed towards peroxide, superoxide and molecular oxygen. Second, the mediators should have optimized oxidation kinetics. To this end, the Marcus theory and the physical meaning behind its parameters can be used and have shown that a redox potential around 3.2 V_{Li/Li^+} should be targeted. Finally, the oxidation mediator chemical nature should be chosen to provide a high quenching activity. Organic hydrazines provide a new class of oxidation mediators, easily tunable through organic chemistry, that could be further optimized according to these design rules to achieve truly efficient metal-O_2 charge mediation.

Bibliography

[1] E. Mourad, Y. K. Petit, C. Leypold, A. Windischbacher, D. Mijailovic, C. Slugovc, S. M. Borisov, E. Zojer, S. Brutti, O. Fontaine, and S. A. Freunberger, "Mechanism of mediated alkali peroxide oxidation reveals strategies to suppress singlet oxygen formation," in revision.

[2] J.-B. Park, S. H. Lee, H.-G. Jung, D. Aurbach, and Y.-K. Sun, "Redox mediators for Li–O_2 batteries: status and perspectives," *Advanced Materials*, vol. 30, no. 1, p. 1704162, 2018.

[3] Y. Chen, S. A. Freunberger, Z. Peng, O. Fontaine, and P. G. Bruce, "Charging a Li–O_2 battery using a redox mediator," *Nature chemistry*, vol. 5, no. 6, p. 489, 2013.

[4] B. D. McCloskey and D. Addison, "A viewpoint on heterogeneous electrocatalysis and redox mediation in nonaqueous Li-O_2 batteries," 2016.

[5] V. Pande and V. Viswanathan, "Criteria and considerations for the selection of redox mediators in nonaqueous Li–O_2 batteries," *ACS Energy Letters*, vol. 2, no. 1, pp. 60–63, 2016.

[6] E. L. Clennan, L. Noe, E. Szneler, and T. Wen, "Hydrazines: new charge-transfer physical quenchers of singlet oxygen," *Journal of the American Chemical Society*, vol. 112, no. 13, pp. 5080–5085, 1990.

[7] D. Kundu, R. Black, B. Adams, and L. F. Nazar, "A highly active low voltage redox mediator for enhanced rechargeability of lithium–oxygen batteries," *ACS central science*, vol. 1, no. 9, pp. 510–515, 2015.

[8] S. Kang, Y. Mo, S. P. Ong, and G. Ceder, "A facile mechanism for recharging Li_2O_2 in Li–O_2 batteries," *Chemistry of Materials*, vol. 25, no. 16, pp. 3328–3336, 2013.

[9] Y. Chen, X. Gao, L. R. Johnson, and P. G. Bruce, "Kinetics of lithium peroxide oxidation by redox mediators and consequences for the lithium–oxygen cell," *Nature communications*, vol. 9, no. 1, p. 767, 2018.

[10] P. Bawol, P. Reinsberg, C. Bondue, A. Abd-El-Latif, P. Königshoven, and H. Baltruschat, "A new thin layer cell for battery related DEMS-experiments: the activity of redox mediators in the Li–O_2 cell," *Physical Chemistry Chemical Physics*, vol. 20, no. 33, pp. 21 447–21 456, 2018.

[11] R. A. Marcus, "Electron transfer reactions in chemistry. Theory and experiment," *Reviews of Modern Physics*, vol. 65, no. 3, p. 599, 1993.

[12] J.-M. Savéant, *Elements of molecular and biomolecular electrochemistry: an electrochemical approach to electron transfer chemistry.* John Wiley & Sons, 2006, vol. 13.

[13] M. C. Henstridge, E. Laborda, N. V. Rees, and R. G. Compton, "Marcus–Hush–Chidsey theory of electron transfer applied to voltammetry: A review," *Electrochimica Acta*, vol. 84, pp. 12–20, 2012.

[14] G. Leverick, M. Tuodziecki, R. Tatara, F. Bardé, and Y. Shao-Horn, "Solvent-Dependent Oxidizing Power of LiI Redox Couples for Li-O_2 Batteries," *Joule*, vol. 3, no. 4, pp. 1106–1126, 2019.

[15] A. Nakanishi, M. L. Thomas, H.-M. Kwon, Y. Kobayashi, R. Tatara, K. Ueno, K. Dokko, and M. Watanabe, "Electrolyte composition in Li/O_2 batteries with LiI redox mediators: solvation effects on redox potentials and implications for redox shuttling," *The Journal of Physical Chemistry C*, vol. 122, no. 3, pp. 1522–1534, 2018.

[16] S. W. Feldberg and N. Sutin, "Distance dependence of heterogeneous electron transfer through the nonadiabatic and adiabatic regimes," *Chemical physics*, vol. 324, no. 1, pp. 216–225, 2006.

[17] W. R. Fawcett, *Liquids, solutions, and interfaces: from classical macroscopic descriptions to modern microscopic details*. Oxford University Press, 2004.

[18] F. Wilkinson and A. Farmilo, "The mechanism of quenching of singlet oxygen $O_2{}^*$ $(^1\Delta_g)$ by molecular iodine," *Journal of Photochemistry*, vol. 25, no. 2-4, pp. 153–160, 1984.

[19] I. Rosenthal and A. Frimer, "The quenching effect of iodide ion on singlet oxygen," *Photochemistry and photobiology*, vol. 23, no. 3, pp. 209–211, 1976.

[20] C. Schweitzer and R. Schmidt, "Physical mechanisms of generation and deactivation of singlet oxygen," *Chemical reviews*, vol. 103, no. 5, pp. 1685–1758, 2003.

[21] F. Wilkinson, W. P. Helman, and A. B. Ross, "Rate constants for the decay and reactions of the lowest electronically excited singlet state of molecular oxygen in solution. An expanded and revised compilation," *Journal of Physical and Chemical Reference Data*, vol. 24, no. 2, pp. 663–677, 1995.

[22] A. P. Darmanyan, W. S. Jenks, and P. Jardon, "Charge-transfer quenching of singlet oxygen O_2 $(^1\Delta_g)$ by amines and aromatic hydrocarbons," *The Journal of Physical Chemistry A*, vol. 102, no. 38, pp. 7420–7426, 1998.

[23] W.-J. Kwak, H. Kim, Y. K. Petit, C. Leypold, T. T. Nguyen, N. Mahne, P. Redfern, L. A. Curtiss, H.-G. Jung, S. M. Borisov *et al.*, "Deactivation of redox mediators in lithium-oxygen batteries by singlet oxygen," *Nature communications*, vol. 10, no. 1, p. 1380, 2019.

Conclusions

This thesis brings to light the importance of the often overlooked $^1O_2$ in metal-air batteries. $^1O_2$ presence and formation mechanisms described here engenders radical implications for the future of metal-air technologies, notably concerning its mitigation.

Firstly, we presented the complex non-aqueous metal-air chemistry arising from its "beyond-intercation" strategy. While many unknowns remain, the overall reaction process has been refined during the last few years. The formation/consumption of peroxide is known to proceed via two possible reaction pathways deeply intertwined with the cell components and cycling parameters. Following the formation of superoxide-like structures after a one-electron reduction/oxidation, the reaction can proceed via another one-electron reduction/oxidation or superoxide disproportionation. The proportion of each pathways governs the morphology and conductivity of the deposit which might form away from the electrode leading to "dead" capacity. Cells components such as the electrodes and electrolyte have also evolved to ensure better stability to the aggressive reduced oxygen species and improve the oxide accommodation. Yet, chemical instability remains the main hurdle to non-aqueous metal-air technologies democratisation, especially during charge.

We partly attribute the parasitic chemistry preventing the cyclability of metal-air batteries to an oxygen singlet excited state ($^1\Delta_g$), $^1O_2$ or singlet oxygen for short. Singlet oxygen is known for its reactivity towards organic molecules, including metal-air cell components. Metal-air batteries involve species in three different states (liquid, solid and gas) and we presented adapted in/ex-situ analytical methods to determine the reaction yield, parasitic products and singlet oxygen production. We associated among others pressure measurement, electrochemistry, UV-vis spectroscopy, mass spectrometry, and high-performance liquid chromatography to in fine provide mechanistic insights. Three formation routes for $^1O_2$ could be identified in metal-air batteries. First, direct alkali oxide oxidation could yield $^1O_2$ above a potential sufficient to overcome the activation energy barrier to its formation which correlates with the increased side reactivity at high overpotentials. Second, we showed that the disproportionation reaction can also produce $^1O_2$ oxygen at all stages of cycling, elucidating the $^1O_2$ presence during discharge. Finally, side product oxidations, such as Li_2CO_3, can result in its formation. Li_2CO_3 is a common passivation agent in lithium chemistry and singlet oxygen is bound to be a harmful influence in non-aqueous alkali based batteries at high potentials.

Disproportionation is the only $^1O_2$ formation route at all stages of cycling and we have deciphered the disproportionation mechanism that was found to be heavily dependent on the cations present. Hard Lewis acidic cations will drive disproportionation; presence of soft Lewis acid favoured, however, the formation of singlet oxygen, up to ~20% of the total O_2 release, and leads to depreciated reaction yields during both charge and discharge. The release of singlet oxygen by disproportionation has severe consequences, notably concerning the discharge product of Na-O_2 which is often identified as NaO_2. Over time, disproportionation will lead to irreversible cell damage and peroxide should be aimed as a reaction product. The action of soft Lewis acid, often found as primary motifs in ionic liquids, could furthermore prevent their uses in metal-air batteries.

The main aftermath of singlet oxygen production by disproportionation is its inevitability with the current knowledge on Li-O_2 and Na-O_2 chemistries. Development of mitigation means is thus a necessary step towards long cell lifetime. To this effect, we presented the influence of an adapted physical $^1O_2$ quencher, namely PeDTFSI. Through organic synthesis tools, the known quencher DABCO was tuned to increase its electrochemical stability and solubility while retaining sufficient quenching activity. PeDTFSI addition as an electrolyte additive demonstrated dramatic improvement on the reaction yields both during charge and discharge. Beside being a first building block for a new class of additives, our $^1O_2$ quencher study provides better insight into the role of singlet oxygen in the deterioration of metal-air cells. Despite the small amount of $^1O_2$ detected in similar conditions without a $^1O_2$ quencher, the carbonate productions were diminished by ~86% in discharge with PeDTFSI addition in high concentration. Hence, $^1O_2$ presence should not be overlooked and is a significant factor to ensure promising reaction yields.

Among promising additives that were hypothesized to reduce parasitic chemistries, we investigated oxidation mediators that would allow complete cell recharge at high rates and low overpotentials. To do so, the mediators ensure the charge transport rather than the insulating oxides and fix the reaction potential to their own redox potential. The exact reaction mechanism was not fully understood to date and we unravelled it thanks to our analytical methods and the $^1O_2$ presence. The mediated reaction appears similar to the classical reaction in terms of a two steps reaction leading to the formation of superoxide as intermediate product. The formation of $^1O_2$ is hence still possible through the same reaction pathways (oxidation at high overpotentials, superoxide disproportionation and possibly Li_2CO_3 oxidation). The occurrence of disproportionation could, however, be reduced if the mediated reaction kinetic is sufficiently high with superoxide. Oxidation mediators are often organic molecules owing to their tunable potentials which present, however, compatibility issues with $^1O_2$ production. We could show that the chemical nature of the mediators is of prime importance in this matter and should be chosen accordingly. Finally, we found that chemical stability of proposed mediators with oxygenated species is often overlooked and would lead to a quick accumulation of unwanted products in the cells.

Drawing conclusions from our mediators study, we have proposed design rules and in-depth mechanical insights to achieve efficient $^1O_2$-free mediated batteries. To exemplify these rules, we used organic hydrazines as a new class of mediators with easily tunable potential and $^1O_2$ quenching moeties. The reaction kinetic was revealed to follow the Marcus theory and hence present a maximum in function of the mediator potentials that was determined to be ~3.2 V_{Li/Li^+} for superoxide. Bipyrrolidine possesses moreover a faster reaction rate than superoxide disproportionation resulting in a lower occurrence of $^1O_2$ formation. The reaction is dominated by the reorganisation energy in the solid phase and the kinetic is, hence, largely unchanged by the chemical nature of the mediators. The chemical class, however, is of prime importance for the stability towards $^1O_2$ reactivity. The presence of quenching moieties as tertiary amines resulted in higher mediated reaction yields arising from the conversion of $^1O_2$ to its ground state. This effect should protect the mediators on long term cycling and is highly desirable. This thesis provides thus three major design rules for efficient oxidation mediators with low $^1O_2$ release: a good chemical stability towards oxygenated species, a redox potential chosen according to the Marcus theory (~3.2 V_{Li/Li^+}) and a chemical nature resulting in efficient $^1O_2$ physical quenching.

Singlet oxygen presence has significant consequences in terms of cell component design and should be mediated either via quenching effects or fast mediated reaction kinetics. This thesis compiles our first attempt to reach long term cyclability in metal-air cells by means of in depth mechanistic understandings of the reactions and their consequences regarding the $^1O_2$ formation which were previously lacking. Following researches should aim to continue to put emphasis on reaction mechanisms to provide realistic metal-air cell designs. Among possible leads, study of the reduction mediators should be conducted to reduce disproportionation proportion during discharge, as well as fine tuning of the kinetic of oxidation mediators using the Marcus theory parameters. If these studies focus on parasitic chemistry sources, investigation of cathode deformations upon oxide formation/consumption should be performed to ensure long lifetime of the electrodes. Metal-air chemistries keep an immense potential for future high capacity storage devices that could be unlock in the future as presented through this work.

Methods

Scientific method is concerned with efficient ways of generating knowledge.
George Box

Contents

Figures

Chapter based on Schafzahl, Petit et al.[1]; Mourad, Petit et al.[2]; Mourad†, Petit†et al.[3]; Petit et al.[4]; Kwak, Petit et al.[5]

A.1 Swagelock cell design and electrode making

If not mentioned otherwise, electrochemical measurements were performed using a three electrodes home-made swagelock cell which design is illustrated in Fig. A.1. The gas-tight swaglock cells are designed to allow recovery of the electrodes and electrolyte. The working electrodes used were made by mixing a slurry comprised of activated carbon (Ketjen black EC600JD, Lion Specialty Chemicals Co. or Super C65, Imerys) and PTFE binder (suspension of 60%$_w$ in H_2O, Sigma Aldrich) in isopropanol at a 9:1 ratio (w/w). The slurry was then coated on a stainless steel mesh current collector or pressed into a free standing electrode after partial isopropanol evaporation. The electrodes were dried at 60°C for 30 minutes, washed in 1:1 acetone/water ratio (v/v) and subsequently dry over for 12 hours at 60°C. After weighing, the electrodes were vacuum dried for at 120°C for 6 hours and stored in an Ar filled glovebox without exposure to air. The counter electrode had three-fold the expected capacity of the working electrode and typical working electrodes had a carbon mass loading of 1 mg.

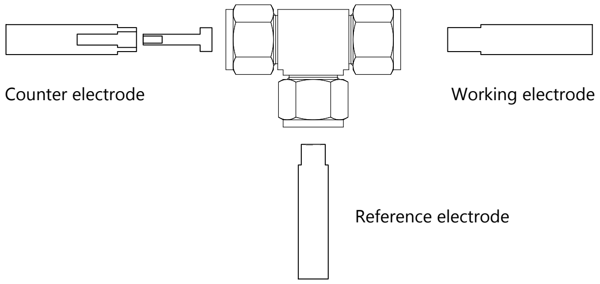

Figure A.1: **Scheme of a home-made swagelock cell.** The gas-tight cell is composed of a tee tube fitting in perfluoroalkoxy polymer (Swagelock) and stainless steel plungers (grade SAE 316L).

In the case of Li_2O_2 prefilled working electrodes, high purity lithium peroxide was first synthesized from lithium metal as previously described[6]. 13 mL of distilled water, bubbled with argon, were added to 0.5 g of lithium under argon atmosphere. After drying under vacuum, the obtained LiOH was added to 18 mL H_2O_2 (30%$_w$, Carl Roth GmbH), previously bubbled with argon, under agitation for 30 minutes under argon atmosphere. Li_2O_2 can then be recovered, after vacuum drying of the suspension, and was further dried at 60°C overnight under vacuum before being stored in Ar atmosphere. The Li_2O_2 purity was confirmed by ATR-FTIR, XRD and carbonate/carboxylate analysis. To form the electrodes, Li_2O_2 was first ground with Super C65 carbon (1:9, w/w) for 1.5 hours in a planetary ball mill (Pulverisette 7, Fritsch) at 200 rpm with ZrO_2 grinding balls under Ar. A Super C65/PTFE mixture (1:1, w/w) was produced as described earlier. Then, the Li_2O_2/C and C/PTFE powders were mixed to form a Li_2O_2/C/PTFE (1:8:1, w/w) slurry which was coated onto steel grids.

Free standing counter electrodes were produced similarly from a slurry of activated carbon, partially delithiated lithium iron phosphate (LFP, MTI Corporation) and PTFE at a 8:1:1 ratio (w/w). Delithiated LFP was obtained by stirring a LFP suspension in acetic acid (200 µL, 99.5%, Sigma Aldrich), H_2O_2 (500 µL, 30%$_w$) and distilled water (5 mL) for 2 hours. The obtained delithiated LFP was recovered by multiple centrifugations and water washings before drying at 60°C overnight.

The reference electrode were either lithium metal or free standing LFP electrodes with a known potential. The electrolyte were absorbed into glass fibre separators which were washed with ethanol and dried 12 hours at 120 °C under vacuum before use.

The cells were built by stacking the counter electrode, a glass fibre separator filled with a known amount of electrolyte (~ 100 μL) and the working electrode inside the central cell cavity and contacted by stainless cell pistons as indicated in Fig. A.1. The reference electrodes were insert with a glass fiber separator on the side cavity and sealed with a stainless steel piston. The cell includes a gas reservoir which was purged with high purity O_2 (N5.0) prior measurements.

A.2 In-situ cell pressure monitoring

Gas consumption/production were monitored by means of a three electrodes PAT-Cell-Press (EL-Cell GmbH) with a built-in pressure transducer in a controlled temperature environment which was relied to a potentiostat/galvanostat (MPG-2, Bio-Logic Science Instruments). The PAT-Cell-press is depicted in Fig. A.2 and can be used in a similar fashion than the swagelock design described in the previous part, including recovering of the electrodes and electrolyte for further analyses. The pressure is recorded over time by the pressure transducer and can be expressed in function of the electrochemical parameters as the current. The pressure can then be converted to the gas production with the ideal gas law given in Eq. A.1 and related to the theoretical gas evolution in function of the capacity by means of the Faraday law expressed in Eq. A.2. An example of the resultant analysis is given in Fig. 2.6(a).

$$P \cdot V = n \cdot R \cdot T \tag{A.1}$$

$$n = \frac{I \cdot t}{F \cdot z} \tag{A.2}$$

with P, the pressure (Pa); V, the gas volume (m^3); n, the number of moles (mol); R, the ideal gas constant (8.314 $J \cdot K^{-1} \cdot mol^{-1}$); T, the temperature (K); I, the current (A); t, the time (s); F, the Faraday constant (96485 $C \cdot mol^{-1}$); and z, the valence number of the ions.

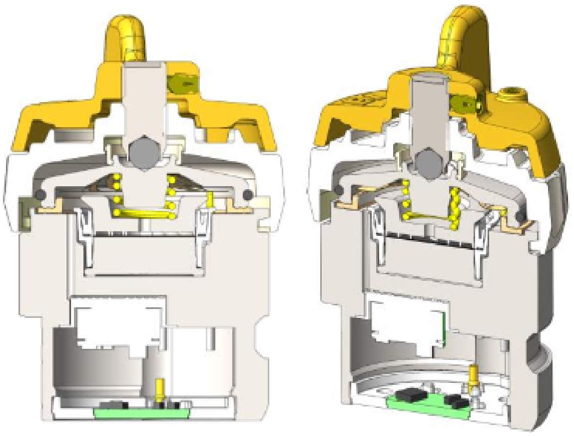

Figure A.2: **Scheme of a PAT-Cell-Press cell.** The gas-tight cell comprises a built-in pressure transducer.

A.3 Controlled $^1O_2$ production

To quantify singlet oxygen production and reactivity, $^1O_2$ was generated photochemically by means of a photosenzitizer, Palladium (II) *meso*-tetra(4-fluorophenyl-9-tetrabenzoporphyrin) (Pd_4F)[7] depicted in Fig. A.3. 1 µM Pd_4F, in continuously O_2 saturated solutions, were illuminated at 643 nm with a LED light source (OSRAM Oslon SSl80, 643 nm, 7 W) in a hermetically sealed cuvette. The irradiation wavelength correspond to the porphyrin macrocyle absorption band as illustrated in Fig. A.3. Upon Pd_4F photoexcitation, $^1O_2$ is produced as described in part 2.2.1.

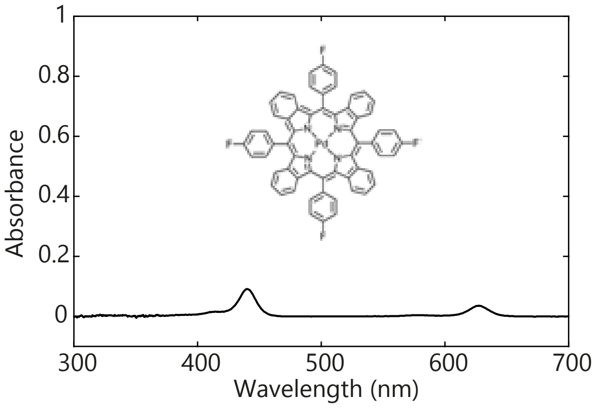

Figure A.3: **Pd_4F UV-vis spectrum and structure.**

Photobleaching and reaction of the photosensitizer with singlet oxygen were considered as negligible in the time span of the experiments. To comfort this hypothesis, no absorbance decay of the sensitizer was observed during the experiments. Pd_4F was synthesized according to a previously reported procedure[7].

A.4 DMA-O_2 quantification by high-performance liquid chromatography

As described in part 2.2.3, $^1O_2$ can be quantified by the DMA-O_2 production. HPLC was performed to characterise the DMA to DMA-O_2 conversion after electrolyte extraction. The swagelock cell can be opened inside an Ar filled glovebox and the electrolyte recovered. The cell components were rinsed with 400 µL of DME and sonicated in an ultrasonic bath for 10 minutes under exclusion of light, heat and air followed by a centrifugation. The supernatant was transferred and DME removed by evaporation under a N_2 stream at room temperature. The residue was dissolved in DME to reach the optimum concentration (~1 $mg_{DMA}\cdot L^{-1}$) and a volume of 2 µL was injected into the HPLC.

The HPLC procedure was optimized for a 1200 Series HPLC (Agilent Technology) using an UV-Vis detector (Agilent Technology G1365C MWD SL). The eluant, composed of water containing 0.01% formic acid (solvent A) and acetonitrile (solvent B), was monitored at the 210 nm wavelength. The analytes were separated by means of a pre-column (UHPLC 3PK, Poroshell 120 EC-C8 3.0 mm x 5 mm, Ø 2.7 µm, Agilent Technology) and a reversed-phase column (Poroshell 120 EC-C8, 3.0 mm x 100 mm, Ø 2.7 µm, Agilent Technology). The elution was maintained at a 0.7 $mL\cdot min^{-1}$ flow rate and a 20°C temperature with a gradient eluant starting at 50/50 solvent A/solvent B (v/v) to 100% solvent B. The resultant spectra are exemplified in Fig. 2.5(a). The surface under the peaks corresponding to each substance retention times can then be used to calculate the amount of each analytes. The HPLC process was calibrated by reacting a known amount of DMA with photochemically produced $^1O_2$ to produce DMA-O_2 in a known quantity subsequently analysed by HPLC.

A.5 $^3O_2$ and carbonate quantifications by mass spectrometry

Quantify $^3O_2$ and carbonate productions either from disproportionation, mediated oxidation or as cell side products were performed with a commercial quadrupole mass spectrometer (Balzers) with a turbomolecular pump (Pfeiffer). The gas flow was 5 mL/min (high purity Ar 6.0) in stainless steel tubing thanks to a membrane pump and a leak inlet controlled by a digital mass flow controller (Bronkhorst). The detector was calibrated for the different gases studied (Ar, O_2, CO_2). All calibrations and quantifications were performed using in-house programs. The gas release can be quantified by integration over time and related to the theoretical amount formed.

The setup itself consists in a glass vial, of a 7 mL volume, sealed via a flat rubber seal and a clamped PEEK cap with glued in exhaust PEEK tubes and exchangeable septums. A stirring bar ensures the solution homogenisation during the experiments. During the measurements, the reagents were added through a septum using a gas tight syringe (Hamilton) and the gas flow was regulated using a four-way valve. Before the measurements were started, all solutions were degassed with N_2 for at least 15 minutes to remove possible dissolved CO_2 and O_2.

In the case of O_2 release by disproportionation and mediated oxidation, an known amount of electrolyte containing the studied cations or mediators in TEGDME was injected onto an known amount of KO_2 or Li_2O_2 powder. To quantify carbonates and Li_2O_2 or Na_2O_2/NaO_2, 0.5 mL of 1 M H_2SO_4 were first injected to quantify inorganic carbonate and a part of the oxide by gas releases. After reaction, a sample was collected to reach 0.1 ml of solution in the MS setup. The solution was then diluted by 3 mL of H_2O. Finally, 0.5 mL of 0.5 M $FeSO_4$ and 0.15 mL of 10%$_w$ H_2O_2 in 0.1 M H_2SO_4 were added to drive CO_2 release form organic carbonates. The peak areas can then be ascribed to the amount of each analytes with low errors as depicted in Fig. A.4.

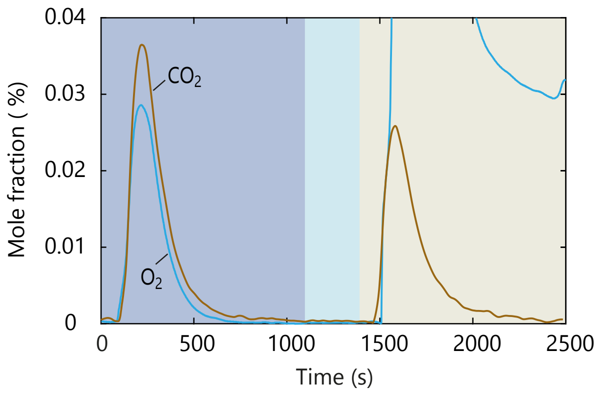

Figure A.4: **O_2 and CO_2 releases during Li-air electrode analysis by MS.** The CO_2 and O_2 production are represented respectively in brown and blue. Each steps of the quantification process is denoted by the coloured background.

A.6 Peroxide and superoxide quantifications by UV-vis spectroscopy

Superoxide and peroxide were quantified by combining UV-vis spectrospcopy and MS measurement. We will consider here the characterisation of peroxide as this thesis focus on Li-O_2 chemistry, the superoxide or mixed peroxide/superoxide calculations can be found more precisely in literature[1]. Acid addition to the M_2O_2 contained in the electrode (with M= Li, Na) will drive the formation of H_2O_2 according to Eq. A.3. H_2O_2 will partly decompose to O_2 following Eq. A.4. The remaining H_2O_2 in solution is then detected through a UV-vis spectrometer (UV-1800, Shimadzu) whereas O_2 evolution is detected by mass spectrometry as decribed in Appendix A.5. 2 w% Ti(IV)-oxysulfate (15 % in dilute H_2SO_4, 99.5% purity, Sigma aldrich) in 1 M H_2SO_4 is added to 0.1 mL of the MS extract to form the photo-active $[Ti(O_2^{2-})]^{2+}$ complex by reaction with H_2O_2.

$$M_2O_2 + 2\,H_2O \longrightarrow H_2O_2 + 2\,MOH \tag{A.3}$$

$$H_2O_2 \longrightarrow H_2O + \frac{1}{2}O_2 \tag{A.4}$$

One mole of O_2 detected by MS is hence equivalent to two moles of M_2O_2 whereas one mole of $[Ti(O_2^{2-})]^{2+}$ correspond to one mole of M_2O_2. $[Ti(O_2^{2-})]^{2+}$ complex present a maximum absorbance at 405 nm, illustrated in Fig. A.5, which was calibrated using high purity Li_2O_2 synthesized as previously described in part A.1. The procedures to quantify superoxide and superoxide/peroxide mixture are similar but different ratio have to be applied to convert the O_2 and $[Ti(O_2^{2-})]^{2+}$ amounts to the starting species amounts. The ratios are given in Eq. A.5 and Eq. A.6 for pure peroxide and superoxide respectively.

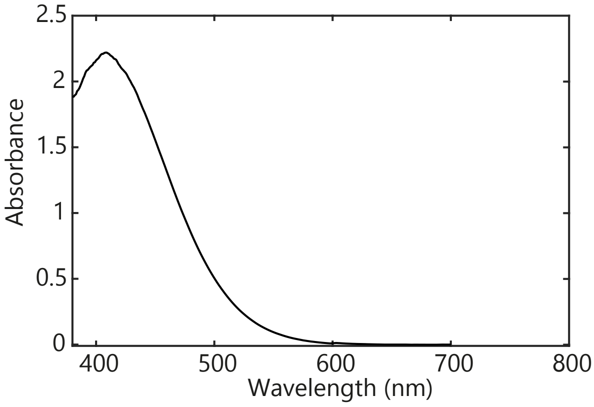

Figure A.5: **$[Ti(O_2^{2-})]^{2+}$ UV-vis spectrum.**

$$n_{M_2O_2} = n_{H_2O_2} + 2 \cdot n_{O_2} \tag{A.5}$$

$$n_{MO_2} = \frac{4}{3}(n_{O_2} + \frac{1}{2} \cdot n_{H_2O_2}) \tag{A.6}$$

With n, the mole amount of the indicated species.

A.7 $^1O_2$ quenching rate determination by UV-vis spectroscopy

The $^1O_2$ quenching rates were measured via a 1 cm high precision quartz cell (Hellma Analytics) with a gas tight injection lid and a UV-vis spectrometer (UV-1800, Shimadzu). The cuvette was filled with 1 mL of a TEGDME solution containing 1 μM Pd4F, 80 DMA μM, a given quencher concentration and a stirring bar placed at the bottom in an Ar glovebox. $^1O_2$ was produced photochemically according to the process described in A.3. The DMA concentration decay upon contact with $^1O_2$ was measured by means of the UV-Vis absorbance at 379 nm, corresponding to a absorbtion band of DMA as depicted in Fig. 2.5. The solution was bubbled with high purity oxygen at a flow rate of 1 mL·min^{-1} for 20 minutes prior measurement as well as during illumination. Photogenation of $^1O_2$ was performed by illuminating at a light density of 6.245 μmol·s^{-1}·m^{-2} for a given time, followed by 60 seconds stirring without illumination to ensure a homogeneous solution. After each illumination step, an absorbance spectrum was recorded. In consideration of the solvent and photosensitizer self-absorbance, all recorded spectra were subjected to solvent background correction and baseline correction. Due to possible overlap of UV-vis spectra between the quenchers and the DMA, a deconvolution of the species spectrum was done using their respective attenuation coefficient if needed. The attenuation coefficients were obtained before hand through Beer-Lambert's law given in Eq. A.7. The decay of the DMA concentration was fitted by pseudo-first order kinetic as described by Eq. A.8 as first approximation, considering the $^1O_2$ concentration as constant through the experiments[8]. The derivatives were used to compare the efficiency of the quenchers.

$$A = \epsilon \cdot C \cdot d \tag{A.7}$$

$$C = C_0 \cdot e^{-kt} \tag{A.8}$$

With A, the absorbance (-); ϵ, the molar attenuation coefficient (L·mol^{-1}·cm^{-1}); C, the concentration (mol·L^{-1}); d, the cuvette pathlength (cm); C_0, the initial concentration (mol·L^{-1}); k , the quenching rate constant (s^{-1}); and t, the time (s).

A.8 Oxidation mediator kinetic by UV-vis spectroscopy

Determination of the oxidation mediator kinetics was performed using 7 mm diameter and 1 mm thick KO_2 or Li_2O_2 pellets, which were placed at the bottom of a 1 cm gas tight high precision quartz cuvette (Hellma Analytics) with a magnetic stirrer. Li_2O_2 and KO_2 pellets were obtained by pressing Li_2O_2 (synthetized in-house) or KO_2 (Sigma Aldrich) powder with a die set in an Ar filled glove box. A solution of the chemically oxidized mediators, to avoid presence of Li^+ ions, at an adequate concentration was injected on top of the pellet.

The consumption of the Med^{ox}/release of Med^{red} were then monitored by the solution absorbance change over time. The concentrations of Med^{ox}/Med^{red} were recalculated thanks to the spectra of the pure mediators in both forms recorded beforehand. The Med^{ox}/Med^{red} decay/appearance were then fitted according to the equations given in Tab. D.2. As for the quenching kinetic, the derivative was used to compare the kinetic rate of the mediator. The kinetic rate constants were recalculated by approximating the reaction kinetic to a pseudo-first order reaction ($\nu = -k \cdot C_0$).

A.9 Disproportionation kinetic by pressure monitoring

7 mm diameter and 1 mm thick KO_2 or Li_2O_2 pellets were used to measure the O_2 evolution rate during the disproportionation reaction. The pellets were placed at the bottom of a tight glass vessel with a known volume connected to a high-precision pressure transducer (PAA35X, Omega). Known amount of electrolytes containing the studied cations in TEGDME were injected with a gas-tight syringe (Hamilton) through glued-in PEEK tubing and placed under agitation, similarly than for the oxidation mediator kinetic determination in Appendix A.8.

The pressure evolution was then monitored as represented by Fig. 5.4 and fitted by a second order reaction kinetic according to Eq. 5.5, Eq. A.9, Eq. A.10 and Eq. A.11. The disproportionation rates were then determined at initial time from translating the pressure to O_2 amount using the ideal gas law (Eq. A.1) considering the temperature change upon injection as negligible.

$$-\frac{\mathrm{d}C}{\mathrm{d}t} = k \cdot C^2 \tag{A.9}$$

with C the concentration (mol·L^{-1}); t, the time (s); and k, the reaction rate constant (mol^{-1}·L·s^{-1}).

$$\frac{1}{C} - \frac{1}{C_0} = k \cdot t \qquad \frac{1}{(P_f - P_0) - (P - P_0)} - \frac{1}{P_f - P_0} = k \cdot t \tag{A.10}$$

with $C_0 = P_f - P_0$ and $C = (P_f - P_0) - (P - P_0)$; P_0 is the initial pressure (Pa), P_f is the final pressure (Pa); Assuming the temperature and the volume constant.

$$P - P_0 = \frac{((P_f - P_0)^2 \cdot k \cdot t)}{((P_f - P_0) \cdot k \cdot t + 1)} \tag{A.11}$$

A.10 Chemical purity and stability characterisation by NMR

NMR spectra were either recorded on a Bruker Avance III 300 MHz FT NMR spectrometer with autosampler (300.36 MHz (^{1}H-NMR), 75.53 MHz (^{13}C-NMR)) or on a Varian Inova 500 MHz spectrometer (470.39 MHz (^{19}F-NMR), 132.22 MHz (^{23}Na-NMR)). Chemical shifts (δ) are referenced to the residual protonated solvent signals as internal standard excepted if mentioned otherwise. ^{13}C spectra were proton decoupled. The deuterated solvents used were $CDCl_3$, CH_3CN-d$_3$, or DMSO-d$_6$ and precised for each experiments.

Signal multiplicities (J) are abbreviated as s (singlet), d (doublet), t (triplet), and m (multiplet). HH-COSY, HMBC and HSQC experiments were recorded if necessary for the correct assignment of the signals. The deuterated solvent, the chemical shifts, the coupling constant, the integral and assignment of the respective signals are moreover given for synthesized molecules.

For measuring stability against superoxide or peroxide, excess of KO_2 or Li_2O_2 were added to 1 mg of the studied species in DME, or directly in $CDCl_3$ if precised, in Ar atmosphere and stirred for a given time. DME solutions were then filtered, dissolved in deuterated solvent and subjected to ^{1}H-NMR. To assess the stability against O_2 and $^1O_2$, 1 mg of the studied species were dissolved in 1 mL DME. The mixture was saturated with a stream of pure O_2. In the case of $^1O_2$, 1 µM Pd_4F was added to the stirred solution which was then irradiated with a red LED (643 nm) for a given time with a pure O_2 headspace as described in Appendix A.3. The resultant solutions were then analysed.

Bibliography

[1] B. Schafzahl, E. Mourad, L. Schafzahl, Y. K. Petit, A. R. Raju, M. O. Thotiyl, M. Wilkening, C. Slugovc, and S. A. Freunberger, “Quantifying total superoxide, peroxide, and carbonaceous compounds in metal–O_2 batteries and the solid electrolyte interphase,” *ACS Energy Letters*, vol. 3, no. 1, pp. 170–176, 2017.

[2] E. Mourad, Y. K. Petit, R. Spezia, A. Samojlov, F. F. Summa, C. Prehal, C. Leypold, N. Mahne, C. Slugovc, O. Fontaine *et al.*, “Singlet oxygen from cation driven superoxide disproportionation and consequences for aprotic metal–O_2 batteries,” *Energy & Environmental Science*, vol. 12, no. 8, pp. 2559–2568, 2019.

[3] E. Mourad, Y. K. Petit, C. Leypold, A. Windischbacher, D. Mijailovic, C. Slugovc, S. M. Borisov, E. Zojer, S. Brutti, O. Fontaine, and S. A. Freunberger, “Mechanism of mediated alkali peroxide oxidation reveals strategies to suppress singlet oxygen formation,” in revision.

[4] Y. K. Petit, C. Leypold, N. Mahne, E. Mourad, L. Schafzahl, C. Slugovc, S. M. Borisov, and S. A. Freunberger, “DABCOnium: an efficient and high-voltage stable singlet oxygen quencher for metal–O_2 cells,” *Angewandte Chemie International Edition*, vol. 58, no. 20, pp. 6535–6539, 2019.

[5] W.-J. Kwak, H. Kim, Y. K. Petit, C. Leypold, T. T. Nguyen, N. Mahne, P. Redfern, L. A. Curtiss, H.-G. Jung, S. M. Borisov *et al.*, “Deactivation of redox mediators in lithium-oxygen batteries by singlet oxygen,” *Nature communications*, vol. 10, no. 1, p. 1380, 2019.

[6] M. M. Ottakam Thotiyl, S. A. Freunberger, Z. Peng, and P. G. Bruce, “The carbon electrode in nonaqueous Li–O_2 cells,” *Journal of the American Chemical Society*, vol. 135, no. 1, pp. 494–500, 2012.

[7] S. Borisov, G. Nuss, W. Haas, R. Saf, M. Schmuck, and I. Klimant, “New NIR-emitting complexes of platinum (II) and palladium (II) with fluorinated benzoporphyrins,” *Journal of Photochemistry and Photobiology A: Chemistry*, vol. 201, no. 2-3, pp. 128–135, 2009.

[8] F. Wilkinson, W. P. Helman, and A. B. Ross, “Rate constants for the decay and reactions of the lowest electronically excited singlet state of molecular oxygen in solution. An expanded and revised compilation,” *Journal of Physical and Chemical Reference Data*, vol. 24, no. 2, pp. 663–677, 1995.

Appendix chapter 3

Contents

Figures

Chapter based on Mourad, Petit et al.[1]

B.1 Chemicals and methods

All chemicals were purchased from Sigma Aldrich, Solvionic and TCI. Unless specified otherwise, chemicals were used without further purifications. Salts contained either the $TFSI^-$ or ClO_4^- anion which was deemed as negligeable influence in Fig. 3.5. LiTFSI, $LiClO_4$, $NaClO_4$, $KClO_4$, TBATFSI and KO_2 were dried under vacuum for 24 hours at 80 °C before use and stored in Ar atmosphere. Lithium peroxide (Li_2O_2) was synthesized as described in part A.1. KO_2 was solubilized by 1,4,7,10,13,16-hexaoxacyclooctadecane (18-crown-6, ≥99%). 9,10-Dimethylanthracene (DMA) was recrystallized from ethanol and its purity confirmed by ^{1}H-NMR spectroscopy and HPLC analysis. Dimethoxyethane (DME) and tetraethylene glycol dimethyl ether (TEGDME) were dried over lithium, distilled, further dried and stored over activated molecular sieves. The water content as measured by Karl–Fischer titration was below 5 ppm.

Pressure was measured in-situ via a PAT-Cell-Press and the electrodes were built as described in Appendices A.1 and A.2. O_2, $^1O_2$, peroxide and carbonate quantifications were performed as explained in Appendices A.4, A.5, and A.6. The chemical stability studies by ^{1}H-NMR were determined as defined in Appendix A.10.

Energies were calculated for solvated species with a solvent dielectric constant of 7.28 (1,1,2-trichloroethane, a value close to short chain glymes, like DME) by density functional theory (DFT) calculations, adopting a computational approach validated previously and benchmarked on post-Hartree–Fock calculations[2]. The M06-2X functional and the 6-31++G(d,p) basis set (unrestricted)[3] was used and solvation effects incorporated using a self-consistent reaction field (SCRF) in continuum solvation model C-PCM.[4].

The final computational accuracy for the reaction energies that do not involve the $^1O_2$ species is estimated to be 0.05 eV. The $^1O_2$ molecule computed at the unrestricted M062X level shows unsatisfactory geometry and frequencies, similarly to the B3LYP functional, due to the well-known spin-contamination problem[5]. This unavoidable computational limitation at DFT level leads to an underestimate of the $^3O_2$ to $^1O_2$ energy difference and thus to a worse computational accuracy for all $^1O_2$ release reactions, estimated to be between 0.1-0.15 eV.

All structures were relaxed to their energy ground state and vibrational stability checked for all the reported reagents, intermediates, and products. The Gibbs energy of each molecular/ionic species was calculated at 298 K by considering zero-point energies and thermal effects. All calculations were done using Gaussian16[6]. The reaction energies for the precipitation form solvated to solid peroxides were calculated with thermochemical cycles starting from DFT calculations, the assessed thermodynamic properties of solid phases and for neutral atoms in the gas phase[7]. The thermodynamics of the $TBA^+O_2^-$ ion couple was calculated at the same level of theory by relaxing the solid ionic couple in the simulated solvent to a ground state minimum[8].

B.2 Supplementary notes

B.2.1 Mass spectrometry experimental errors

O_2, $^1O_2$, peroxide and carbonates produced via superoxide disproportionation in presence of 0.5 M Li^+ and Na^+ and either 0.1 $MTBA^+$, $EmIm^+$, $EmIm^{2+}$, F3CCOOH or no addition in

TEGDME were quantified at least three times to obtain the measurement errors which are depicted in Fig. B.1. The errors demonstrate sufficient accuracy of our quantifications to determine the cation influence on disproportionation.

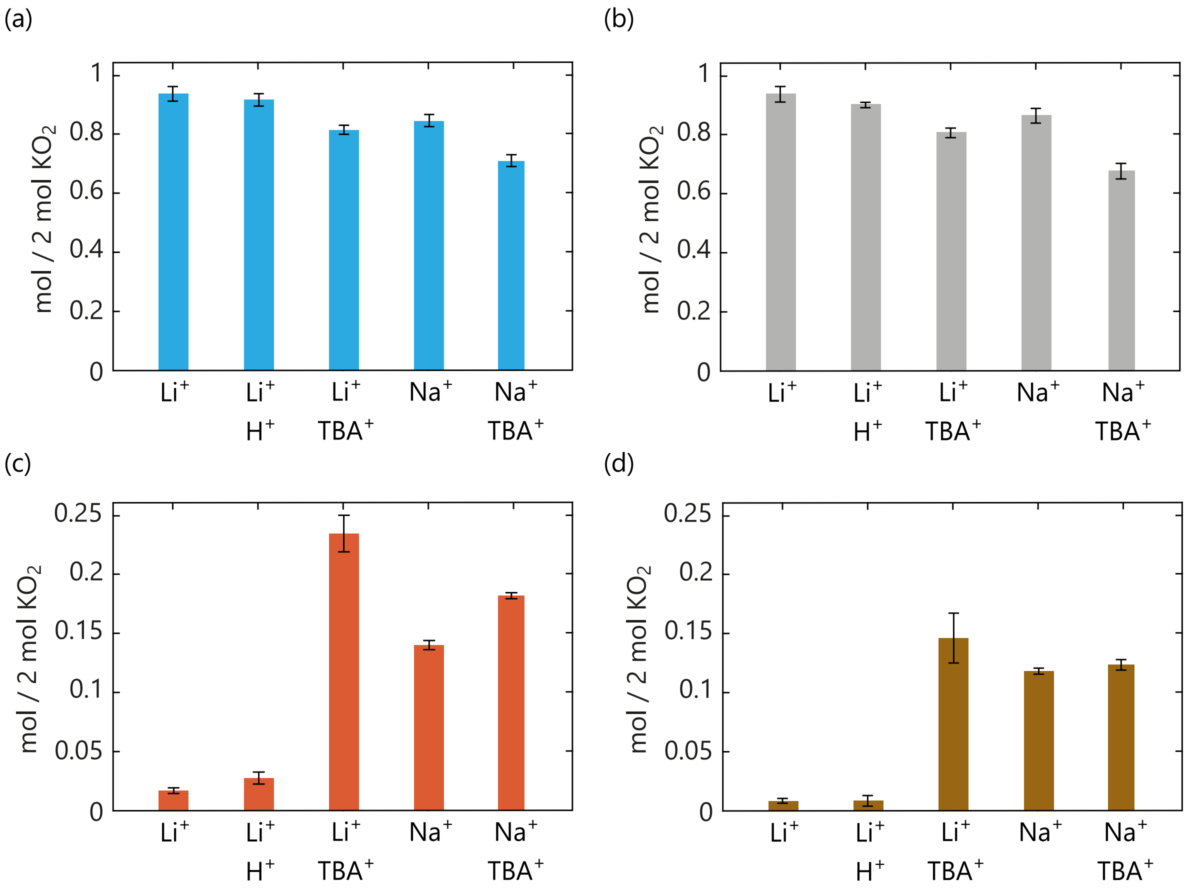

Figure B.1: **O_2, $^1O_2$, peroxide and carbonates produced via superoxide disproportionation and associated error bars.** The measurements are shown in Fig. 3.2.

B.2.2 Dissociation and ion exchange reaction free energies

Table B.1: **Superoxide dissociation free energies and KO_2 ion exchange free energies at 298 K in absence and presence of TFSI⁻counterions.**

Reaction	$\Delta_r G^0_{298\ K}$ (eV)
$LiO_2 \longrightarrow Li^+ + O_2^-$	1.21
$NaO_2 \longrightarrow Na^+ + O_2^-$	1.36
$KO_2 \longrightarrow K^+ + O_2^-$	0.71
$TBAO_2 \longrightarrow TBA^+ + O_2^-$	0.44
$Li^+ + TFSI^- + KO_2 \longrightarrow LiO_2 + KTFSI$	−0.87
$Na^+ + TFSI^- + KO_2 \longrightarrow NaO_2 + KTFSI$	−1.02
$TBA^+ + TFSI^- + KO_2 \longrightarrow TBAO_2 + KTFSI$	−0.10
$Li^+ + KO_2 \longrightarrow LiO_2 + K^+$	−0.50
$Na^+ + KO_2 \longrightarrow NaO_2 + K^+$	−0.64
$TBA^+ + KO_2 \longrightarrow TBAO_2 + K^+$	0.27

B.2.3 Relative stability of $^1M(O_2)_2M$ and $^3M(O_2)_2M$ dimers

Table B.2: **Gibbs free energies of $^1M(O_2)_2M$ and $^3M(O_2)_2M$ dimers with M = Li, Na, K at 298 K.** * corresponds to vibrationally unstable configuration.

Stochiometry	$\Delta_r G^0_{298\ K}$ singlet (eV)				$\Delta_r G^0_{298\ K}$ triplet (eV)			
	Bi-pyramide	Cage	Chain	Chair	Bi-pyramide	Cage	Chain	Chair
$Li(O_2)_2Li$	1.07	*	*	*	1.23	**0.00**	*	0.01
$Na(O_2)_2Na$	**0.00**	*	*	*	0.35	*	*	*
$K(O_2)_2K$	**0.00**	*	*	0.72	0.47	*	*	*

B.2.4 Superoxide dimerization free energies

Table B.3: **Calculated superoxide dimerization free energies at 298 K in presence of respectively Li^+, TBA^+ and H^+ traces or Na^+, TBA^+ and H^+ traces illustrated in Fig. 3.8 and Fig. 3.9.** * represents a vibrationally unstable molecules. More details on the calculations are given in Appendix B.1

Reaction	$\Delta_r G^0_{298\ K}$ singlet (eV)	$\Delta_r G^0_{298\ K}$ triplet (eV)
$2\ LiO_2 \longrightarrow Li(O_2)_2Li$	0.99	−0.08
$LiO_2 + O_2^- \longrightarrow Li(O_2)_2^-$	−0.49	−0.52
$LiO_2 + HO_2 \longrightarrow H(O_2)_2Li$	0.45	*
$2\ NaO_2 \longrightarrow Na(O_2)_2Na$	0.83	1.18
$NaO_2 + O_2^- \longrightarrow Na(O_2)_2^-$	−0.29	−0.32
$NaO_2 + HO_2 \longrightarrow H(O_2)_2Na$	0.38	*

B.2.5 Electrochemical curves

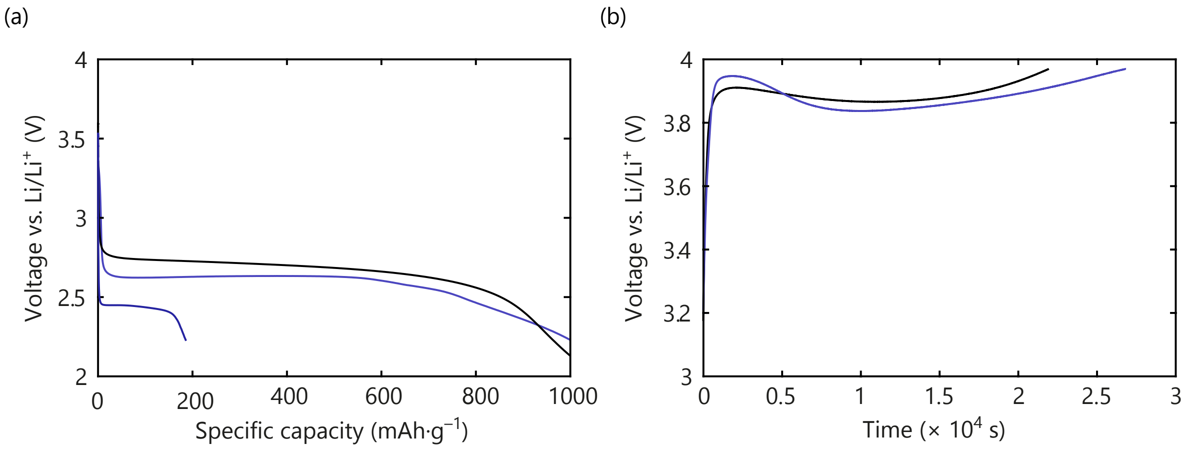

Figure B.2: **Influence of TBA^+ on Li-O_2 (dis)charge curves.** The curves correspond to the pressure evolution plotted in Fig. 3.13 and Fig. 3.14. (a) Galvanostatic discharge at 100 $mA{\cdot}g_c^{-1}$ of Li-O_2 cells. (b) Galvanostatic charge at 100 $mA{\cdot}g_c^{-1}$ of Li-O_2 cells. The cells are composed of carbon working electrodes and LFP counter electrodes as described in Appendix A.1. The electrolyte used are 30 mM DMA and 0.1 M LiTFSI in black or a total of 1 M Li^+/TBA^+ in TEGDME, 1:9 ratio in light purple and 1:99 ratio in dark purple.

It can be noted that the discharge voltage plateau decrease with TBA^+ addition due to increased viscosity of the electrolyte, and hence an increased reaction resistance.

Bibliography

[1] E. Mourad, Y. K. Petit, R. Spezia, A. Samojlov, F. F. Summa, C. Prehal, C. Leypold, N. Mahne, C. Slugovc, O. Fontaine *et al.*, “Singlet oxygen from cation driven superoxide disproportionation and consequences for aprotic metal–O_2 batteries,” *Energy & Environmental Science*, vol. 12, no. 8, pp. 2559–2568, 2019.

[2] M. Carboni, A. G. Marrani, R. Spezia, and S. Brutti, “1,2-Dimethoxyethane degradation thermodynamics in Li-O_2 redox environments,” *Chemistry–A European Journal*, vol. 22, no. 48, pp. 17 188–17 203, 2016.

[3] Y. Zhao and D. G. Truhlar, “The M06 suite of density functionals for main group thermochemistry, thermochemical kinetics, noncovalent interactions, excited states, and transition elements: two new functionals and systematic testing of four M06-class functionals and 12 other functionals,” *Theoretical Chemistry Accounts*, vol. 120, no. 1-3, pp. 215–241, 2008.

[4] M. Cossi, N. Rega, G. Scalmani, and V. Barone, “Energies, structures, and electronic properties of molecules in solution with the C-PCM solvation model,” *Journal of computational chemistry*, vol. 24, no. 6, pp. 669–681, 2003.

[5] M. Gonzalez, R. Valero, J. M. Anglada, and R. Sayos, “Ab initio $^1A'$ ground potential energy surface and transition state theory kinetics study of the $O(^1D)+N_2O \longrightarrow 2\,NO, N_2+O_2\,(a\,^1\Delta_g)$ reactions,” *The Journal of Chemical Physics*, vol. 115, no. 15, pp. 7015–7031, 2001.

[6] M. J. Frisch, G. W. Trucks, H. B. Schlegel, G. E. Scuseria, M. A. Robb, J. R. Cheeseman, G. Scalmani, V. Barone, G. A. Petersson, H. Nakatsuji, X. Li, M. Caricato, A. V. Marenich, J. Bloino, B. G. Janesko, R. Gomperts, B. Mennucci, H. P. Hratchian, J. V. Ortiz, A. F. Izmaylov, J. L. Sonnenberg, D. Williams-Young, F. Ding, F. Lipparini, F. Egidi, J. Goings, B. Peng, A. Petrone, T. Henderson, D. Ranasinghe, V. G. Zakrzewski, J. Gao, N. Rega, G. Zheng, W. Liang, M. Hada, M. Ehara, K. Toyota, R. Fukuda, J. Hasegawa, M. Ishida, T. Nakajima, Y. Honda, O. Kitao, H. Nakai, T. Vreven, K. Throssell, J. A. Montgomery, Jr., J. E. Peralta, F. Ogliaro, M. J. Bearpark, J. J. Heyd, E. N. Brothers, K. N. Kudin, V. N. Staroverov, T. A. Keith, R. Kobayashi, J. Normand, K. Raghavachari, A. P. Rendell, J. C. Burant, S. S. Iyengar, J. Tomasi, M. Cossi, J. M. Millam, M. Klene, C. Adamo, R. Cammi, J. W. Ochterski, R. L. Martin, K. Morokuma, O. Farkas, J. B. Foresman, and D. J. Fox, “Gaussian-16 Revision C.01,” 2016, gaussian Inc. Wallingford CT.

[7] M. W. Chase, “NIST-JANAF thermochemical tables.” 1998.

[8] P. D. Dietzel, R. K. Kremer, and M. Jansen, “Tetraorganylammonium superoxide compounds: Close to unperturbed superoxide ions in the solid state,” *Journal of the American Chemical Society*, vol. 126, no. 14, pp. 4689–4696, 2004.

Appendix chapter 4

Contents

Figures

Chapter based on Petit et al.[1]

C.1 Chemicals and methods

All chemicals were purchased from ABCR Chemicals, Fluka, Merck, Sigma Aldrich, Solvionic, VWR Chemicals and TCI. Unless specified otherwise, chemicals were used without further purification. Dichloromethane (DCM) was dried by heating refluxing for 12 h over P_4O_{10} under inert atmosphere followed by a distillation using a Schlenk flask. Tetrahydrofuran (THF) was dried thanks to an aluminum oxide column. LiTFSI was dried under vacuum for 24h at 80°C. Dimethoxyethane (DME) and tetraethylene glycol dimethyl ether (TEGDME) were dried over lithium, distilled, further dried and stored over activated molecular sieves. The water content was determined by Karl-Fisher titration and found to be below 5 ppm. 9,10-Dimethylanthracene (DMA) was recrystallized from ethanol and its purity confirmed by ^{1}H-NMR spectroscopy and HPLC analysis. 1,4-diazabicyclo[2.2.2]octane (DABCO) was recrystallized from absolute diethyl ether.

Pressure was measured in-situ via a PAT-Cell-Press and the electrodes were built as described in Appendices A.1 and A.2. O_2, $^1O_2$, peroxide and carbonate quantifications were performed as explained in Appendices A.4, A.5, and A.6. NMR spectra were determined as defined in Appendix A.10. The $^1O_2$ quenching rates were obtained by UV-vis spectrometry and photochemically produced $^1O_2$ according to Appendix A.7. Differential Scanning Calorimetry (DSC, Perkin Elmer DCS 8500) measurements were performed under a nitrogen purge gas flow of 20 mL·min^{-1} and a heating/cooling rate of 10 °C·min^{-1}. Cyclic voltammetries were performed in a three-electrodes cell with a 1 mm glassy carbon working electrode (BAS Inc.), partially delithiated LFP in 0.1 M $LiClO_4$/TEGDME behind a vycor glass frit as the reference and a Pt counter electrode inside a glass vial with a PTFE lid. The cells were run inside an Ar filled glovebox using a potentiostat/galvanostat (SP-300, Bio-Logic Science Instruments).

C.2 Synthesis

1-pentyl-1,4-diazabicyclo[2.2.2]octan-1-ium bis(trifluoromethanesulfonyl)imide (PeDTFSI) was synthetized from 1,4-Diazabicyclo[2.2.2]octan (DABCO) using the following protocol. 1.00 g (8.92 mmol, 2.0 eq.) DABCO and 10mL acetonitrile were placed in a dried round-bottom flask. The colorless solution was stirred for 5 minutes at room temperature by dint of a PTFE covered stirring bar. Once a homogeneous solution was obtained, 552 µL (4.37 mmol, 1.0 eq.) of 1-bromopentane were added to initiate DABCO quaternization. The solution was stirred for 16 hours at 70 °C. The production of DABCOnium was verified by ^{1}H-NMR spectroscopy.

To perform the ions exchange from Br^- to $TFSI^-$, the reaction mixture was diluted with 30 mL of diethyl ether (Et_2O) leading to the apparition of two phases. The denser layer was washed with Et_2O (5 mL) three times. The crude product was dried under vacuum at 10^{-2} mbar for 5 hours and redissolved in 5 mL of water. 6.66 mL of a 0.5 M lithium bis(trifluoromethane)sulfonimide (LiTFSI) solution in H_2O were afterwards added at room temperature. The synthesis process is resumed in Fig. C.1.

The mixture was stirred for 5 min and transferred into a separatory funnel for further purification. The aqueous phase was extracted with DCM (20mL) three times. The recovered organic phase was then washed three times with water (10 mL) and dried. The residue was redissolved in acetone (40 mL) and purified by addition of activated charcoal. After 3 hours stirring, the solution was filtered on activated alumina. Finally, the product was dried at 10^{-2} mbar for 3 hours and recovered for characterisations by ^{1}H-NMR, ^{13}C-NMR, ^{19}F-NMR and DSC analysis which are depicted in Fig. C.3. The NMR peaks correspond to the number given in Fig. C.2 and the shifts further described below.

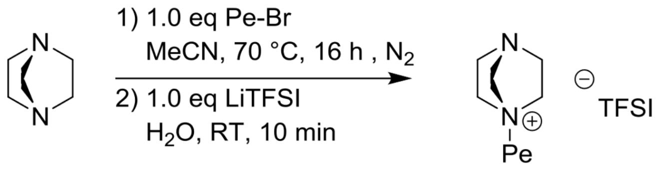

Figure C.1: **Overview of the synthesis route for PeDTFSI.**

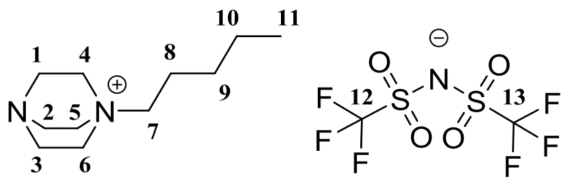

Figure C.2: **Structure and NMR index of PeDTFSI.**

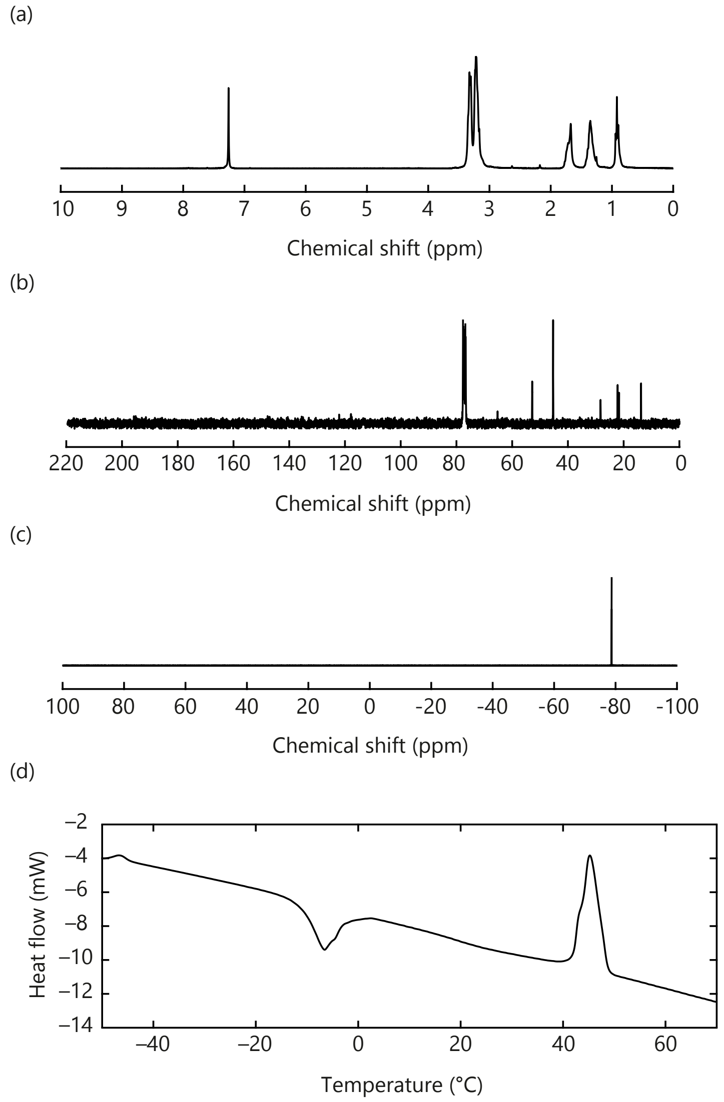

Figure C.3: **NMR and DSC characterisations of PeDTFSI.** a) ^{1}H-NMR in $CDCl_3$. b) ^{13}C-NMR in $CDCl_3$. c) ^{19}F-NMR in $CDCl_3$. d) DSC analysis during the third heating phase (endothermal up).

Yield: 1.83 g (2.97 mmol, 68% o. th.), colorless oil
$C_{13}H_{23}F_6N_3O_4S_2$ [463.45g/mol]
mp: 43-49°C

^{1}H-NMR (300.36 MHz, $CDCl_3$): δ = 3.32 (t, 6H, $^{3}J_{H}H$ = 6.6 Hz, H-4, H-5, H-6), 3.13-3.27 (m, 8H, $^{3}J_{H}H$ = 6.6 Hz, H-1, H-2, H-3, H-7), 1.61-1.79 (m, 2H, H-8), 1.26-1.44 (m, 4H, H-9, H-10), 0.91 (t, 3H, $^{3}J_{H}H$ = 6.8Hz, H-11).

^{13}C^{1}H-NMR (75.53 MHz, $CDCl_3$): δ = 120.0 (J_{CF} = 322.0 Hz, C-12, C-13), 65.3 (J_{CN} = 2.4Hz, C-7), 52.8 (J_{CF} = 3.1Hz, C-4, C-5, C-6), 45.3 (C-1, C-2, C-3), 28.3 (C-10), 22.2 (C-9), 21.6 (C-8), 13.8 (C-11).

^{19}F-NMR (470.39 MHz, DMSO-d_6): δ = -78.9.

C.3 Supplementary notes

C.3.1 Donor number determination by ^{23}Na-NMR

The PeDTFSI donor number was determined using ^{23}Na-NMR following a procedure described in literature[2]. The NMR shifts of 10 mM NaFSI dissolved in solvents with known DN were recorded to create a trend line after calibration by 1 M NaCl in D_2O, as depicted in Fig. C.4. Using this trendline, the PeDTFSI donor number could be estimated to 12.5 as shown in Tab. C.1.

Table C.1: **Donor numbers and ^{23}Na-shifts of known solvents and PeDTFSI.**

	Donor Number	^{23}Na-NMR shift (ppm)
TEGDME	12	−9.13
MeCN	14	−6.43
DME	20	−5.83
NMP	27	−2.67
DMSO	30	−0.14
1,2-diaminoethane	55	12.96
PeDTFSI	12.5	−0.14

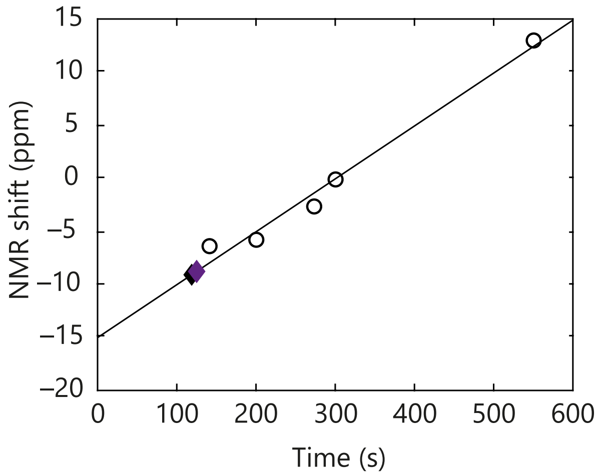

Figure C.4: **NaFSI ^{23}Na-NMR shift dependency on solvent donor number.** PeDTFSI is noted in purple and TEGDME in black. The line correspond to the linear fit used to obtain PeDTFSI value.

C.3.2 Li-Li cell cycling

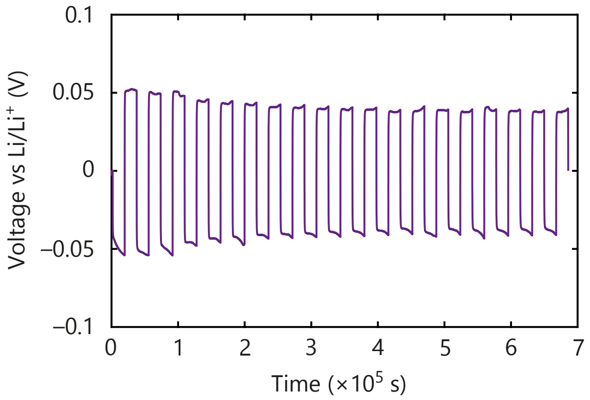

Figure C.5: **Cycling of a Lithium metal-lithium metal cell in presence of PeDTFSI.** The cell was cycled at |131| µA for 5 hours steps in a 380 mM PeDTFSI and 1 M LiTFSI TEGDME electrolyte.

C.3.3 DABCO stability characterisation by ^{1}H-NMR

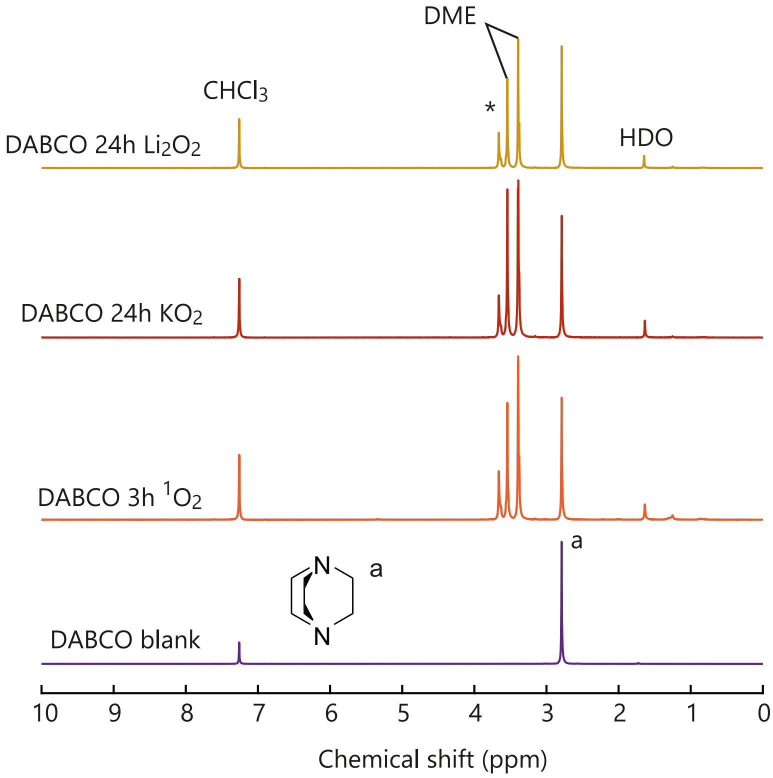

Figure C.6: **Stability of DABCO in contact with Li_2O_2, KO_2, and $^1O_2$ by ^{1}H-NMR.** The spectra were recorded in $CDCl_3$. The ^{1}H-NMR spectra characterise DABCO (in purple), DABCO after 3h contact with $^1O_2$ (in orange), DABCO after 24h contact with KO_2 (in red), and DABCO after 24h contact with Li_2O_2 (in yellow). The * denotes a residue from DME evaporation, which amounts to a content of 1 ppm in the DME; the ° denotes H from grease. $^1O_2$ was produced photochemically, according to Appendix A.3, by means of 1 µM Pd_4F and illumination at 643 nm.

C.3.4 Excited sensitizer lifetime and Stern-Volmer relationship

The $^1O_2$ quenching efficiency was determined using photochemically produced $^1O_2$ according to Appendix A.3. $^1O_2$ quencher could also efficiently quench the excited sensitizer T_1 state and influence $^1O_2$ photogeneration. This effect can be described by the Stern-Volmer relationship given in Eq. C.1.

$$\frac{\tau_0}{\tau} = 1 + K_{SV} \cdot C_Q \tag{C.1}$$

With τ_0, the excited state lifetime without quencher (s); τ, the excited state lifetime with a quencher at C_Q (s); K_{SV}, Stern-Volmer constant (L·mol^{-1}); and C_Q, the quencher concentration (mol·L^{-1}). K_{SV} represent the quenching rate multiplied by τ_0.

We measured the sensitizer T1 state lifetime by means of a pulsed LED illumination (λ max 392 nm) and a fluorescence spectrometer (Horiba Scientific). Prior measurements, the solution containing the sensitizer, and possibly a quencher, were purged with high purity nitrogen (99,9999%, Linde gas) for at least 15 min. The solution was then placed in a gas-thigh cuvette (Hellma). The sensitizer emission at 780 nm was monitored overtime, as depicted in Fig. C.7. The sensitizer excited state decay followed a first-order reaction rate from which the lifetime could be estimated. Using the obtained lifetime, the K_{SV} constant can be re-calculated as depicted in Fig. C.8. DABCO very poorly quench the excited sensitizer ($K_S V$ = 1.44 L·mol^{-1}) whereas PeDTFSI does not provide any significant quenching. In any case, the values obtained are largely lower to the oxygen quenching efficiency towards the excited sensitizer.

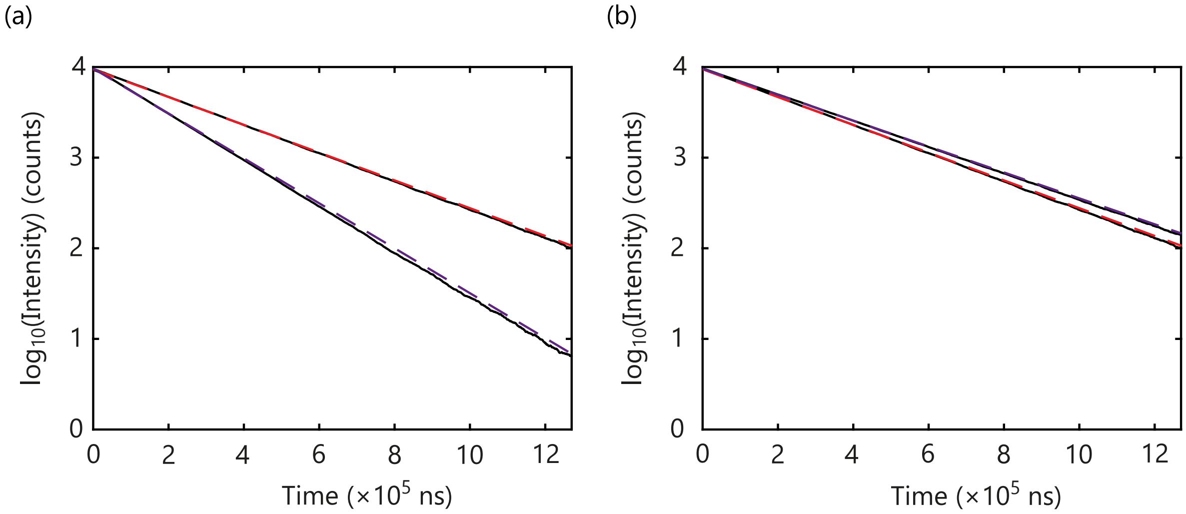

Figure C.7: **Quencher influence of the excited sensitizer lifetime.** The decay of the 780 nm light emission over time, which characterise the excited sensitizer, is given in presence of (a) DABCO and (b) PeDTFSI in otherwise similar conditions. The purple curves represente the decay with quencher and the red without. The exponential fit is represented in dashed line.

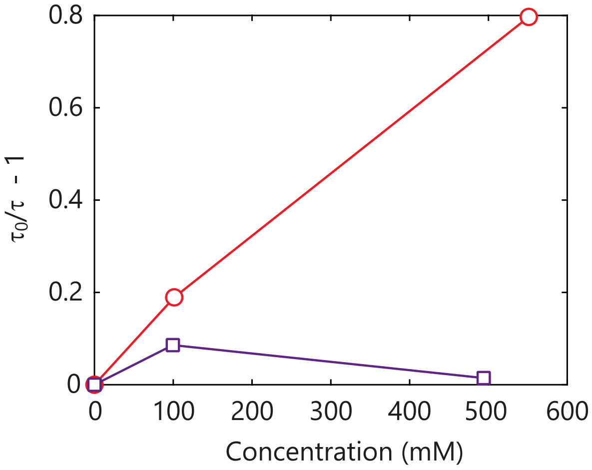

Figure C.8: **Stern–Volmer relationship applied to the excited sensitizer quenching.** The red curve represents DABCO and the purple one PeDTFSI.

Bibliography

[1] Y. K. Petit, C. Leypold, N. Mahne, E. Mourad, L. Schafzahl, C. Slugovc, S. M. Borisov, and S. A. Freunberger, “DABCOnium: an efficient and high-voltage stable singlet oxygen quencher for metal–O_2 cells,” *Angewandte Chemie International Edition*, vol. 58, no. 20, pp. 6535–6539, 2019.

[2] L. Johnson, C. Li, Z. Liu, Y. Chen, S. A. Freunberger, P. C. Ashok, B. B. Praveen, K. Dholakia, J.-M. Tarascon, and P. G. Bruce, “The role of LiO_2 solubility in O_2 reduction in aprotic solvents and its consequences for Li–O_2 batteries,” *Nature chemistry*, vol. 6, no. 12, p. 1091, 2014.

Appendix chapter 5

Contents

Figures

Chapter based on Mourad†, Petit†et al.[1]

D.1 Chemicals and methods

All chemical were purchased form Fluka, Sigma Aldrich, VWR, Solvionic and TCI. 2,2,6,6-tetramethyl-1-piperidinyloxy (TEMPO), tris[4-(diethylamino)phenyl]amine (TDPA), N,N,N',N'-tetramethyl-p-phenylenediamine (TMPD), ferrocene (Fc), 5,10-dihydro-5,10-dimethylphenazine (DMPZ), 1,4,7,10,13,16-hexaoxacyclooctadecane (18-crown-6, ≥99%), water, and acetonitrile (anhydrous, 99.8%, stored over molecular sieves) were used as purchased. Lithium bis(trifluoromethane)sulfonimide (LiTFSI) and KO_2 were dried under vacuum for 24 h at 80°C. 2,2'-dithiobis(benzothiazole) (MBT_2), and I_2 were recrystallized from ethanol or sublimated, respectively. Dimethoxyethane (DME) and tetraethylene glycol dimethyl ether (TEGDME) were dried over lithium, distilled under Ar, further dried and stored over activated molecular sieves. The water content was determined by Karl-Fisher titration and found to be below 5 ppm. 9,10-Dimethylanthracene (DMA) was recrystallized from ethanol and its purity confirmed by ^{1}H-NMR spectroscopy and HPLC analysis. Lithium peroxide (Li_2O_2) was synthesized as described in Appendix A.1.

Oxidized mediators were either obtained by chemically oxidizing the reduced forms . One equivalent of nitrosonium tetrafluoroborate ($NOBF_4$) reacted with the reduced mediator form in CH_3CN during 3 hours under agitation. The resulting oxidized mediators were purified by precipitation in cold ether, filtration, and dried under vacuum at 30°C for 12 hours. MBT_2 (2,2'-dithiobis(benzothiazole)) and $FcBF_4$ were purchased and used as received.

O_2, $^1O_2$, peroxide and carbonate quantifications were performed as explained in Appendices A.4, A.5, and A.6. NMR spectra were determined as defined in Appendix A.10. Oxidation mediator and disproportionation kinetics were evaluated respectively by UV spectroscopy and pressure measurements as described in Appendices A.8 and A.9. Cyclic voltammetries were performed in a three-electrodes cell with a 1 mm glassy carbon working electrode (BAS Inc.), partially delithiated LFP in 0.1 M $LiClO_4$/TEGDME behind a vycor glass frit as the reference and a Pt counter electrode inside a glass vial with a PTFE lid. The cells were run inside an Ar filled glovebox using a potentiostat/galvanostat (SP-300, Bio-Logic Science Instruments).

D.2 Supplementary notes

D.2.1 Determination of oxidation mediator potentials by cyclic voltammetry

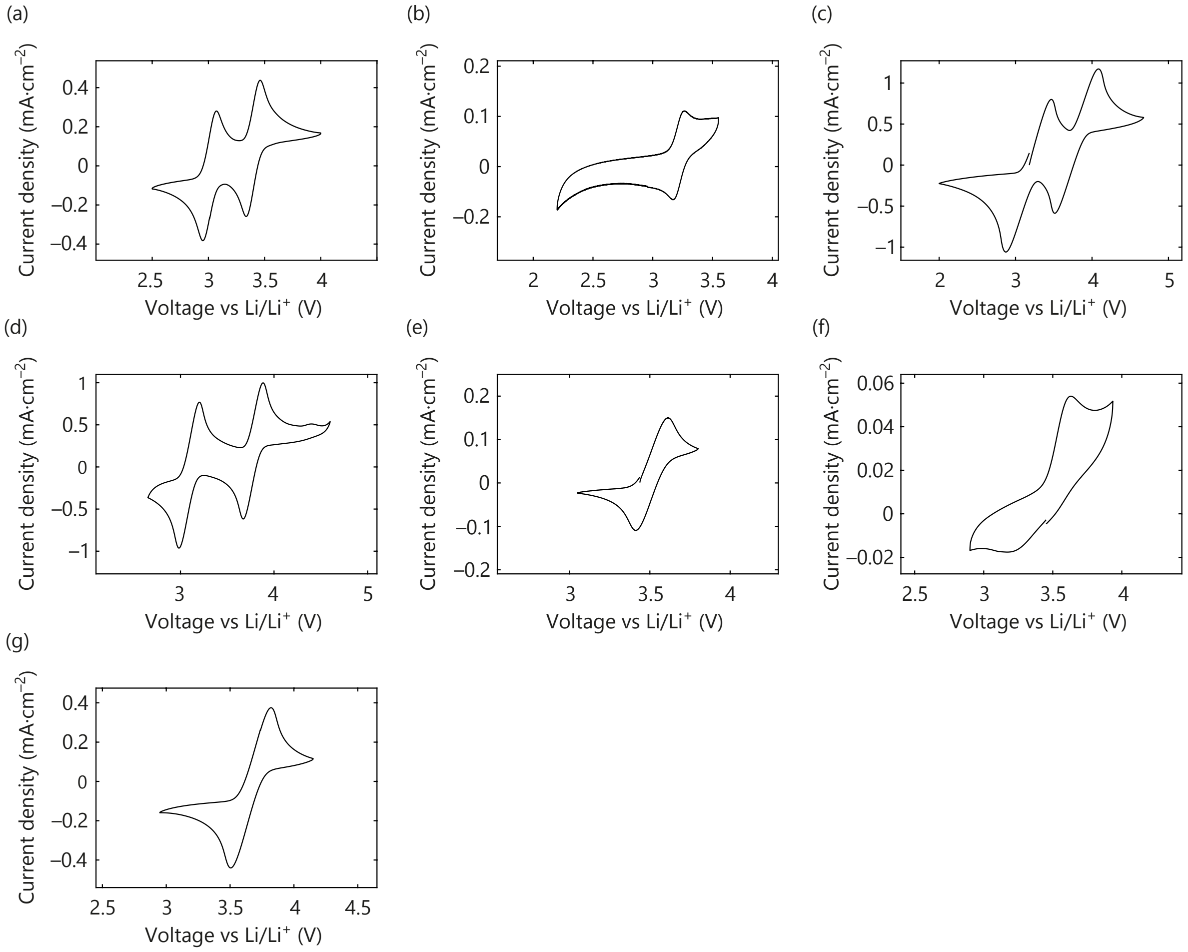

Figure D.1: **Cyclic voltammetry of the used mediators.** The mediators are (a) TDPA$^+$ (b) MBT$_2$ (c) TMPD$^+$ d, DMPZ$^+$ (e) Fc$^+$ (f) I$_2$ and (g) TEMPO$^+$. 2 mM of mediators were measured in a 0.1 M LiTFSI TEGDME electrolyte at a scan rate of 100 mV·s^{-1} and using the setup described in Appendix D.1.

Table D.1: **Oxidation mediator potentials.**

Oxidation mediator	Potential (V_{Li/Li^+})
TDPA$^+$	3.09
MBT$_2$	3.1
TMPD$^+$	3.24
DMPZ$^+$	3.29
Fc$^+$	3.56
I$_2$	3.63
TEMPO$^+$	3.76

D.2.2 Oxidation mediator kinetics by UV-vis spectroscopy

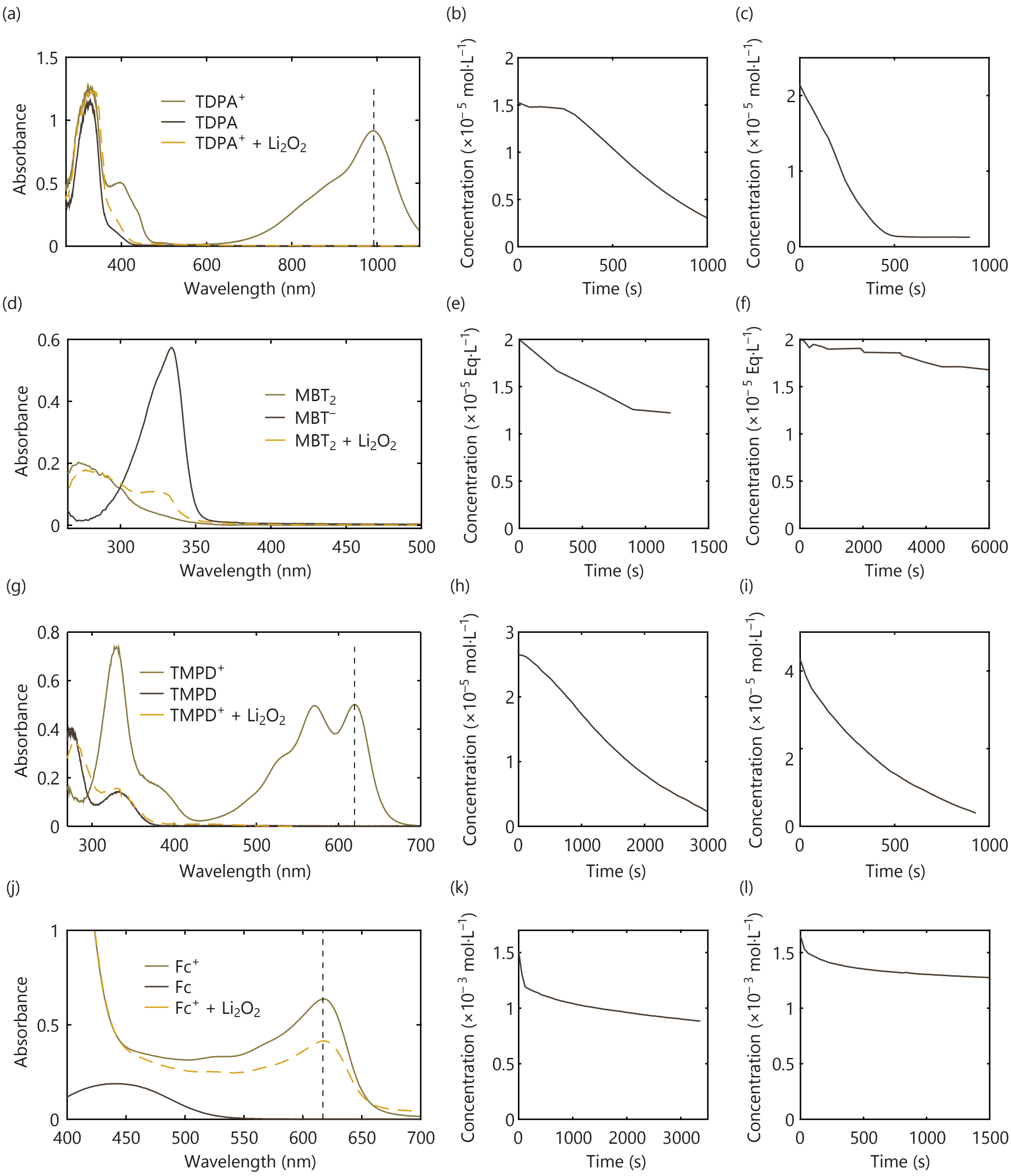

Figure D.2: **Mediated oxidation reaction rates obtained by UV-vis spectroscopy.** The first column represents the UV-vis spectra of the indicated mediators. The reduced forms are in brown, the oxidized ones in light brown and the oxidized forms after reaction on Li_2O_2 in dashed yellow. The black dashed lines denote the wavelength used for kinetic measurements. The second and third columns are the oxidized mediator concentrations over time in contact with KO_2 or Li_2O_2 pellets respectively, as described in Appendix A.8.

Table D.2: **Oxidation mediator potentials.**

Oxidation mediator	Fitting equation
$TDPA^+$	linear interpolation (due to instability)
MBT_2	exponential
$TMPD^+$	exponential
$DMPZ^+$	exponential
Fc^+	two exponentials (due to instability)
I_2	exponential

D.2.3 Oxidation mediator kinetics: comparison with the literature

The reactions between Li_2O_2 and oxidation mediators have previously been studied using scanning electrochemical microscopy (SECM)[2]. The rate constants obtained from UV-vis spectroscopy are compared to the one obtained by SECM in Fig. D.3. The reaction kinetics are in the same magnitude order with a maximum corresponding to ~3.4 V_{Li/Li^+}, notwithstanding the measurement method. The kinetic of the nitroxides class, presenting the fastest kinetic by SECM, were disregarded due to the instability of TEMPO as discussed in part 5.4.1.

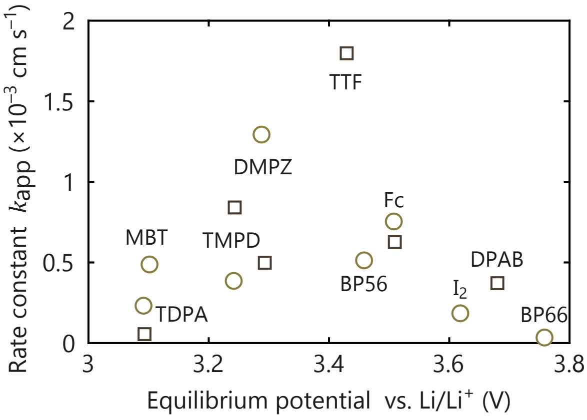

Figure D.3: **Li_2O_2 mediated oxidation rate constants.** The kinetics were either studied by (a) UV-vis and (b) SECM[2]. The latter results were corrected to account for the Li_2O_2 surface fraction of 35% estimated by the authors.

D.2.4 DFT calculation protocol

DFT calculations of TDPA were done with Gaussian16[3]. The CAM-B3LYP[4] functional with the def2-TZVP basis set[5,6] and Grimme's dispersion correction was used[7]. To simulate the methanol influence (dielectric constant of 32.613), all calculations were carried out using the Polarizable Continuum Model (PCM)[8]. The geometries of the molecules were first optimized. The neutral and dicationic species were computed as closed shell singlets, whereas the cationic molecule was computed as an open shell doublet. Based on the obtained structures, the vertical energies of the first 40 excited states were calculated. The vertical excitations were computed via the linear-response approach as implemented in Gaussian[9,10].

Bibliography

[1] E. Mourad, Y. K. Petit, C. Leypold, A. Windischbacher, D. Mijailovic, C. Slugovc, S. M. Borisov, E. Zojer, S. Brutti, O. Fontaine, and S. A. Freunberger, "Mechanism of mediated alkali peroxide oxidation reveals strategies to suppress singlet oxygen formation," in revision.

[2] Y. Chen, X. Gao, L. R. Johnson, and P. G. Bruce, "Kinetics of lithium peroxide oxidation by redox mediators and consequences for the lithium–oxygen cell," *Nature communications*, vol. 9, no. 1, p. 767, 2018.

[3] M. J. Frisch, G. W. Trucks, H. B. Schlegel, G. E. Scuseria, M. A. Robb, J. R. Cheeseman, G. Scalmani, V. Barone, G. A. Petersson, H. Nakatsuji, X. Li, M. Caricato, A. V. Marenich, J. Bloino, B. G. Janesko, R. Gomperts, B. Mennucci, H. P. Hratchian, J. V. Ortiz, A. F. Izmaylov, J. L. Sonnenberg, D. Williams-Young, F. Ding, F. Lipparini, F. Egidi, J. Goings, B. Peng, A. Petrone, T. Henderson, D. Ranasinghe, V. G. Zakrzewski, J. Gao, N. Rega, G. Zheng, W. Liang, M. Hada, M. Ehara, K. Toyota, R. Fukuda, J. Hasegawa, M. Ishida, T. Nakajima, Y. Honda, O. Kitao, H. Nakai, T. Vreven, K. Throssell, J. A. Montgomery, Jr., J. E. Peralta, F. Ogliaro, M. J. Bearpark, J. J. Heyd, E. N. Brothers, K. N. Kudin, V. N. Staroverov, T. A. Keith, R. Kobayashi, J. Normand, K. Raghavachari, A. P. Rendell, J. C. Burant, S. S. Iyengar, J. Tomasi, M. Cossi, J. M. Millam, M. Klene, C. Adamo, R. Cammi, J. W. Ochterski, R. L. Martin, K. Morokuma, O. Farkas, J. B. Foresman, and D. J. Fox, "Gaussian-16 Revision C.01," 2016, gaussian Inc. Wallingford CT.

[4] T. Yanai, D. P. Tew, and N. C. Handy, "A new hybrid exchange–correlation functional using the Coulomb-attenuating method (CAM-B3LYP)," *Chemical Physics Letters*, vol. 393, no. 1-3, pp. 51–57, 2004.

[5] F. Weigend and R. Ahlrichs, "Balanced basis sets of split valence, triple zeta valence and quadruple zeta valence quality for H to Rn: design and assessment of accuracy," *Physical Chemistry Chemical Physics*, vol. 7, no. 18, pp. 3297–3305, 2005.

[6] F. Weigend, "Accurate coulomb-fitting basis sets for h to rn," *Physical chemistry chemical physics*, vol. 8, no. 9, pp. 1057–1065, 2006.

[7] S. Grimme, J. Antony, S. Ehrlich, and H. Krieg, "A consistent and accurate ab initio parametrization of density functional dispersion correction (DFT-D) for the 94 elements H-Pu," *The Journal of chemical physics*, vol. 132, no. 15, p. 154104, 2010.

[8] M. Cossi, V. Barone, R. Cammi, and J. Tomasi, "Ab initio study of solvated molecules: a new implementation of the polarizable continuum model," *Chemical Physics Letters*, vol. 255, no. 4-6, pp. 327–335, 1996.

[9] R. Cammi, B. Mennucci, and J. Tomasi, "Fast evaluation of geometries and properties of excited molecules in solution: a Tamm-Dancoff model with application to 4-dimethylaminobenzonitrile," *The Journal of Physical Chemistry A*, vol. 104, no. 23, pp. 5631–5637, 2000.

[10] M. Cossi and V. Barone, "Time-dependent density functional theory for molecules in liquid solutions," *The Journal of chemical physics*, vol. 115, no. 10, pp. 4708–4717, 2001.

Appendix chapter 6

Contents

Figures

Chapter based on Mourad†, Petit†et al.[1]

E.1 Chemicals and methods

All chemical were purchased form Fluka, Sigma Aldrich, VWR, Solvionic and TCI. 2,2,6,6-tetramethyl-1-piperidinyloxy (TEMPO), tris[4-(diethylamino)phenyl]amine (TDPA), N,N,N',N'-tetramethyl-p-phenylenediamine (TMPD), ferrocene (Fc), 5,10-dihydro-5,10-dimethylphenazine (DMPZ), 1,4,7,10,13,16-hexaoxacyclooctadecane (18-crown-6, ≥99%), water, and acetonitrile (anhydrous, 99.8%, stored over molecular sieves) were used as purchased. Lithium bis(trifluoromethane)sulfonimide (LiTFSI) and KO_2 were dried under vacuum for 24 h at 80°C. 2,2'-dithiobis(benzothiazole) (MBT_2), and I_2 were recrystallized from ethanol or sublimated, respectively. Dimethoxyethane (DME) and tetraethylene glycol dimethyl ether (TEGDME) were dried over lithium, distilled under Ar, further dried and stored over activated molecular sieves. The water content was determined by Karl-Fisher titration and found to be below 5 ppm. 9,10-Dimethylanthracene (DMA) was recrystallized from ethanol and its purity confirmed by ^{1}H-NMR spectroscopy and HPLC analysis. Lithium peroxide (Li_2O_2) was synthesized as described in Appendix A.1.

Oxidized mediators were either obtained by chemically oxidizing the reduced forms. One equivalent of nitrosonium tetrafluoroborate ($NOBF_4$) reacted with the reduced mediator form in CH_3CN during 3 hours under agitation. They were purified by precipitation in cold ether, filtration, and drying under vacuum at 30°C for 12 hours. MBT_2 (2,2'-dithiobis(benzothiazole)) and $FcBF_4$ were purchased and used as received.

O_2, $^1O_2$, peroxide and carbonate quantifications were performed as explained in Appendices A.4, A.5, and A.6. NMR spectra were determined as defined in Appendix A.10. Oxidation mediator and disproportionation kinetics were evaluated respectively by UV spectroscopy and pressure measurements as described in Appendices A.8 and A.9. Cyclic voltammetries were performed in a three-electrodes cell with a 1 mm glassy carbon working electrode (BAS Inc.), partially delithiated LFP in 0.1 M $LiClO_4$/TEGDME behind a vycor glass frit as the reference and a Pt counter electrode inside a glass vial with a PTFE lid. The cells were run inside an Ar filled glovebox using a potentiostat/galvanostat (SP-300, Bio-Logic Science Instruments).

E.2 Synthesis

E.2.1 1,1'-bipyrrolidine-2,2',5,5'-tetraone

A monowave vial equipped was charged with 1.01 g (10.0 mmol, 2.0 eq.) succinic anhydride. After cooling to 0°C, 250 mg (5.0 mmol, 1.0 eq.) hydrazine hydrate and 5 mL acetic acid were added to the reaction vessel. The reaction flask was heated to 140°C for 15 min using a monowave reactor (Anton Paar). The resulting precipitate was isolated by filtration, recrystallized from EtOH and characterised as shown below. The reaction route is summarized in Fig. E.1. The atoms corresponding to each NMR peaks are noted in Fig. E.2.

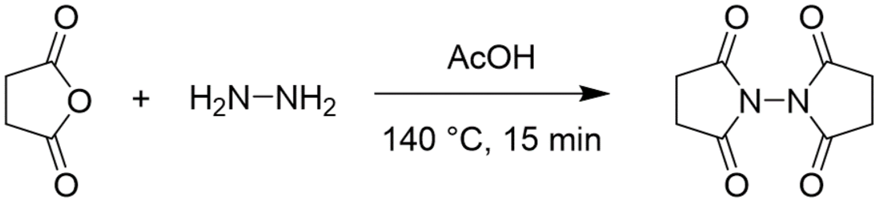

Figure E.1: **Overview of the synthesis route for 1,1'-bipyrrolidine-2,2',5,5'-tetraone.**

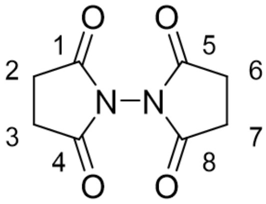

Figure E.2: **Structure and NMR index of 1,1'-bipyrrolidine-2,2',5,5'-tetraone.**

Yield: 280 mg (1.43 mmol, 29% o. th.), colorless solid
$C_8H_8N_2O_4$ [196.16]
mp: 295-300°C
^{1}H-NMR (300.36 MHz, $CDCl_3$): δ = 2.95 (s, 8H, H-2, H-3, H-6, H-7).
Elementary analysis: 48.98 %C, 3.84 %H, 14.38 %N.

E.2.2 1,1'-bipyrrolidine (BP55)

An oven dried 250 mL Schlenk flask was charged with 1.60 g (8.15 mmol, 1.0 eq.) 1,1'-bipyrrolidine-2,2',5,5'-tetraone and 40 mL of absolute THF. The reaction mixture was stirred for 10 min and cooled to −50°C. 2.00 g (52.7 mmol, 6.4 eq.) lithium aluminium hydride were then added slowly over a period of 5 min. After 1 h of stirring at −50°C under N_2 atmosphere, the solution was slowly heated to 70°C and stirred overnight. The reaction product was confirmed by NMR as presented below. The reaction route is summarized in Fig. E.3. The atoms corresponding to each NMR peaks are noted in Fig. E.4.

The product was then purify by slow addition of 1 mL H_2O, followed by 1 mL of a 15% NaOH-solution and 3 mL H_2O. The organic phase was subsequently transferred into a separatory funnel and washed three times with saturated $NaHCO_3$ (15 mL). For increased recuperation, the aqueous phase was extracted three times with DCM (15 mL) and the organic phase combined. This phase was washed with brine (20 mL), dried over Na_2SO_4, filtered and dried over vacuum to recover the BP-55. Finally, the product was vacuum distilled.

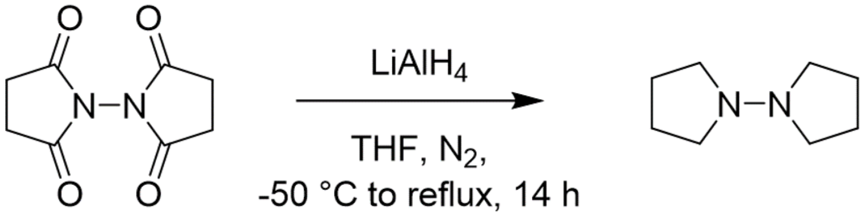

Figure E.3: **Overview of the synthesis route for 1,1-bipyrrolidine.**

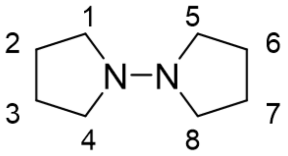

Figure E.4: **Structure and NMR index of BP55.**

Yield: 190 mg (1.36 mmol, 16.2% o. th.), colorless oil
$C_8H_{16}N_2$ [140.23]
bp: 95-105 °C at 10 mbar
^{1}H-NMR (300.36 MHz, $CDCl_3$): δ = 2.77 (t, 8H, H-1, H-4, H-5, H-8), 1.79 (t, 8H, H-2, H-3, H-6, H-7).
^{13}C-NMR (75.53 MHz, $CDCl_3$): δ = 51.0 (C-1, C-4, C-5, C-8), 21.9 (C-2, C-3, C-6, C-7).

E.2.3 1,1′-bipiperidine (BP66)

An oven dried 100 mL round bottom flask was charged with 2.5 g (29.4 mmol, 1.0 eq.) piperidine, 2.35 g (58.8 mmol, 2.0 eq.) NaOH, 250 mg (1.47 mmol, 5 mol%) silver nitrate and 15 mL H_2O. The brown reaction mixture was cooled to 0°C and stirred for 15 min. 6.99 g (29.9 mmol, 1.0 eq.) $Na_2S_2O_8$ were afterwards dissolved in 20 mL H_2O and slowly added to the reaction vessel. The reaction was heated up to RT under stirring for 4 h and N_2 atmosphere. The reaction product was confirmed by thin layer chromatography and NMR as presented below. The atoms corresponding to each NMR peaks are noted in Fig. E.5.

The resulting solution was transferred into a separatory funnel and extracted three times with EtOAc (20 mL). The organic phase was subsequently washed three times with H_2O (10 mL) and one time with brine (20 mL), dried over Na_2SO_4, filtered and dried over vacuum to recover the BP-66. The product was further purified via flash column chromatography (350 g SiO_2 500 × 50 mm, eluent: EtOAc/cyclohexane = 1:4 (v/v), fraction size: 80 mL, detection: $KMnO_4$).

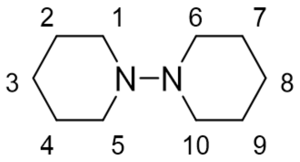

Figure E.5: **Structure and NMR index of BP66.**

Yield: 1.2 g (7.2 mmol, 49% o. th.) yellow oil

$C_{10}H_{20}N_2$ [168.28]

Rf = 0.36 (EtOAc/cyclohexane = 1:4 (v/v)), ($KMnO_4$)

^{1}H-NMR (300.36 MHz, $CDCl_3$): δ = 2.64 (t, 8H, H-1, H-5, H-6, H-10), 1.58 (t, 8H, H-2, H-4, H-7, H-9), 1.27-1.39 (m, 4H, H-3, H-8).

^{13}C-NMR (75.53 MHz, $CDCl_3$): δ = 49.4 (C-1, C-5, C-6, C-10), 26.7 (C-2, C-4, C-7, C-9), 24.9 (C-3, C-8).

E.2.4 1-(piperidin-1-yl)pyrrolidine-2,5-dione

A monowave vial was charged with 1.05 g (10.5 mmol, 1.1 eq.) succinic anhydride and cooled to 0°C. 930 mg (9.3 mmol, 1.0 eq.) 1-aminopiperidine and 1 mL acetic acid were then added. The solution was heated to 140°C for 30 min using a monowave reactor (Anton Paar). The reaction product was confirmed by thin layer chromatography and NMR as presented below. The reaction route is summarized in Fig. E.6. The atoms corresponding to each NMR peaks are noted in Fig. E.7.

The organic phase was transferred into a separatory funnel and was washed three times with saturated. $NaHCO_3$ (15 mL). Subsequently the aqueous phase was reextracted four times with EtOAc (15 mL) to increase recuperation. The combined organic phases were washed with brine (20 mL), dried over Na_2SO_4, filtered and the solvent was removed under vacuum. The product was purified via flash column chromatography (150 g SiO_2 400 × 30 mm, eluent: EtOAc/cyclohexane = 2:1 (v/v), fraction size: 80 mL, detection: KMnO4).

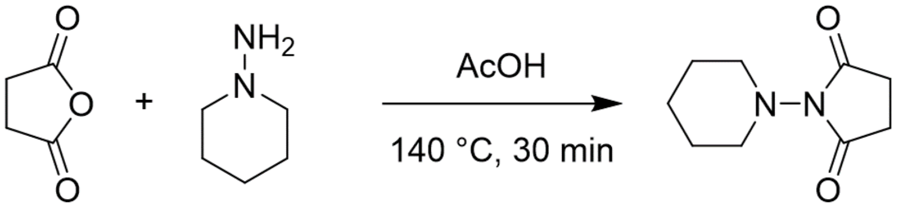

Figure E.6: **Overview of the synthesis route for 1-(piperidin-1-yl)pyrrolidine-2,5-dione.**

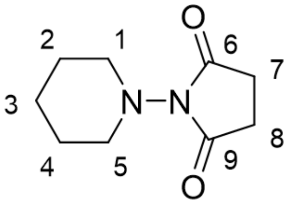

Figure E.7: **Structure and NMR index of 1-(piperidin-1-yl)pyrrolidine-2,5-dione.**

Yield: 1.7 g (7.2 mmol, 49% o. th.) colorless oil
$C_9H_{14}N_2O_2$ [182.22]
Rf = 0.32 (EtOAc/cyclohexane = 2:1 (v/v)), ($KMnO_4$)
^{1}H-NMR (300.36 MHz, $CDCl_3$): δ = 3.21 (t, 4H, 3JHH = 5.3 Hz, H-1, H-5), 2.66 (s, 4H, H-7, H-8), 1.71 (t, 4H, 3JHH = 5.3 Hz, H-2, H-4), 1.40-1.54 (m, 2H, H-3).
^{13}C-NMR (75.53 MHz, $CDCl_3$): δ = 175.6 (C-6, C-9), 52.2 (C-1, C-5), 26.7 (C-2, C-4), 26.0 (C-7, C-8), 23.0 (C-3).

E.2.5 1-(pyrrolidin-1-yl)piperidine (BP56)

An oven dried 100 mL Schlenk flask was charged with 1.69 g (9.27 mmol, 1.0 eq.) 1-(piperidin-1-yl)pyrrolidine-2,5-dione and 40 mL of absolute THF. The reaction mixture was stirred for 10 min and cooled to −50°C. 1.05 g (27.6 mmol, 3.0 eq.) aluminium hydride were added slowly over a period of 5 min. After 1 h of stirring at −50°C under N_2 atmosphere, the solution was slowly heated to 70°C and stirred overnight. The reaction product was confirmed by NMR as presented below. The reaction route is summarized in Fig. E.8. The atoms corresponding to each NMR peaks are noted in Fig. E.9.

The product was then purify by slow addition of 0.5 mL H_2O, followed by 0.5 mL of a 15% NaOH-solution and 1.5 mL H_2O. The organic phase was subsequently transferred into a separatory funnel and washed three times with saturated $NaHCO_3$ (15 mL). For increased recuperation, the aqueous phase was extracted three times with DCM (15 mL) and the organic phases combined. This phase was washed with brine (20 mL), dried over Na_2SO_4, filtered and dried over vacuum to recover the BP-56. Finally, the product was vacuum distilled.

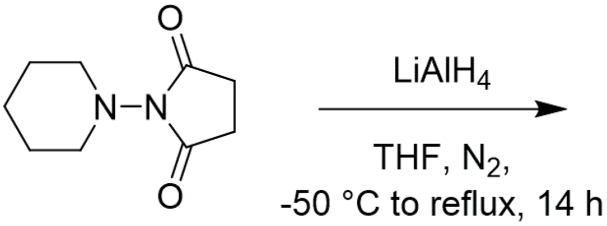

Figure E.8: **Overview of the synthesis route for 1-(pyrrolidin-1-yl)piperidine.**

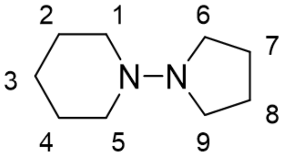

Figure E.9: **Structure and NMR index of BP56.**

Yield: 372 mg (2.41 mmol, 26.0% o. th.), colorless oil
$C_9H_{18}N_2$ [154.26]
bp: 110-120°C at 10 mbar
^{1}H-NMR (300.36 MHz, CDCl3): δ = 2.76 (t, 4H, H-6, H-9), 2.67 (t, 4H, H-1, H-5), 1.70 (t, 4H, H-7, H-8), 1.62 (t, 4H, H-2, H-4), 1.30-1.44 (m, 2H, H-3).
^{13}C-NMR (75.53 MHz, CDCl3): δ = 50.5 (C-1, C-5), 45.8 (C-6, C-9), 26.4 (C-2, C-4), 24.7 (C-3), 21.9 (C-7, C-8).

E.3 Supplementary notes

E.3.1 Determination of organic hydrazine potentials by cyclic voltammetry

Table E.1: **Organic hydrazine potentials.**

Organic hydrazine mediator	Potential (V_{Li/Li^+})
BP55	3.2
BP56	3.46
BP66	3.76

The voltammograms are given in Fig. 6.2.

E.3.2 Organic hydrazine kinetics by UV-vis spectroscopy

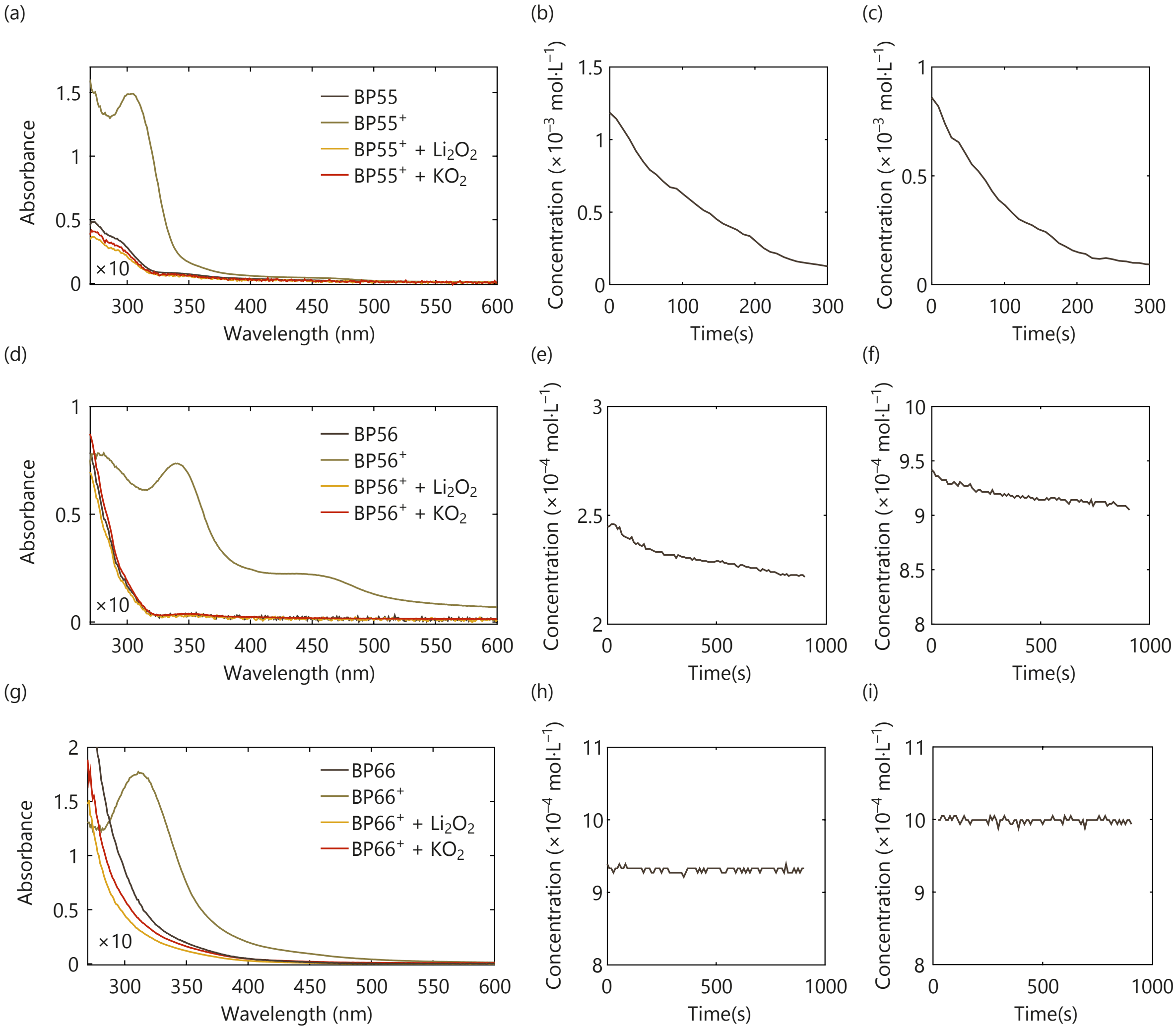

Figure E.10: **Organic hydrazine reaction rates obtained by UV-vis spectroscopy.** The first column represents the UV-vis spectra of the indicated amines at the same concentration. The reduced forms are in brown, the oxidized ones in light brown, and the oxidized forms after reaction on KO_2 in red and on Li_2O_2 in yellow. The second and third columns are the oxidized hydrazine concentrations over time in contact with KO_2 or Li_2O_2 pellets respectively, as described in Appendix A.8.

The reaction rates were modelled by a pseudo first-order kinetics.

E.3.3 $^1O_2$ quenching rates of oxidation mediators by UV-vis spectroscopy

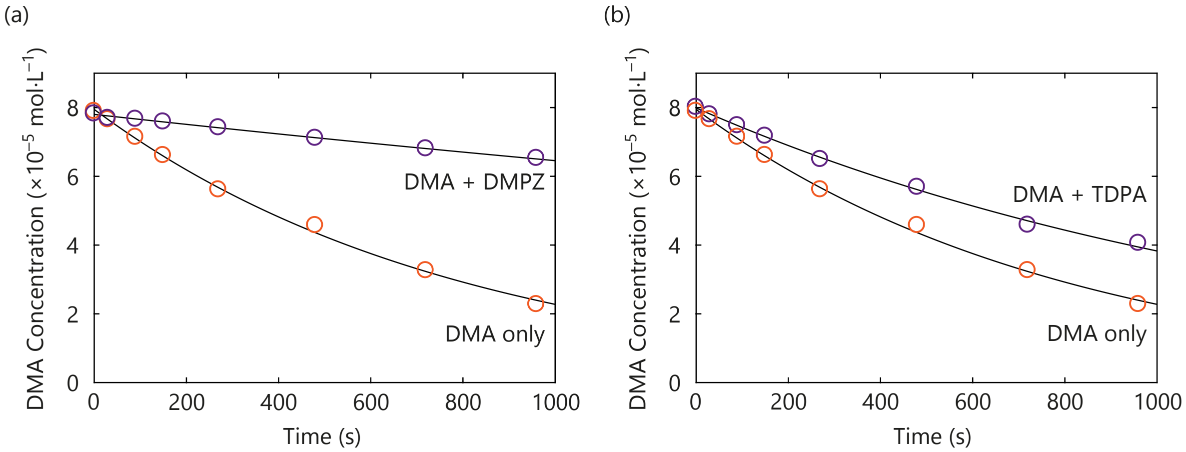

Figure E.11: **DMA decay over time in presence of photochemically produced $^1O_2$ with or without oxidation mediators.** (a) DMA consumption either alone (orange) or in presence of 80 μM DMPZ (purple) and the first-order kinetic fits (in black). (b) DMA consumption either alone (orange) or in presence of 80 μM TDPA (purple) and the first-order kinetic fit (in black). The electrolytes used are based on 80 μM DMA and 1 μM Pd_4F in O_2 saturated TEGDME illuminated at 643 nm, as described more lengthy in Appendix A.7.

E.3.4 Na_2O_2 mediated oxidation mechanism

Considering their respective potentials, a two-electron Na_2O_2 oxidation has a $^1O_2$ threshold of 2.82 V_{Na/Na^+}, whereas the one for NaO_2 oxidation is at 3.25 V_{Na/Na^+} as shown in part 2.3.2. The slow disproportionation rate in presence of Na^+ imposes a notable singlet oxygen production to be expected only by direct oxidation. A direct two-electron oxidation should hence produce $^1O_2$ below 3.25 V_{Na/Na^+} while a two steps reaction would only yield $^1O_2$ above. We measured $^3O_2$ and $^1O_2$ productions upon Na_2O_2/NaO_2 mediated oxidation by BP mediators (2.87, 3.13, 3.43 V_{Na/Na^+}, respectively for BP55, BP56 and BP66), according to the protocol given in Appendices A.4, A.5, and A.6. The results are plotted in Fig. E.12.

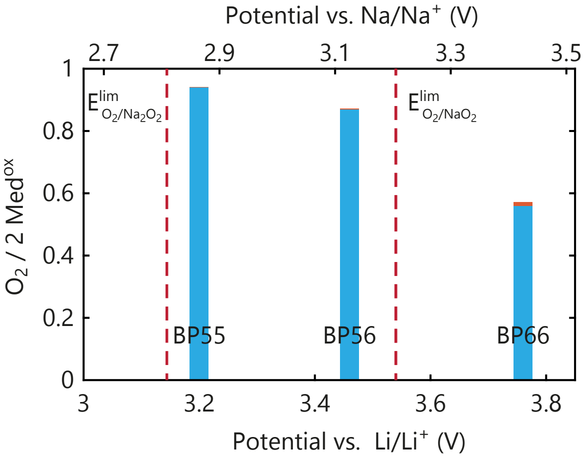

Figure E.12: **$^3O_2$ and $^1O_2$ yields upon mediated peroxide and superoxide oxidations by BP55, BP56 and BP66.** $^3O_2$ and $^1O_2$ evolutions were obtained by the addition of 10 mM oxidized mediators in TEGDME to an excess of Na_2O_2. The red dashed line indicates the thermodynamic thresholds for $^1O_2$ evolution from Na_2O_2 and NaO_2 oxidations.

Sodium peroxide oxidation by both BP55, BP56 (situated below 3.25 V_{Na/Na^+}) resulted in negligible $^1O_2$ amounts and $^3O_2$ yields superior to ~85%. In contrast, BP66 oxidation results in a significant lack of $^3O_2$ (~55%) and presence of $^1O_2$. $^1O_2$ appearance only above the superoxide thermodynamic threshold indicates a two step mechanism with the formation of superoxide species similarly to Li_2O_2 oxidation.

E.3.5 Sankey plots

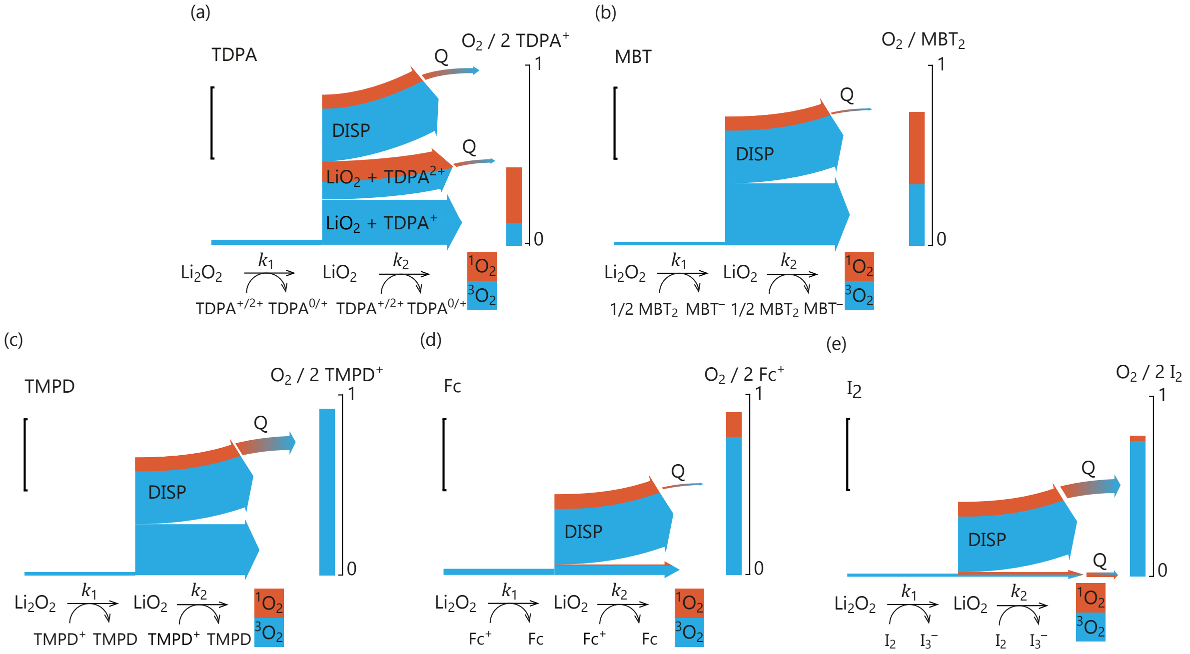

Figure E.13: **Sankey plots of relative reaction rates during mediated Li_2O_2 oxidation.** The width of the arrows is proportional to the rate assuming 10 mM of (a) $TDPA^+$, (b) MBT_2, (c) $TMPD^+$, (d) Fc^+ and (e) I_2. The vertical scale bar corresponds to 1×10^{-7} $mol{\cdot}cm^{-2}{\cdot}s^{-1}$. $^1O_2$ quenching by the mediator is denoted by Q. The $^3O_2$ and $^1O_2$ yields per 2 equivalent of oxidized mediators are given at the right of each panel.

The values for $TDPA^{2+}$ were chosen arbitrarily for the sake of the representation due to the mediator instability.

Bibliography

[1] E. Mourad, Y. K. Petit, C. Leypold, A. Windischbacher, D. Mijailovic, C. Slugovc, S. M. Borisov, E. Zojer, S. Brutti, O. Fontaine, and S. A. Freunberger, “Mechanism of mediated alkali peroxide oxidation reveals strategies to suppress singlet oxygen formation,” in revision.

Publications

The secret is comprised in three words — Work, finish, publish.
Michael Faraday

Peer reviewed papers

- B. Schafzahl, E. Mourad, L. Schafzahl, Y. K. Petit, A. R. Raju, M. O. Thotiyl, M. Wilkening, C. Slugovc, and S. A. Freunberger, “Quantifying total superoxide, peroxide, and carbonaceous compounds in metal–O_2 batteries and the solid electrolyte interphase,” ACS Energy Letters, vol. 3, no. 1, pp. 170–176, 2017.
- Y. K. Petit and S. A. Freunberger, “Thousands of cycles,” Nature materials, vol. 18, no. 4, p. 301, 2019.
- Y. K. Petit, C. Leypold, N. Mahne, E. Mourad, L. Schafzahl, C. Slugovc, S. M. Borisov, and S. A. Freunberger, “DABCOnium: an efficient and high-voltage stable singlet oxygen quencher for metal–O_2 cells,” Angewandte Chemie International Edition, vol. 58, no. 20, pp. 6535–6539, 2019.
- W.-J. Kwak, H. Kim, Y. K. Petit, C. Leypold, T. T. Nguyen, N. Mahne, P. Redfern, L. A. Curtiss, H.-G. Jung, S. M. Borisov, S. A. Freunberger and Y.-K. Sun, “Deactivation of redox mediators in lithium-oxygen batteries by singlet oxygen,” Nature communications, vol. 10, no. 1, p. 1380, 2019.
- E. Mourad, Y. K. Petit, R. Spezia, A. Samojlov, F. F. Summa, C. Prehal, C. Leypold, N. Mahne, C. Slugovc, O. Fontaine, S. Brutti and S. A. Freunberger, “Singlet oxygen from cation driven superoxide disproportionation and consequences for aprotic metal–O_2 batteries,” Energy & Environmental Science, vol. 12, no. 8, pp. 2559–2568, 2019.
- E. Mourad†, Y. K. Petit†, C. Leypold, A. Windischbacher, D. Mijailovic, C. Slugovc, S. M. Borisov, E. Zojer, S. Brutti, O. Fontaine, and S. A. Freunberger, “Mechanism of mediated alkali peroxide oxidation reveals strategies to suppress singlet oxygen formation,” in revision.

Other work

- Y. K. Petit, E. Mourad, and S. A. Freunberger, “Encyclopedia of electrochemistry, section on batteries, ch. 19 lithium–oxygen batteries,” in revision.

Selected talks and poster presentations

- "Singlet oxygen in non-aqueous battery: origin, consequences and mitigation," DocDays, Graz, Austria, 2019 (talk).
- "Singlet oxygen in non-aqueous battery: origin, consequences and mitigation," Journées d’électrochimie 2019, Toulouse, France, 2019 (talk).
- "Singlet oxygen in non-aqueous battery: origin, consequences and mitigation," Lithium Battery Discussions, Arcachon, France, 2019 (talk and poster).